# Power Generation by Resonant Self-Actuation

Zur Erlangung des akademischen Grades eines

**DOKTORS DER INGENIEURWISSENSCHAFTEN (Dr.-Ing.)**

von der KIT-Fakultät für Maschinenbau des

Karlsruher Instituts für Technologie (KIT)

genehmigte

**DISSERTATION**

von

MSc. Joel Joseph

Tag der mündlichen Prüfung:  05.09.2023

Hauptreferent:  Prof. Dr. Manfred Kohl

Korreferent:  Prof. Dr. Andrej Kitanovski

Karlsruher Institut für Technologie (KIT)

Institut für Mikrostrukturtechnik (IMT)

Hermann-von-Helmholtz-Platz 1

76344 Eggenstein-Leopoldshafen

For my family

# Acknowledgements

# Abstract

Research into micro energy harvesting systems has been driven by the need for self-sustaining, stable power sources for interconnected wireless sensors. Waste heat, particularly at temperatures below 200 °C, presents a promising but challenging energy source to recover using current conversion technology. The progress of high-performance thermomagnetic generators (TMGs) has been impeded by the lack of advancements in thermomagnetic materials. This study builds upon previous research on small-scale TMGs. The main objectives are;

- Development of a Lumped element model (LEM) simulation of the TMG to analyze and optimize the performance.
- Utilizing LEM and experiments to understand the effect of various design parameters.
- Upscaling of the TMG's active material volume to increase the absolute power output of a single device.
- Upscaling of TMG by operating multiple TMGs in parallel to increase the lateral size.
- Extending the operation range of heat source temperatures to near room temperatures without losing resonant self-actuation.

Experimental measurements and LEM simulations explore TMGs based on various materials such as the Ni-Mn-Ga Heusler alloy film, Gadolinium and La-Fe-Si-H. The effect of various design parameters on the performance of the TMG is investigated. LEM simulations describe the coupled dynamic properties of TMGs utilizing magnetic shape memory alloy (MSMA) films. The TMG employ self-actuation by leveraging temperature-dependent changes in magnetization and rapid heat transfer through thermomagnetic thin films.

Detailed LEM simulations examine the temperature change, magnetic field change, and resulting magnetization of the TM films over time and position. Optimal conditions for resonant self-actuation are achieved through careful device parameter design, leading to continuous, undamped oscillation of the cantilever. The thesis discusses various design parameters affecting resonant self-actuation for the case of Ni-Mn-Ga thin films, emphasizing the importance of fine-tuning each parameter for maximum output power. The impact of

factors like magnet, coil turns, cantilever stiffness, load resistance ($R_L$), Curie temperature ($T_c$), heat transfer coefficient ($h_f$), and thermal resistance ($R_b$) are investigated to understand their influence on the TMG performance. LEM simulations reveal critical values of $h_f$ and $R_b$ that enable stable energy generation with significant stroke and frequency, resulting in substantial electrical output.

Upscaling the TMG with Ni-Mn-Ga thin film demonstrates opposing effects on power output and footprint, with an improved electrical power per footprint achieved by increasing film thickness from 5 to 40 µm. At a temperature change of only 3 °C and a frequency of 146 Hz, values of 50 µW/cm$^2$ are achieved. The parallel architectures are essential for generating sufficient energy for direct application. Thermal cross coupling affects the dynamic performance and power output of TMGs operating in parallel. Notably, thermal effects become noticeable at low device separations and high heat source temperatures, but no magnetic or mechanical interaction is observed between the parallel-operating TMGs.

Using gadolinium as the active TM film, near-room temperature operation is possible at a low heat source temperature ($T_{source}$) of 40 °C. The TMG is able to generate 1.3 µW of power at a frequency of 54 Hz at this $T_{source}$, equivalent to a power output per footprint of 10 µW/cm$^2$. At a $T_{source}$ of 65 °C, this value sharply rises to 24 µW/cm$^2$ with an oscillation frequency of 117 Hz. Even though $T_{amb}$ of 11 °C is required for this optimum performance, the device can sustain resonant self-actuation up to an ambient temperature ($T_{amb}$) of 19 °C while still producing 8.7 µW/cm$^2$ of power for a $T_{source}$ of 50 °C. Moreover, the sharp boundaries of operation temperatures in terms of $T_{source}$ and $T_{amb}$ are investigated and presented. The TMG using hydrogenated La-Fe-Si alloys as active TM film can generate 38 µW/cm$^2$ from a $T_{source}$ of 90 °C while operating at a frequency of 137 Hz. TMGs are shown to be able to function across a broad range of $T_{source}$ temperatures while producing significant power output per device footprint. Thus, making them extremely competitive not just with other TMGs but also with the best commercially available thermoelectric generators.

# Kurzfassung

Die Forschung im Bereich der Mikro-Energiegewinnung wurde durch den Bedarf an autarken sowie stabilen Energiequellen für vernetzte und drahtlose Sensoren vorangetrieben. Abwärme, insbesondere bei Temperaturen unter 200 °C, stellt eine vielversprechende, aber mit den derzeitigen Umwandlungstechnologien schwer zu gewinnende Energiequelle dar. Der Fortschritt von thermomagnetischen Generatoren (TMGs) mit hoher Leistung wurde durch den Mangel an Weiterentwicklungen von thermomagnetischen Materialien behindert. Diese Arbeit stützt sich auf frühere Forschungsarbeiten zu TMGs im kleinen Maßstab. Die Hauptziele sind:

- Entwicklung eines LEM-Modells (Lumped Element Model) zur Simulation des TMG, um die Leistung zu analysieren und zu optimieren.

- Nutzung von LEM und Experimenten, um die Auswirkungen verschiedener Designparameter zu verstehen.

- Die Hochskalierung des Volumens des aktiven Materials eines TMG, um die absolute Ausgangsleistung eines einzelnen Generators zu erhöhen.

- Die Hochskalierung des TMG durch Parallelbetrieb mehrerer TMGs zur Vergrößerung der lateralen Größe.

- Erweiterung des Betriebsbereichs der Wärmequelle auf Temperaturen nahe der Raumtemperatur, ohne die resonante Selbstaktivierung zu verlieren.

Zunächst werden mittels experimenteller Messungen und LEM-Simulationen TMGs, die auf verschiedenen Materialien wie dem Ni-Mn-Ga Heusler-Legierungsfilm, Gadolinium und La-Fe-Si-H basieren, grundsätzlich erforscht. Die Auswirkung verschiedener Designparameter auf die Leistung des TMGs wird untersucht. Dabei beschreiben LEM-Simulationen die gekoppelten dynamischen Eigenschaften von TMGs, die Filme aus magnetischen Formgedächtnislegierungen (MSMA) verwenden. Die TMG nutzen Selbstaktivierung, indem ein temperaturabhängige Magnetisierungsänderungen und einen schnellen Wärmetransfer durch thermomagnetische Dünnschichten ausgenutzt wird.

Detaillierte LEM-Simulationen zeigen die Temperaturänderung, die Magnetfeldänderung und die daraus resultierende Magnetisierung der TM-Filme über Zeit und Position. Optimale Bedingungen für eine resonante Selbstaktivierung werden durch sorgfältiges Design der TMG-Parameter erreicht, was zu einer kontinuierlichen, ungedämpften Oszillation des TMG-Ausleger führt. In dieser Arbeit werden verschiedene Design-Parameter erörtert, die sich auf die resonante Selbstaktivierung im Falle von Ni-Mn-Ga-Dünnschichten auswirken, wobei die Bedeutung der Feinabstimmung jedes Parameters für eine maximale Ausgangsleistung hervorgehoben wird. Die Auswirkungen von Faktoren wie Magnet, Spulenwindungen, Auslegersteifigkeit, Lastwiderstand ($R_L$), Curie-Temperatur ($T_c$), Wärmeübergangskoeffizient ($h_f$) und Wärmewiderstand ($R_b$) werden untersucht, um ihren Einfluss auf die TMG-Leistung zu verstehen. LEM-Simulationen zeigen kritische Werte für $h_f$ und $R_b$, die eine stabile Energieerzeugung mit signifikantem Hub und Frequenz ermöglichen, was zu einer deutlichen Steigerung der elektrischen Leistung führt.

Die Hochskalierung des TMG mit Ni-Mn-Ga-Dünnschicht zeigt gegensätzliche Auswirkungen auf die Leistungsabgabe und die Grundfläche, wobei eine verbesserte elektrische Leistung pro Grundfläche durch eine Erhöhung der Schichtdicke von 5 auf 40 µm erreicht wird. Bei einer Temperaturänderung von nur 3 °C und einer Frequenz von 146 Hz werden Werte von 50 µW/cm$^2$ erreicht. Die parallelen Architekturen sind entscheidend für die Erzeugung ausreichender Energie für die direkte Anwendung. Die thermische Kreuzkopplung beeinträchtigt die dynamische Leistung und die Leistungsabgabe von parallel betriebenen TMGs. Thermische Effekte machen sich vor allem bei geringen Abständen zwischen den Bauelementen und hohen Temperaturen der Wärmequelle bemerkbar, wobei jedoch keine magnetischen oder mechanischen Wechselwirkungen zwischen den parallel arbeitenden TMGs beobachtet werden.

Bei Verwendung von Gadolinium als aktiver TM-Schicht ist ein Betrieb bei einer niedrigen Wärmequellentemperatur ($T_{source}$) von 40 °C möglich. Der TMG kann bei dieser $T_{source}$ eine Leistung von 1,3 µW bei einer Frequenz von 54 Hz erzeugen, was einer Ausgangsleistung von 10 µW/cm$^2$ pro Fläche entspricht. Bei einer $T_{source}$ von 65 °C steigt dieser Wert sprunghaft auf 24 µW/cm$^2$ bei einer Frequenz von 117 Hz an. Obwohl für eine optimale Leistung eine $T_{amb}$ von 11 °C erforderlich ist, kann das Bauelement die resonante Selbstaktivierung bis zu einer Umgebungstemperatur ($T_{amb}$) von 19 °C aufrechterhalten und dabei immer noch 8,7 µW/cm$^2$ Leistung bei einer $T_{source}$ von 50 °C erzeugen. Außerdem werden die scharfen Grenzen der Betriebstemperaturen in Bezug auf $T_{source}$ und $T_{amb}$ untersucht und vorgestellt. Ein TMG, bei den hydrierten La-Fe-Si-Legierungen als aktiven TM-Film verwendet, kann 38 µW/cm$^2$ aus einer $T_{source}$ von 90°C erzeugen, während es mit einer Frequenz von 137 Hz arbeitet.

# Publications

Parts of this thesis have been published in peer reviewed scientific journals and presented in scientific conferences by the author.

## Journal articles

"Upscaling of thermomagnetic generators based on Heusler alloy films"

**J. Joseph**, M. Ohtsuka, H. Miki, M. Kohl,

Joule, vol. 4, no. 12, p. 2718-2732, **2020**.

" Lumped Element Model for Thermomagnetic Generators Based on Magnetic SMA Films"

**J. Joseph**, M. Ohtsuka, H. Miki, M. Kohl,

Materials, vol. 14, no. 5, p. 1234, **2021**.

" Thermal Processes of Miniature Thermomagnetic Generators in Resonant Self-Actuation Mode"

**J. Joseph**, M. Ohtsuka, H. Miki, M. Kohl,

iScience, vol. 25, no. 7, p. 104569, **2022**.

" A Gd Film Thermomagnetic Generator in Resonant Self-Actuation mode"

**J. Joseph**, E. Fontana, T. Devillers, N. Dempsey, M. Kohl,

Advanced Functional Materials, vol. 13, no. 34, p. 2301250, **2023**

" Resonant Self-Actuation Based on Bistable Microswitching"

**J. Joseph**, M. Ohtsuka, H. Miki, M. Kohl,

Actuators, vol. 12, no.6, p. 245, **2023.**

"Energy Harvesting Using Magnetic Shape Memory Alloys"
M. Kohl, **J. Joseph**, L. Seigner
Encyclopedia of Smart Materials, vol. 4, p. 96-103, **2022**

# Conferences

## Proceedings

"Coupling Effects in Parallel Thermomagnetic Generators Based on Resonant Self-Actuation "

**J. Joseph**, M. Wehr, H. Miki, M. Ohtsuka, M. Kohl,

21st International Conference on Solid-State Sensors, Actuators and Microsystems (Transducers), pp. 463-466, **2021**.

## Oral presentations

 "Coupling Effects in Parallel Thermomagnetic Generators Based on Resonant Self-Actuation"

**J. Joseph**, M. Ohtsuka, H. Miki, M. Kohl

21st International Conference on Solid-State Sensors, Actuators and Microsystems (Transducers), **2021**.

"Thermomagnetic Thin Film Energy Harvester "

**J. Joseph**, M. Ohtsuka, H. Miki, M. Kohl

9th Forum on New Materials CIMTEC, **2022**.

"Thermal Processes in Thermomagnetic Energy Generators"

**J. Joseph**, M. Ohtsuka, H. Miki, M. Kohl

ELyT workshop, **2022**

"Miniature Thermomagnetic Generators with Resonant Self-Actuation"

**J. Joseph**, M. Kohl

International Conference on Ferromagnetic Shape Memory Alloys (ICFSMA), **2023**.

## Poster presentations

"Thermomagnetic Energy Generation by Magnetic Shape Memory Alloy Thin Film Actuation"

**J. Joseph**, M. Kohl

International Conference on Programmable Materials, **2022**

# Patents

J. Joseph, M. Kohl

"ACTUATION MECHANISM, ACTUATION DEVICE AND METHODS FOR USING SAID ACTUATION MECHANISM AND ACTUATION DEVICE"

Patent pending

# Abbreviations and parameters

| | | |
|---|---|---|
| LEM | - | Lumped element modeling |
| TMG | - | Thermomagnetic generators |
| TM | - | Thermomagnetic |
| $T_{amb}$ | - | Ambient temperature |
| $T_{source}$ | - | Source temperature |
| SMA | - | Shape memory alloy |
| $T_c$ | - | Curie temperature |
| c axis | - | Magnetic easy axis |
| Ni-Mn-Ga | - | Nickel manganese gallium alloy |
| Gd | - | Gadolinium |
| La-Fe-Si | - | Lanthanum iron silicon alloy |
| La-Fe-Si-H | - | Hydrogenated lanthanum iron silicon alloy |
| La-Fe-Mn-Si-H | - | Hydrogenated lanthanum iron manganese silicon alloys |
| TM film | - | Thermomagnetic material |
| SmCo | - | Samarium Cobalt magnets |
| NdFeB | - | Neodymium Iron Boron magnets |
| TM cycle | - | Thermomagnetic cycle |
| PDE | - | Partial differential equation |
| $h_f$ | - | Contact heat transfer coefficient |
| $T_{film}$ | - | Temperature of film |
| $R_b$ | - | Bonding layer thermal resistance |
| $R_L$ | - | Load resistance |
| $\Delta T$ | - | Temperature change in TM film |
| $T_{cant}$ | - | Cantilever temperature |

# Table of contents

# 1. Introduction

With the increase in IoT (Internet of Things) devices and connected technology, there is a growing need for energy in remote and hard-to-access places. Health monitoring of buildings by wireless sensor networks embedded inside constructions, wearable devices that are embedded with sensors to monitor human health, implantable devices, and smart home sensors are a few examples of devices that have such an energy demand.[1,2] These devices usually require electrical power in the range of tens of µW up to 100 mW.[3] Such high demands for remote access to energy are currently met by batteries but these pose a great disadvantage as it has limited storage capacity which means they have to be either recharged or replaced at regular intervals.[4] Thus, new innovative solutions to generate energy in situ from environmental sources are required if the world is moving towards a connected world which increases energy demand and at the same time needs to keep the goal of carbon neutralization in the near future[5].

## 1.1. Energy harvesting

Energy harvesting is a term used to define the collection of ambient energy in small amounts (in range of µWs to mWs) to power a remote wireless device where using batteries or wires is impractical. The principle is similar to large-scale renewable energy generation but at miniature scale.[6] Energy harvesters generate very low amounts of power at miniature  scale making it attractive for inaccessible devices and networks with a large number of nodes.[7] The block diagram shown in **Figure 1** illustrates a complete energy harvesting circuit. When an energy harvester or power generator is mentioned in this thesis, an energy converter is referred. There are several forms of ambient energy sources like mechanical energy in the form of vibrations, solar energy, wind energy, radio frequencies, and finally thermal energy.[6,8] The load system refers to a microsystem that needs

Energy source ➡ Energy Converter ➡ Input regulation ➡ Energy storage ➡ Output regulation ➡ Load system
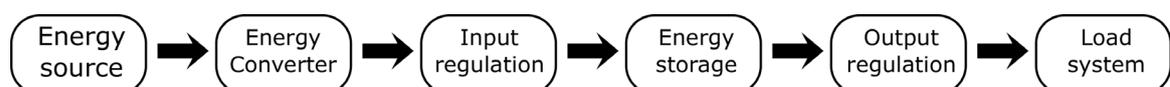
**Figure 1** Energy harvesting circuit adapted from Bader et al.[9]

1

very little amount of energy to operate like a wireless temperature sensor or a strain gauge. Most of these devices are on standby and only have an activity mode for a few milliseconds at regular intervals where it powers up, takes a reading, sends it wirelessly to a hub, and goes back to standby mode with very low power consumption.[10]

### 1.1.1. Kinetic power generation

Kinetic energy harvesters consist of devices that convert kinetic energy like mechanical vibrations or movements into electrical energy.[8,11] Vibrational devices convert ambient vibrations into electrical energy using electromagnetic induction[12] or by straining piezoelectric crystals.[13] There are piezoelectric energy harvesters that directly convert a mechanical strain into electrical energy.[14,15] Typical vibrational energy harvester contains a cantilever beam with an attached tip mass, which vibrates in response to ambient vibrations. The device only performs with high efficiency when the device resonance matches the ambient vibrations.[16] But there are also other forms of energy harvesters that harvest vibrational ambient energy.[17]

### 1.1.2. Solar power generation

Solar energy conversion by utilizing photoelectric conversion is one of the most common ways of energy harvesting.[18,19] Photovoltaic power generation is scalable to very large scales and there are several large solar power plants currently operating without output range of Megawatts around the world.[20] One of the advantages of a solar energy harvester is that it generates a DC output that can directly be utilized by microsystems. The disadvantage is that sunlight is only available during the day and inaccessible areas might not have adequate access to sunlight.

### 1.1.3. RF power generation

This is an interestingly popular research topic that has gained attention after the introduction of RFID technology (Radio Frequency Identification). But due to impedance mismatch and losses (e.g., conduction, thermal, reflective, conversion etc.) that affect the performance of an RF energy harvesting device, it is not widely adopted.[21] An RF harvesting device converts electromagnetic energy from the ambient into usable electrical energy in the form of DC voltage. One of the advantages of RF energy is that this is not limited by location or time of the day and is available outdoors and indoors throughout the day in most locations around the world.[22]

## 1.2. Thermal power generation

Thermal energy is abundantly available as ambient waste energy. Most of this energy is available in the low temperature regime of below 200 °C which falls below the range of normal power plants and conventional energy generation cycles.[23–25] This is of particular interest as a large proportion of energy consumed in the industrial sector and urban areas is rejected as waste heat. There are several forms of thermal energy harvesting principles, a few relevant principles will be introduced.

Thermoacoustic engines utilize sound waves to pump heat or use heat to pump sound waves. Typically, a gas-filled acoustic resonator is positioned appropriately with thermo-acoustic elements.[26] Thermogalvanic energy harvesting operates based on the dependence of electrode potential on temperature. An electrochemical cell is used to charge and discharge at different temperatures to create a cycle that will convert heat into electricity.[27] However, as the temperature gradient becomes small, the conversion of energy becomes inefficient.[28] The current state-of-the-art technology for energy harvesting at a miniature scale is thermoelectric generation using the Seebeck effect.[29–31] Thermoelectric devices can generate an electric potential from a constant temperature gradient. These devices suffer from scaling restrictions and low efficiency at low temperature differences.[32] Disadvantage of thermoelectric devices is the requirement for a large heat sink which usually is several times larger than the device itself to maintain a reasonable temperature gradient required for energy generation.[33] There are also other forms of thermal energy harvesters like pyroelectric energy harvesting which utilizes the pyroelectric effect.[34–36] Disadvantage is that it requires a temperature change ($\Delta T$) in the material to generate electricity, unlike TEG which only requires a constant gradient.

**Scaling requirements**

The energy harvesting devices typically need to be scaled according to the power requirement of the microsystem. Hence scalability is one of the major criteria that need to be fulfilled when considering an energy harvesting device.[37] Thermoelectric devices are not scalable to smaller dimensions due to the inability to maintain a temperature gradient without the use of a larger heat sink.[33] Thus, a sustainable energy harvesting device should possess an active heat dissipation mechanism that can maintain highly efficient power conversion even when scaled to miniature dimensions.

## 1.3.  Thin film microsystems

Miniaturization is considered a fundamental element of technological advancement, since more devices are being made in miniature scales to increase portability, decrease cost, and reduce weight.[38] The development of MEMS (micro-electro-mechanical systems) has pushed the technology to downsize rapidly. MEMS devices tend to be highly durable, portable, and only require a very small amount of energy to operate.[39] Thin film actuation plays an important role in microsystems developments due to the limited number of actuation mechanisms available at this dimensional scale. The major actuation mechanisms at the microscale include electrostatic and thermal micro-actuators. SMA actuators,[40,41] microscanners[42] and magnetic thin film actuators[43] based on thermomagnetic (TM) actuation utilize thin films to achieve small-scale actuation. Thin film devices have the advantage of a very large surface-to-volume ratio enabling a high frequency of operation due to the fast heat transfer. Thin films are usually fabricated by either vapor deposition, cold rolling, or melt spinning. More details about thin film fabrication are detailed in section **2.7.** Thin film fabrication is also quite straightforward, and most structures can be realized using laser machining or UV lithography followed by wet etching.[44,45]

### 1.3.1.  Smart materials

Thin film actuators and energy harvesters are fabricated out of smart materials. These are categorized as materials that exhibit multifunctional properties. Such materials show a significant change in their properties in response to an external stimulus in the form of a thermal, magnetic, electric, or mechanical stress field. The majority of smart materials are ferroic or multiferroic materials, which exhibit several ferroic properties like ferroelectricity, ferromagnetism or ferroelasticity. Such materials show a coupling between the primary order parameters and the multiferroic property, which allows the material to perform smart actuation.[46] **Figure 2** shows the coupling between thermal, magnetic, and mechanical properties of a multiferroic material. In this case, by changing the magnetic field, the magnetization of the material could be changed but at the same time, a strain can also be achieved in the material. Heusler alloys are a prime example of smart materials.[47] These are ordered intermetallics that exhibit multiferroic transformations as electronic spin interactions strongly depend on interatomic distances and local symmetry. Some of the examples of Heusler alloys are Ni-Mn-Z and Ni-Co-Mn-Z (Z=Ga, In, Sn, etc.) that exhibit giant effects including magnetic-field induced strains,[48] magnetoresistances,[49] magnetocaloric effects[50] and magnetic field induced shape memory effects.[51]
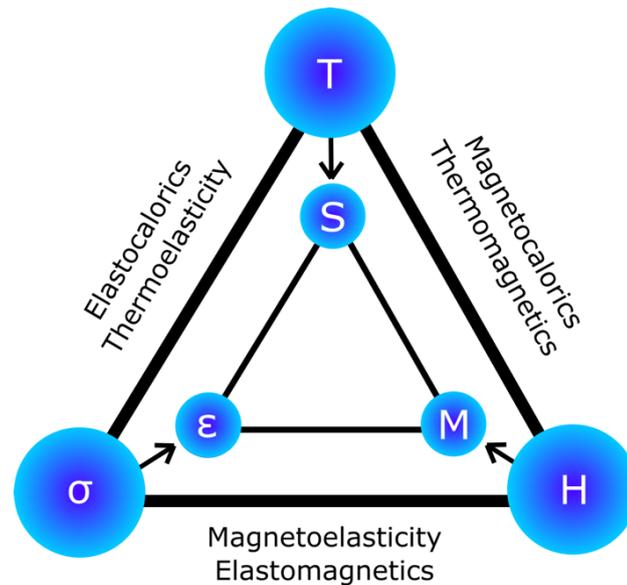
**Figure 2** Mechanical, magnetic, and thermal coupling in multiferroic materials.[52]

## 1.4.  Aim of this work

The overall goal of this work is to develop novel miniature thermomagnetic generators (TMGs) operating in resonant self-actuation mode that are scalable in terms of size and power output to suit the application. The are several objectives listed as follows:

- Using low-grade waste heat below 200 °C for power generation
- To develop a LEM model to represent the multiphysical characteristics of the TMG operation, so as to optimize and maintain resonant self-actuation, and large power output when the various device parameters are changed.
- To use LEM to analyze the thermal processes in the TMG.
- To utilize experimental measurements and LEM simulations to develop in depth understanding of effect of various TMG design parameters.
- To upscale the TMG's active material volume to increase the power output of a single device and to understand the effects of scaling on performance.
- To upscale the TMG in lateral size by operating TMGs in parallel to increase the overall output from the array and to understand the coupling effects.
- Maintain resonant self-actuation that results in large power output over a wide range of operating sources and ambient temperatures.
- To develop TMG's operating near room temperature while still maintaining resonant self-actuation even though the temperature change achieved in the active material volume would be small.

## 1.4.1. Outline of this document

Section **2** describes the relevant background information regarding TM energy generation, fabrication methods, and measurement techniques.

Section **3** presents different thermomagnetic generators that have been demonstrated in literature over the years. The previous generation of TMGs from the Smart Materials and Devices group in KIT is also presented, based on which this work has been completed.

Section **4** introduces the Lumped element model utilized to analyze the TMG performance and the thermal processes within the TMG. The operation principle of the TMG and results from the TMG using Ni-Mn-Ga is presented.

Section **5** discusses various parameters that have an impact on the performance of the TMG and ability to sustain resonant self-actuation. LEM simulation results for parameter study are presented.

Section **6** describes the upscaling of the TMG when the active material volume of the device is increased and when the lateral size is increased by multiple devices operating at close distances. The increase in power output and the coupling effects of multiple device operation are presented.

Section **7** describes TMGs operating near room temperature with Gadolinium film and La-Fe-Si film as active TM film materials. The performance of the TMG using Gd film and La-Fe-Si-H films are investigated. The boundary conditions observed are then analyzed.

Section **8** discusses the effects of different parameters and the performance of different TMGs.

Section **9** summarizes the presented results of the thesis.

# 2. Basic principles

The most important principles like ferromagnetism, shape memory effect, power conversion and heat transfer, and LEM modelling information that are relevant to this thesis will be described in this section.

## 2.1. Magnetism

There are several types of magnetism discovered and explained in physics like ferromagnetism, paramagnetism, diamagnetism, and antiferromagnetism. But ferromagnetism is the strongest type of magnetism of the group. When exposed to a magnetic field, ferromagnetic materials become highly magnetized. The magnetic moments of the atoms within ferromagnetic materials align in the same direction, producing a net magnetic field that is significantly larger than the applied magnetic field. Iron, cobalt, gadolinium, and nickel are some of the materials that are ferromagnetic in an elemental state. Ferromagnetism also depends on the lattice structure. A combination of non-magnetic materials could be ferromagnetic like Heusler alloys if they contain at least one ferromagnetic element, and a combination of magnetic materials could be non-ferromagnetic like stainless steel.[53–55]

### 2.1.1. Ferromagnetism

An electron carries a charge but also has a magnetic dipole moment. A magnetic dipole moment is a measure of the strength and orientation of a magnetic dipole. A magnetic dipole is a fundamental entity that consists of a current loop, or a pair of opposite magnetic poles separated by a small distance. When a magnetic dipole is placed in an external magnetic field, it experiences a torque that tends to align the dipole with the field. The electron acts like a small magnet producing its own magnetic field because of the quantum mechanical spin. This can either be pointing up or down depending on its state and is the source of ferromagnetism. The contribution from the orbital angular momentum of the electron when revolving around the nucleus also adds to the ferromagnetism.

9

For a magnetic dipole consisting of a pair of opposite magnetic poles separated by a distance d, the magnitude of the magnetic dipole moment is given by:[56]

$$m = I\,A.\hat{e}$$

where m is the magnetic dipole moment vector, I is the current flowing through the loop, and A is the area of the loop and $\hat{e}$ is the unit vector corresponding to the direction.

$$|m| = I\,A\,sin(\theta) = \mu\,d$$

where μ is the magnetic moment per unit volume and θ is the angle between the magnetic dipole moment vector and the direction of the external magnetic field, while d is the distance between magnetic poles.
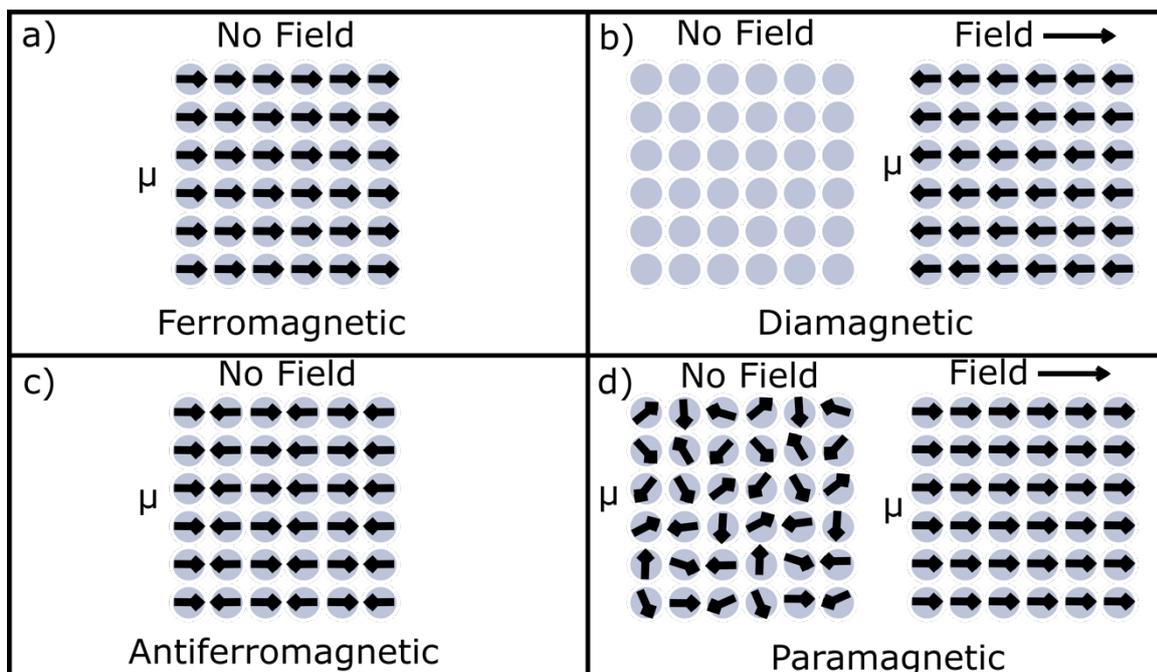


**Figure 3** Schematic diagram of magnetic dipole moment arrangement in various type of magnetic materials. Adapted from Hui et al.[57]

In a macroscopic view, a high field would be generated when magnetic dipoles of electrons in a piece of material are aligned in the same direction. But the electrons are always present in pairs of opposite spin, hence an atom with a filled shell would mean a total dipole moment of zero. But the material in which atoms have partially filled shells would have a net dipole moment. By Hund's rules,[58] the first few electrons in a shell tend to have the

same spin and hence the net dipole moment tends to be large. Exchange interaction, also known as exchange coupling, is a type of interaction between magnetic moments in a material. It results from the transfer of electrons between nearby atoms or ions, which can cause the alignment or anti-alignment of nearby magnetic moments. One common way to represent exchange interaction in a spin model is through the Heisenberg Hamiltonian equation, which is given by:[59]

$$H = -\sum J_{ij} \cdot \vec{S}i \cdot \vec{S}j - \mu\overrightarrow{B_a} \cdot \sum \vec{S}i$$

Eq ( 3 )

where $Si$ and $Sj$ are the spin vectors at sites $i$ and $j$, respectively, $\sum < i$, represents the sum over all nearest-neighbor pairs of spins, and $J$ is the exchange interaction energy. The exchange interaction energy $J$ in this Hamiltonian equation reflects the intensity of the contact between adjacent spins. $Si.Sj$ shows whether the interaction is ferromagnetic (positive number) or antiferromagnetic (negative value). The term "magnetic anisotropy" describes how a material's magnetic characteristics vary depending on its direction. It specifically refers to a material's propensity to exhibit various magnetic characteristics (such as magnetization or susceptibility) depending on the direction or orientation of the measurement. Although, exchange interaction keeps the magnetic dipoles aligned but not necessarily in any particular direction due to magnetic anisotropy.[60] **Figure 3** shows the magnetic dipole moment orientation in various materials. Ferromagnetic materials are usually divided into small regions or areas called magnetic domains as the exchange interaction is a short-range force. In other words, it is a small region within a material where the magnetic field created by the electrons in the atoms all point in the same direction. While, within these domains, the material tends to have spins aligned in one direction, these domains being not all aligned together would cause them to cancel each other and the effective magnetization would be either low or zero since the bulk material usually is found in its lowest energy state. These domains are not fixed in any way and can be altered by using an external magnetic field. When exposed to high external fields, the magnetic domains tend to reorient themselves to keep more of the dipoles in the same direction as the external field. This is called the magnetization of the material. Total Magnetization $\bar{M}$ of the material is given by Eq ( *4* ).

$$\bar{M} = N_{vol} < \bar{m} >$$

Eq ( 4 )

11

Usually, the material tends to return to its unmagnetized state once the magnetic field is removed. Materials that retain a large portion of magnetization upon removal of the external magnetic field are hard magnetic materials and are used to make permanent magnets which are used in induction motors and other magnetic applications. The remaining magnetic field in the material is known as the remanent magnetic field.

## 2.1.2. Curie temperature

First-order changes are distinguished by an abrupt shift between the two phases, during which the substance experiences a discontinuous change in its characteristics across the phase border. These transformations generally entail a shift in the material's internal energy and are followed by heat release or absorption. The melting of a solid to create a liquid is an established example of a first-order transformation. The solid experiences a first-order phase transition and melts into a liquid at the melting point, resulting in a significant change in the material's physical characteristics such as density, viscosity, and thermal conductivity. In contrast to first-order transition, second-order transitions are distinguished by a gradual shift in the properties of the substance rather than a sharp transition between discrete stages. These changes frequently involve a shift in the material's internal energy but do not usually involve the release or absorption of heat.[61,62] When the temperature of a material increases, random thermal motion, and entropy of material causes re-orientation of dipoles. When the temperature increases beyond a specific point (specific to the material), called Curie temperature ($T_c$), the material undergoes a second-order transformation losing its ability to maintain spontaneous magnetization. The material will still paramagnetically respond to external fields but will not attract to it like in the case of a ferromagnetic state. $T_c$ is a critical point at which the magnetic susceptibility is infinite in theory. Being a second-order transformation, the material transformation at $T_c$ is not associated with any hysteresis or latent heat.

## 2.2. Shape memory effect

### 2.2.1. The one-way shape memory effect

The one-way shape memory effect is the ability of a material to restore its original shape or configuration above a characteristic temperature. Shape memory alloys are a group of material alloys that exhibit shape memory effect. This ability has made SMAs interesting for a wide range of applications. The shape memory effect is shown in the stress-strain

curve of a typical SMA material in **Figure 4**. Let us assume a SMA material that is currently at a sufficiently low temperature denoted by point 1 in **Figure 4**. Martensitic phase transformation is a first-order solid-state phase transformation in which a parent phase changes crystal structure into a new phase. External variables such as mechanical deformation, thermal shifts, or chemical preparation can all cause this transition. The martensitic transition usually includes a rapid and irreversible shift in the material's crystal structure, resulting in a new metastable phase. The new low temperature phase, known as martensite, has a twisted and/or twinned crystal structure and can have distinct mechanical, electrical, and thermal characteristics. The martensite has a low symmetry lattice structure which allows for twin boundaries to be present, due to various orientations of the variants. Twin boundaries are interfaces or planes within a crystal where the orientations of two areas of the crystal lattice are different. These areas, known as twin domains, are mirror copies of each other across the twin boundary. The twin border is a narrow planar defect that divides the twin domains. These twin boundaries can move easily and cause reorientation of martensite. When this material is loaded, the initial response from the material is elastic and the material could be assumed to be in a phase of twinned martensite, where all several martensite variants exist together. Once the strain and stress reach point 2 in **Figure 4**, the material exhibits reordering of martensite variants and the response is similar to plastic deformation. The reordering is completed once the material reaches point 3 in **Figure 4**, after which the material behaves elastically when a further load is applied up to point 4.
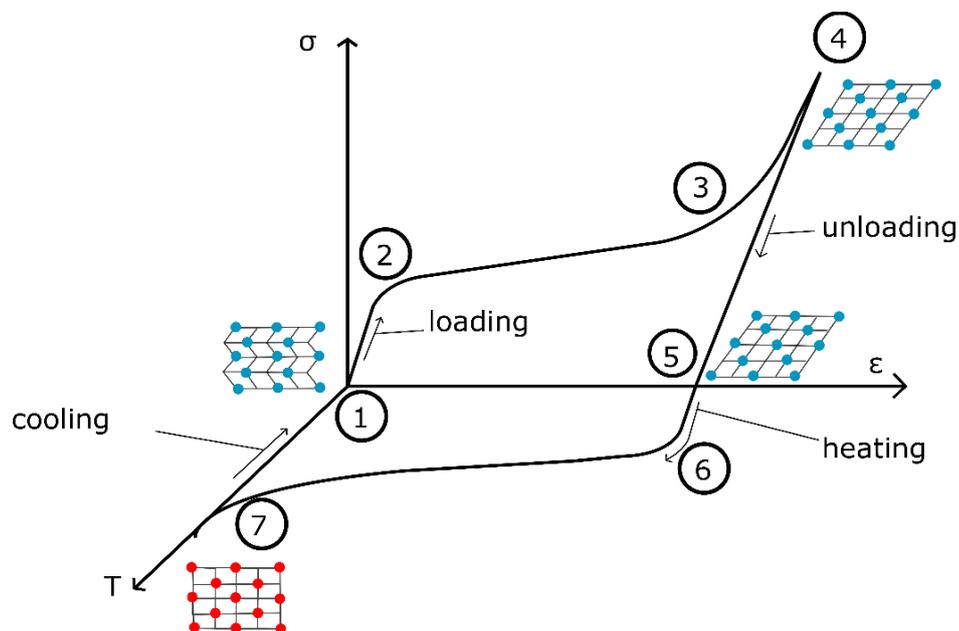


**Figure 4** Shape memory effect, the stress-strain-temperature diagram of the one-way effect of shape memory alloys (SMAs).[63]

The material has now been de-twinned completely by reorientation of various variants along the direction of the dominant variant. From point 4 to point 5 in **Figure 4**, the material is unloaded, and the resulting behavior exhibited by the material is elastic. But once it is fully unloaded a residual deformation remains in the material. This residual deformation could be reversed by heating the material above a specific temperature, denoted by point 6. After point 6 is reached the material experiences a phase change into de-twinned austenite. The lattice structure of austenite has high symmetry and thus only a single shape is possible at this high-temperature state. Further increase in temperature causes the material to completely transform into austenite at which point the material has also recovered its original shape completely. Cooling the material does not have any effect on the material shape and the material transforms into twinned martensite. This completes a closed loop and is also known as the one-way effect.

## 2.2.2. Superelasticity

The free energy equilibrium of martensite and austenite affect the transformation temperature of SMA. Superelasticity occurs when there is a change in external energy of the material by a mechanical load resulting in a shift of transformation temperatures. This effect is shown in **Figure 5**. When stress is applied to SMA in its austenite state, the material behaves elastically up to critical stress.
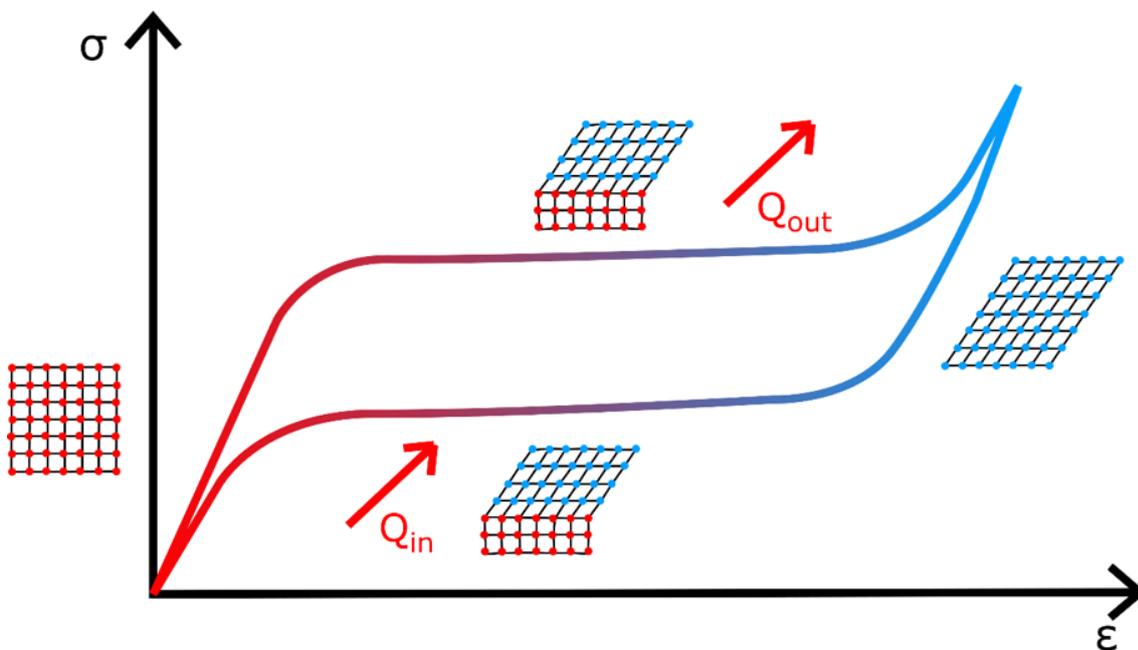


**Figure 5** SMA superelastic effect stress-strain characteristics.[64]

At critical stress, the material starts transforming to martensite, displaying a large change in strain and if further stress is applied, then the material transforms completely to martensite releasing heat in the process and elastic behavior reappear after transformation.

When the load is released, the material transforms back to austenite by absorbing energy, and the original shape is recovered. The large stress-strain plateau is shown in **Figure 5**. The heat release and heat absorption of material on loading and unloading of the material form the basis of elastocaloric effects.

## 2.3. Magnetic shape memory effect

In the conventional shape memory effect explained in section **2.2,** the material has high-temperature austenite and a low-temperature martensite phase. The switching between these two phases could either be driven by a change in temperature or by mechanical deformation. In Magnetic shape memory alloys, a magnetic field could be applied to initiate a field induced reorientation. When an external magnetic field is applied to the MSMA material, the magnetic domains reorient themselves in a particular direction (field induced reorientation), resulting in a shift in the shape or mechanical characteristics of the material.
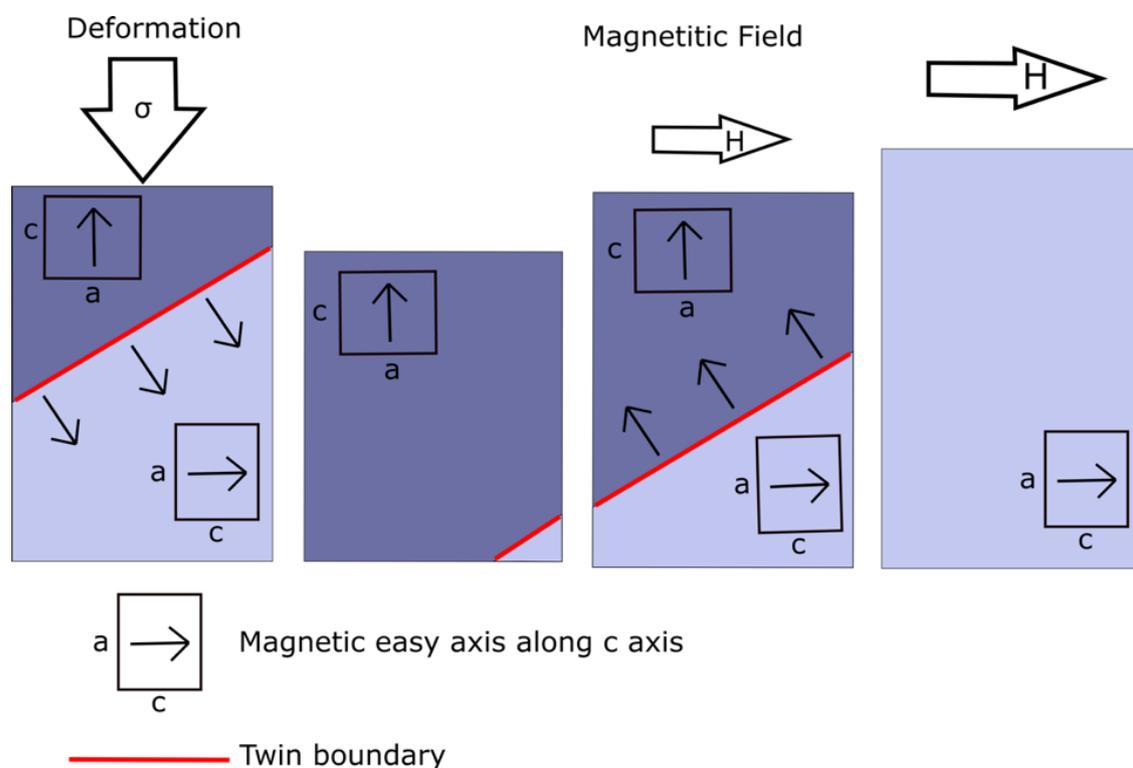


**Figure 6** Schematic diagram of the tetragonal structure of Ni-Mn-Ga single crystal showing reorientation.[3]

A typical schematic of a single crystal Ni-Mn-Ga is given in **Figure 6**. It can be seen that on the application of load, causing deformation in the material, the crystallographic variants are oriented along the direction of load with the magnetic easy axis (c axis) parallel to the force direction. Given its crystallographic structure or anisotropy, the magnetic easy axis is the direction in which the magnetic moment of the magnetic material chooses to position itself. It is the path along which the magnetization of the material needs the least amount of energy for alignment. The material remains in this state and the magnetic-field-induced-strain could be recovered by applying a magnetic field perpendicular to the c axis, which causes the magnetic domains to realign and results in a shift in the material's shape due to the magnetostriction effect. This reorients the c axis in the direction of the magnetic field. These transformations or reorientation of variants occurs in the material by a movement of twin boundaries. In contrast the magnetic properties of the material changes as the magnetic moments of the material are reoriented when it is subjected to a mechanical stress or strain. This inverse magnetostriction effect is called Villari effect and allows to control the magnetic properties of the material by using mechanical deformation.

## 2.3.1. Ferromagnetic shape memory alloys
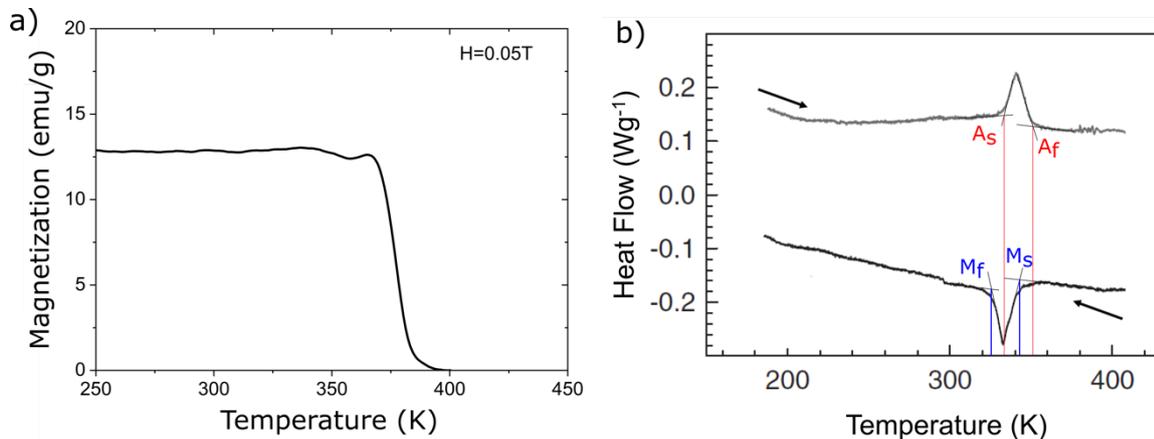


**Figure 7** material characterization of $Ni_{53.5}$-$Mn_{23.8}$-$Ga_{22.7}$ alloy, (a) Magnetization measurement with the second-order transformation, (b) Differential scanning calorimentry (DSC) measurement showing the first-order transformation. Adapted from Joseph et al.[28]

The discovery of large magnetically induced strains in Ni-Mn-Ga alloys by Ullakko et al.[48] showed that magnetostriction as a result of magnetic field induced reorientation takes place in such alloys up to a few percent have sparked high attention to such alloys. These

belong to the family of Heusler alloys that exhibit multiferroic phase transformations.[48,51,65,66] Such material is ferromagnetic in both martensitic austenitic phase and undergoes a second-order transformation at $T_c$, after which the magnetization of the material abruptly drops and becomes paramagnetic. **Figure 7**a shows the Ferromagnetic-paramagnetic phase transformation in Ni-Mn-Ga. The initial small change in magnetization denotes the first-order transformation in the material. The Differential scanning calorimetry (DSC) measurement curve in **Figure 7**b shows the martensitic start and finish temperatures, as well as the austenitic start and finish temperatures.

## 2.3.2. Metamagnetic shape memory alloys
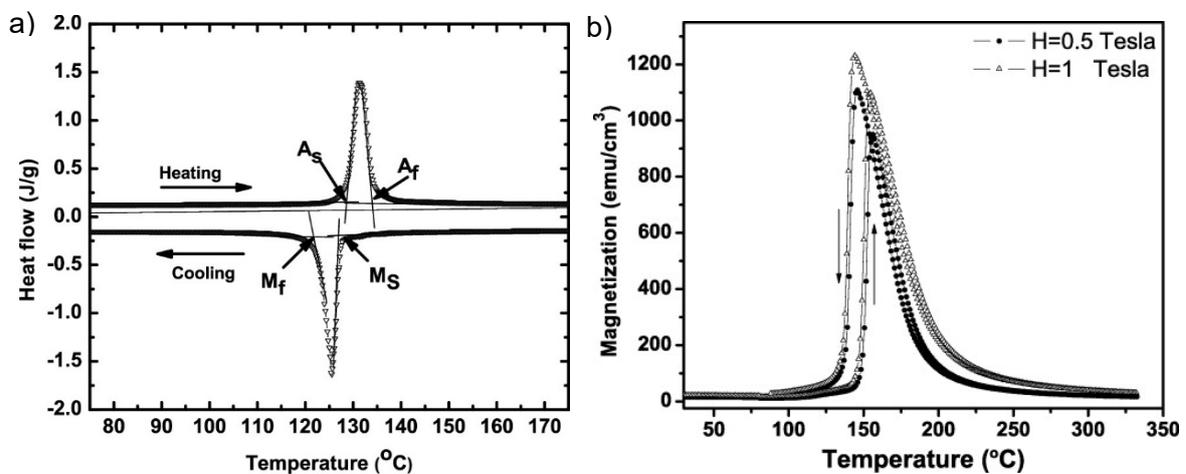


**Figure 8** (a)DSC measurement and (b) Magnetization measurement data for a sample of Ni$_{45}$Co$_5$Mn$_{40}$Sn$_{10}$.[67] Reprinted with permission from AIP Publishing.

Metamagnetic shape memory alloys are a subset of magnetic shape memory alloys that are not ferromagnetic shape memory alloys. Ni-Mn-X (X=In, Sb, Sn) is a representative material of the category.[68] These materials tend to have para or antiferromagnetic martensitic phase and the austenitic phase is ferromagnetic below the $T_c$. Such materials have a large rapid change in magnetization at the phase transformation, this can be observed in **Figure 8**b. But in this case, the material has latent heat and hysteresis associated with the transformation, being a first-order transformation. The quantity of heat energy absorbed or released during the phase transformation of a material without producing a change in its temperature is referred to as latent heat. While the phenomenon of hysteresis describes how a material's response to a specific stimulus, such as temperature, pressure, or magnetic field, relies on its history of exposure to that stimulus. The hysteresis can be tuned by changing the lattice parameters of martensite and austenite unit cells.[67] **Figure 7**a

shows the DSC measurement which shows the latent heat associated with the transformation and **Figure 8**b shows the magnetization data plotted against temperature. The austenite phase experiences a reduction in magnetization with an increase in temperature at $T_c$.

# 2.4. Energy conversion to electrical energy

## 2.4.1. Electromagnetic induction

The physical interaction that is observed in electrically charged particles moving through a magnetic field is commonly called electromagnetic force or Lorentz force. This has magnetic and electric components and plays an important role in determining the force on a moving point charge in an electromagnetic field. The magnitude of the Lorentz force on a charged particle is provided by the equation:[53]

$$F = q(v \times B)$$

Eq ( 5 )

Where F represents the force, q represents the particle's charge, v represents its velocity, and B represents the magnetic field. The right-hand formula determines the force orientation, which is perpendicular to both the velocity vector and the magnetic field vector. The process of producing an electric current in a circuit by varying the magnetic field through the circuit is known as electromagnetic induction. Faraday's rule of induction states that the electromotive force (EMF) generated in a circuit is proportional to the rate of change of the magnetic flux through the circuit. Electromagnetic induction is the fundamental operating principle of transformers, inductors, electrical motors, generators, and solenoids. It is also known as Faraday's Induction.[69] Faraday's law of induction explains how an emf is generated in a conductive loop when the magnetic flux through the surface enclosed by the loop is varied in time.

$$EMF = -d\Phi/dt$$

Eq ( 6 )

Where EMF is the electromotive force, Φ is the magnetic flux, and dt is the time interval over which the magnetic flux changes. It also works in reverse and magnetic flux can be

generated by a conductive loop which is the working principle of solenoids. The emf generated will try to resist the varying magnetic field and hence this principle is used for damping applications. [70]

## 2.4.2. Pyroelectricity

Polarization is the separation of positive and negative charges in a material, which produces an electric dipole moment. When the material is polarized, it acquires a net electric charge, with one end of the material positive and the other end negative. Pyroelectric effect is observed in polarized materials and can be explained as the change in polarization due to the temperature change.[71] This change in polarization results from a reorganization of electric charges in the material, produced by a temperature-induced shift in crystal symmetry. This shift in polarization can be detected as a shift in the electric charge on the material's surface. There are two main effects:

- Direct effect- the temperature induced shift in charge distribution.
- Indirect effect – The change in temperature causes temperature induced strain in the material and this results in strain induced polarization of the material.

Materials that exhibit the pyroelectric effect are called pyroelectric materials and the change in electric charge per unit area of surface for a temperature change (ΔT) of 1 °C is known as the pyroelectric coefficient. Polarization change of the material is given by:[72]

$$\Delta P = p.\Delta T$$

<div align="right">Eq ( 7 )</div>

Where $\Delta P$ denotes polarization and $\Delta T$ denotes temperature, while $p$ is the pyroelectric coefficient. Eq ( 7 ) explains the linear connection between polarization and temperature in a pyroelectric substance and can be used to compute polarization at a given temperature or to calculate temperature change based on observed polarization change.
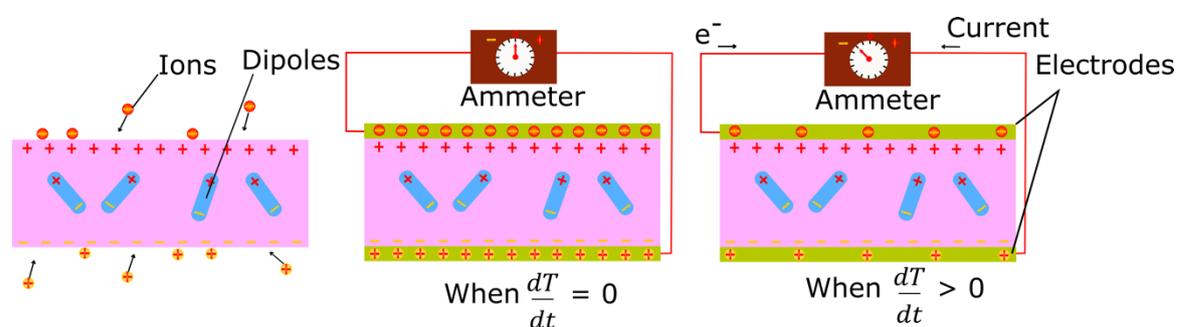


**Figure 9** Schematic of pyroelectric effect. Adapted from Whatmore et al. [73]

The change in surface charge is collected by using an electrode coating on the surface and this develops a potential whenever the material experiences a ΔT. [72]

$$\Delta Q \;=\; p \times A \times \Delta T$$

<div align="right">Eq ( 8 )</div>

Where, Q is the electric charge generated, $p$ is the pyroelectric coefficient, which is a material-specific constant that relates the change in electric polarization to the change in temperature, ΔT is the change in temperature and $A$ is the surface area of the material. According to Eq ( *8* ), the amount of the electric charge produced by the pyroelectric effect is proportional to the pyroelectric coefficient and the temperature change. **Figure 9** explains the simple working principle of a pyroelectric effect.

## 2.5. Heat transfer

Heat transfer is the term used to broadly describe the various processes by which thermal energy is transferred either within the material or from one material to another. There are three types of heat transfer mechanisms or processes, conduction, convection, and radiation. Heat transfer by conduction is the result of mutual interaction of vibrating atoms without changing their mean position. This type of heat transfer mechanism is only observed in solids. Contact heat transfer is a special case of heat transfer by conduction in which one material is in contact with another (without bonding and sometimes intermittent). Contact heat transfer would be further explained in detail in Section **2.5.4.**

Heat transfer by convection involves the movement of atoms or molecules (also aggregates of molecules) carrying the heat from one position to another. Such heat transfer is observed in liquids and gases. Convective heat transfer can also occur at the boundary between solids and liquids/gases. Radiative heat transfer is a heat transfer mechanism through space as photons of electromagnetic radiations of wavelengths of more than 10000 Å. Unlike conduction and convection which require a medium for transfer of heat from one position to another, the radiative heat transfer can occur without any material medium present and no physical contact is required between the two materials (or objects) between which the heat transfer is occurring.[74]

## 2.5.1. Conductive heat transfer

Conductive heat transfer, also known as thermal conduction, is the movement of thermal energy between objects in direct contact with each other or between various temperature zones within a single object. Heat is transmitted through conduction in a solid substance by the impact of vibrating atoms and free electrons with adjacent atoms and electrons. Thermal energy is moved from the hotter to the colder regions of the item until the temperature is uniform throughout. Fourier's law governs the rate of heat transfer by conduction, which says that the rate of heat transfer is proportional to the temperature difference in the direction of heat movement and thermal conductivity of the substance, while inversely proportional to the distance. Mathematically, Fourier's law can be written as:[75]

$$q = -kA(dT/dx)$$

Eq ( 9 )

Where, $q$ is the heat flow, $k$ is the thermal conductivity of the material, $A$ is the cross-sectional area through which heat flows, $dT/dx$ is the temperature gradient in the direction of heat flow.

## 2.5.2. Convective heat transfer

Convection is the heat transmission between a solid surface and a moving fluid (liquid or vapor). It happens when the temperature of the solid surface and the fluid differs, causing the fluid to flow and transfer heat away from the surface. Convection heat transfer entails both the transfer of energy through heat transmission between the solid surface and the neighboring fluid layer and the transfer of energy through fluid motion. The rate of heat transmission by convection is determined by fluid characteristics such as velocity, temperature, and viscosity, as well as solid surface geometry and flow circumstances. Convective heat transfer $Q$ is given by:[76]

$$Q = h * A * (T_s - T_f)$$

Eq ( 10 )

Where, Q is the heat flow, h is the convective heat transfer coefficient, A is the surface area of the solid in contact with the fluid, $T_s$ is the temperature of the solid surface, $T_f$ is the temperature of the fluid.

## 2.5.3. Thermal capacity

Thermal capacity of a material is the amount of heat that needs to be transferred to the material in order to increase its temperature by 1 °C. The specific heat capacity is the amount of heat that is required to increase the temperature of a unit mass of the material by 1 °C. Thermal capacity per unit volume can be calculated by multiplying specific thermal capacity by the material density. Thermal heat capacity of a sample of material is denoted by $C_p$ and is given by:[76]

$$C_p = \lim_{\Delta T \to 0} \frac{\Delta Q}{\Delta T}$$

Eq ( 11 )

Where the amount of heat that must be added to the material sample (of mass M) in order to increase its temperature by ΔT is denoted by ΔQ. Based on the material sample's initial temperature (T) and the pressure (P) that is being applied to it, the value of $C_p$ often varies significantly.

## 2.5.2. Thermal conductivity

The thermal conductivity of a material defines the ability of a material to conduct heat. It is the ratio of heat flow through the unit area of a material to the temperature difference across its two surfaces. This relation is given by the equation Eq ( *12* ) which is derived from Fourier's Law given in Eq ( *9* ). It is a material property, and the negative sign indicates that the flow of heat is from the high-temperature to the low-temperature side.[75]

$$\kappa = -\frac{Q}{\nabla T}$$

Eq ( 12 )

Where $Q$ is the heat flow through the material, $\kappa$ is the thermal conductivity of the material, and $\nabla T$ is the temperature gradient between the two surfaces of the material. Under steady-state conditions, the value of the temperature gradient remains constant, and this results in a constant heat flow through the material. But in the case of changing temperature gradient in a general transient state, Eq ( *13* ) describes the heat transfer through the material. [75]

$$\left(\rho C_p \, {\partial T}/{\partial t}\right) = \kappa \, * \, \left(\frac{\partial^2 T}{\partial x^2} + \frac{\partial^2 T}{\partial y^2} + \frac{\partial^2 T}{\partial z^2}\right) = \nabla(\kappa \nabla T)$$

Eq ( 13 )

The transient temperature distribution within a material over time when heat conduction is not in a steady state is given by Eq ( *13* ), and this depends on the density of the material ($\rho$), the thermal capacity of the material ($C_p$), the spatial gradient and the thermal conductivity of the material ($\nabla(\kappa \nabla T)$). The heat flow in the material and $\nabla T$ experienced by the material will follow Eq ( *13* ) whenever the material is exposed to a disturbance in the steady state condition either by intermittent contact with a heat source or sink, or by internal heat generation or a change in boundary conditions until a steady state temperature distribution can be reached again.

## 2.5.3. Thermal resistance

Thermal resistance describes how effectively the material or component opposes against the transfer of heat through it. Materials with very high thermal resistance per unit length are called insulators and materials with low thermal resistance per unit length are called thermal conductors. Thermal resistance can be calculated by Eq ( *14* ). [77]

$$R = \frac{l}{\kappa A}$$

Eq ( 14 )

Where $l$ is the thickness of the material, $\kappa$ is the thermal conductivity of the material and $A$ is the area of the material side (cross-sectional area). This shows that thermal resistance is inversely proportional to thermal conductivity which is a material property. Since the thermal resistance also has dimensional dependence like cross-sectional area and thickness, it is possible to tune the thermal resistance by tuning the dimensions.

## 2.5.4. Contact resistance

When two solid surfaces are in contact, the actual contact occurs only in discrete spots of micro areas and the rest of the space is either filled with vacuum or with some other media (air, water, oil etc.) due to the roughness that is present in the solid surfaces. This media would have a thermal conductivity that may be largely different from the thermal conductivity of the solids in contact and hence would influence the heat transfer through such a

contact. The limitation in heat transfer due to the influence of the interface material (media or vacuum) is called thermal contact resistance. In classical heat transfer, conduction, convection, and radiation are the three mechanisms by which heat is transferred. In this case, it could be similar but, in most cases, only conduction needs to be considered since the convection and radiation at this interface is negligible compared to conduction.[78]

**Figure 10** shows the micro area contact between surfaces. The total heat transfer will be the sum of all the individual heat transfers through the microcontact areas. The rate of contact heat transfer between two surfaces can be estimated using the following equation:

$$Q = h * A * \Delta T$$

Eq ( 15 )

Where, Q is the heat flow between the two surfaces, h is the overall heat transfer coefficient, which includes the contributions of both materials in contact, A is the actual contact area between the two surfaces, ΔT is the temperature difference between the two surfaces. The overall heat transfer coefficient (h) depends on the thermal conductivity and roughness of each material surface in contact, as well as the nature of the contact between the two surfaces (such as whether there is air or other fluids present in between).
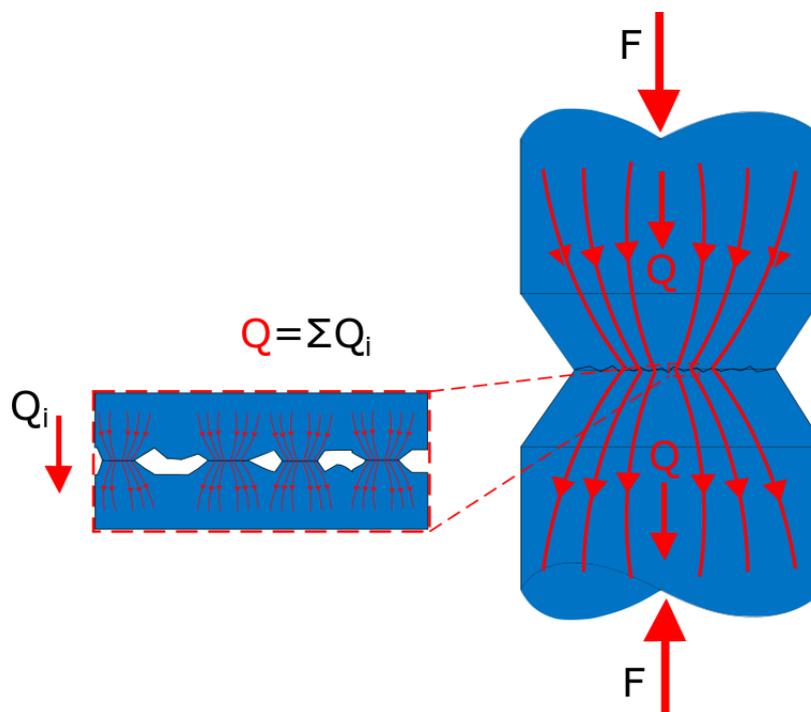


**Figure 10** Contact heat transfer between the solid surfaces in contact. Adapted from Wang et al.[78]

## 2.6. Lumped element modeling

In electrical and electronic systems, resistance is considered to be a single physical component with linear relation $V = IR$, but this involves interactions of atoms and electrons with enormous complexity in geometry, random thermal motion, and collisions. This type of simplification by the concept of the "law of large numbers" in probability allows us to make a simplified model of a complex system by breaking it down into discrete blocks with a few inputs and outputs. Each block would describe the behavior of a discrete element at an average or aggregate level by employing algebraic, numerical of conceptual abstractions. If the limits of those abstractions and approximations are understood and employed properly, these blocks can be cascaded together by using their inputs and outputs. A perfect lumped element model would be the simplest model that can be used to design or analyze a complex system but not simpler as this would cause errors to get cascaded and approximations would start to deviate the solution too much from the actual solution.

### 2.6.1. Mechanical systems

A mechanical system with elastic behavior, several damping factors, and attached mass can be simplified into a spring mass damper system. For example, a cantilever beam that bends upwards would have its tip moving in two dimensions. But this could be simplified into a one-dimensional spring damper system. With the addition of tip mass and cantilever mass into the equation, this would represent the oscillatory behavior of the system. Such systems could be used to describe complex dynamic systems by simplifying them into manageable spring mass damper systems.

### 2.6.2. Thermal equivalent circuits

When heat flow is considered to be analogous to electric current, the voltage will be analogous to temperature and the thermal resistance and thermal mass will be analogous to resistance and capacitance. Thus, a complex heat transfer problem can be broken down into blocks of electrically equivalent components and a circuit could be designed that would represent the heat flow and ΔT in a device. Such thermal equivalent circuits are used commonly to solve complex heat transfer problems. In the course of this thesis, MATLAB SIMULINK (SIMCSAPE) is used to design and evaluate thermal circuits to describe the device's heat transfer characteristics. Commonly used approaches include Foster and Cauer thermal networks.[79]

## 2.7. Fabrication methods

Several fabrication methods are used either directly at IMT or at partner universities to fabricate the films, cantilever, pick-up coil, and substrates of the device. The following section outlines the important fabrication methods.

### 2.7.1. Magnetron sputtering

Magnetron sputtering is a physical vapor deposition method that falls under the category of vacuum coating techniques. This method is commonly used to deposit metals, alloys, and other compounds onto a wide variety of materials and up to a thickness of a millimeter. This method, although developed as a coating technique is used to deposit thin films on substrates that can be later released to have free-standing thin films. Magnetron sputtering is capable of producing thin coatings ranging in thickness from a few nanometers to several micrometers. However, parameters such as deposition rate, uniformity of deposition, and target substance can restrict the thickness range.[80] The high deposition rates, ease of sputtering any metal, high adhesion of films, and high purity film deposition make it very attractive over other deposition methods to fabricate thin films of materials.
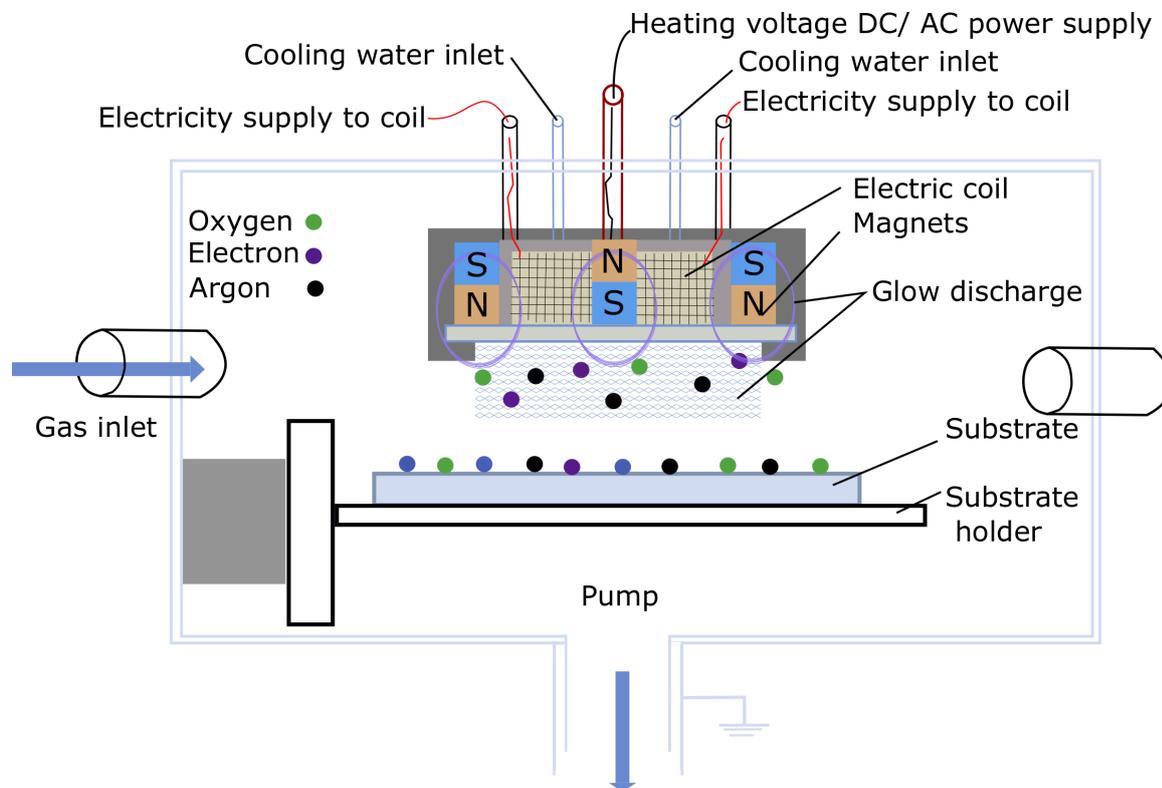


**Figure 11** Schematic of Magnetron Sputtering. Adapted from Hassan et al.[81]

**Figure 11** shows the schematic of the magnetron sputtering machine. When power is supplied to the magnetron, the target is supplied with a negative voltage (typically 300 V or higher). This negative voltage pulls positive ions to the target surface, generating a lot of kinetic energy at the same time. When a positive ion collides with atoms at the surface of a solid, an energy transfer occurs. Primary recoil atoms can be formed if the energy delivered to a lattice site is larger than the binding energy. These atoms can then collide with other atoms and disperse their energy via collision cascades. If the energy transferred in a direction normal to the surface is three times the surface binding energy, sputtering occurs (approximately equal to the heat of sublimation).[82]

One of the probable outcomes of ion bombardment of a surface is the sputtering of a target atom. Aside from sputtering, the emission of secondary electrons from the target surface is another significant activity. The glow discharge can be prolonged thanks to these secondary electrons. The target materials for the sputtering process are nearly limitless, ranging from pure metals that can be sprayed with DC power to semiconductors and isolators that require either RF power or pulsed DC. Deposition can be done with single or multi-elemental targets in either nonreactive (inert gas only) or reactive (inert and reactive gas) discharges.[82]

## 2.7.2. Melt spinning

The melt spinning method is used to rapidly solidify metallic alloys by melting the metal and then fast cooling it by exposing it to a revolving wheel or cylinder chilled by a stream of gas or liquid. The molten metal is swiftly quenched when it comes into contact with the spinning wheel, resulting in a fine-grained solidified substance with unique characteristics. The method is frequently employed in the manufacturing of amorphous metallic alloys, also known as metallic glasses, which have mechanical, physical, and chemical characteristics that differ from those of typical crystalline metals. Unfortunately, only the side of the ribbon that touches the wheel directly is completely amorphous. Amorphous metallic alloys may be manufactured in a number of forms, such as ribbons, wires, and powders, and are utilized in a variety of applications. The melt spinning process offers several advantages, including the capacity to generate huge amounts of material in a short period of time and materials with unique qualities that are not achievable with typical casting and processing procedures. However, the process is difficult, necessitating precise control of the temperature, cooling rate, and other process factors in order to generate materials with the appropriate qualities. **Figure 12** illustrates the schematic of melt spinning.
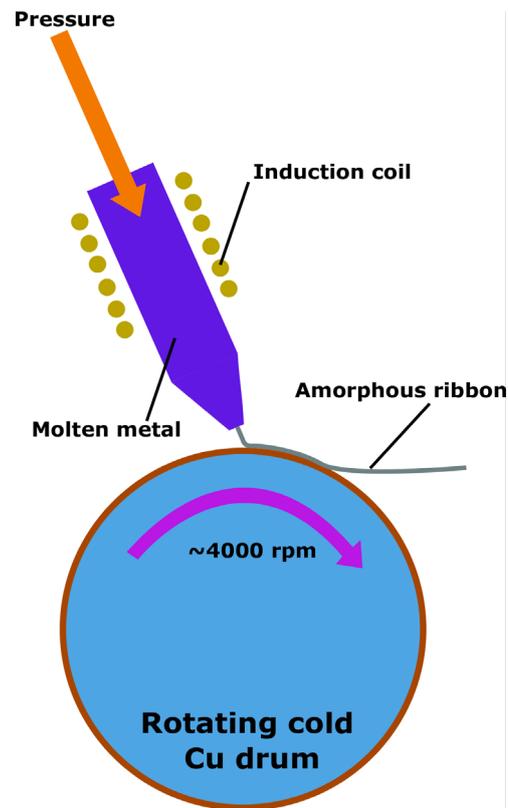
**Figure 12** Schematic of fabrication by melt spinning.

## 2.7.3. 3D printing

Additive manufacturing (also known as 3D printing) is a parallel design and production process that incorporates materials, structures, and functions. 3D printing works by placing consecutive layers of material to create a three-dimensional structure. Fused deposition modeling, inkjet printing, selective laser sintering, electron beam melting, stereolithography, and digital light processing are some of the 3D printing processes available. Typically, polymers are used as printing material either as filaments or in liquid resin form that is cured using UV light. However, selective laser sintering and electron beam melting are commonly used to print metal parts.

Recently magnetic shape memory alloys have been 3D printed.[83] Induction melting of high purity Ni, Mn, and Ga elements in an argon environment produces Ni-Mn-Ga polycrystal-line ingots. A Retsch planetary mill is used to crush and ball grind Ni-Mn-Ga ingots for 3 hours. Sieving is used to obtain a powder with a particle size of less than the desired limit.

These powders are used to 3D print Ni-Mn-Ga magnetic shape memory alloys with regulated densities ranging from 45 to 99 percent using binder jet printing. The 3D printed Ni-Mn-Ga alloy is then subsequently sintered to avoid oxidation, composition changes, and gradients. Further information regarding the 3D printing of magnetic shape memory films and their properties can be found in Mostafaei et al.[83]

## 2.7.4. Heat treatment

Heat treatment is an effective method used to achieve the desired mechanical properties for metallic alloys. The phase transformations occurring within the material can be fine-tuned by controlling the temperature and time of heat treatment. Both the temperature and time need to be precisely controlled to achieve repeatable results for the material properties. Heat treatment can produce a variety of alterations in the microstructure of the SMA film, including recrystallization, grain growth, and phase transition. In the instance of a nickel-titanium (Ni-Ti) SMA, the heat treatment procedure can result in the creation of a crystalline phase known as R-phase, which improves the shape memory effect. The heat treatment procedure can also enhance the SMA film's mechanical characteristics, such as rigidity and ductility. The chemical composition of the magnetron sputter deposited films is determined by the sputtering power, and the thickness of the film is determined by the duration of sputtering. The material properties of the deposited films can be adjusted by heat treatment post deposition. As an example, in Ohtsuka et al. [84] the martensite phase was changed from cubic to tetragonal after heat treatment which is confirmed using XRD measurements. The deposited films had columnar grain structure as deposited, which increased in its width upon heat treatment. The heat treatment would slightly change the composition if any of the contents are evaporating at high temperatures.[84] In some cases heat treatment process results in an increase in magnetization of the Ni-Mn-Ga films and sharper transition with higher magnetization change per unit change in temperature. [85]

## 2.7.5. Optical lithography

Optical lithography is a method used to pattern and copy a desired image onto a substrate, such as a silicon wafer. A chemical compound called photoresist, which is light-sensitive, is coated on a surface or substrate. Usually, photoresist is coated on the substrate surface using spin coating process. The photoresist will be exposed either by using a mask in case of UV lithography or directly writing on the resist by using a UV laser in case of multiphoton lithography.
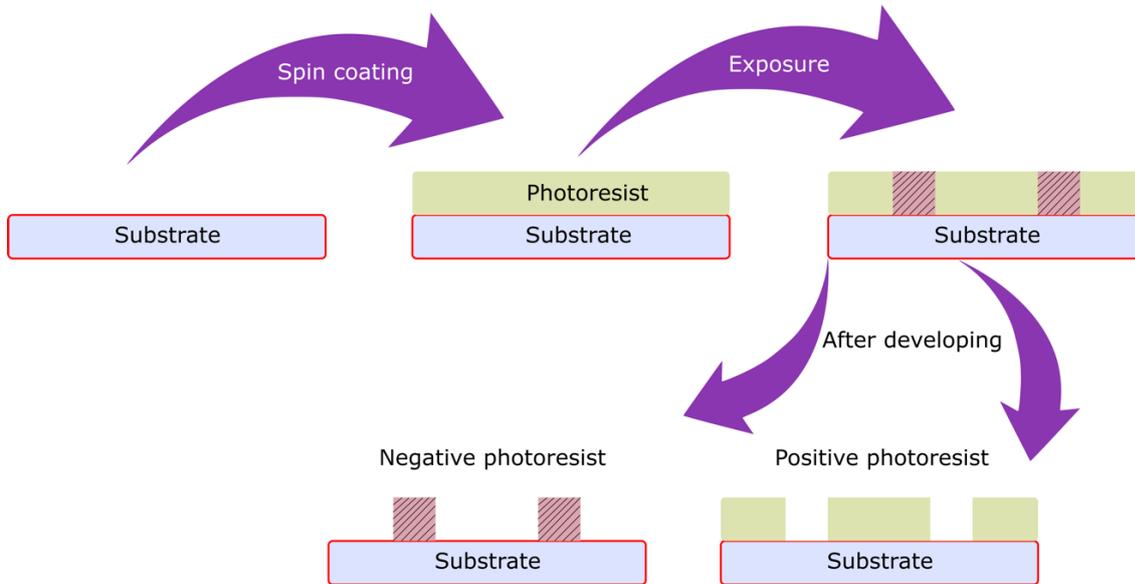
**Figure 13** Schematic of fabrication using a lithography process.

Both of the methods will result in a 2D image of the structure being transferred to the resist layer. This layer is then developed using a suitable developing solution removing either the exposed areas in case of positive resist or the unexposed areas in case of negative resist. The selection and application of a positive or negative resist depends on by the intended design and the processing specifications. Positive resists are usually used for simpler patterns with bigger features, whereas negative resists are used for more complicated patterns with smaller features. **Figure 13** shows the process flow diagram for optical lithography by which a pattern can be impressed on the photoresist.

### 2.7.5.1. UV lithography

UV lithography uses electromagnetic waves of ultraviolet wavelengths to produce a pattern on the spin-coated photoresist. A photomask is used to generate the pattern on the photoresist by blocking some areas and exposing other areas selectively as shown in **Figure 14**. Light diffraction restricts optical system resolution, which limits the smallest feature size that can be resolved. The Abbe diffraction limit determines the diffraction limit, which is affected by the wavelength of light used for the procedure.[86]

UV lithography is a common procedure used in the semiconductor industry to create integrated circuits (ICs). It's also utilized to make microelectromechanical systems (MEMS), microfluidic devices, and other micro- and nano-scale structures. It is a popular choice for many applications due to its high resolution, rapid throughput, and outstanding repeatability.
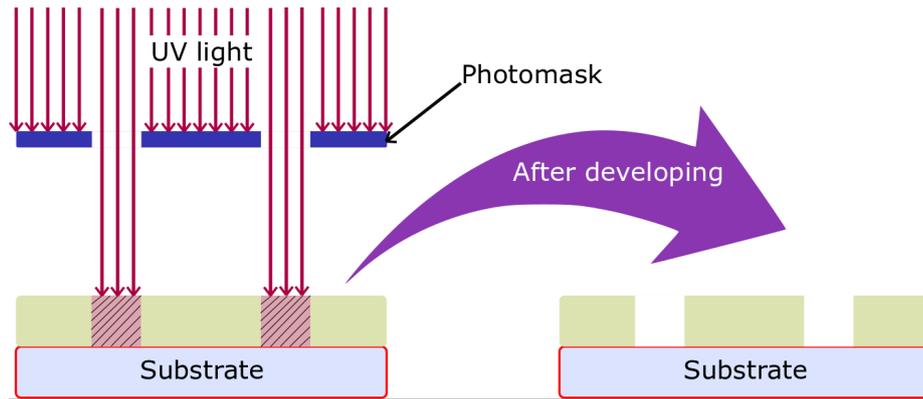
**Figure 14** Schematic using UV lithography.

## 2.7.5.2. Multiphoton lithography

Multiphoton lithography also known as direct laser writing is a process of exposing negative-tone or positive-tone photoresists with laser light of a certain wavelength. Structuring is performed similarly to conventional photolithography methods. However, the avoidance of reticles or photomask is the key distinction. In place of that, two-photon absorption is used to cause a significant alteration in the solubility of the resist for the right developers. This technique makes use of a multi-photon absorption procedure in a substance that is transparent at the laser's pattern-creating wavelength. **Figure 15** illustrates the schematic of the direct laser lithography. A chemical change (often polymerization) takes place at the laser's focus point and may be managed to produce any desired three-dimensional periodic or non-periodic pattern by scanning and modulating the laser appropriately.[87] This technique has been used to quickly prototype intricate structures.
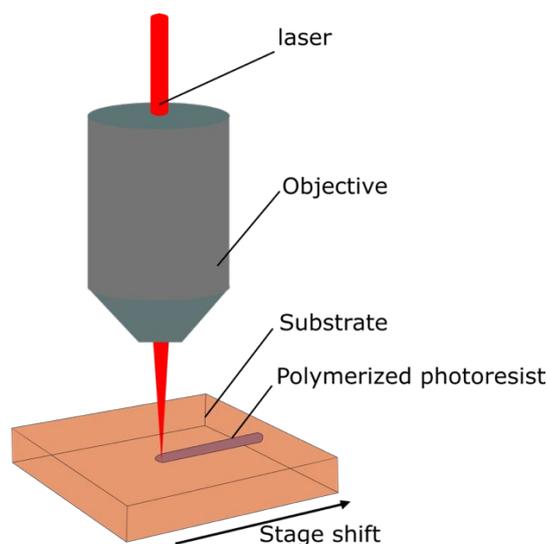


**Figure 15** Schematic of multiphoton lithography or direct laser writing.

## 2.7.6. Wet etching

Wet etching is a method for removing materials off substrates utilizing liquid etchants or chemicals. Photoresist masks on the wafer specify the precise patterns that are achieved by lithography. Liquid chemicals are used to etch away areas that are not shielded by this mask. In cases where the etching times are longer, a hard mask with chromium and gold deposition on top of the material is used. Multiple chemical reactions that take place during a wet etching process use up the initial reactants and generate new ones. Three fundamental steps may be used to summarize the wet etch process. (1) The liquid etchant is diffused into the structure to be eliminated. (2) The interaction between the substance being etched away and the liquid etchant. Typically, a reduction-oxidation (redox) process takes place. In this process, the substance is first oxidized, and subsequently, the oxidized material is dissolved. (3) Diffusion of reaction byproducts away from the surface that underwent the reaction.[88]

### 2.7.6.1. Isotropic and anisotropic etching

A material will either be removed by isotropic etching (uniformly in all directions) or by anisotropic etching when it is attacked by a liquid or vapor etchant (uniformity in the vertical direction). The schematic illustration of various etching processes is given in **Figure 16** Wet etching often removes material at rates that are quicker than many dry etching methods, and it is simple to alter these rates by adjusting the temperature or the concentration of active species.
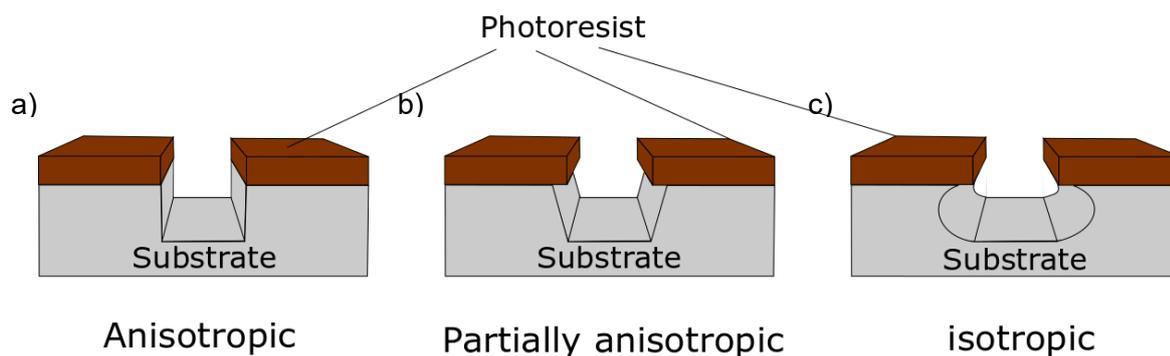


**Figure 16** Schematic of various wet etching processes (a) anisotropic etching, (b) partially anisotropic, (c) isotropic etching.

## 2.7.7. Laser cutting

By use of so-called "ablation processes," the energy of a concentrated laser beam may be utilized to remove material. A high-power laser's output is typically directed through optics in a laser cutter. To focus the laser beam on the material, laser optics and CNC (computer numerical control) are utilized. Using a motion control system, a commercial laser used for material cutting can follow a CNC or G-code that specifies the pattern to be etched onto the substrate. When a concentrated laser beam is pointed at a substance, it either melts, burns, vaporizes or is blasted away by a jet of gas, leaving an edge with a high-quality surface finish.

### 2.7.7.1. Ultra-short pulse laser ablation

Because of the speed at which the energy is supplied by ultrashort laser pulses, ablation occurs before heat conduction to the bulk material. In order to treat materials without thermally impacting the surrounding bulk material, ultrashort laser pulses are utilized. With significantly less heat-related negative thermal effect, this may be utilized to fabricate structures more accurately. Treating materials with ultrashort pulses has the additional benefit of processing almost any substance. This results from the extraordinarily high energy densities that permit multi-photon absorption. It is also possible to process materials that are transparent to the laser's wavelength as explained in the section **2.7.5.2.**

## 2.7.8. Semi-automatic coil winder

The pick-up coil for TMGs is made in this work utilizing an in-house manufactured semi-automatic coil winder. By spinning the core and counting and showing the number of turns in the pick-up coil, the semi-automatic winder enables for reliable and reproducible pick-up coil construction. This guarantees that the pick-up coil's internal resistance remains within the tolerance limit, resulting in more reliable and precise readings. The gadget is outfitted with a programmed Arduino Nano microprocessor that offers fine control over the winding process. In addition, the gadget has a motor with an integrated magnetic encoder, allowing for precise and exact measurements of the number of turns in the pick-up coil. **Figure 17** depicts the setup as 3D rendering from CAD software. Furthermore, the combination of the Arduino Nano and motor with magnetic encoder allows for further expansion of the winder to be automatic completely getting rid of human intervention requirements.
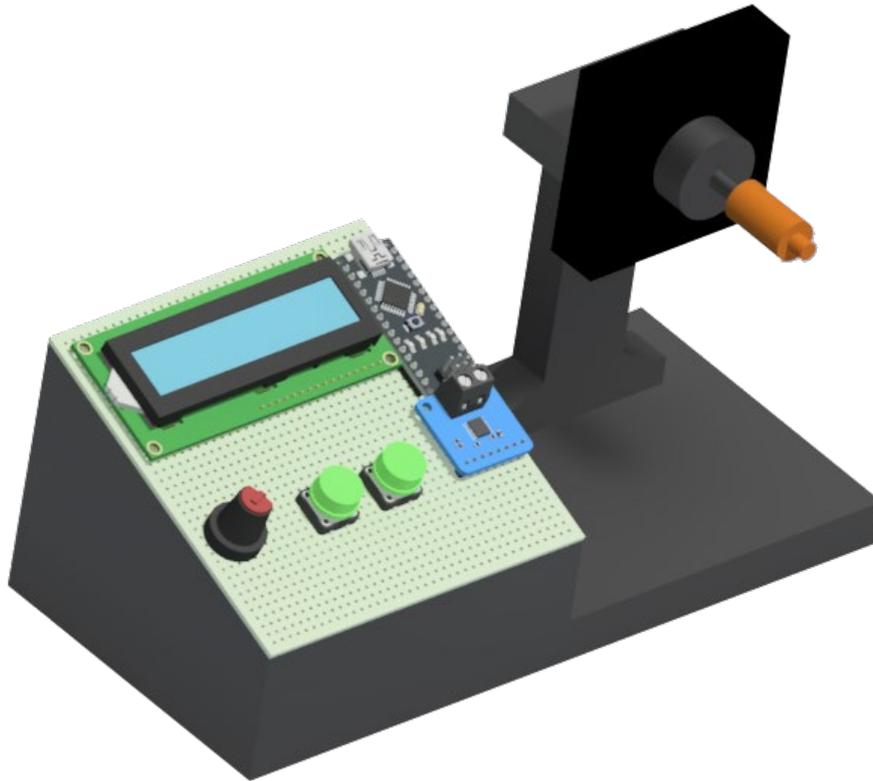
**Figure 17** 3D model of the Semi-Automatic coil winder built in-house for fabricating pick-up coils.

## 2.8. Thermomagnetic materials

Magnetic shape memory alloys like Heusler alloys and ferromagnetic materials like gadolinium (Gd) and lanthanum iron silicon (La-Fe-Si) alloys that undergo ferromagnetic ordering at a particular temperature can be commonly categorized as thermomagnetic materials (TM films). These materials exhibit a change in their magnetization in response to changes in magnetic field and temperature. Both of these can be used for achieving self-actuation in TMGs. **Figure 18** a and b, show the magnetization change in the material Ni-Mn-Ga and La-Fe-Si-Mn-H with respect to change in both magnetic field and temperature. In some alloy compositions, the material might still have remanent magnetization even after the transformation of the material at $T_c$ as shown in **Figure 18**b. The dependence of magnetization value on the magnetic field is also dependent on the alloy composition. **Figure 18**c shows that the given Ni-Mn-Ga alloy composition has a very low saturation magnetic field at room temperature, thus showing less dependence of the magnetization value on the magnetic field.
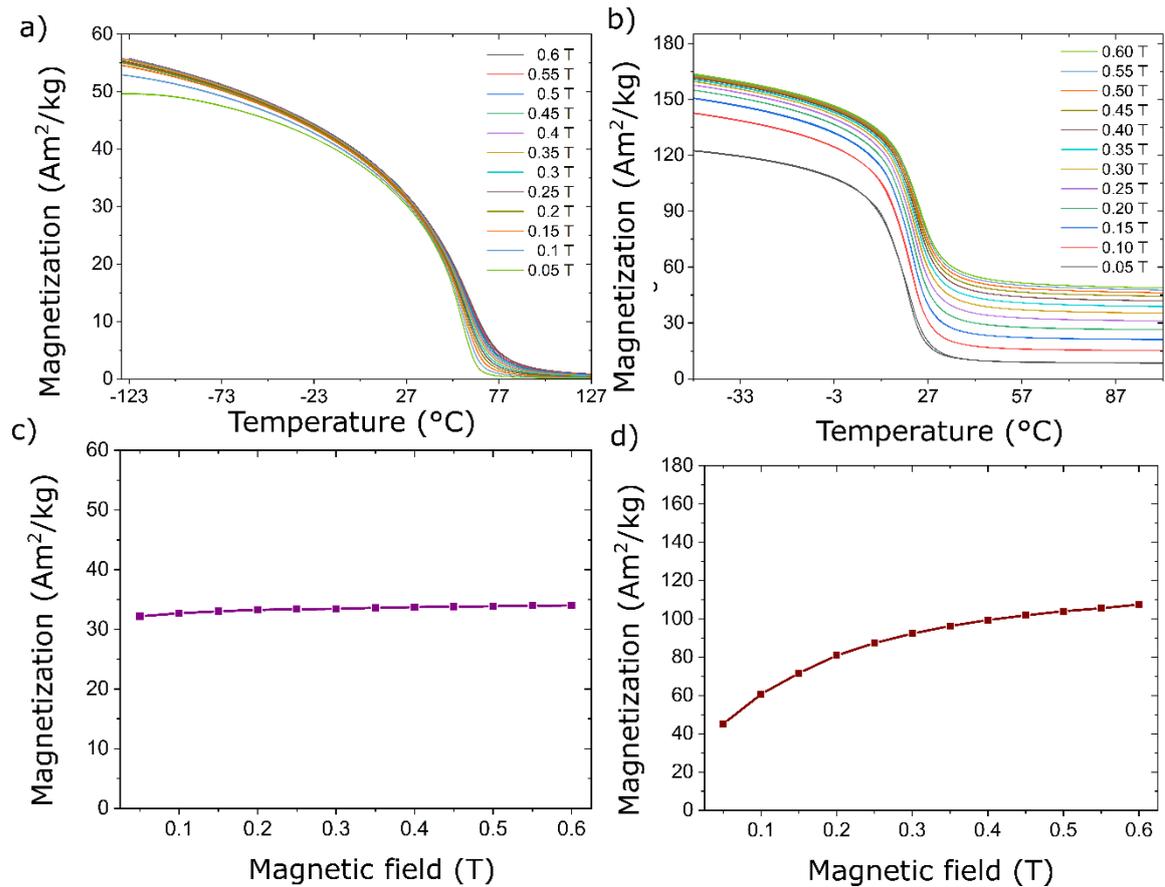
**Figure 18** (a) Magnetization vs temperature graph for a Ni-Mn-Ga alloy. (b) Magnetization vs temperature graph for a La-Fe-Si-Mn-H alloy (c) Magnetization vs magnetic field for Ni-Mn-Ga alloy at room temperature (d) Magnetization vs magnetic field for La-Fe-Si-Mn-H at room temperature.

The given composition of La-Fe-Si-Mn-H alloy has a higher saturation field as shown in **Figure 18**d, as the value of magnetization is increasing with the increase in the value of the magnetic field. It is also important to note that the ferromagnetic to paramagnetic transformation in TM films is a continuous second-order transformation. But there are also materials like metamagnetic shape memory alloys (MSMAs) which present paramagnetic or antiferromagnetic martensite to ferromagnetic austenite transformation through first-order transformation. In first-order transformations, the material would abruptly transform into a phase often accompanied by Hysteresis.

## 2.9. Operation principle of TMG self-actuation

**Figure 19** illustrates the design layout and operating principle of the TMG. A cantilever with the free end mounted on a ceramic substrate. Cantilevers often have a greater natural frequency than bridge beams, allowing them to operate at higher frequencies and power densities.[89] Cantilevers can be created utilizing well-established and reasonably affordable microfabrication processes. A cantilever's resonance frequency may be changed by modifying its size, making it easier to optimize performance for a specific application. Brass is chosen for the cantilever material due to its mechanical and thermal properties. The mechanical and magnetic parts allow for each to be tuned separately as shown by Gueltig et al..[90] At the free end of the cantilever, a thin film of thermomagnetic material (TM film) is placed by using a bonding layer. A pick-up coil is placed underneath the beam which is used to convert mechanical motion into electrical energy using electromagnetic induction. The whole cantilever assembly is placed beneath a tilted permanent magnet to achieve maximum contact once the cantilever is bent. The permanent magnet is made of Samarium Cobalt (SmCo) which can tolerate high operating temperatures up to 350 °C and serves as the heat source for the system with a temperature higher than the $T_c$ of the TM film. When the temperature of the TM film is below its $T_c$, the material is ferromagnetic and hence has large magnetization when placed under the magnetic field. The magnetic field gradient and magnetization results in large magnetic attraction force between the TM film and the magnet, which pulls the free end of the cantilever tip to bend up to the magnet surface.
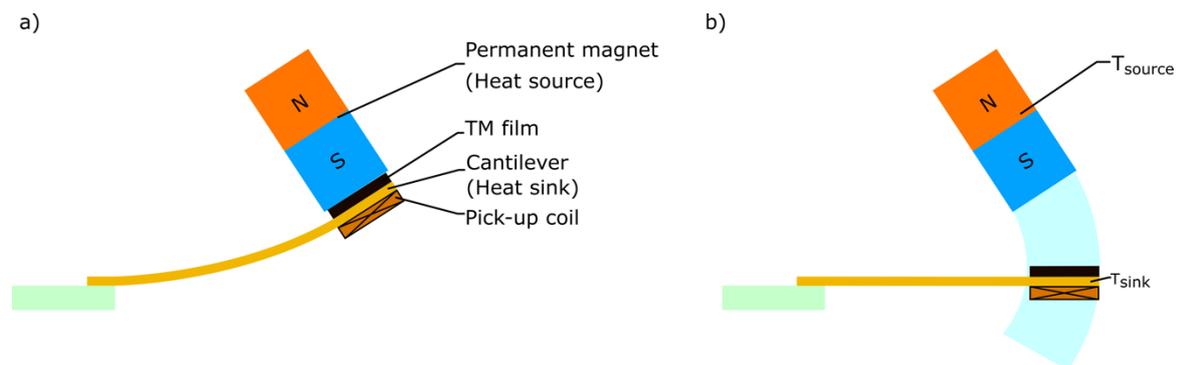


**Figure 19** Schematic of the thermomagnetic generator self-actuation (a) heating at contact with the permanent magnet as the heat source, (b) cooling during the self-actuation. Reprinted from Joseph et al.[91]

This increases the temperature of the TM film above its $T_c$ and the material becomes paramagnetic causing a sudden drop in magnetization of the material, resulting in an abrupt change in magnetic force. When the restoring force is larger than the magnetic force, the cantilever bends back to its original position with an overshoot due to the inertia of the tip mass. Once the TM film loses contact with the magnet, it starts to cool down and this results in increasing magnetization and hence magnetic force. When the magnetic force is larger than the restoring force, the cantilever is bent back to the magnet surface. This cycle results in a repeating self-actuated movement of the cantilever tip towards the magnet surface and away from it.

## 2.9.1. Thermomagnetic cycle for self-actuation

The thermomagnetic cycle (TM cycle) involved in the operation of the TMG under self-actuation, could be broken down into four stages. **Figure 20** illustrates all four stages of the TM cycle followed by the TMG under self-actuation. In an ideal TM cycle, Stage I is an increase in the magnetic field which increases the magnetization of the TM film, this is achieved when the cantilever tip moves towards the magnet. Stage II denotes the decrease in magnetization in the TM film, and this is the result of increasing temperature at contact with the magnet surface. Stage III describes the decrease in the magnetic field,
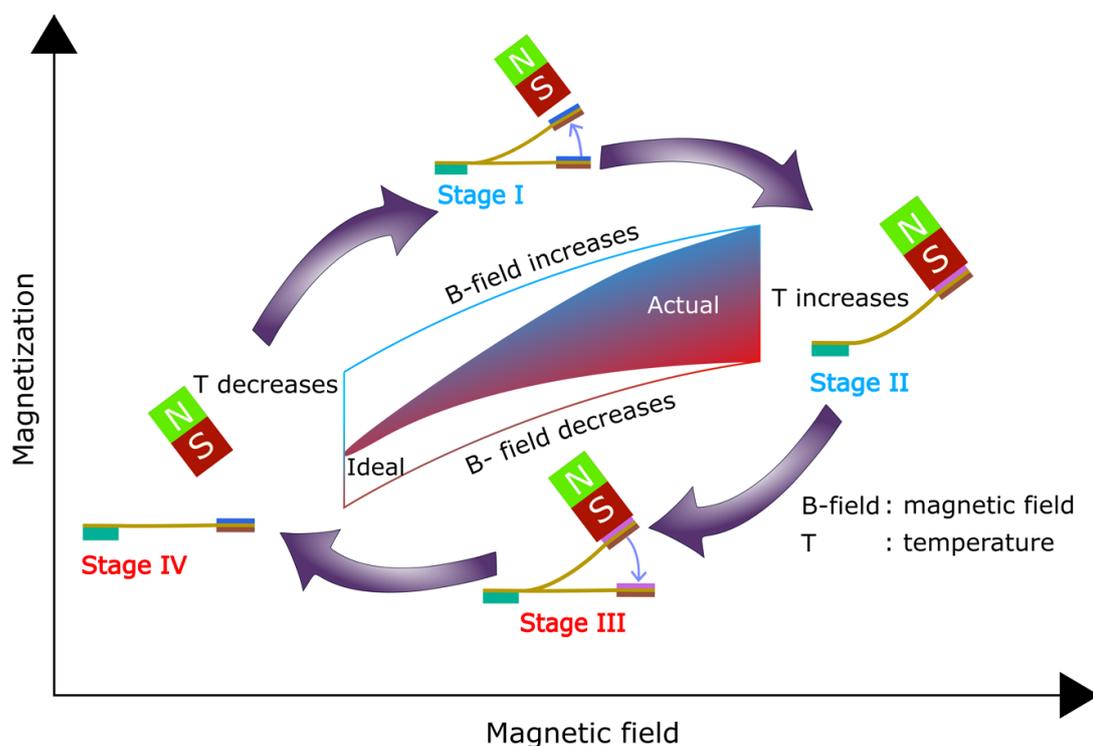


**Figure 20** TM cycle showing stages I-IV in a TMG. Adapted from Joseph et al.[28]

this is achieved when the cantilever tip moves away from the magnet and the TM film then experiences a decrease in the magnetic field and therefore the magnetization also reduces. Stage IV indicates the TM film cooling down, causing an increase in magnetization within the material. The actual TM cycle under which the presented TMG operates does not have defined Stages III-IV-I as the TM film starts to cool down as soon as it leaves the surface of the magnet. Hence there is no isothermal actuation in Stages I and III. The actual cycle is represented by the shaded area inside. This results in a more gradual increase of magnetization over the cooling cycle which is also combined with the change in magnetization due to the reduction and increase in magnetic field during the cooling cycle.

## 2.9.2. Resonant self-actuation

Self-actuation is the key working principle utilized in this work. There is heat intake at contact and heat dissipation during the oscillation away from the magnet surface. This results in tip displacement as shown in **Figure 21**a. The short duration in which the displacement
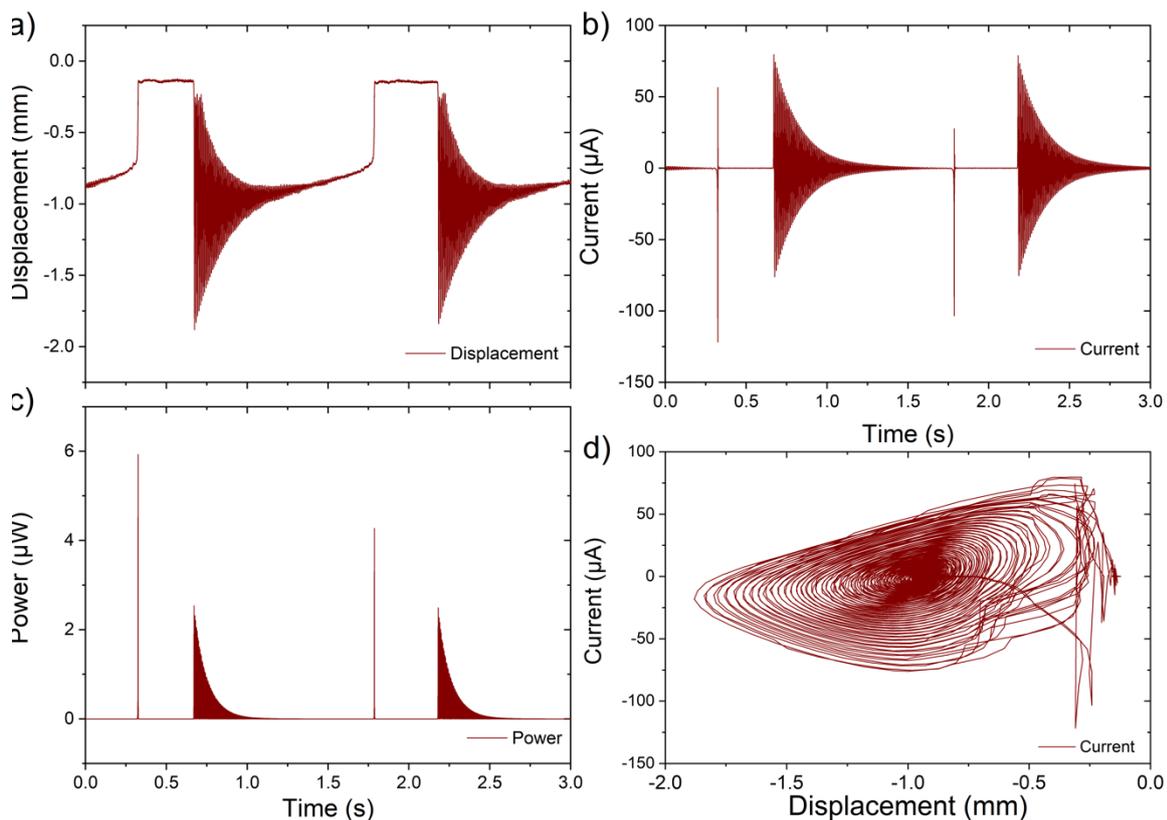


**Figure 21** Self-actuation without resonance, (a) displacement, (b) current, (c) power, (d) plotting displacement vs current to check cyclic behavior.

is constant without oscillations denotes the TM film in contact with the magnet for heat intake. The cooling of TM film is achieved by the damped oscillations that eventually cool the TM film by conduction and convection, enough for it to be attracted back to the magnet surface. **Figure 21**b shows the current generated in the pick-up coil for cantilever tip displacement in **Figure 21**a. It can be observed that the current value depends on the stroke and since the stroke is decreasing in each oscillation until it goes back to the magnet, the current decreases accordingly. **Figure 21**c shows the power generated for the oscillations and that there is still potential to improve the power output by increasing stroke of these additional oscillations or by increasing the frequency of operation.
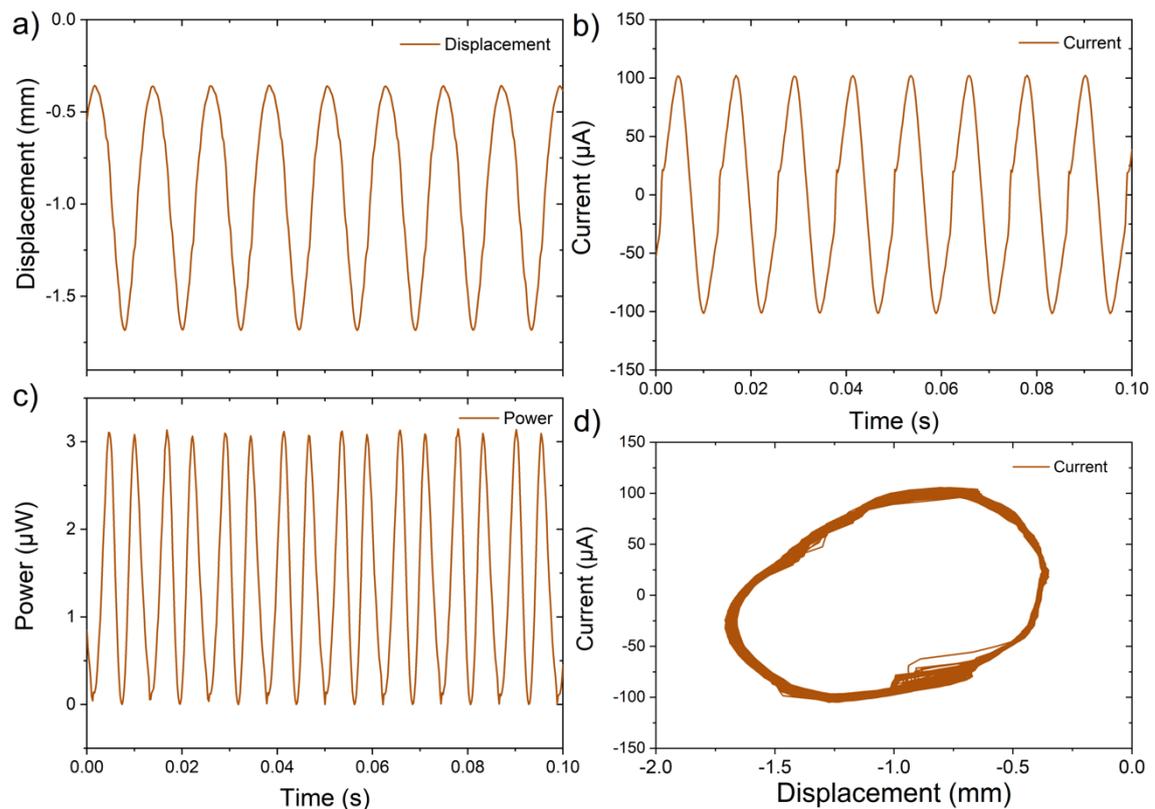


**Figure 22** (a) displacement measures (b) current measurements, (c) instantaneous power derived from current, (d) current vs displacement to check cyclic behavior.

Since the power is largest when the stroke is largest, it would be ideal to have the cantilever making contact with the surface of the magnet in each oscillation and not after having any additional damped oscillations. This can be achieved by optimizing device design, which includes:

- fabrication technology (bonding layers and material selection)
- electrical load resistance

- optimization of cantilever geometry affecting footprint
- heat intake during contact between the TM film and heat source (permanent magnet)
- heat dissipation by conduction and convection

Both heat intake and heat dissipation are dependent on the dynamics of cantilever motion. The heat taken in during the contact should be just enough to cause a drop in magnetic force, which results in restoring forces taking over. This would enable fast operation at high frequency by taking only a small amount of heat in each cycle. Heat dissipation also needs to be optimized by blocking most of the heat at contact so that the temperature increases quickly and then dissipate the heat into the cantilever over the cooling cycle. This can be achieved by using a non-conductive bonding layer with large thermal resistance between the TM film and cantilever. Once the heat intake and heat dissipation are brought in balance with the oscillation of the TMG, current and power output becomes periodic with identical cycles.[28,91] Resonant self-actuation was first presented in Gueltig et al.[92] **Figure 22** shows the displacement, current and instantaneous power output of the TMG in resonant self-actuation. The major challenge is to have TMGs with heat transfer optimized to have heat intake in a short contact time with the magnet and to have heat dissipation completed over the rest of the cycle to have regular and periodic $\Delta T$. If $\Delta T$ is not regular the device will experience heat buildup and would either have an additional oscillation or a complete stop.

# 3. State-of-the-art thermomagnetic devices

Initial concepts were first proposed in the nineteenth century and numerous theoretical and experimental investigations on the use of ferromagnetic materials, such as cobalt (Co), iron (Fe), and gadolinium (Gd), have been conducted since then. The interest in TM generation has recently regained momentum.[25,93,94] Although the theoretical relative efficiencies of ferromagnetic materials operating at or near their $T_c$ can reach up to 55 % of Carnot efficiency, the actual values achieved in experiments are much lower.[93,95] Several concepts have been introduced over the years and all of them could be categorized into two different types, the first one being direct conversion in which the change in magnetization is directly converted into electrical energy. The second type of device uses an intermediate stage of mechanical self-actuation achieved by periodic heating of TM material and then using the mechanical actuation for energy conversion. Direct conversion is usually called active TM conversion and indirect conversion is called passive TM conversion.[93]

## 3.1. Early devices

Early TMGs had iron as the ferromagnetic material which needs 700 °C for demagnetization and had very complicated designs. This limitation stagnated further development as such high temperatures had unfavorable effects on the permanent magnet used in these devices.[23]

### 3.1.1. Pyromagnetic motor

Thomas Edison proposed the idea of a pyromagnetic motor in 1888, which produced heat by burning coal or wood.[96] Design of the pyromagnetic motor by Thomas Edison is shown in **Figure 23**. The device is built with an interstitial armature with interstices or tubes extending longitudinally through it using a thin iron sheet. The armature is positioned between the magnetic poles of permanent or electromagnets and is installed vertically using a shaft. Underneath the armature is a furnace with two outputs covering the lower ends the armature tubes on the opposing sides. These two groups of tubes are subjected to hot

air blowing from the furnace outlets, while the remaining group of tubes situated in between the hot tubes is subjected to cold air. There are cold tubes in the center and hot tubes on the opposing sides. The configuration did not restrict the armature's ability to rotate. The magnetization of the armature varied across various portions because of the temperature variation, producing an unbalanced force. As long as the armature tubes are periodically heated and cooled, this resulted in a continuous rotation of the armature.
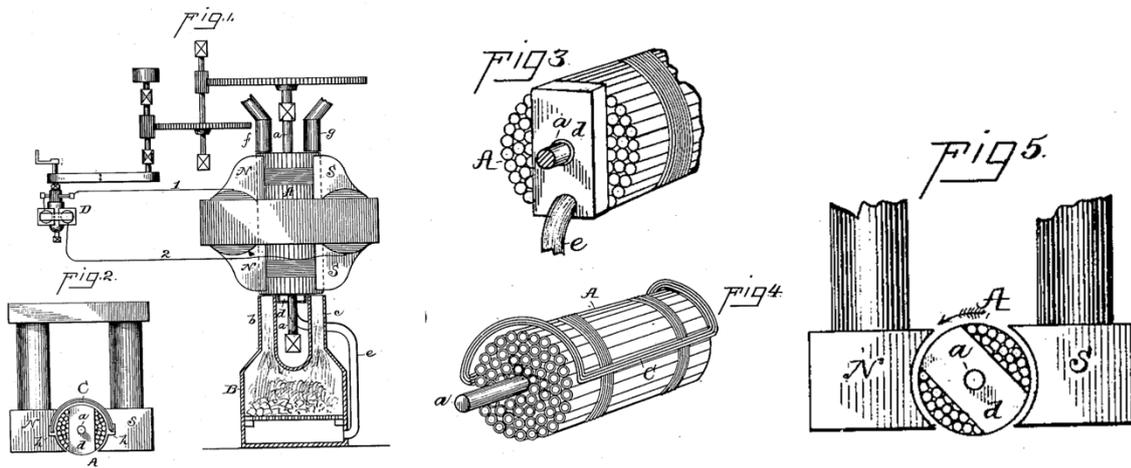


**Figure 23** Pyromagnetic motor from US patent 380100 by Thomas Edison[96]

## 3.1.2. Thermomagnetic motor

Nikola Tesla patented a thermomagnetic motor under US Patent 396121 in the year 1889.[97] **Figure 24** shows some of the early concepts of Nikola Tesla. By using the combined effects of heat, magnetism, and stiffness of a spring, the presented devices are able to generate mechanical energy through a reciprocating or rotational action. In Tesla's thermomagnetic motor, an armature is in contact with an electromagnet or permanent magnet that produced a magnetic field. A hinged arm with the armature attached to it could freely rotate. The armature is separated from the permanent/electro-magnet when the temperature of the armature is increased over its $T_c$ as a result of the heating burner. After a while, the armature is cooled below the $T_c$, at which point the magnetic force increased more than the spring force and returned the armature to its initial position. As long as the heating and cooling cycles persisted, this process is repeated. However, because of their poor performance, these TMGs were never deployed in either domestic or industrial applications.

44
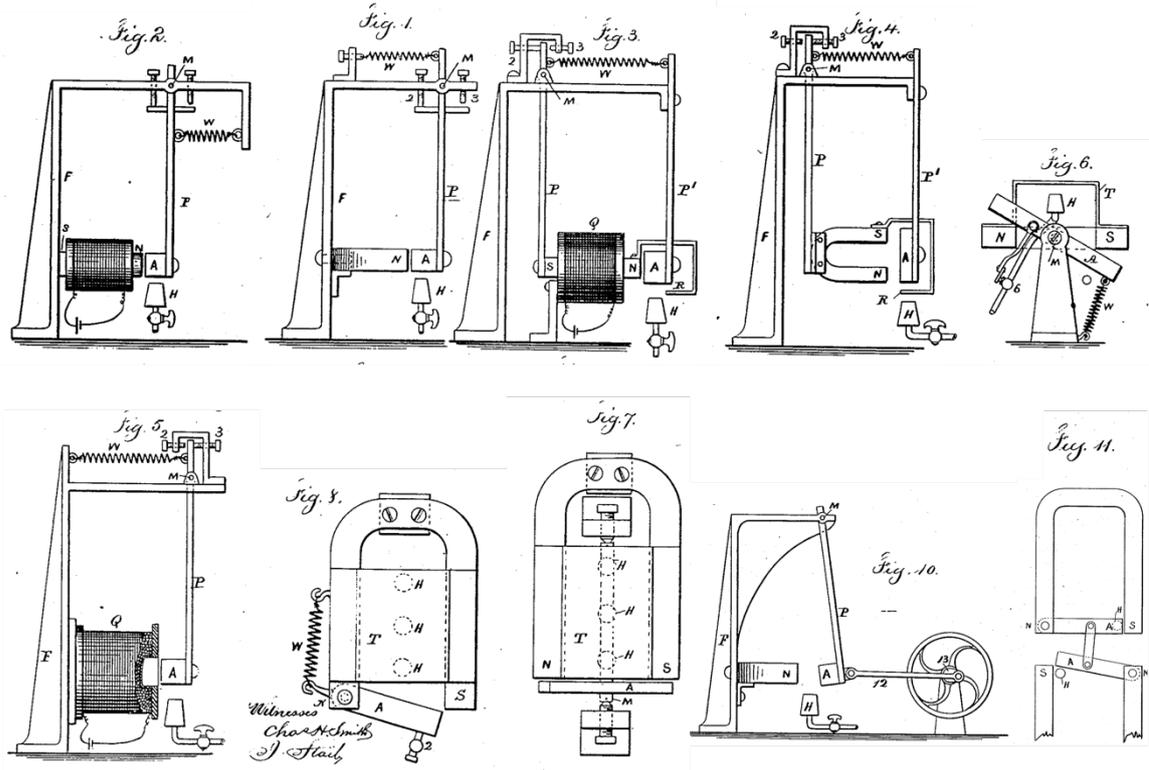
**Figure 24** Designs of the thermomagnetic motor by Nikola Tesla in US patent 396121[97]

### 3.1.3. Pyromagneto-Electric Generator
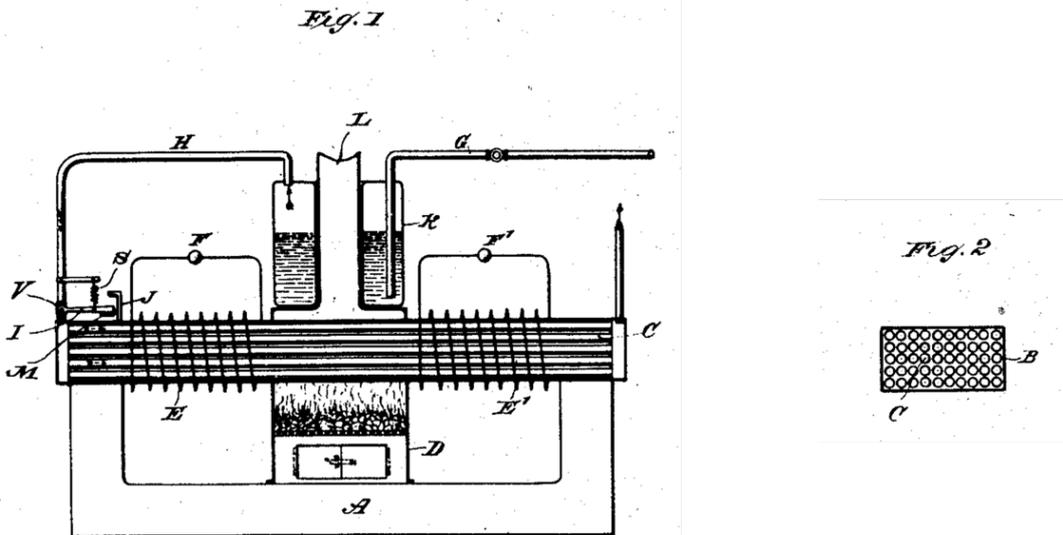


**Figure 25** Pyromagneto-Electric Generator patented by Nikola Tesla in US patent 428057[98]

A patent for a pyromagnetic electric generator was first introduced by Nikola Tesla in 1890.[98] A device that directly produces electric current without mechanical motion is described in this patent. An armature core made of a few iron tubes is used to bridge a permanent magnet, as seen in **Figure 25**. Around the armature core are two conductors that would serve as the source of the electric current. A furnace placed beneath the center of the armature core will heat it, while steam originating from a boiler can cool it. Alternately cooling and heating the armature turned on and off the magnetic circuit, changing the magnetic field, which eventually led to an electrical signal in the leads.

## 3.1.4. Pyromagnetic Generator
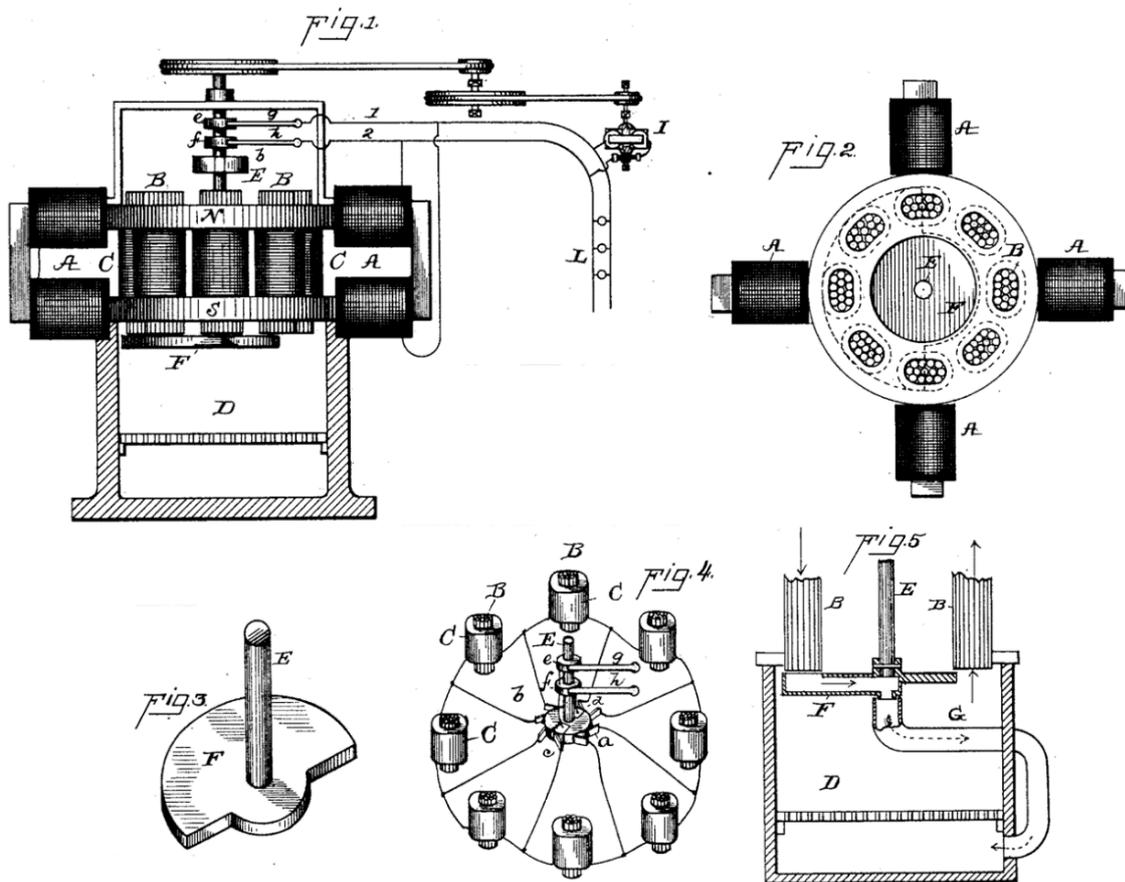
**Figure 26** Pyromagnetic generator design patented by Thomas Edison in US patent 476983[99]

Another type of pyromagnetic generator with bundles of thin iron tubes arranged circumferentially inside two iron rings was invented by Thomas Edison in 1892.[99] **Figure 26** provides an illustration of this gadget. These iron tube configurations are magnetized using

46

strong permanent magnets or electromagnets so that the rings formed the two poles of a long magnet. Each bundle of tubes had a wrap around it. Under the lower iron ring is a furnace, and some of the tubes' lower ends are shielded with shields in the shape of half disks. The open tubes heated up after receiving the hot furnace air. However, because the barrier shielded the tubes from the furnace's heat, they are able to cool. The tubes are always thermally unstable because the shield is gently rotated around its axis by a motor. Iron tubes are gradually cooled and heated, changing their magnetization in the process, which produced current in the coil turns. This device along with the previous device designs explained until now is not used in any form in any commercial or domestic applications due to the very low efficiency, high temperature requirement, and lack of permanent magnet materials that had high $T_c$ to sustain performance at such high temperatures.

## 3.2. Recent thermomagnetic energy generators

Due to the extremely low efficiencies that the available materials could achieve, research on TMGs has advanced very gradually over the past century. Brillouin and Iskenderian reexamined the concept of TM power generation for the first time in 1948 and reviewed the design of a static TMG for the direct conversion of heat into energy.[100] Gadolinium is an intriguing material and is used as an active material for subsequent research.[101–103] Gadolinium, which was then more widely available, is primarily considered for experimental work since it has a $T_c$ close to room temperature.[104] Kirol and Mills put out various theories based on the fluidic heating and cooling of TM film.[105] Solomon carried out more computations and optimizations in 1988 and created a general model.[106] Devices described from section **3.2.1** to section **3.2.3** are examples of direct conversion or active TMGs. Devices presented from section **3.2.4** to section **3.2.7** are examples of passive TMGs.

### 3.2.1. Direct energy conversion using first-order transformation

Srivastava et. al. presents a TMG that directly converts the change in temperature to electricity using the change in magnetization of a shunt material. **Figure 27** shows the image of the prototype demonstrator and the schematic of the device. A pick-up coil surrounds the sample, which is secured (to restrict movement) close to a pole of a permanent bar magnet. An external heat gun provides the heat. The fundamental concept is that through a transformation during heating, the specimen's average magnetization M increases, producing a significant change in magnetization for a unit temperature change $(\Delta M/\Delta T)$. The

proximity of the permanent magnet prevents the demagnetization of the material. A field is generated during transformation and the pick-up coil is designed with the goal of providing the maximum component of the field parallel to the wire, which will cause a current to flow in accordance with Faraday's law. On the reverse phase change after cooling, a potential difference of opposite polarity is produced across the pick-up coil. Although the promised high-power density competes with cutting-edge thermoelectric energy harvesters, the experimental efficiencies are quite low. In reference,[107] a theoretical model of the efficiency is provided. The hysteresis of the phase transformation must be near zero for energy harvesting at low temperature differences. The demonstrator generates around 50 µW of power and this corresponds to a power output per footprint value of 28 µW/cm$^2$ in ideal conditions where the temperature is externally oscillating between approximately 25 °C and 40 °C.
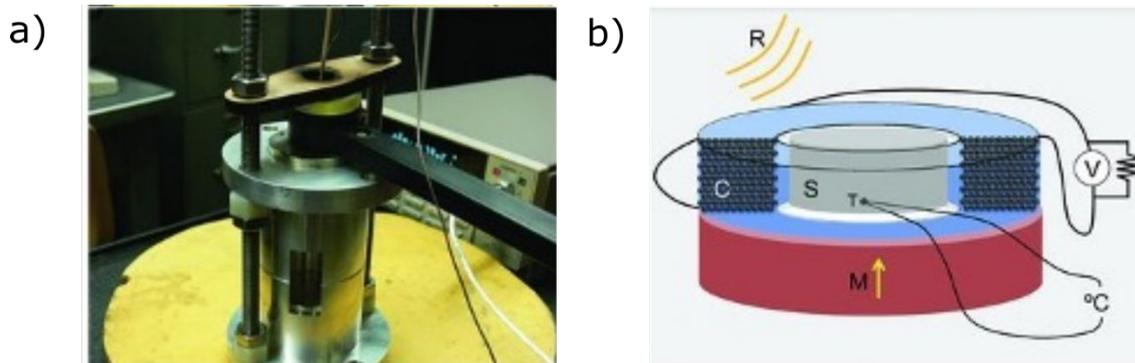


**Figure 27** Adapted image from,[108] (a) photograph of the demonstrator, (b) schematic of the demonstrator. Reprinted with permission from John Wiley and Sons.

$Ni_{45}Co_5Mn_{40}Sn_{10}$, a quaternary Heusler alloy, is presented by Srivastava et al.,[108] demonstrating highly sharp transitions and hysteresis of only 6 °C. Along with narrow hysteresis, good martensite, austenite phase compatibility and good first-order phase transition reversibility ensure low functional fatigue.

## 3.2.2. Static thermomagnetic generator

The device shown in **Figure 28** from Christiaanse et al.[109] consists of two active regenerators made from (Mn,Fe)2(P,As) materials suspended in a magnetic circuit, and a permanent magnet acting as a field source. The regenerators are made up of 48 disks of (Mn,Fe)2(P,As) material with four different Curie temperatures, and microchannels are laser cut into each plate. By stacking these plates in series, two regenerators with a gradient

temperature span are built. As a result, magnetic stray fields are prevented since the permanent magnet's generated magnetic flux is always directed through one of the TM disk. To determine the highest power output at the optimal frequency, the material is cycled at various frequencies.
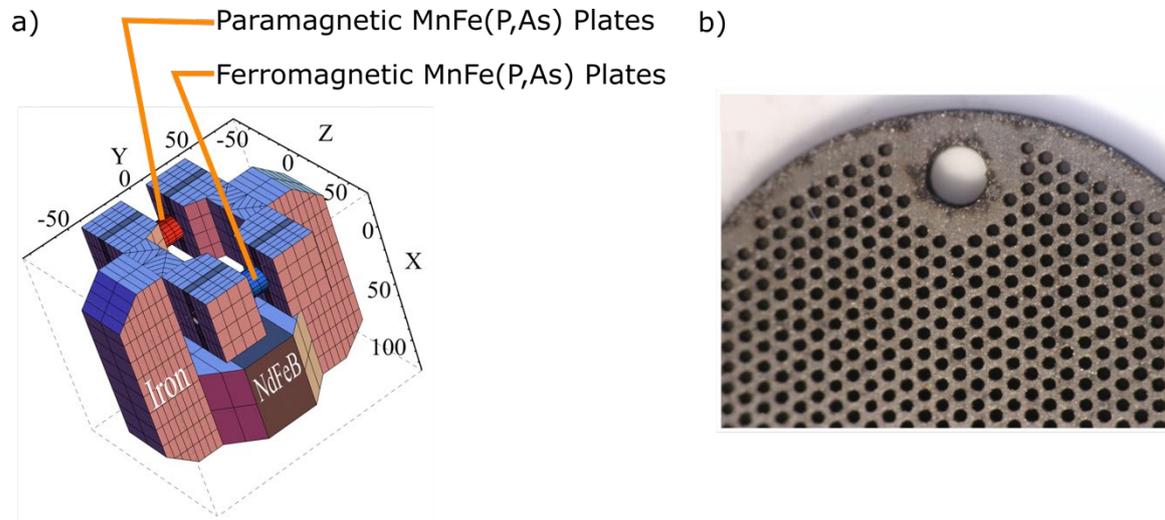


**Figure 28** Adapted image from Christiaanse et al.[109] a) Three-dimensional representation of the proposed device in Christiaanse et al..[109] Paramagnetic state magnetocaloric material in red, and Ferromagnetic state magnetocaloric material in blue. b) Shows the MnFe(P,As) plates with microchannels. Reprinted with permission from Springer Nature.

The device uses the regenerative Ericsson cycle, which consists of two isothermal curves and two isofield curves, to achieve higher efficiencies. The researchers tested the device by cycling the materials at different speeds to find the maximum power output at the optimum frequency. They found that a more tapered design and different materials would be critical to a better design. The tapered design ensures a greater external field and a larger external field change across the material.

Additionally, the materials for devices that use water as a heat-transfer fluid should have a lower latent heat while maintaining their magnetic properties to increase cycling speed and improve power output. This will increase the speed of the process cycle and boost the device's power output. At a frequency of 0.17 Hz, the power production is at its highest. The heat transfer to the regenerator is decreased when frequency is increased further, preventing the material from cycling through the magnetic phase transition, which results in the power reduction. The fundamental cause of this relatively poor cycling behavior is

the laser treatment's degradation of the magnetic characteristics while the microchannels were cut. In essence, the walls of the water channels are transformed by heat from the cuts into a material that is not magnetic, but simply has thermal resistance and heat capacity.

## 3.2.3. TMG with pretzel-like magnetic topology

The magnetization should, in an ideal scenario, abruptly change $\Delta M$ around $T_c$ of the TM film to consider the TM material as a thermal switch. Waske et. al. has shown a pretzel-like topology for the magnetic circuit to avoid stray fields and to double the flux change in the circuit.[110] This is achieved by the sign reversal of the magnetic flux within the connecting yokes when the temperature of the TM materials is changed alternatively. This design is an extension of the thermomagnetic generator presented by Nikola Tesla.[98]
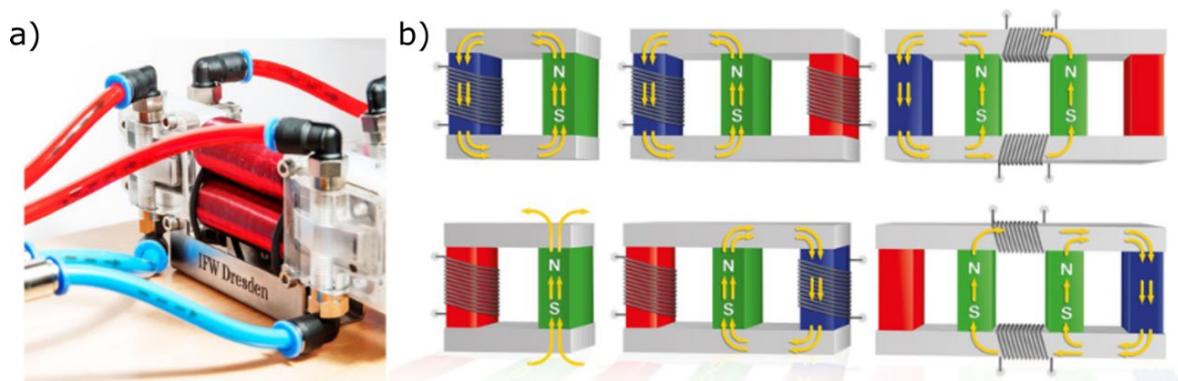


**Figure 29** Thermomagnetic generator with a pretzel-like magnetic topology introduced in Waske et al.,[110] (b) image of the TMG prototype, (b) different topology of magnetic circuits discussed. Reprinted with permission from Springer Nature.

The magnetic circuit depicted in **Figure 29** includes the TM material as a component. Permanent magnets are the source of the magnetic flux in this circuit, and two soft magnetic yokes are used to direct the flux. The TM materials of this magnetic circuit act as a thermal switch for the magnetic flux. The developed TMG with the new topology allows the device to achieve a high power output of 1.25 mW from a very small $\Delta T$ of 30 °C resulting in a power per footprint of 32 µW/cm$^2$. However, the pump and other fittings to circulate the fluids for heat transfer are not taken into account. By making some design changes to improve the cycling frequency of the device, it is claimed by authors to be possible to increase the power output and efficiency of conversion.

### 3.2.4. Miniature ferromagnetic thermal energy harvester

A miniature energy-harvesting prototype developed by UCLA researchers is based on the change of Gadolinium's magnetization with temperature change.[111] As seen in **Figure 30**, a piezoelectric spring mechanism carries the ferromagnetic material between a hot and cold reservoir. The findings include a description of the mechanical energy present in the system and an analytical method for calculating the potential electrical output. High-efficiency piezoelectric energy conversion is proposed by the authors capable of converting up to 3.6 mW/cm$^2$ from a temperature difference of 50 °C. In the following research by Bulgrin et. al.[112], the system design is theoretically examined in terms of power output and efficiency, and it is concluded that with optimizations, an average power output of more than 250 μW is feasible, translating to a power per footprint of up to 62 μW/cm$^2$. However, the experimental verification is still pending for the claimed large power per footprint.
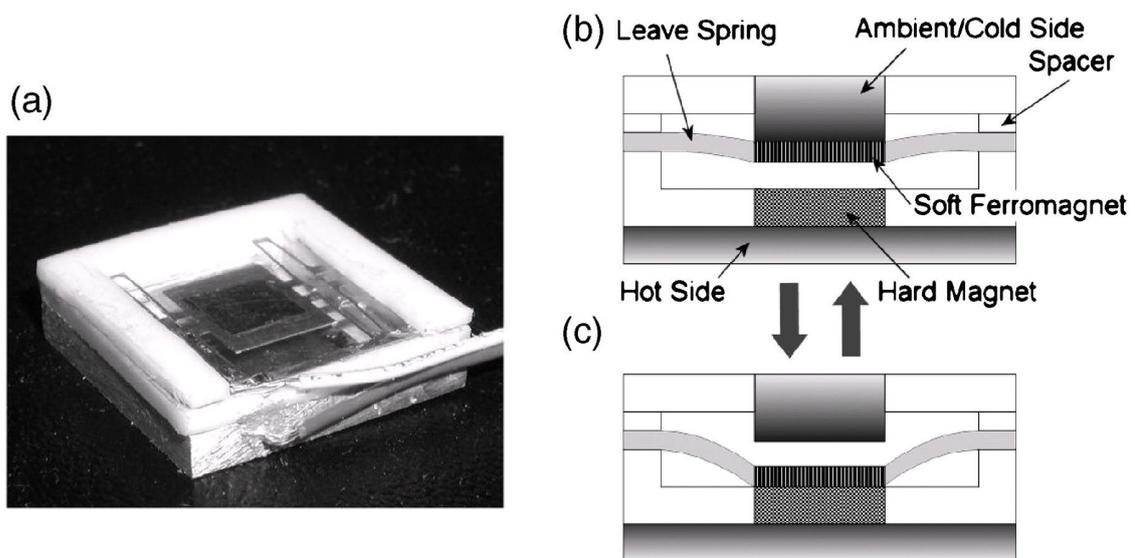


**Figure 30** TMG using ferromagnetic Gadolinium as active material presented in, (a) actuation device, (b) cross-sectional view during cooling, (c) cross-sectional view during heating.[111] Reprinted with permission from AIP publishing.

### 3.2.5. La-Fe-Si based thermomagnetic generator

In 2019, Ahmim et. al. presented a TMG based on La-Fe-Si-H alloy.[113] After two years, in 2021 an updated version of the device is presented.[114] The TMG shown in **Figure 31** is constructed using an magneto caloric material (MCM) plate, a field source, a thermal energy source, a heat sink, and a disc spring. Two piezoelectric buzzers are used to create

the disc spring. Through a miniature CuBe ring, they are inversely bonded to one another. NdFeB parallelepiped magnets are used to construct the Halbach structure, which serves as the field source. In comparison to the field produced by a single magnet, this combination is claimed to provide a larger force with a steeper change across small displacements. While the cold reservoir is constructed with a water-cooled heat exchanger, the temperature of the heat source is maintained through electrical resistance heating. The MCM has direct thermal contact with the heat sink through a hole in the piezoelectric buzzer. The presented device is capable of generating a maximum output of 4.2 µW from a small temperature difference of 35 °C. The resulting power per footprint is around 0.12 µW/cm$^2$. The low value is due to the large size of the device even though the power density with respect to active material volume is around 240 µW/cm$^3$.
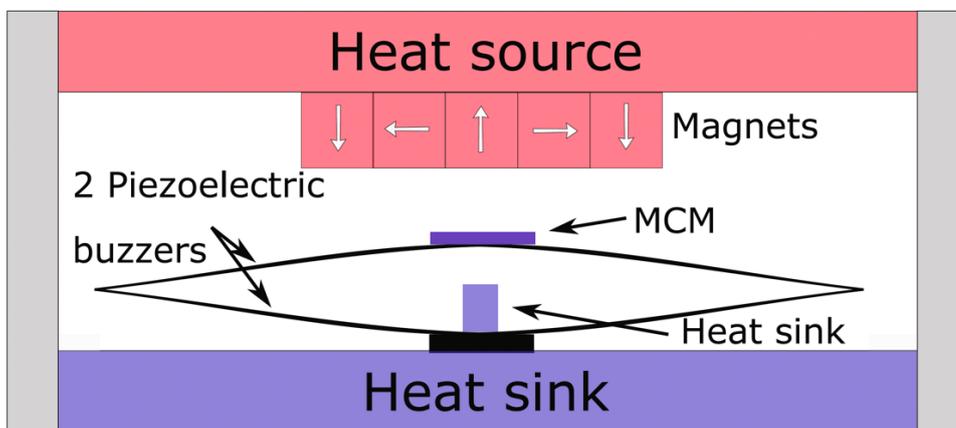


**Figure 31** Schematic of the TMG with La-Fe-Si as active material and piezo spring as energy transducing material.[114] Reprinted with permission from Elsevier.

## 3.2.6. Hybrid thermomagnetic generator

A hybrid device that combines TM and triboelectric effects to produce electricity is demonstrated by Rodrigues et al.[115] In the presence of slight temperature gradients close to room temperature below 30 °C, the TM effect enables the periodic and sustained movement of the ferromagnetic material with the second-order transition. Using a triboelectric nanogenerator (TENG), this mechanical actuation is subsequently transformed into electrical energy. A TENG is generally made up of two materials having opposing electron affinities that are brought into contact with one another. Electrons move from one substance to the other when the materials are rubbed or forced together, resulting in charge separation and the production of an electrical potential. This energy may be captured and utilized to power small electrical gadgets or charge batteries.[116] The presented hybrid TM and triboelectric

nanogenerator is depicted in **Figure 32**. This concept's application is shown in both the cold (15 to 37 °C) and hot (60 to 90 °C) sides of a wide range of operating temperatures. The electrical output produced by the hybrid TENG is further claimed to have 35 times more than that produced by a typical TM generator driven by magnetic induction. The device generates a large power output of 481 µW but with a power per footprint of 5.47 µW/cm$^2$. Owing to the large area of the device, the power per footprint is still low compared to other TMGs with magnetic induction.[92]
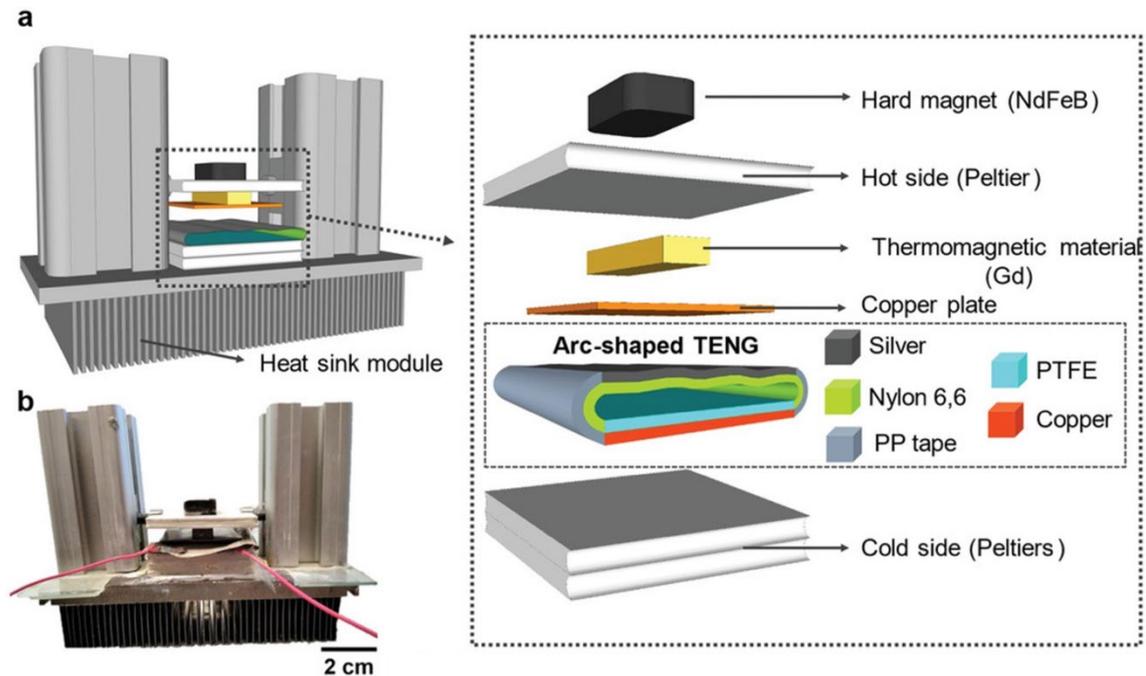


**Figure 32** Hybrid thermomagnetic and triboelectric nanogenerator presented in Ahmim et al.[115] Reprinted with permission from John Wiley and Sons. Legend: TENG- triboelectric nanogenerator, PP tape- polypropylene tape, PTFE- polytetrafluoroethylene.

## 3.2.7. Pyroelectric conversion using thermomagnetic actuation

A novel method of energy generation that uses a hybrid method of both TM actuation and pyroelectric energy transduction is presented in Lallart et al.[117] The authors of this study describe the development of a heat engine for small-scale energy harvesting in which a TM film transfers its heat to a pyroelectric element. It converts thermal energy into electrical energy, resulting in a hybrid method of direct energy conversion path as opposed to conventional electromechanical heat engines as shown in **Figure 33**. Additionally, faster cooling of the TM film, which accounts for a higher thermal cycling frequency, is made possible by thermally separating the pyroelectric element from it. The power per footprint
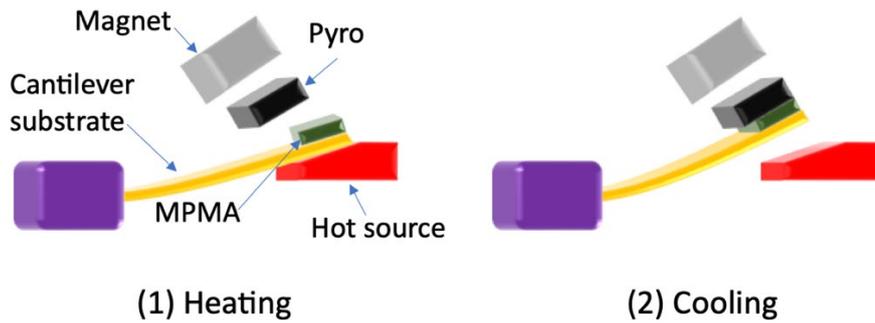
**Figure 33** The schematic of the TMG with a pyroelectric element for energy conversion directly from heat to electricity.[117] Reprinted with permission from Applied Energy.

generated by the device is 0.02 µW/cm². These results show that hybridizing does yield some advantages but until now none of the presented results have generated more power than the TMG with magnetic induction. Several other devices have also been published in recent times which utilize the TM energy generation principle using various designs.[118–123] These devices have shown that TM energy generation is gaining huge research interest due to its high-power density and high efficiency in low temperature differences.

## 3.3. Preceding work on TM energy generation

This thesis work is built upon previous generation TMGs that are developed at KIT. [42,43,90,92,124–126] This section explains the previous work at KIT.

### 3.3.1. Thermomagnetic actuations
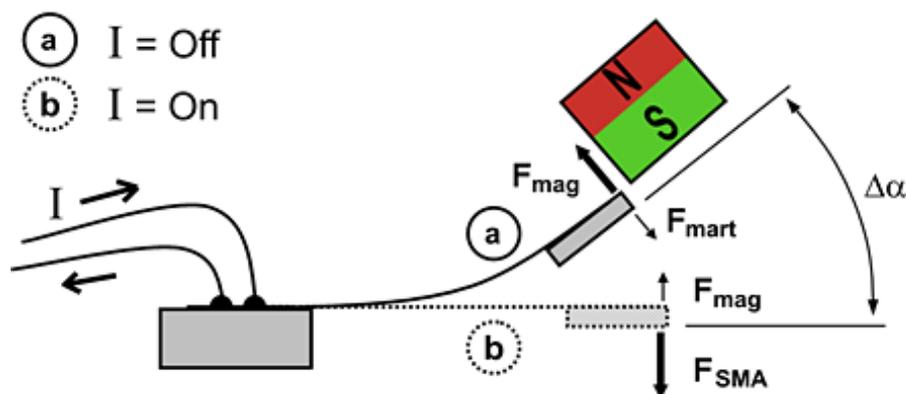


**Figure 34** Microscanner using Ni-Mn-Ga film as cantilever material and a micromirror attached to the tip.[42] Reprinted with permission from IOS press.

54

TM conversion principles can be employed for thermal actuation in addition to generating power from heat. Kohl et. al provides an overview of miniature magnetic SMA-based actuators.[43] A micro scanner is presented that utilized magnetic shape memory alloy film in the form of a cantilever to achieve actuation based on the electrical input.[42,127] A mirror is mounted to the front end of a double beam cantilever that is formed from free-standing Ni-Mn-Ga films and anchored to a substrate at the other end as illustrated in **Figure 34**. The double-beam cantilever may be heated by recurrent electric heating pulses since it is electrically connected. A magnet is positioned above the cantilever, deflecting it in its initial state. The temperature of the cantilever beam is controlled by the electrical pulses (heating) and convection is used to cool it. Thus, periodically heating the beam allows the microscanner to achieve oscillations with frequencies up to 200 Hz with extremely large deflections which allow this system to be adapted to portable mobile optical sensor systems. This actuation principle laid the basis for the subsequent development of energy harvesters with an oscillating cantilever design.

## 3.3.2. TMG with Ni-Co-Mn-In
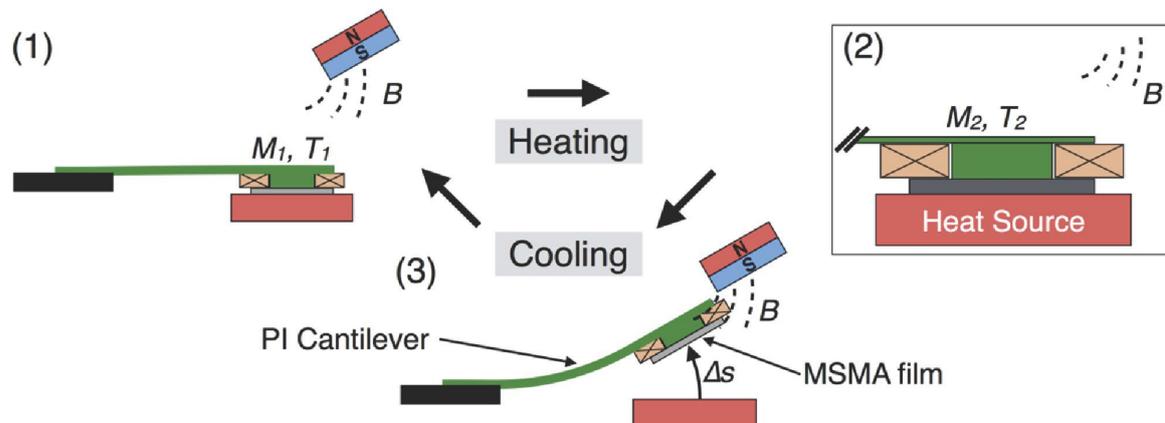


**Figure 35** Schematic of energy harvester based on MSMA film $Ni_{45}$-$Mn_{40}$-$In_{15}$ that is presented in Gueltig et al.[124] Reprinted with permission from John Wiley and Sons.

TMGs using MSMA ($Ni_{50.4}Co_{3.7}Mn_{32.8}In_{13.1}$) are presented in Gueltig et al.[124] **Figure 35** shows the schematic of the device. This study demonstrated that MSMA films provide many pathways for energy conversion and intrinsic actuation. It is necessary to minimize heat transfer durations while also optimizing the effective change in magnetization ($\Delta M$) in a constrained temperature change ($\Delta T$) in order to make the best use of these multifunctional features for thermal energy harvesting. It has been shown that the Faraday effect's direct conversion of thermally induced $\Delta M$ to electricity is less effective for MSMA film

devices than its indirect method, which involves resonant stimulation of large oscillation amplitudes at high frequency. An example MSMA film cantilever device is shown and put to the test for various energy conversion configurations. The device produced significant power densities when it is self-actuating with mechanical frequency up-conversion. The average power density is 0.5 mW/cm$^3$ with respect to the TM film, which is approaching the range of thermoelectrics, for a ΔT of 10 °C. Initially, the MSMA film is heated using a laser to induce ΔM in the MSMA material, this caused an electrical pulse in the pick-up coil that is attached to the cantilever tip as shown in **Figure 36**a. Then in the second method, the cantilever is moved using an external actuator to come in contact with the heat source to induce ΔM as depicted in **Figure 36**b. The magnet is attached with the cantilever tip in both cases.
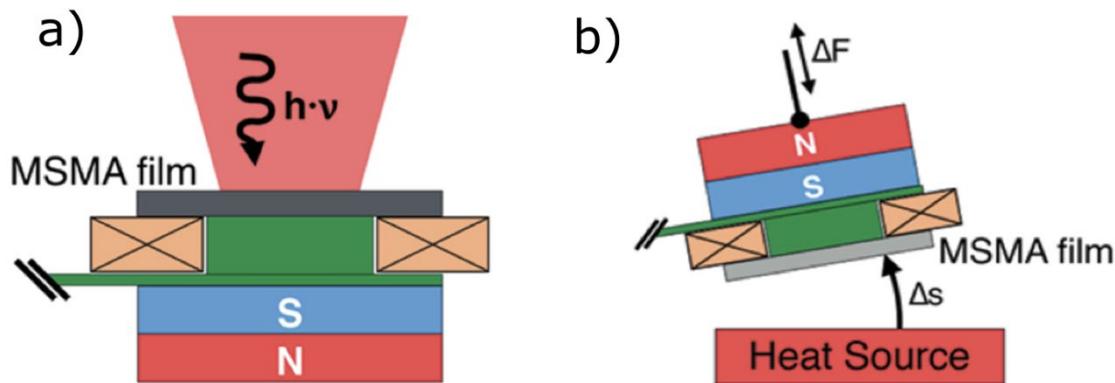


**Figure 36** Schematic of the TMG, (a) heating MSMA with laser, (b) external actuation of the MSMA film.[124] Reprinted with permission from John Wiley and Sons.

Finally, the cantilever is separated from the magnet and the self-actuation capability of the MSMA film is used to break contact with the heat source and to move towards the magnet. There are two mechanisms contributing to the energy conversion. The self-actuating MSMA device resulted in an induced change in magnetization (ΔM) due to thermal energy and also additionally due to the changing magnetic field, the overall change in magnetization is higher, which resulted in a higher electrical signal in the pick-up coil. Additionally, the pick-up coil is also experiencing an additional change in magnetic field gradient due to the actuation. Thus, this study is the foundation of energy generation using the self-actuation of magnetic shape memory films with a cantilever-based design. MSMA films like $Ni_{45}$-$Mn_{40}$-$In_{15}$ undergo the first-order transformation from a paramagnetic martensite phase to a ferromagnetic austenitic phase. This phase transformation is abrupt and large but due to the presence of hysteresis, the optimization of the thermal cycle is limited.

### 3.3.3. TMG with N-Mn-Ga
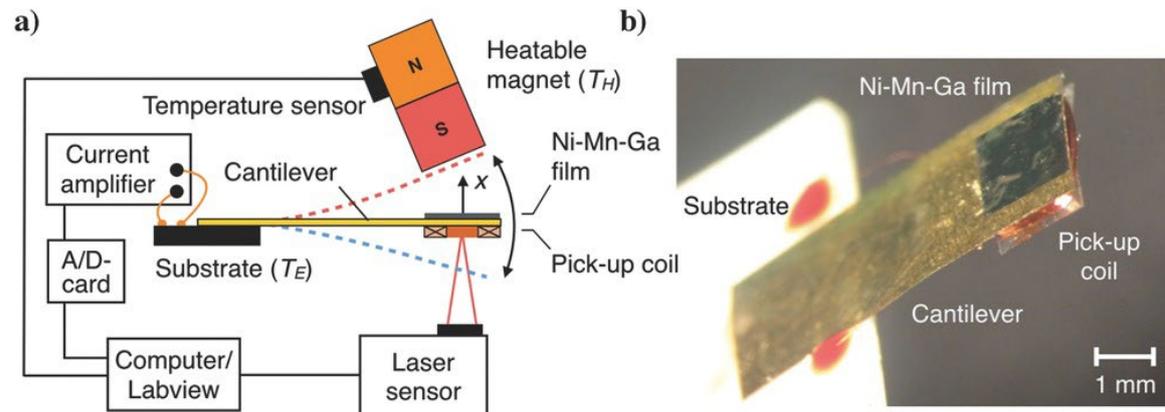


**Figure 37** Schematic of second-generation TMGs from KIT, using FSMA film Ni-Mn-Ga,[92] (a) measurement setup with the schematic of the device, (b) photograph of the device. Reprinted with permission from John Wiley and Sons.

The second generation of thermomagnetic generators developed at KIT is presented in **Figure 37**.[92] In this generation, the drawbacks of optimization of the thermal cycle are addressed by using a magnetic shape memory alloy with second-order transformation (ferromagnetic shape memory alloys). Heusler alloy film of composition $Ni_{51.4}$ -$Mn_{28.3}$- $Ga_{20.3}$ and a thickness of 5 µm is used in this device. Optimizing the heat intake and heat dissipation from the film by changing the polyamide cantilever to brass to increase the thermal dissipation of the device, resonant self-actuation is achieved for the first time. This resulted in a very large power output of 2.4 µW at 84 Hz for a heat source temperature ($T_{source}$) of 160 °C. Experimental evidence has shown that the TMG is for the first time at eye level with the state-of-the-art thermoelectric generators at miniature length scales (mm and cm-range). It became possible to gather local thermal energy with a small temperature differential thanks to the high power density that is observed. A very high power density of 118 mW/cm$^3$ is achieved with respect to the volume of the active material. Even when the footprint is taken into account, the device still has power per footprint of 14.2 µW/cm$^2$. Several other iterations are done prior to reaching these milestones, which are presented in detail in.[90]

# 4. Multi-physical analysis of TMG

The multi-physical LEM simulation model of the TMG is created using the MATLAB SIM-CAPE toolbox within MATLAB Simulink. Simulink is a graphical programming environment with a unidirectional linear flow of data through blocks. Although for most simulation models this is acceptable and sometimes preferred, in the case of a TMG there are several different parameters affecting the operation of the TMG and each of them defines the current state of the device at every time step. There are several different data loops within the model which makes the Simulink toolbox in its native form incompatible with creating the LEM model for the TMG. The SIMSCAPE on the other hand has bidirectional data transfer between blocks. SIMSCAPE blocks include a variety of partial differential equations (PDEs), linear equations, and expressions. The connections and dependencies between these equations are defined by the physical ports. Thus, each time step is solved numerically to converge. This allows for incorporating multiple data loops without following a linear pattern of data flow. Since the blocks are also solved numerically additionally to the blocks being connected analytically, it allows for modelling complex multiphysics systems in a dynamic environment with less computational power.

## 4.1. Operation principle
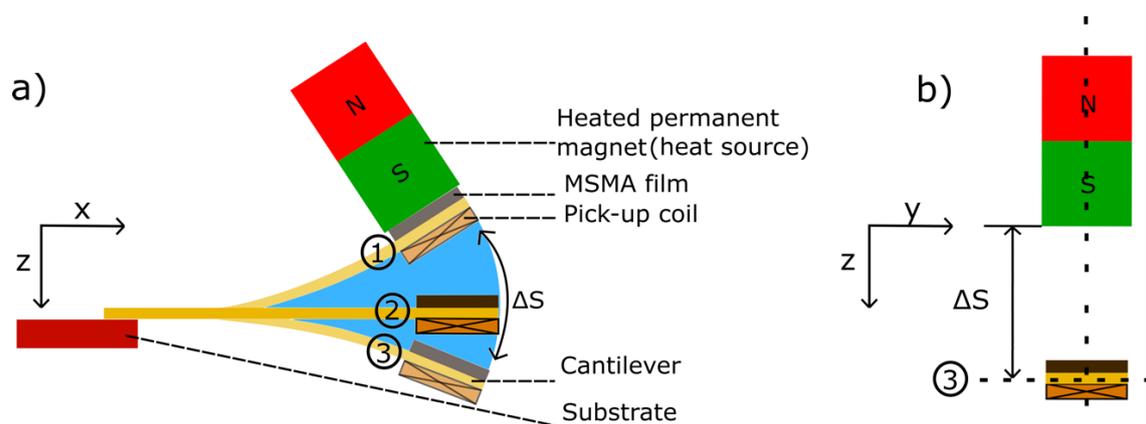


**Figure 38** Schematic of the TMG, (a) Side view of the TMG, (b) front view of the TMG. Reprinted from Joseph et al. [128]

---

[a]Section 4.1 has been published in similar form by the author in Joseph et al.[128]

The TMG device is shown schematically in **Figure 38** and is made up of a cantilever beam that is affixed to a substrate and has an active TM film and a pick-up coil affixed to its freely movable end. The magnetic force that pulls the free end of the cantilever towards the magnetic surface is produced by a heated magnet, which is subsequently utilized to produce electrical energy. Heat transfer takes place as the cantilever makes contact with the magnet, creating a ferromagnetic transition in the TM film. The TM film cools as the cantilever oscillates back, which restores the magnetic attraction force. The result is an uninterrupted oscillation that is maintained by the cantilever front's inertia force due to the tip mass of the coil. As a result, the oscillatory action aids in cooling the TM film. When cooling and heating result in an adequate change in magnetization and associated magnetic actuation force within a cycle, resonant self-actuation begins to occur. This is recognized by periodic oscillation of the cantilever tip without showing any damped oscillations and each cycle is a repetition of the previous one. In this instance, thermal energy is most effectively transformed into mechanical and magnetic energy. The pick-up coil then transforms this mechanical and magnetic energy into electrical energy.

## 4.2. Lumped element model

By combining the mechanical motion of the cantilever front, magnetization changes in the MSMA film, and heat flows during film heating and cooling, the LEM should represent the energy conversion processes in the TMG. By maintaining the harvester in resonant self-actuation mode, the model should enable optimization of the design parameters to achieve maximum power and efficiency. For each position and time step during simulation, the various physics components exchange data. The LEM parameters used for simulations are given in a table for each section of the results. The model is divided into 4 parts, mechanical, magnetic, thermal, and electrical sections. Each section deals with a part of the TMG cycle. The mechanical section deals with oscillations and damping using the magnetic field, magnetic field gradient, and magnetic force derived from the magnetic section. The thermal part simulates the heat transfer processes and finally, the electrical section derives the electrical output.

### 4.2.1. Mechanical section

The center of mass at the movable cantilever beam tip is moved in one dimension to approximate the mechanical deflection of the cantilever tip while ignoring the lateral displace-

---

[b]Section 4.2 has been published in similar form by the author in Joseph et al.[128]
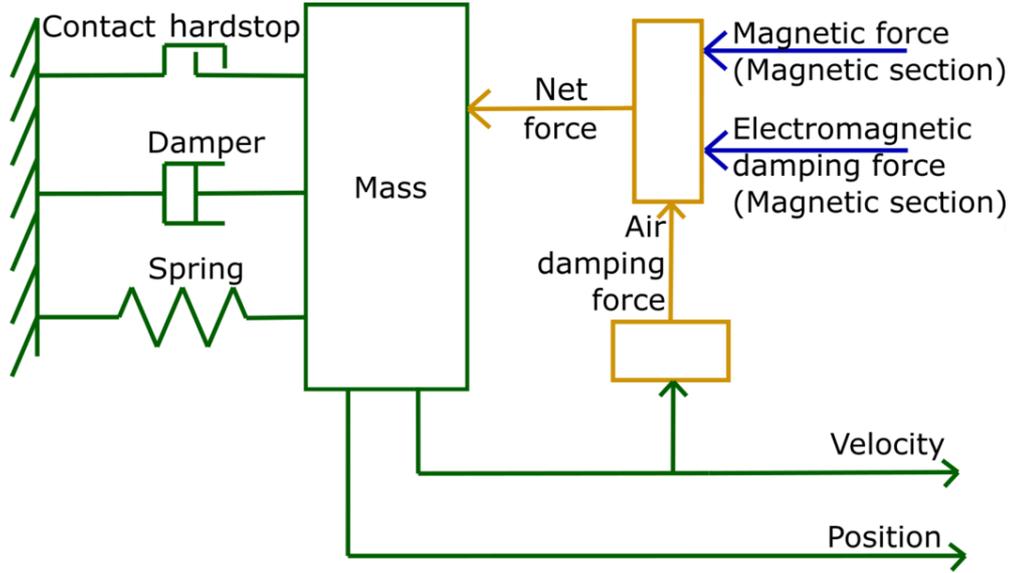
**Figure 39** Mechanical section with inputs of magnetic force and electromagnetic damping force and outputs of velocity and position of the beam front. Reprinted from Joseph et al.[128]

ment brought on by bending. Gravitational force affects the movable mass while using the TMG in a vertical direction, however, it is insignificant in comparison to magnetic and restoring forces. The magnetic force $F_{mag}$, inertia force, damping force, and the elastic force of the cantilever all contribute to the net force $F_{net}$ acting on the cantilever front. For computing the effective force at the cantilever tip, the section uses the magnetic force and electromagnetic damping force as input parameters. Thus, the damping forces brought about by structural damping, viscous air damping $F_{air}$,[129] and electromagnetic damping $F_{em}$[130] are taken into consideration. The center of mass's position and velocity are taken as the output parameters by solving the equation of motion considering the influencing forces.

$$F_{net} = m\frac{d^2x}{dt^2} + c\frac{dx}{dt} + kx + F_{mag} - F_{em} - F_{air}$$

Eq ( 16 )

The movable mass of the m  is taken as:[131]

$$m = \frac{33}{140} \times m_{cant} + m_{coil} + m_{film}$$

Eq ( 17 )

The cantilever tip experiences an additional elastic impact force as it comes into contact with the magnet surface, which causes it to abruptly halt movement at the surface. **Figure 39** shows a schematic representation of the mechanical section of the LEM. With a damping coefficient of c, the damper represents structural damping, and the spring specifies the

stiffness of the beam cantilever, k. The contact hard stops with contact stiffness and the impact damping coefficient provide the impact force at contact. With the use of a firm reference, the beam is fastened at one end. The mass serves as a point load at the opposing free-moving end.

## 4.2.2. Magnetic section

The magnetic section is depicted schematically in **Figure 40.** The temperature of the TM film, the location of the cantilever tip, and the current flowing through the pick-up coil are input parameters. A lookup table that contains experimental data on the relationship between the temperature and magnetic field and the magnetization of the TM film enables the simulation to choose the magnetization value that is most suited given the inputs for temperature and magnetic field as there is no hysteresis in transformation. The magnetic force $F_{mag}$ on the TM film is calculated with the inclusion of magnetization. The magnetic field is calculated along the symmetry axis z direction to determine $F_{mag}$, using an adapted version of Biot Savart law.[132,133]
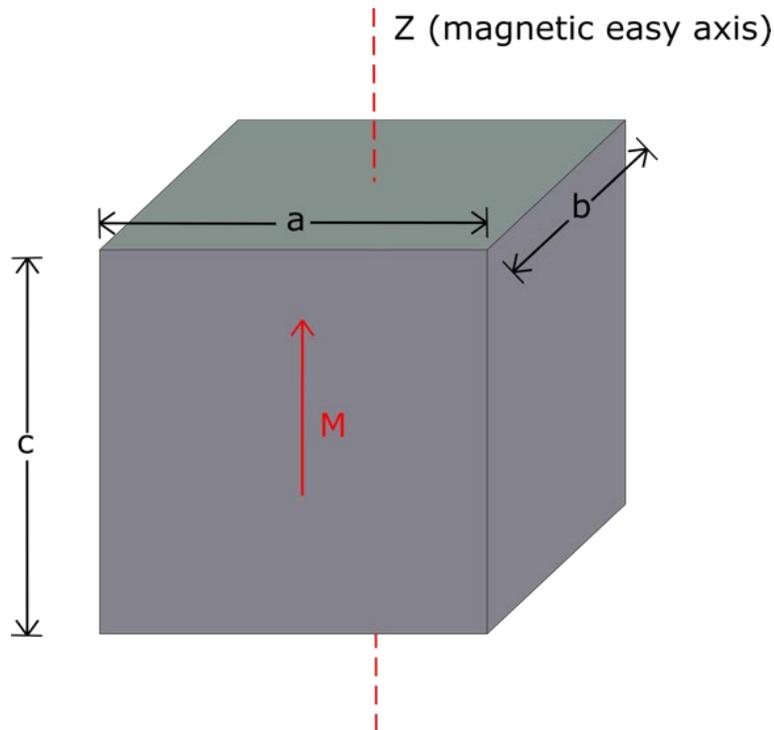


$$B(z) = \frac{Br}{\pi} \left\{ \arctan\left(\frac{ab}{2z\sqrt{4z^2 + a^2 + b^2}}\right) - \arctan\left(\frac{ab}{2(c + z)\sqrt{4(c + z)^2 + a^2 + b^2}}\right) \right\}$$

Eq ( 18 )
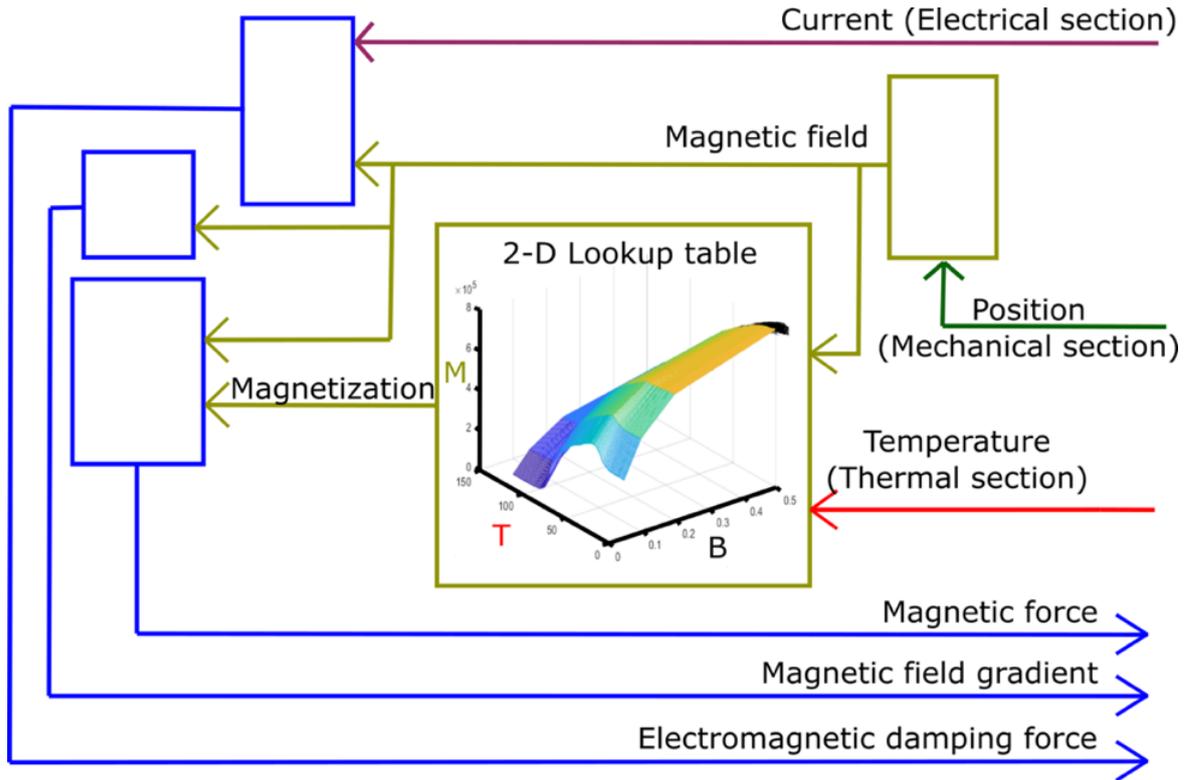
**Figure 40** Magnetic Section with the temperature of the TM film and position of the beam front as inputs. The magnetic force, magnetic field gradient, and electromagnetic damping force are the outputs of the section. Reprinted from Joseph et al.[128]

Eq ( 18 ) lets us calculate the magnetic field at a distance z from the magnet surface. This can also be extended to three dimensions if required.[133] Taking the derivative of the equation Eq ( 18 ) with respect to z gives us Eq ( 19 ), which is the magnetic field gradient at any distance z. Here the assumption is made that the cantilever deflection is a 1- dimensional motion.

$$
\frac{\partial B(z)}{\partial z} = \frac{Br}{\pi} \left\{ \left( \frac{-\dfrac{ab}{2z^2\sqrt{4z^2 + a^2 + b^2}} - \dfrac{2ab}{(4z^2 + a^2 + b^2)^{\frac{3}{2}}}}{\dfrac{a^2b^2}{4z^2(4z^2 + a^2 + b^2)} + 1} \right) \right.
$$
$$
\left. - \left( \frac{-\dfrac{ab}{2(c + z)\sqrt{4(c + z)^2 + a^2 + b^2}} - \dfrac{2ab}{(4(c + z)^2 + a^2 + b^2)^{\frac{3}{2}}}}{\dfrac{a^2b^2}{4(c + z)^2(4(c + z)^2 + a^2 + b^2)} + 1} \right) \right\}
$$

<div align="right">Eq ( 19 )</div>

$$F_{mag} = V_{mag} M_T \frac{\partial B_z}{\partial z}$$

<div align="right">Eq ( 20 )</div>

Equations Eq ( 18 ) and Eq ( 19 ) are used to predict analytically the magnetic field $B_z$ and field gradient ($\partial B_z/\partial z$) as a function of the position of the MSMA film (distance from the magnet surface along the z-direction). The TM film volume is taken as $V_{mag}$. Using the generated current in the pick-up coil and magnetic field as inputs, the electromagnetic damping is calculated. Magnetic force $F_{mag}$, magnetic field gradient, and electromagnetic damping force are the output parameters. These forces depend on the temperature and position of the TM film. Eq ( 20 ) gives the final magnetic force acting on the magnetizable material.

## 4.2.3. Thermal section

The numerous heat transfer processes that take place in the device are schematically shown in **Figure 41.** Heat transfer between a heat source and TM film (process 1) depends on the contact heat transfer coefficient ($h_f$), and the temperature difference between the $T_{source}$ and the temperature of TM film ($T_{film}$). A large contact area is an advantage of thin film geometry due to its large surface-area-to-volume ratio. The permanent magnet's polished surface results in a smooth surface finish, which is crucial for optimum thermal contact. Heat convection from the TM film to the surrounding air via the top and side surface is denoted by processes 2 and 3, respectively. Along with the temperature difference between the TM film and the surrounding air, the convective heat transfer coefficient, which is heavily influenced by the speed of the cantilever tip determines these processes.



1. Heat transfer from heat source to TM film
2. Convection from film to ambient air (enhanced by oscillation)
3. Lateral convection to ambient air (TM film and bonding layer)
4. Heat transfer from film to bonding layer
5. Heat transfer from bonding layer to cantilever
6. Heat conduction through cantilever
7. Convection from cantilever to ambient air (enhanced by oscillation)
8. Heat transfer to ceramic substrate

**Figure 41** Heat transfer processes in the TMG assembly. Reprinted from Joseph et al.[91]

When the $T_{source}$ rises, the oscillation frequency increases, and the heating time required to achieve a significant $\Delta T$ decreases.[28] Because the cantilever front moves more quickly with increasing frequency, there is a rise in convective heat transfer, which enables the device to adapt to changes in the temperature of the heat source. The thermal section of the LEM simulation models the heat flow and thermal interaction between different components of the TMG. The common approach for modeling heat flow is by utilizing either a Foster or Cauer model in which an electrical analogy is used with resistance and capacitors representing thermal resistance and thermal capacitances of different components.[79]
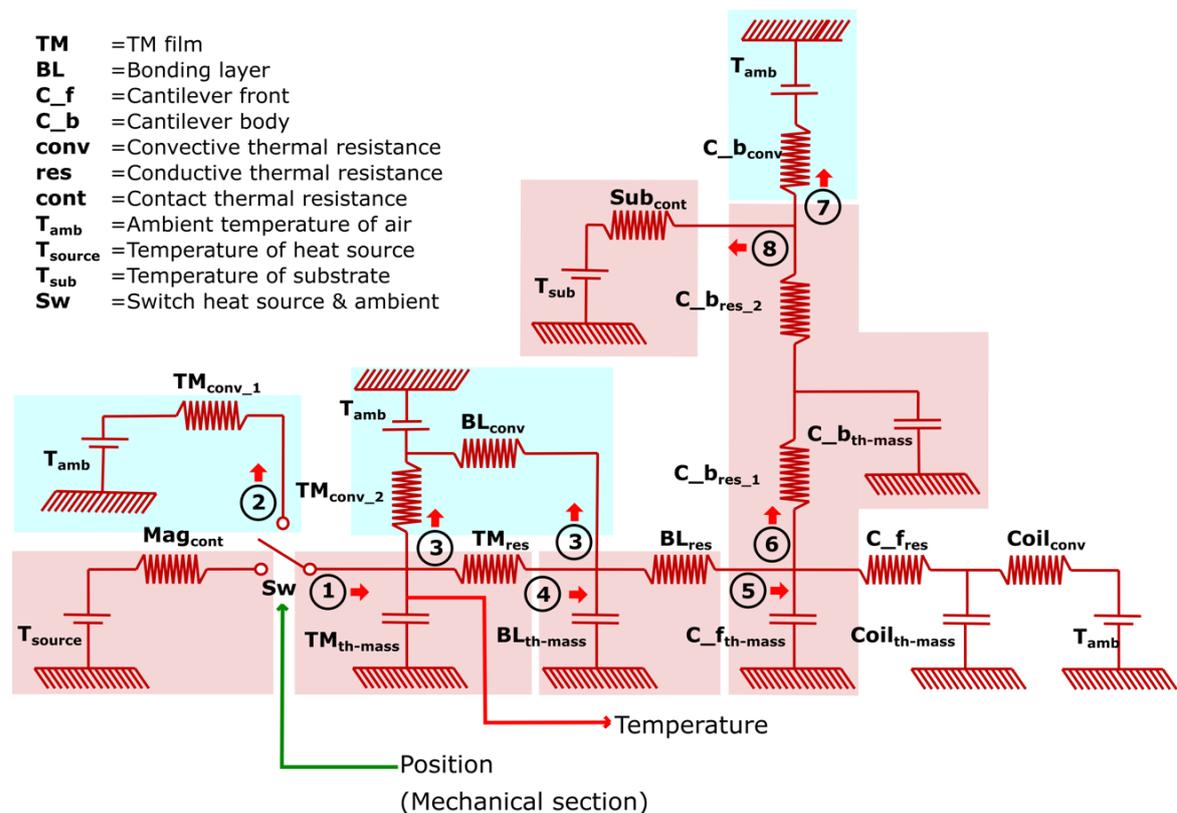


**Figure 42** LEM of thermal section takes in position as input and generates the temperature of different components (like film, cantilever, etc.) as the outputs. Reprinted from Joseph et al.[91]

Although both models can give an accurate heat flow, the Foster model does not represent the system on the component level, thus it is hard to model the heat flow path within the components and also to know the temperature of each component. Hence in the presented LEM model, a Cauer thermal model, which is a continuous fraction model, is used. This allows modeling of thermal behavior and performance on a component level within the TMG. The TMG's thermal section is shown schematically in **Figure 42** with different heat

transfer processes marked with a box that corresponds to **Figure 41**. Eq ( 21 ), which gives the overall thermal impedance $Z_{th}$ of the device, represents the continuous fraction equation of the thermal network used in the work: Thereby 'n' is the total number of nodes, and $C_{th(i)}$ and $R_{th(i)}$ are the thermal capacitance and resistance of a given node, respectively. A section of the device assembly is represented by each node in the model; for example, the first section would be the TM film, the second would be the non-conductive bonding layer, etc.

$$Z_{th} = \cfrac{1}{C_{th(1)} + \cfrac{1}{R_{th(1)} + \cfrac{1}{C_{th(2)} + \cfrac{1}{R_{th(2)} + \cdots \cfrac{1}{C_{th(n)} + \cfrac{1}{R_{th(n)}}}}}}}$$

Eq ( 21 )

Using this method, it is also possible to think of individual parts as a combination of several thermal resistors and capacitors, allowing us to calculate the temperature gradient across each component of the device with a resolution equal to the number of thermal resistors and capacitors. However, only one thermal resistor and thermal capacitor are utilized for each part generally because the heat flow and average layer temperature are of greater importance. Depending on its dimensions and thermal characteristics, each section's ΔT can be calculated and the heat flow direction can be identified.[134]

## 4.2.4. Electrical section

The schematic of the electrical section is shown in **Figure 43**. It computes the induced voltage $V_{ind}$ using Faraday's law based on the inputs of the magnetic field gradient and pick-up coil velocity.[69]

$$V_{ind} = N_{coil} A_{coil} \frac{\partial B_z}{\partial z} \frac{\partial z}{\partial t}$$

Eq ( 22 )

$N_{coil}$ and $A_{coil}$ are used to denote the pick-up coil's area and the number of turns, respectively. $\frac{\partial z}{\partial t}$ represents the film/pick-up coil velocity. The electrical section's output, the induced current is calculated from $V_{ind}$, and the internal pick-up coil resistance as a function of load resistance ($R_L$). As a minor effect in the case of TM film, the change in flux density

brought on by the change in magnetization of the TM film is disregarded. This is due to the low volume of the active material, which causes a change in magnetic flux density which is several orders less than the change due to the stroke of the beam.
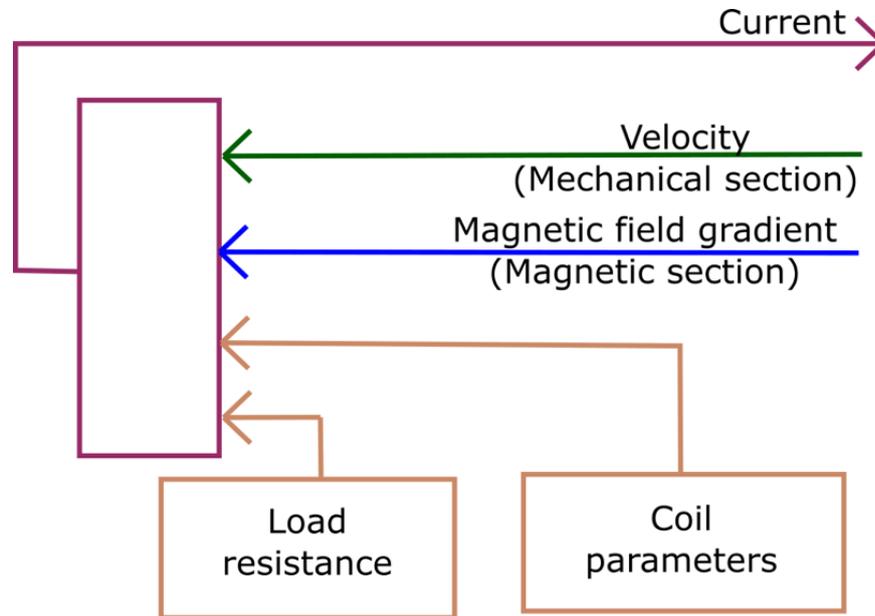


**Figure 43** Electrical section takes in the velocity of the beam front and magnetic field gradient as the input to the section and generated current is given out as output. Pick-up coil parameters and $R_L$ do not change during the simulation of one configuration and hence are given as constants. Reprinted from Joseph et al.[128]

## 4.3. Experimental setup

A modular measurement setup is assembled using position stages and adapters. The magnet holder is designed to achieve 360° rotation while keeping an edge of the magnet at the same position. The position of the magnet in relation to the sample should only change in one direction when adjusting to achieve proper contact with the TM film. Achieving proper physical contact between the TM film and magnet surface is significant to having a large value of contact heat transfer coefficient ($h_f$). The thin films (Ni-Mn-Ga and Gadolinium) are usually smooth as they are fabricated by magnetron sputtering, the magnet surface in contact is wet polished to a mirror finish to achieve maximum contact. In some fabrication processes, like the melt spinning used for La-Fe-Si-H samples, the surface of the TM film prepared is rough and hence the value of $h_f$ at contact is lower compared to the sputter deposited films.

**Figure 44** illustrates the electromechanical circuit diagram of the TMG. A resistive heater built into the magnet holder is used to heat the permanent magnet, and an RTD sensor (PT100) affixed close to the magnet's tip is used to monitor its temperature. The RTD sensor is connected to a temperature sensor module USB-TEMP from MCC, and temperature data retrieved using InstaCal software on the PC. For the purpose of measuring deflection, a Panasonic HL-G103SJ laser triangulation sensor is employed. The sensor is connected to a USB 6211 A/D card from National Instruments and is used in analog mode. The cantilever moves in two dimensions because it is bending upward, which causes a measuring error that is equivalent to a 5 percent error in terms of the entire stroke. To measure the generator's output, a load resistor ($R_L$) is attached to the TMG. To measure the current flowing through the $R_L$, a current pre-amplifier with the model number SR570 from Stanford Research Systems is connected in series. Under low noise conditions, a sensitivity of 100 µA/V is used, with a resolution of 60 pA. Additionally, an A/D card is attached to the output of the current pre-amplifier. The USB 6211 A/D card is connected to a PC running LabVIEW, which is used for data acquisition at 5000 Hz and performs basic data processing, including the computation of instantaneous power from the measured current, which is exported as an excel file (xlsx format). Data is recorded for a duration of either 3s or 10s, and 10 sets of such measurements are taken for every point of operation of the TMG (for averaging). Different loads are connected to the TMG to investigate the optimum $R_L$ for the maximum power output of the TMG. A python script is used to analyze the data. Average power is calculated by integrating instantaneous power for the entire time and dividing it by the duration of data acquisition. By doing peak to peak analy-
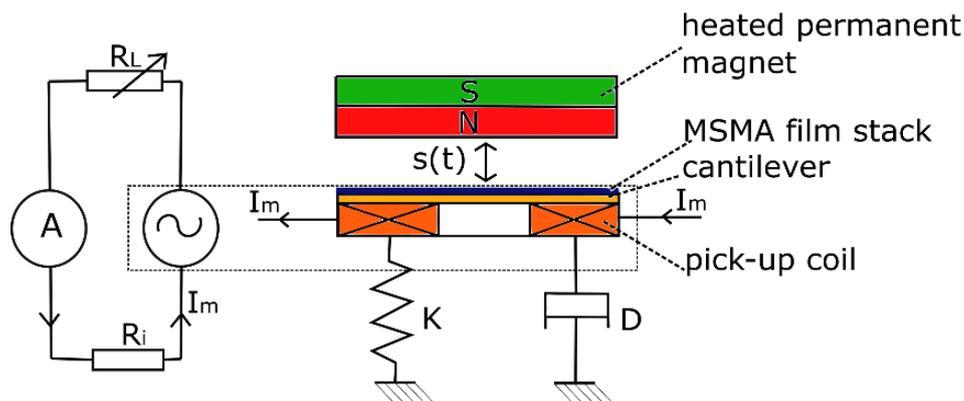


**Figure 44** Electromechanical circuit diagram of a TMG. A spring-mass-damper system with stiffness K and damping constant D make up the mechanical component. The pick-up coil's internal resistance ($R_i$) and the $R_L$ are both included in the electrical component. $I_m$ stands for the induced electrical current. Adapted from Joseph et al.[28]

sis of deflection measurement data, the stroke is computed and averaged over the entire measurement. The frequency of the device operation is determined by converting deflection measurements from the time domain into the frequency domain by doing an FFT analysis. Power, stroke, and frequency are calculated for ten measurements taken consecutively and then the mean is calculated to get the average power, average stroke, and average frequency for that measurement point. **Figure 45** shows a schematic model of the experimental setup used to characterize samples.



- rotational stage
- permanent magnet
- magnet holder with heater
- stage with pitch and yaw dof
- 3-axis linear stage
- laser displacement sensor
- linear rail
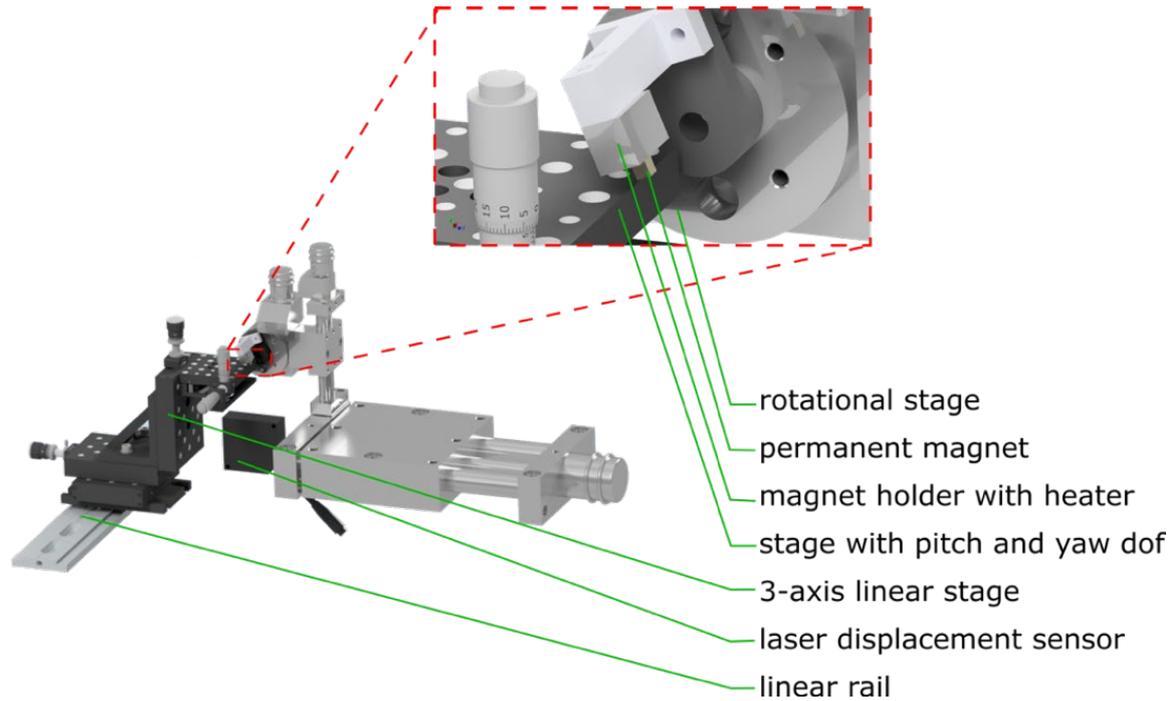
**Figure 45** 3D model of the experimental setup used to measure the output of the thermomagnetic generators, allowing for several degrees of freedom.

## 4.4. TMG with Ni-Mn-Ga

### 4.4.1. Material properties

Heusler alloys are ordered intermetallics that display multiferroic phase transformations because electronic spin interactions are highly influenced by variations in interatomic distances and local symmetry.[48,51,65,66,135,136] The alloys Ni-Mn-Z and Ni-Co-Mn-Z (Z = Ga, In, Sn...) are notable examples. These materials display strong effects such as magnetic field-induced strains,[48,137] magnetoresistances,[49] magnetocaloric effects,[50] and magnetic-field-induced shape memory effects.[51] In this study, the focus is on $Ni_{53.5}Mn_{23.8}Ga_{22.7}$ films,

---

[c]Section 4.4 has been published in similar form by the author in Joseph et al.[28,128]
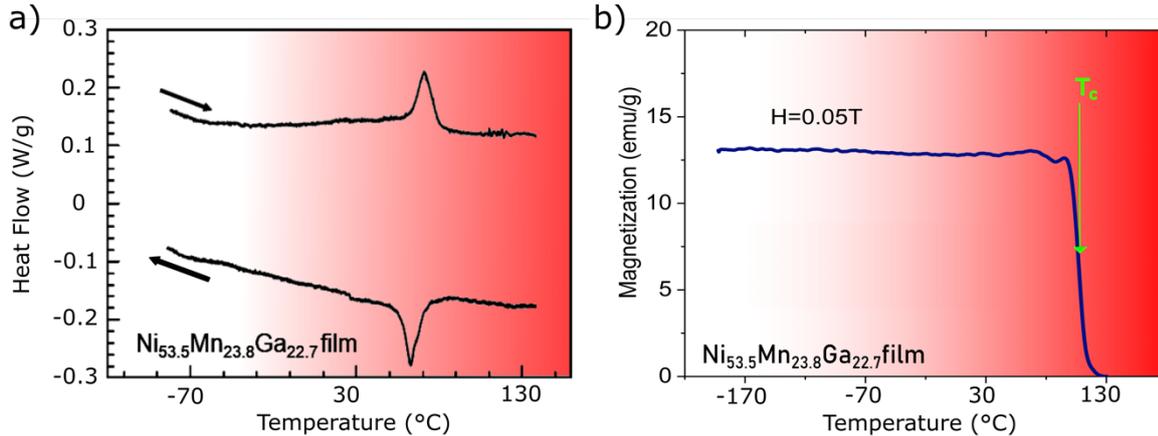
**Figure 46** (a) DSC measurement of Ni-Mn-Ga alloy (b) Magnetization measurement for varying temperatures for Ni-Mn-Ga film. Reprinted from Joseph et al.[28]

which exhibit both a first-order martensitic transformation and a second-order ferromagnetic transition. By using RF magnetron sputtering to create the Ni-Mn-Ga films, the Ni concentration and, consequently, the phase transition temperatures, are controlled.[138–140] Due to limitations in sputtering duration and associated film homogeneity, the film thickness has usually a thickness below 10 µm. The material properties are finalized by heat treatment of 10 hours at 800 °C. Differential scanning calorimetry is used to determine the film's phase change over temperatures (DSC). **Figure 46**a depicts the DSC measurement for the Ni-Mn-Ga film. With transformation temperatures between 57 °C and 83 °C, the peaks represent the first-order martensitic transition.

The fact that the transition temperatures are heavily influenced by chemical composition and the associated electron concentration per atomic unit (e/a-ratio) provides for a wide range of tailoring.[141] A temperature-dependent magnetization measurement of a Ni-Mn-Ga film at 0.05 T of the low magnetic field is shown in **Figure 46**b. The material is in the martensitic and ferromagnetic state at room temperature. The martensitic phase change is responsible for a small step-like characteristic that appears at around 70 °C. The $T_c$ occurs at about 102 °C, the magnetization undergoes a rapid ferromagnetic transition with a substantial change in magnetization ($\Delta M$) occurring within a small $\Delta T$ which is much less influenced by chemical composition.[126] Due to the second-order nature of this transition, it does not show hysteresis. To drive the TMG's resonant self-actuation in a magnetic field gradient at a low magnetic field (<0.5 T), we use the abrupt change of $\Delta M/\Delta T$ at $T_c$. The magneto-caloric effect is thought to be minimal in situations with a low magnetic field and separated first-order and second-order transitions.

## 4.4.2. Fabrication

In a high-purity argon environment, RF magnetron sputtering is used to create the Ni-Mn-Ga films. The Ni concentration and subsequently the phase transformation temperatures are controlled by adjusting the sputtering power.[138] To customize the temperature-dependent change in magnetization at the $T_c$, a heat treatment lasting 10 hours is conducted at 800 °C. By using an inductively coupled plasma technique, it is discovered that the crystallized freestanding films are composed of $Ni_{53.5}Mn_{23.8}Ga_{22.7}$. The sputtering time is regulated to produce a layer with a thickness between 5 and 10 μm. Ohtsuka et al.[142] provide information about the films within the experiment's structure. The pick-up coils are created by sandwiching a 250 μm thick PMMA core with a 1 x 1 mm² surface area between two 25 μm thick Kapton foils with a 2 x 2 mm² surface area. Using a semi-automatic setup (Semi-automatic coil winder) and insulated copper wire with a diameter of 15 μm, the pick-up coils are fabricated.

The device is fabricated in five steps as shown in **Figure 47**. Step I show the ceramic substrate which is prepared using laser cutting from an alumina sheet using a pulsed laser. The brass cantilever is fabricated using laser processing by an ultra-short pulse femtosecond laser from a brass sheet. In step II this cantilever is attached to the ceramic substrate. The pick-up coil fabricated by the semi-automatic coil winder is attached to the underside of the cantilever tip in step III. Using a non-conductive bonding layer, the TM film is attached to the cantilever tip in step IV.
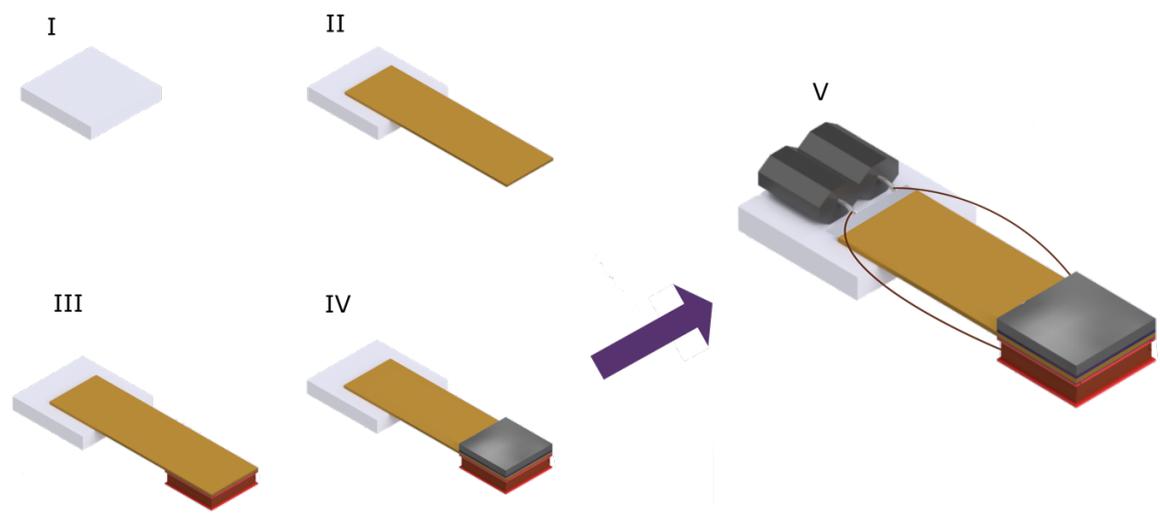


**Figure 47** Fabrication steps for preparing a TMG prototype.

Finally, in step V the connector bush pins are added and attached to the pick-up coil. The connector bush pin allows external connections to the pick-up coil for electrical measurements. The completed device assembly is placed under a permanent magnet for providing the magnetic field to magnetize the TM film and the magnetic field gradient for the magnetic force. Using a digital microscope, the magnet is placed in relation to the Ni-Mn-Ga film surface at the ideal distance and angle to guarantee maximum contact while minimizing the impact on the magnet surface during operation. The wires are only 15 μm, which is thin enough to avoid any mechanical effects on the cantilever motion. Before conducting experiments, the magnet is heated until a stationary temperature is attained. Data are gathered by varying $R_L$ of each reading while maintaining a constant temperature at source. For every set of $T_{source}$, these procedures are repeated.

### 4.4.3. Device characterization

Since several different TMGs are fabricated and performance is analyzed for all of them, it is necessary to have a standard performance characterization for the device so that different materials could be compared with each other. The size of the magnet is kept constant (3 mm x 3 mm x 8 mm) to avoid the effect of the magnet on the performance comparison between the devices. To keep consistency, the lateral dimensions of the TM film are also kept constant, the magnetic force is only tuned by changing the thickness of the film. The width of the cantilever is kept at 2 mm to avoid any overhanging which increases air damping. The stiffness of the cantilever is adjusted by changing the length of the beam, if the length of the beam exceeds 6 mm, the thickness of the cantilever is reduced.

If the length of the cantilever required for appropriate stiffness to balance mechanical and thermal cycle is less than 4.3, the thickness of the beam is increased, and the length is tuned accordingly. This is to avoid increasing the stroke more than 2.5 mm (in the case of long cantilevers) and to avoid a very large bending angle within the cantilever (for short cantilevers). A stroke of more than 2.5 mm would result in a very low magnetic field gradient. This is explained in detail in section **5.1.** A large bending angle would result in higher stress within the cantilever beam causing fatigue and other undesirable effects. The dependence of performance of the TMG on $R_L$ and $T_{source}$ is shown in **Figure 48**. **Figure 48** shows the performance of a TMG with a magnetron sputtered Ni-Mn-Ga film as the TM film. The composition of the film is $Ni_{53.5}$-$Mn_{23.8}$-$Ga_{22.7}$.
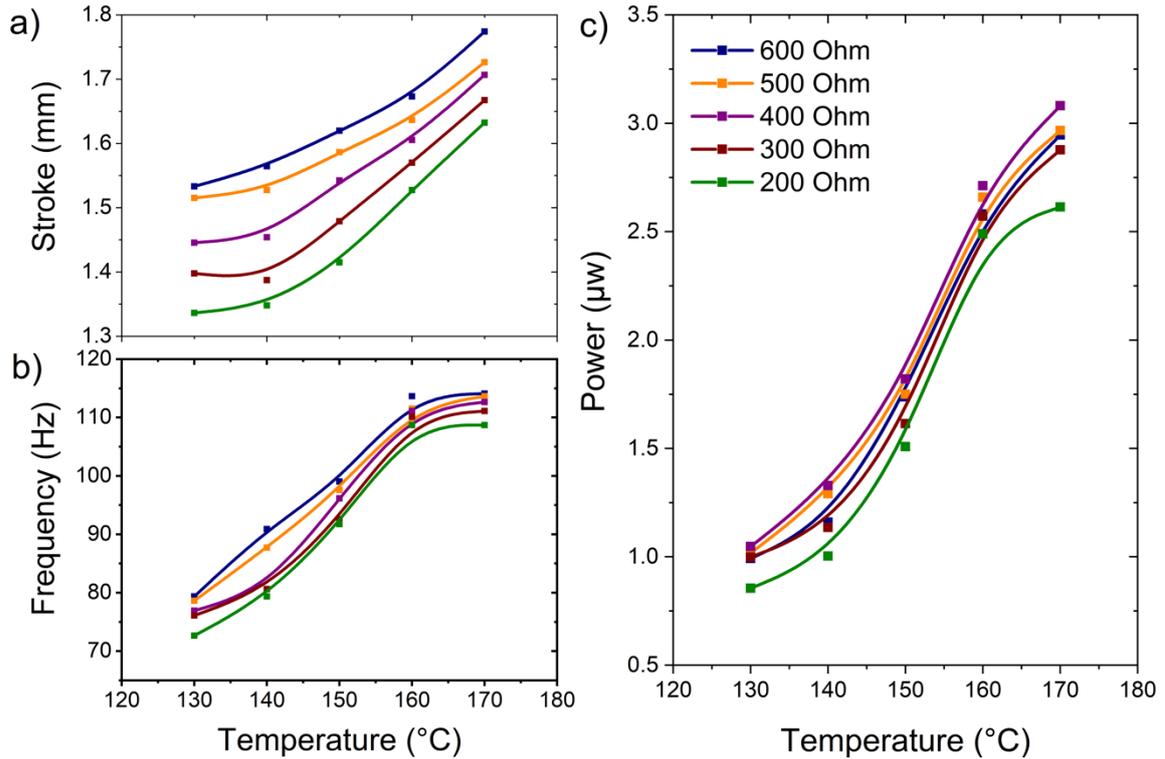
**Figure 48** Effect of $R_L$ on the performance of the TMG (a) stroke of deflection, (b) frequency of oscillation, (c) power output from the pick-up coil. Part of data pre-published in Joseph et al.[28,91,128]

The thickness of the film is 10 µm with a lateral dimension of 2 mm × 2 mm. The cantilever is a single beam with a lateral dimension of 2 mm x 5.7 mm and a thickness of 20 µm. The cantilever is attached to the substrate using a non-conductive bonding layer. The TMG is operated at a $T_{amb}$ of 23 °C. The maximum performance is reached at a $T_{source}$ of 170 °C and an $R_L$ value of 400 Ohm. The power output increase as the $R_L$ is increased from 200 Ohm and reached a peak value of 3.1 µW. The power output shows a reduction when the $R_L$ is increased further. The stroke increases as the $T_{source}$ is increased. The stoke continuously shows an increase as the $R_L$ is increased from 200 to 600 Ohm without presenting an optimum value of the $R_L$. Frequency is also affected by the change in $R_L$ and shows an increase as the value of $R_L$ is increased. Although both the stroke and frequency increase with an increase in $T_{source}$, the transfer efficiency decreases as the $R_L$ is increasing, as the value is moving further away from the internal resistance of the device. The performance of the device increases as the current through the pick-up coil is reduced when $R_L$ increases, causing a reduction of electromagnetic damping. Thus, these contradicting features cause the device to have an optimum $R_L$ of 400 Ohm at which the maximum power output is observed.

73

## 4.4.4. Model validation
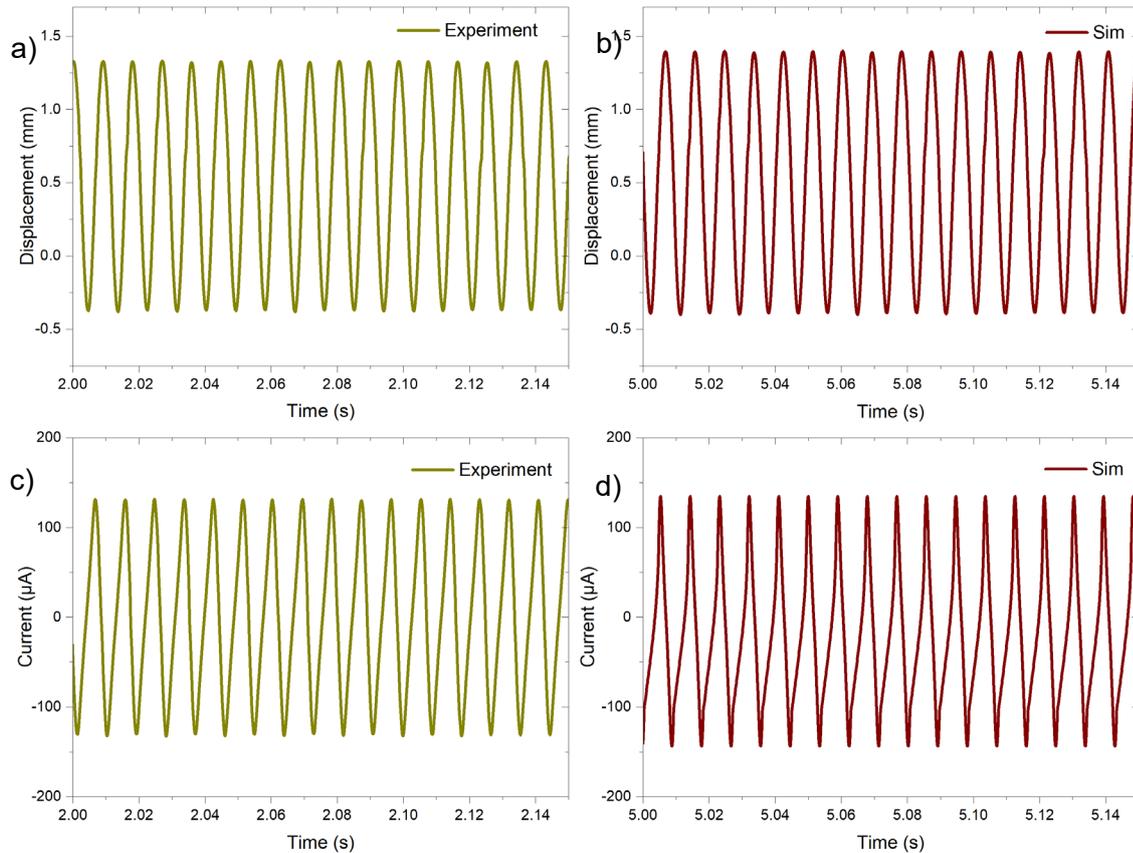


**Figure 49** Model validation for the case of the TMG with NiMnGa at a $T_{source}$ of 170 °C and an $R_L$ of 400 Ohm (a) displacement measurement, (b) LEM simulation of displacement, (c) current measurement, (d) LEM simulation of current. Reprinted from Joseph et al.[91]

For a $T_{source}$ of 170 °C and an $R_L$ of 400 Ohm, time-resolved experimental and simulated properties of center-of-mass displacement and corresponding electrical current induced in the pick-up coil are examined for a TMG with Ni-Mn-Ga as TM film are shown in **Figure 49**. The simulation model is validated by the good agreement between simulation and experiment results. The results shown are obtained under stationary operating conditions, which are attained after a short period of time in continuous resonant oscillation and then last for hours with no discernible performance change. Once the time resolved performance of the simulated the TMG is matched with experiments, it allows for the estimation of the contact heat transfer coefficient ($h_f$) and the heat transfer coefficient of convection. These values are dependent on the surface conditions, impact force, velocity of the cantilever tip and the ambient conditions. These values could not be measured experimentally without affecting the performance of the TMG.

## 4.5. Thermal cycle in TMG under resonant self-actuation

The LEM is used to investigate the time-dependent variations in temperature, magnetic field, magnetic field gradient, and associated magnetization of TM film in a TMG with Ni-Mn-Ga as the active TM film during TM cycling. Cantilever motion can be divided into four phases, as shown in **Figure 50**a. Stage (1) corresponds to the instance when the Ni-Mn-Ga film comes into mechanical contact with the heat source, resulting in the transfer of heat into the film. The magnetization of the film is reduced due to the increase in temperature of the film, even though, the magnetic field experienced by the film is constant as can be inferred from **Figure 50**d and **Figure 50**c respectively. Stage (2) represents the instance when the Ni-Mn-Ga film and pick-up coil are accelerated to maximum speed upon deflection from the magnet, which corresponds to a maximum induced voltage. At the greatest distance from the magnet, stage (3) is attained which also corresponds to the lowest field and magnetization within the TM film. Stage (4) denotes a second maximum induced voltage that occurs in the opposite direction when the pick-up coil is moving at its fastest speed towards the magnet as it attracts the Ni-Mn-Ga film. The actual cycle is more gradual with increasing magnetization over the entire oscillation, unlike the case of an ideal cycle with a heat sink causing the magnetization to increase suddenly at stage (3). **Figure 50**b shows the time-resolved $\Delta T$ that occurs during resonant self-actuation in the Ni-Mn-Ga film. The film depicts a $\Delta T$ of around 10 °C in a period of time of about 8.7 ms during one oscillation cycle. The temperature of the film exhibits a sharp rise within approximately 1 ms while in mechanical contact (1). The subsequent temperature drop happens more gradually as it moves through stage (2) - (4). Rapid heat transfer during mechanical contact with the heat source makes the relatively substantial $\Delta T$ possible, whereas heat loss by heat conduction and convection is constrained. The temperature difference between the Ni-Mn-Ga film's lowest temperature and the cantilever below it is less than 0.5 °C. The cantilever temperature rises over time and saturates with very small temperature cycling. The film cools by both conduction and convection, as the film approaches the temperature of the cantilever, the conduction heat transfer is reduced, but if the oscillation is still not complete the convection continues as the ambient temperature is at a much lower temperature. This causes the Ni-Mn-Ga in some cases to cool down to a temperature slightly below cantilever temperature. This is aided by the thermal resistance of the bonding layer that prevents a sudden heat flow from cantilever back into the film.

---

[d]Section 4.5 upto but not including section 4.5.1 has been published in similar form by the author in Joseph et al.[128]
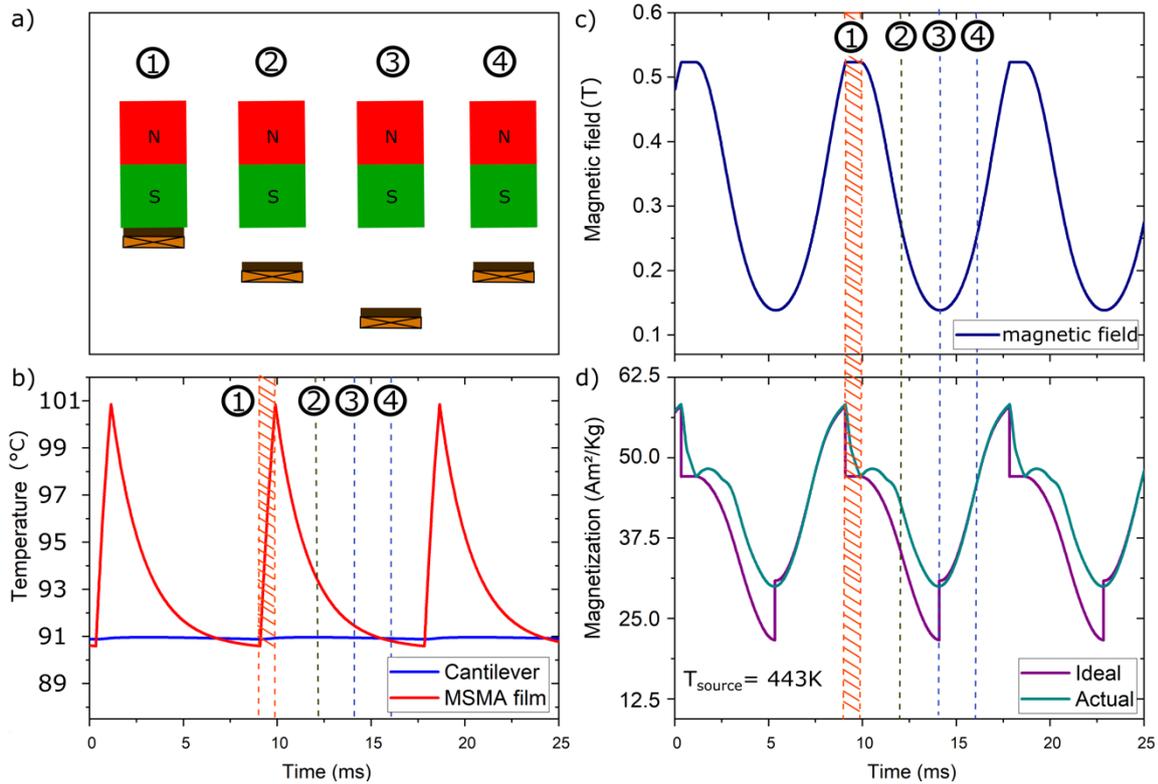
**Figure 50** (a) Device operating stages (b) temperature change within Ni-Mn-Ga film, (c) magnetic field change, (d) magnetization change in the Ni-Mn-Ga film. Reprinted from Joseph et al. [128]

## 4.5.1. Achieving resonant self-actuation by design

To achieve resonant self-actuation, it is crucial to tune the TMG parameters like the volume of the active material, cantilever dimensions, bonding layer thermal resistance and coil parameters (size and number of turns) according to the TM film properties like the magnetization under the applied magnetic fields and the change in magnetization per change in temperature ($\Delta M/\Delta T$). From the magnetization measurements, the $\Delta M/\Delta T$ values can be obtained by taking derivative of the magnetization based on temperature. **Figure 51**a shows the typical magnetization curve for Ni-Mn-Ga and **Figure 51**b shows the derived $\Delta M/\Delta T$. The peaks in the $\Delta M/\Delta T$ values show the point of operation for the device where the $\Delta T$ in the material should be concentrated to achieve the largest change in magnetization for a small $\Delta T$. The key is to adjust the stiffness, bonding layer thermal resistance ($R_b$), and $T_{source}$ range accordingly to achieve the $\Delta T$ in the TM film around the peaks in $\Delta M/\Delta T$ values. Achieving this ensures that the TMG is operating with maximum change in magnetization allowing the device to operate at high frequencies.

76
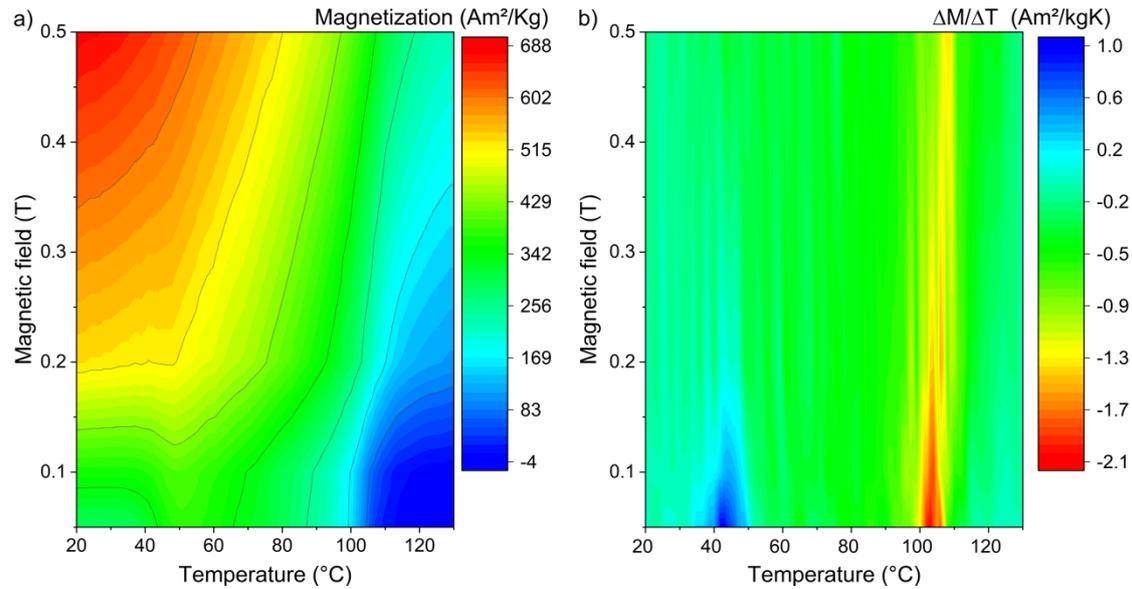
**Figure 51** Typical properties of Ni-Mn-Ga. (a) Magnetization of the Ni-Mn-Ga film, (b) ΔM/ΔT derived from magnetization to observe the change in magnetization with respect to temperature change. The data for this graph was extracted from Gueltig et al.[92]

The LEM model is supplied with the measured magnetization values as a lookup table. Then the parameter ranges are supplied to an optimization program that finds the operating range of temperatures under which the device is in resonant self-actuation and then further optimizes the performance by adjusting the parameters. The procedure for optimization is illustrated using a schematic in **Figure 52**.Once the optimal parameters are found, like the $R_b$ and the stiffness of the cantilever beam, a device prototype is fabricated with the optimized parameters by keeping tolerance to the minimum. Optimal parameters are determined by the maximum power output from the device under the constraints provided.

After conducting experiments, the simulation is readjusted to match the heat transfer coefficient of convection ($h_f$) and convective heat transfer coefficient in experiments as these values are assumed in the beginning. The TM film properties determine the optimum frequency of operation, stroke of the device, and operating temperature range of the device. Although frequency can be modified by changing the stiffness, the optimum frequency would still be determined by the TM film. The key challenge is to design TMGs with optimum heat transfer such that heat intake occurs in a limited contact time with the magnet and heat dissipation occurs across the balance of the cycle to provide regular and periodic ΔT. If ΔT in the TM film is not regular, the device will overheat, resulting in an extra oscillation or a full halt. An example of additional oscillation and operation halt due to heat buildup is given in **Figure 53** a and b respectively. It can be observed that the additional
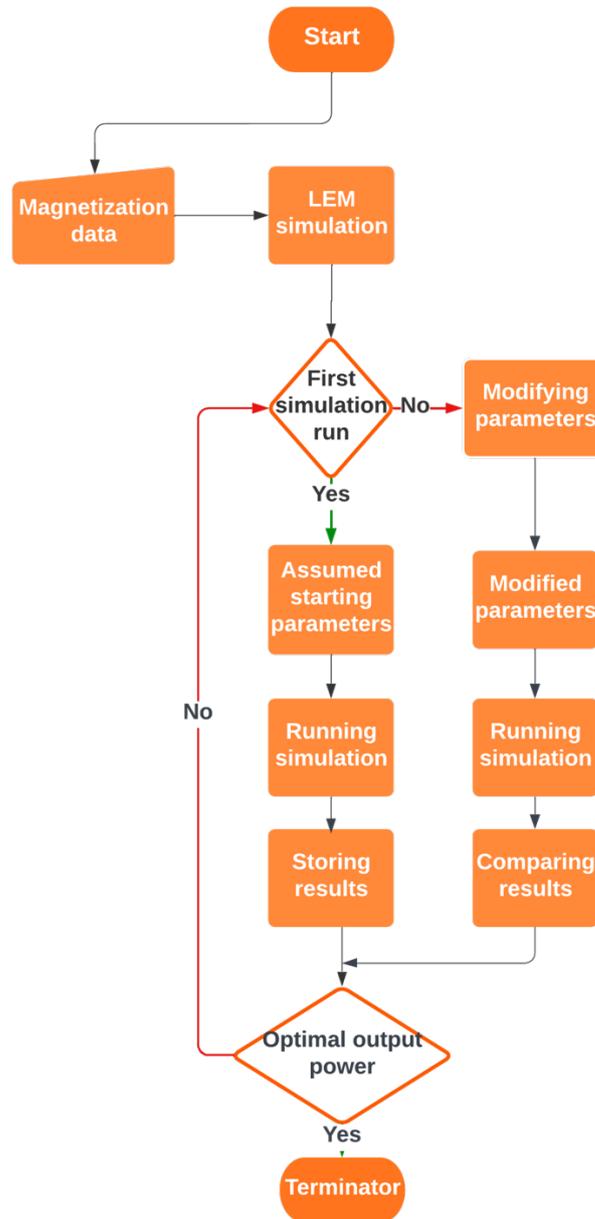
**Figure 52** Flowchart showing the optimization procedure to obtain the parameters like the operating temperature range, dimensions of cantilever and bonding layer thermal re-sistance.

oscillation is caused by the mismatch between the thermal cycle and the mechanical os-cillation. Ideally, the device should perform with maximum oscillation and velocity. Since the velocity depends on the ΔT of the film which affects the magnetic force (stiffness is constant and hence will not contribute to a change in velocity) higher change in magneti-zation will result in higher velocity (matching the tip velocity at the natural frequency of the beam). When the ideal conditions change, the device still exhibits resonant self-actuation by adjusting its frequency to match the thermal cycle. The thermal cycle is affected by the
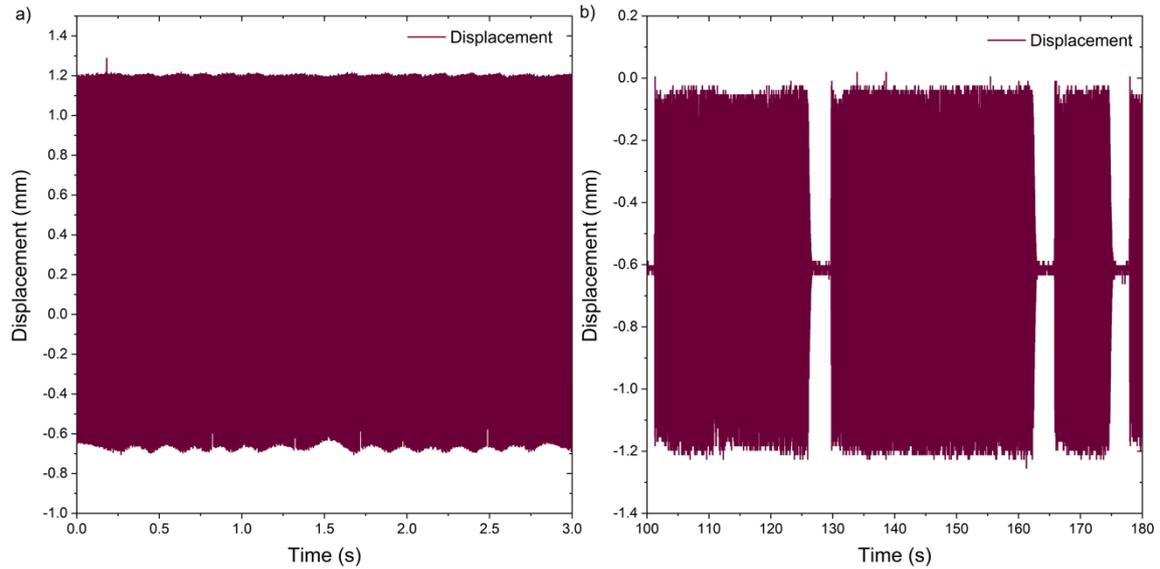
**Figure 53** Resonant self-actuation (a) with additional oscillation due to uneven heating and cooling cycles (b) heat buildup causing the device to stop operating.

ΔT in the material, which also determines the magnetic force, the velocity of the tip and the stroke. However, this window of operation depends a lot on the properties of TM film, $T_{amb}$, $T_{source}$, and device design. If the TM film exhibits a gradual and continuous drop in magnetization, then the device shows much more tolerance to change in ideal conditions, but if the material is exhibiting an abrupt drop in magnetization over a few Kelvin, then the TMG performance would be heavily affected by the change in ideal conditions. The frequency of operation also changes during operation in the case of non-resonant self-actuation as the thermal cycle is not in balance with the mechanical cycle. **Figure 54**a shows
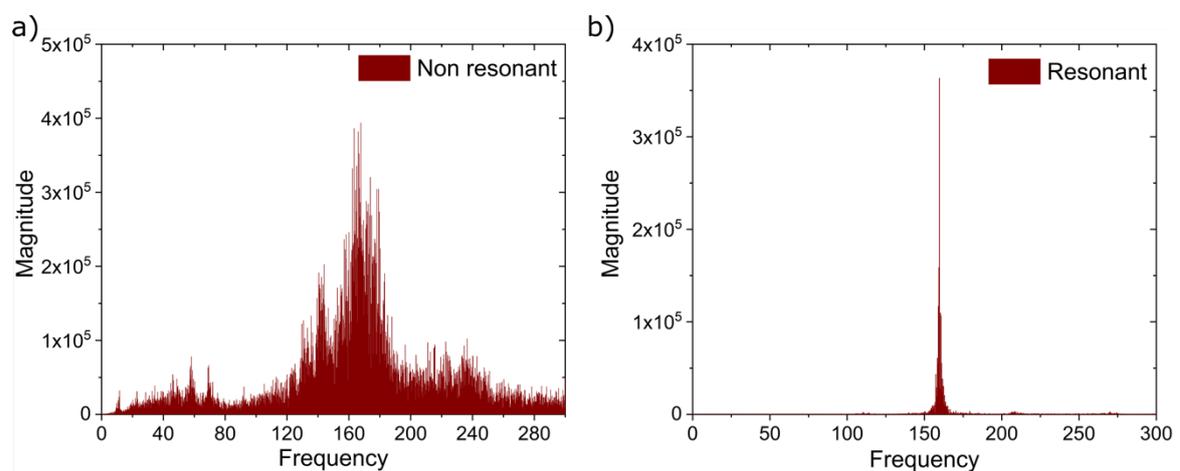


**Figure 54** FFT of time domain current measurement, (a) non-resonant self-actuation with multiple peaks, (b) resonant self-actuation with a single large peak.

the Fast Fourier Transform (FFT) for non-resonant self-actuation and it is clear that the frequency within oscillations is spread over a span. In the case of resonant self-actuation, the frequency of operation is much more stable and does not change during the operation provided the source and ambient conditions remain the same. **Figure 54**b shows the FFT for resonant self-actuation with a large single peak.

# 4.6. Discussion

The coupled thermo-magneto-mechanical performance of the TMG is described and each physical component of the device is examined using the LEM approach. Here, we concentrate on the TM film's ΔT, the magnetic field's dependency on the film's position, and the associated film magnetization which results in changes to the magnetic actuation force needed to maintain resonant self-actuation. At contact, the time-dependent temperature profile shows a quick temperature rise of 10 °C in just 1 ms, followed by a temperature fall in just 8 ms. This performance is caused by the rapid heat absorption during mechanical contact between the magnet and the Ni-Mn-Ga film and the slower heat dissipation through convection and conduction via the bonding layer and cantilever. The non-conductive bonding layer between the cantilever and the Ni-Mn-Ga film serves as a thermal boundary layer and helps to retain the majority of the input heat, which is why the temperature fall occurs considerably more slowly. It is required to assume the value of $h_f$ between the magnet and the film as well as the convective heat transfer coefficient because these quantities are challenging to measure and challenging to theoretically deduce due to a large number of unknown variables.

**Table 1** Modeling parameters for LEM simulation of the TMG. Part of data pre-published in Joseph et al.[28,91,128]

| Mechanical parameter | Unit | Value | References |
|---|---|---|---|
| Pick-up coil mass | Kg | $6 \times 10^{-6}$ | This work |
| Cantilever density | $Kg/m^3$ | 8500 | [143] |
| TM film density | $Kg/m^3$ | 8020 | [144] |
| Bonding layer density | $Kg/m^3$ | 1250 | [145] |
| Structural and air damping | Ns/m | $2.8 \times 10^{-5}$ | This work |
| Impact damping | Ns/m | 0.1 | This work |
| Contact stiffness | N/m | 10000 | This work |

| | Unit | Value | References |
|---|---|---|---|
| Young's modulus | Pa | $1 \times 10^{11}$ | [146] |
| Length of the Ni-Mn-Ga film | mm | 2 | This work |
| Width of the Ni-Mn-Ga film | mm | 2 | This work |
| Thickness of the Ni-Mn-Ga film | μm | 10 | This work |
| Length of the Cantilever beam | mm | 5.7 | This work |
| Width of the Cantilever beam | mm | 2 | This work |
| Thickness of the Cantilever beam | μm | 20 | This work |
| | | | |
| **Electrical & Magnetic Parameters** | **Unit** | **Value** | **References** |
| Remanent magnetic field | T | 1.07 | This work |
| Number of turns | - | 400 | This work |
| Area of pick-up coil | $m^2$ | $1.96 \times 10^{-6}$ | This work |
| Pick-up coil internal resistance | Ω | 250 | This work |
| Load resistance ($R_L$) | Ω | 400 | This work |
| | | | |
| **Thermal Parameters** | **Unit** | **Value** | **References** |
| Cantilever thermal conductivity | W/mK | 109 | [147] |
| TM film thermal conductivity | W/mK | 23.2 | [148] |
| Bonding layer thermal conductivity | W/mK | 0.33 | [145] |
| Cantilever heat capacity | J/kgK | 400 | [143] |
| TM film heat capacity | J/kgK | 490 | [148] |
| Bonding layer heat capacity | J/kgK | 2100 | [145] |
| Contact heat transfer coefficient | W/m²K | 7700-8400 | This work |
| Convective heat transfer coefficient | W/m²K | 40-140 | This work |
| Operation temperature | °C | 130-170 | This work |

**Table 1** shows the parameters that have been utilized in the LEM to reproduce the results of the experiment. By matching the simulation with the experiments, values of contact heat transfer coefficient and convective heat transfer coefficient have been obtained which shows good agreement with values suggested from the literature.[149] The actuation force which is determined by the magnetic field gradient, magnetization, and the impact force at the point of contact with the magnet are both factors that affect the heat intake. The maximum attraction force is 5.48 mN due to the maximum magnetization of $4.7 \times 10^5$ A/m at the

point of contact with the magnet. While the temperature rises adiabatically from about 91 °C by about 10 °C during contact, the magnetization rapidly decreases by about $10^5$ A/m. The magnetization value depicted in **Figure 7** for Ni-Mn-Ga film has a high value of ΔM/ΔT for unit volume, which is approximately $10^4$ A/(mK) for the volume of the TM film. It turns out that the best performance takes place when the ferromagnetic transition first starts, while the magnetization is still high. In order to complete the TM cycle, sufficiently strong magnetic forces are therefore preserved. The cantilever's stiffness is adjusted to balance out the forces of inertia and actuation, resulting in a relatively high operation frequency of 114 Hz.

The $R_L$ has severe effects on the performance as it causes a variation in the current generated from the pick-up coil resulting in varied electromagnetic damping. The transfer efficiency is maximum when the $R_L$ is matched to the internal resistance of the pick-up coil, which would be 200 Ohm in the presented case. But it can be seen that the power output increases as a result of the increase in both frequency and stroke as the $R_L$ increased from 200 to 300 Ohm. This is due to the decreased current in the circuit resulting in reduced electromagnetic damping. Thus, the power increases with an increase in $R_L$ even though the transfer efficiency is still reduced when the difference between $R_L$ and internal resistance increases. Thus, after increasing the $R_L$ beyond 400 Ohm the frequency and stroke still increase but the power output is reduced as the increase in frequency and stroke is not enough to compensate for the subsequent loss in transfer efficiency. This causes the TMG to have a peak performance at 400 Ohm in the presented configuration.

**Table 2** presents the experimental and simulation findings for the TMG under investigation utilizing a Ni-Mn-Ga film with a 10 μm bonding layer. According to the impact force at the magnet's surface, as previously demonstrated, the contact $h_f$ values are shifting somewhat.[28] Data pre-published in Joseph et al.[28]

| $T_{source}$ | Power | | Frequency | | Stroke | | Heat in take | Heat dissipation | | ΔT | $h_f$ |
|---|---|---|---|---|---|---|---|---|---|---|---|
| (°C) | (μW) | | (Hz) | | (mm) | | (mW) | (mW) | | (°C) | [W/(m²K)] |
| | Exp | Sim | Exp | Sim | Exp | Sim | | Cond | Conv | | |
| 170 | 3.08 | 3.15 | 114.1 | 114.3 | 1.77 | 1.78 | 228 | 192.3 | 35.7 | 10.2 | 8400 |
| 160 | 2.71 | 2.72 | 110.6 | 110.9 | 1.67 | 1.68 | 196.8 | 167.4 | 29.4 | 8.79 | 8350 |
| 150 | 1.82 | 1.82 | 99.1 | 99.5 | 1.62 | 1.59 | 145.8 | 127.7 | 18.1 | 7.56 | 8000 |
| 140 | 1.32 | 1.37 | 91 | 91.2 | 1.56 | 1.55 | 120.5 | 107.5 | 13 | 6.93 | 7850 |
| 130 | 1.05 | 1.07 | 80 | 82.7 | 1.52 | 1.49 | 106.1 | 95.3 | 10.8 | 6.79 | 7700 |

# 5. Design parameters

Parts of this section has been published in Joseph et al.[91] There are several parameters like magnetic field, field gradient, stiffness, pick-up coil turns, contact heat transfer coefficient ($h_f$), and bonding layer thermal resistance ($R_b$) that affect the performance of the device. These parameters also determine if the device is operating in resonant self-actuation mode, as the balance between all of these parameters is required for achieving resonant self-actuation.

## 5.1. Magnet

### 5.1.1. Effect of distance from the magnet surface
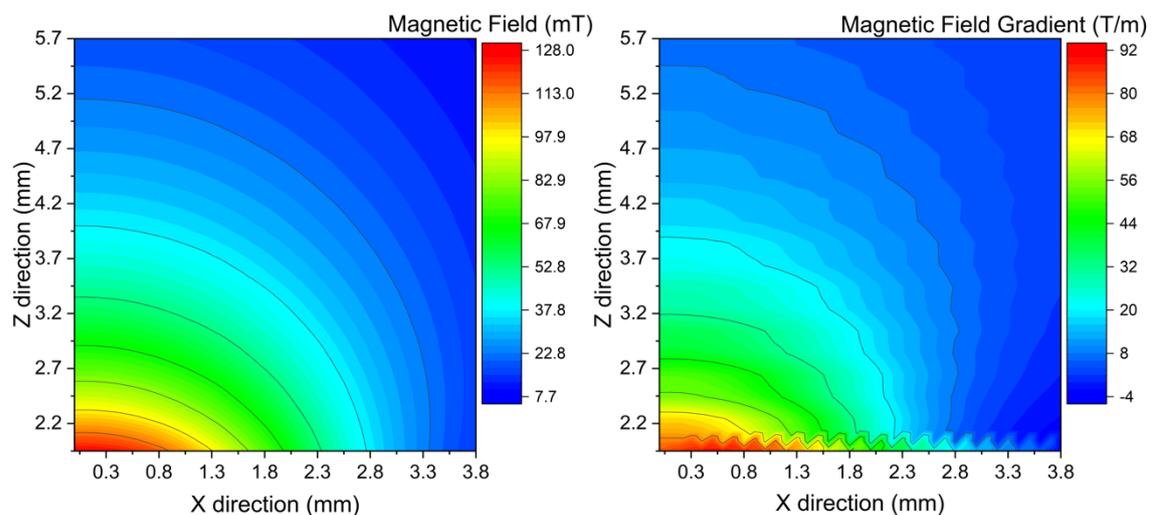


**Figure 55** Magnetic properties of Samarium Cobalt (Sm2Co17) magnet with cross-sectional area 3 mm x 3 mm and length of 8 mm at a distance of 1.94 mm from the magnet, (a) magnetic field measured from the center (0 mm) and moving towards the edge (1.5 mm), (b) magnetic field gradient derived from the magnetic field measurement.

Both the magnetic field and magnetic field gradient can be adjusted by changing the dimensions of the magnet and by changing the composition of the magnetic material which

determines the remanent magnetic field. The higher the remanent magnetic field, the higher will be the magnetic field and field gradient around the magnet. This is clear from the equations Eq ( *18* ) and Eq ( *19* ). The material for the magnet is chosen as SmCo with a maximum operating temperature of 350 °C and a remanent magnetic field of 1.07 T. The drop in magnetic flux density is only 0.05 % per 1 °C, showing high stability in high-temperature operation. Although it is possible to use Neodymium magnets (NdFeB) for low-temperature applications below 80 °C, the same SmCo magnets are used to keep measurement consistency. Also, the magnetic flux density for a NdFeB magnet changes 0.11 % for every 1 °C change in its temperature. The lateral dimensions of the magnet used in the presented work are 3 mm x 3 mm, and a length of 8 mm. **Figure 55** shows the magnetic field measurements using a precision Gauss meter and resulting magnetic field gradient values. The simulated magnetic field and magnetic field gradients are shown in **Figure 56,** and are compared to the measured values for the distance between 1.9 mm and 5.7 mm for which magnetic field measurements are available, The measurements are taken from 1.94 mm away from the magnet, this is due to the limitation to get the probe closer in the precision Gauss meter.
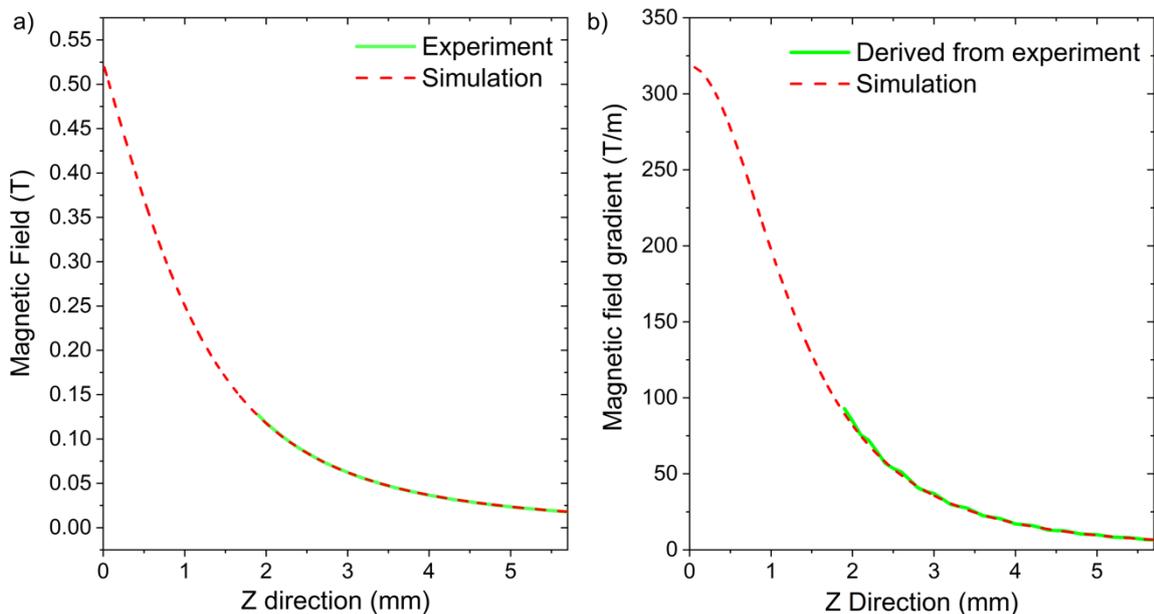


**Figure 56** Direct comparison of magnetic field measurements and magnetic field simulation. (a) Magnetic field along the z direction at the center determined by measurement and simulation, (b) magnetic field gradient derived from magnetic field measurement and simulation along the z direction at the center.

Magnetic field simulation from the LEM model could be used to analyze the magnetic field along the z direction by considering it as 1-dimensional. **Figure 56** shows the computed magnetic field and magnetic field gradient using LEM simulation. The magnetic field measurements and the simulation values are almost identical, thus, validating the magnetic section of the LEM simulation.

## 5.1.2. Effect of dimensions of the magnet

Using the LEM simulation, it is possible to study how the magnetic field and magnetic field gradient are affected by the change in the cross-sectional area and the length of the magnet along easy axis. A permanent magnet's magnetic easy axis is the direction in which magnetization requires the least energy. In a ferromagnetic material, such as a magnet, with a preferred orientation for the magnetic domains within it, it refers to the preferred direction of magnetization. The material's asymmetry and crystal structure both affect the easy axis. As it affects the direction of the magnetic field the magnet produces, this easy axis is crucial for understanding how permanent magnets behave in applications. **Figure 57** shows the effect of dimensions on the magnetic field and magnetic field gradient at the surface of the magnet. The magnetic field increases when the length of the magnet along the easy axis is increased. The number of magnetic domains aligned along the easy axis rises as the length  along the easy axis' increases, resulting in a higher degree of magnetization. A larger magnetic field results from this in turn.
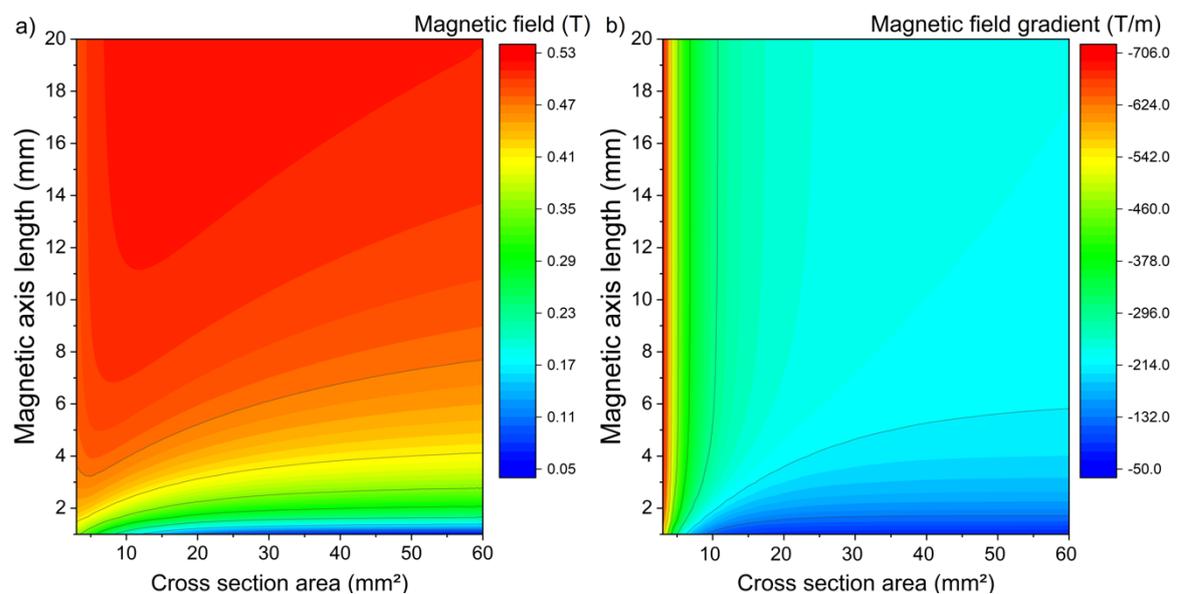


**Figure 57** LEM simulation of the effect of dimensions of magnet on (a) magnetic field, and (b) magnetic field gradient, at the surface of the magnet.

87

As a result, if the magnetization stays constant, the magnetic field of a permanent magnet will grow as the length along easy axis does as well. But it decreases as the area is increased. The same effect is seen on the magnetic field gradient. The dependence of the magnetic field and the magnetic field gradient on the dimensions is crucial in designing a TMG for an application. The increase in the magnetic field causes an increase in magnetization of the TM film and the increase in the magnetic field gradient results in an increase in the magnetic force. This shows that having a small cross-sectional area and long magnet along easy axis is better for having high surface field density and magnetic field gradient. **Figure 58** shows the effect of the cross-sectional area and length of magnet. Contrary to the magnetic field and field gradient trend at the surface of the magnet, it can be seen that at a distance of 2 mm (**Figure 58**a, **Figure 58**b) and 6 mm (**Figure 58**c, **Figure 58**d) from the magnet surface, the effect of cross-sectional area is different from that observed at the surface in **Figure 57**. The peak magnetic field and magnetic field gradient are shifting as we move away from the magnet surface. This is because the increase in cross sectional area results in steep reduction of magnetic field gradient at the surface, thus the reduction in magnetic field in the z direction is lower. This results in higher values of magnetic field and field gradients at a distance. Thus, as the distance from the magnet surface increases the peak is observed towards large cross sectional area magnets. The initial self-actuation cycle is not accompanied by the inertia force which drives the subsequent oscillations. For achieving the first cycle, the magnetic force needs to be large enough at the initial position of the cantilever tip. This means the magnetic field for magnetization of film and magnetic field gradient for magnetic force need to be large at a distance (at the initial position of the cantilever tip), favoring a large cross-sectional area of the magnet. But this would result in a lower surface magnetic field and magnetic field gradient, causing a reduction in the generated power output as it is only dependent on magnetic field gradient and velocity. The effect of cross-sectional area and length of the magnet along easy axis is a fundamental aspect in designing a TMG, as the cross-sectional area is determined by the size of the film which needs a large aspect ratio to benefit from the large surface to volume ratio. Thus, compared to the thickness of the TM film, the area of the film must be large, which means the magnet also needs to have a large enough cross-sectional area to achieve optimum contact. The length of the magnet along easy axis needs to be comparable to the cross-sectional dimensions of the magnet else it would result in the loss of benefits of miniature dimensions of the TMG. Considering these factors, it is possible to find an optimum dimension of the magnet that is guided by the TM film properties, operating temperature, and desired dimensions of the final TMG in most cases.
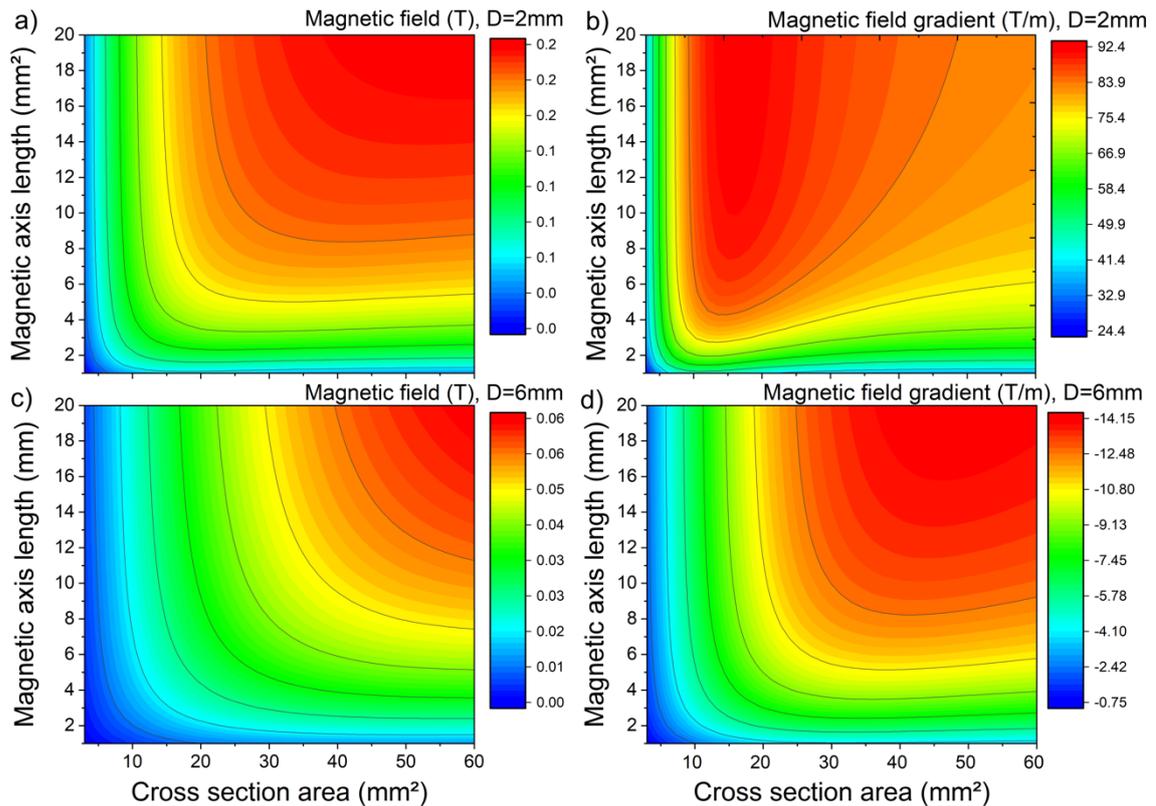
**Figure 58** LEM simulation of the effect of dimensions of magnet, (a) magnetic field at a distance (D) of 2 mm from magnet surface, (b) magnetic field gradient at D = 2 mm, (c) magnetic field at D = 6 mm, (d) magnetic field gradient at D = 6 mm.

## 5.2. Effect of design parameters

To understand the effects of various parameters, the LEM simulation is utilized and as a reference TMG sample operating at 170 °C $T_{source}$ is chosen. The TMG has 10 µm Ni-Mn-Ga film as active material. The design of the device is taken as the same as presented in section **4.4.** By default, $T_{amb}$ is 22 °C, $R_L$ is 400 Ohms, number of turns in coil is 400, thermal resistance of the bonding layer is 10 K/W and contact heat transfer coefficient is 8.4 kW/m$^2$K unless it is stated otherwise. In each subsection from **5.2.1** to **5.2.5** one of the parameter is varied while keeping all other parameters constant to rule out effects of other parameters. The goal is to describe the effects of change in each parameter and to check if there is an optimum value of parameter where the device performance is optimum in terms of power output. The results would serve as a guideline for optimizing the design of the TMG as critical parameters that affect the performance can be tuned for maximum power output. The trends of the results would be similar for other TMG's with similar design even though the absolute values would be different.

## 5.2.1. Effect of heat intake

**Figure 59** shows the effect of contact heat transfer coefficient ($h_f$) on the performance of the TMG like stroke, frequency and power. Stroke and frequency increases with an increase in the $h_f$ which in turn causes the increase in the power output. Thus, there is no optimum value of contact heat transfer coefficient that could be derived from this result. But when the $h_f$ is below the critical value of 8 kW/m$^2$K, the device shows a large reduction in performance driven by a large reduction in heat intake. As the $h_f$ is reduced below 8 kW/m$^2$K, the stroke decreases, and finally, the device enters a secondary mode of operation with very low stroke and high frequency which is not suitable for energy harvesting. The performance is heavily affected by the reduced value of $h_f$ at higher $T_{source}$ of 160 °C and above compared to lower $T_{source}$ of 150 °C and below.
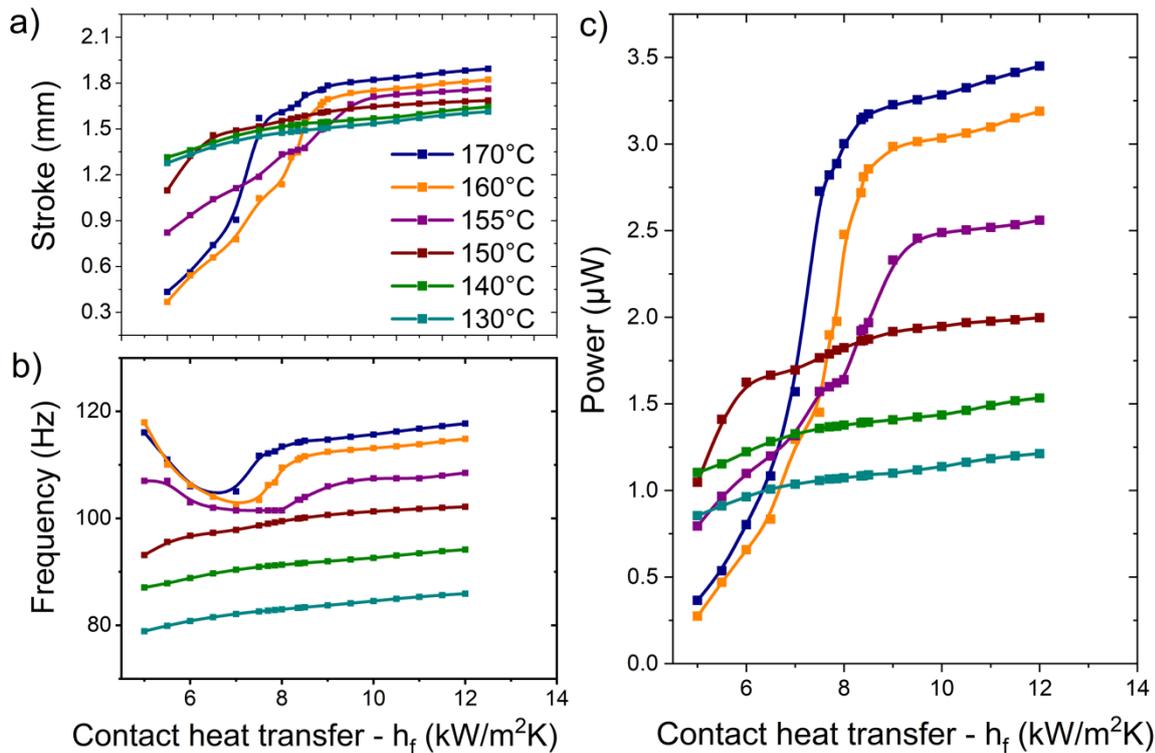


**Figure 59** LEM simulation of the effect of Contact heat transfer coefficient ($h_f$) on the performance of the TMG with 10 μm Ni-Mn-Ga film, (a) stroke of the cantilever deflection, (b) frequency of oscillation of cantilever, (c) power output from the pick-up coil. Legend shown is $T_{source}$. Data pre-published in Joseph et al.[91]

**Figure 60** shows that both the heat intake and ΔT are reducing with the decrease in $h_f$. When the $h_f$ falls below the critical value of 8 kW/m$^2$K, the decrease in heat intake and

---

<sup>e</sup>Section 5.2.1 has been published in similar form by the author in Joseph et al.[91]
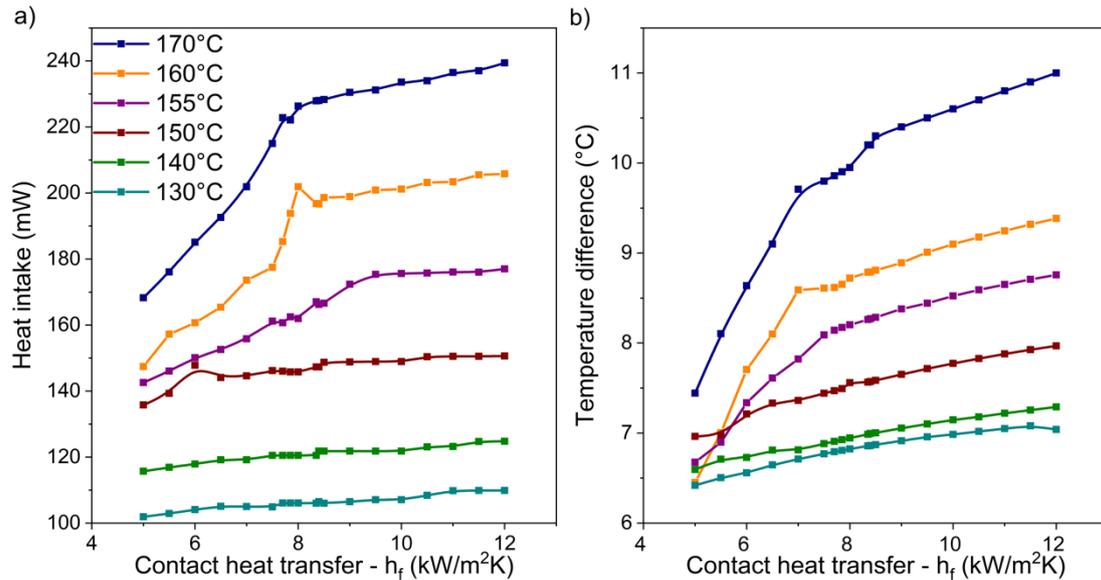
**Figure 60** LEM simulation of the TMG with 10 µm Ni-Mn-Ga film, (a) Heat intake into film, and (b) temperature change (ΔT) within the film. Legend shown is $T_{source}$. Data pre-published in Joseph et al.[91]

temperature change ( ΔT) is accelerated. But the ΔT is still above the critical limit of 6 °C, thus, the device sustains resonant self-actuation, more information about the critical limit is given in section **5.2.2.** At lower $T_{source}$ of 150 °C and below, the effect of $h_f$ is not so pronounced as the decrease in heat intake and temperature is more gradual. The convection losses tend to increase when the frequency increases as the convective heat transfer is dependent on the velocity of the cantilever tip.
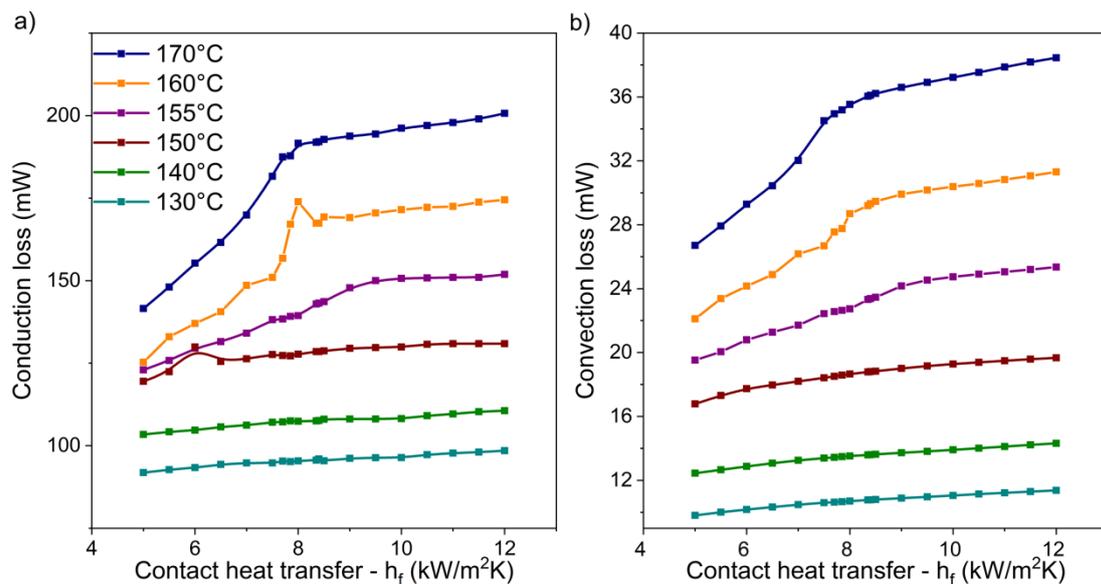


**Figure 61** LEM simulation of the TMG with 10 µm Ni-Mn-Ga film, (a) conduction losses, (b) convection losses. Legend shown is $T_{source}$. Part of data pre-published in Joseph et al.[91]

But when the TMG enters the secondary mode of operation with a small stroke and high frequency, the convective losses are still reducing as the stroke is not enough to cause an increase in the losses. The cantilever tip stays close to the magnet. When the $T_{source}$ is increasing, heat intake, $\Delta T$, and heat losses tend to increase. This is due to the higher heat flow as the result of the higher temperature difference between the TM film and the thermal heat source (in this case magnet). Heat intake at contact has major effects on the performance of the TMG as it determines the $\Delta T$ of the TM film. There is a minimum $\Delta T$ required in the TMG which is determined by parameters like material properties and device configuration. Achieving this critical $\Delta T$ within a very short interval to keep up with the mechanical oscillation frequency is crucial to sustaining resonant self-actuation.

## 5.2.2. Effect of heat dissipation

The thermal resistance of the bonding layer ($R_b$) used to bond the TM film onto the tip of the cantilever beam has a major effect on thermal dissipation by conduction from the TM film to the cantilever. An optimum $R_b$ would allow a thermal boundary letting the TM film
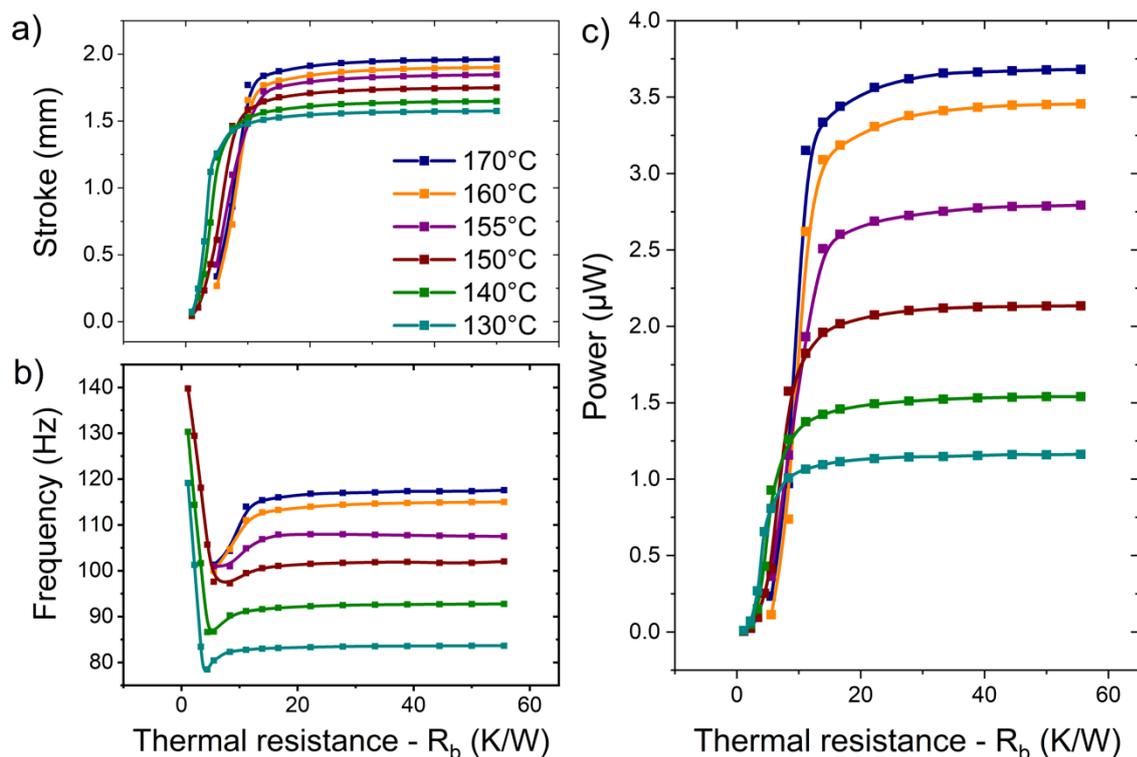


**Figure 62** LEM simulation of $R_b$ on the performance of a TMG with 10 µm Ni-Mn-Ga film, (a) stroke, (b) frequency, (c) power output. Legend shown is $T_{source}$. Data pre-published Joseph et al. [91]

[f]Section 5.2.2 has been published in similar form by the author in Joseph et al.[91]

achieve high ΔT when in contact and then would allow it to transfer all the heat into the cantilever beam over the cooling cycle. **Figure 62** shows the effect of $R_b$ on the performance of the TMG. The performance of the TMG increases when the $R_b$ of the bonding layer is increased. Both the stroke and frequency are increasing for the TMG and consequently, resulting in a higher power output. When the value of $R_b$ is increased from 10 K/W to 45 K/W, because the film retains more heat without cooling much. If the ΔT in the TM film is below the critical value, a change in magnetic force is not enough to sustain continuous resonant self-actuation. In the present case, this limit follows from **Figure 63** which shows the break in operation of the TMG at $T_{source}$ of 160 °C and above to be around 6 °C. The ΔT in TM film is directly dependent on heat intake and heat dissipation. When the $R_b$ is below 5 K/W, the TM film and cantilever become thermally coupled, and at higher $T_{source}$ values, the temperature of the cantilever increases and causes the device to stop operation due to the drop in the TM film's heat dissipation capability.
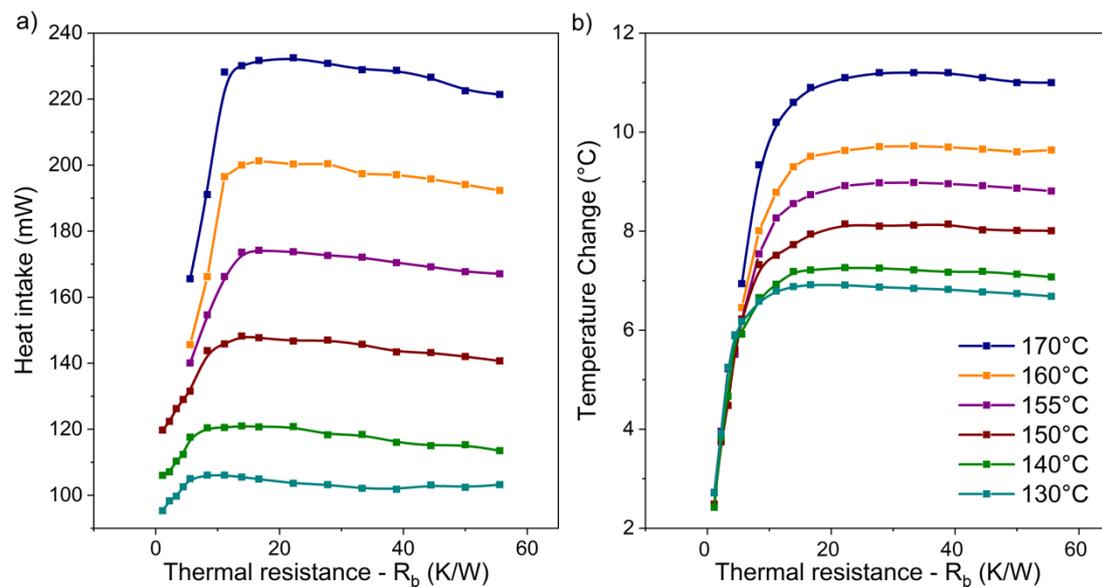


**Figure 63** LEM simulation of the effect of $R_b$ on the TMG with 10 μm Ni-Mn-Ga film, (a) heat intake at contact, and (b) temperature change within the TM film. Legend shown is $T_{source}$. Data pre-published in Joseph et al.[91]

This causes the overall ΔT in the TM film to drop below the critical temperature limit and the TMG drops out of resonant self-actuation  **Figure 63** and **Figure 64** show the heat intake, ΔT, and losses in the TMG respectively. The heat intake and the ΔT does drop when the $R_b$ reaches critical value of 10 K/W thermal resistance of bonding layer regardless of the $T_{source}$.  The heat intake and heat dissipation by conduction are almost identical

in trend. A large value of $R_b$ above the threshold would result in the TM film not being able to cool within the cooling cycle as can be observed with the reduction in heat intake and heat dissipation beyond 20 K/W. Too low $R_b$ would thermally couple TM film and the cantilever beam resulting in very low $\Delta T$ within the TM film. Such a drop in $\Delta T$ below the critical limit of $\Delta T$ would result in the failure of the TMG to operate in resonant self-actuation.
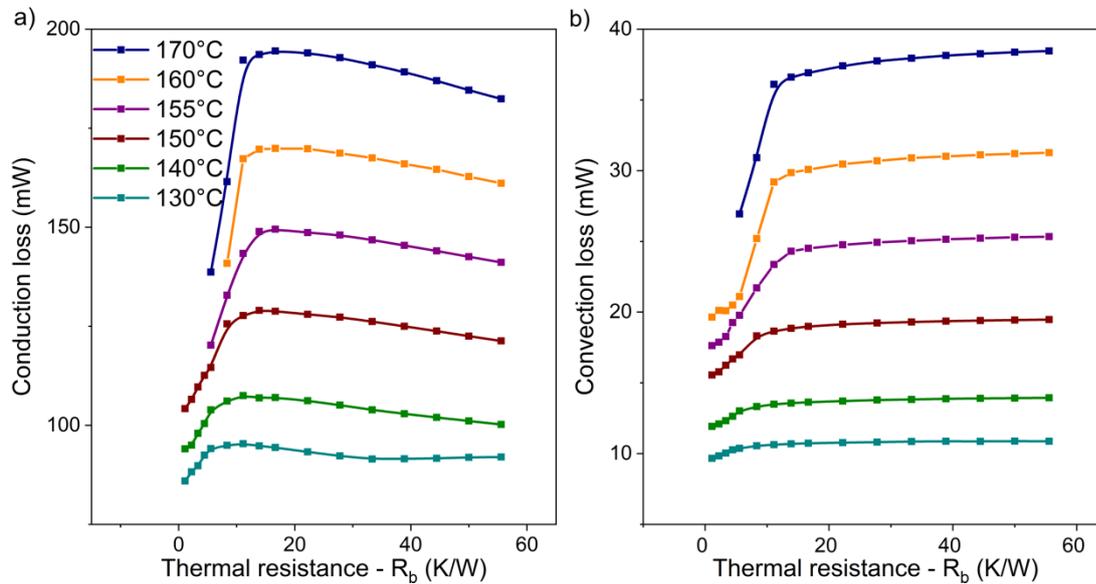


**Figure 64** LEM simulation of the effect of $R_b$ on heat dissipation in the TMG with 10 µm Ni-Mn-Ga film, (a) conduction losses, (b) convection losses. Legend shown is $T_{source}$. Part of data pre-published in Joseph et al.[91]

## 5.2.3. Effect of cantilever stiffness

Stiffness determines the magnetic force required for the first cycle of self-actuation when the inertia force is missing like in the dynamic operation. The stiffness also determines the natural frequency of oscillation of the beam which needs to be in balance with the thermal cycle to achieve resonant self-actuation. The stiffness of the cantilever beam can be modified by either increasing the thickness or width of the cantilever beam. The stiffness increases when the length of the beam is reduced.

The moment of inertia ($I$) of a cantilever beam is given by the equation Eq ( *23* ).

$$I = \frac{bh^3}{12}$$

Eq ( 23 )

Where b is the width of the cantilever beam and h is the thickness of the cantilever beam.
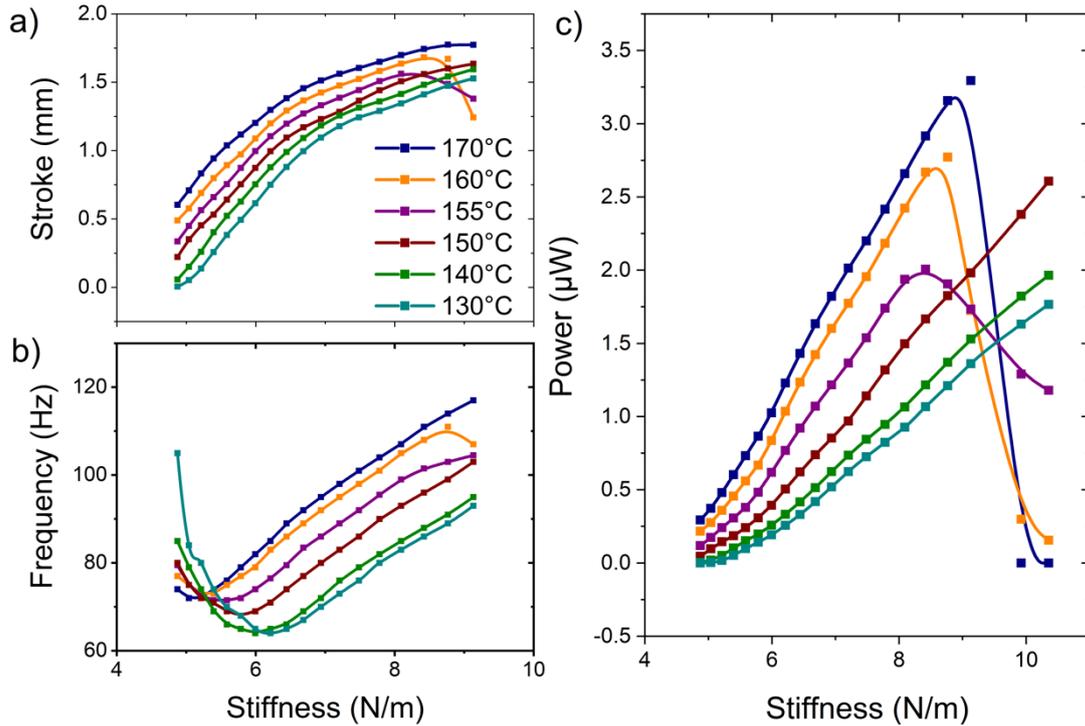
**Figure 65** LEM simulation of the effect of cantilever stiffness on the performance of the TMG with 10 µm Ni-Mn-Ga film, (a) stroke of deflection, (b) frequency of operation, (c) power output. Legend shown is $T_{source}$.

The stiffness of the cantilever beam ($k$) is given by the equation Eq ( *24* ).

$$k = 3EI/l^3$$

Eq ( 24 )

Where l is the length of the cantilever beam. Thus, changing the thickness of the beam by a few micrometers would result in a very large increase in stiffness. Changing the length of the cantilever beam also increases the stiffness with a large effect. Thus, it is possible to choose the thickness and width of the cantilever beam in the range of the optimum stiffness of the cantilever beam and use the length of the cantilever beam to fine-tune the stiffness for optimum performance. This is done to keep the stroke of the cantilever beam in the range of the magnetic field and field gradient of the chosen magnet. **Figure 65** shows the effect of cantilever beam stiffness on the performance of the device.

Increasing stiffness by decreasing the length until the stroke and bending angle are in a reasonable range (in which the bending angle does not cause fatigue failure in cantilever) in relation to the dimension of the cantilever. Once the stroke is almost half of the cantilever, the stiffness of the cantilever beam is increased so that the length of the cantilever beam can be increased to keep the ratio of stroke and length, as this affects the bending angle. The performance of the TMG increases when the stiffness of the cantilever beam

95

is increased, this continues until the optimum value of stiffness is reached. If the stiffness is increased beyond this limit, the device drops out of resonant self-actuation at higher $T_{source}$ values. Like the effects of $h_f$ and $R_b$, the effect of stiffness is more pronounced at higher $T_{source}$ values. At lower $T_{source}$ values, the increase in performance is also not pronounced, and the change in performance is observed only at higher stiffness closer to optimum and the device is not producing any reasonable power output when the stiffness is too low. **Figure 66** shows the heat intake and $\Delta T$ in the TM film in the TMG. Unlike the
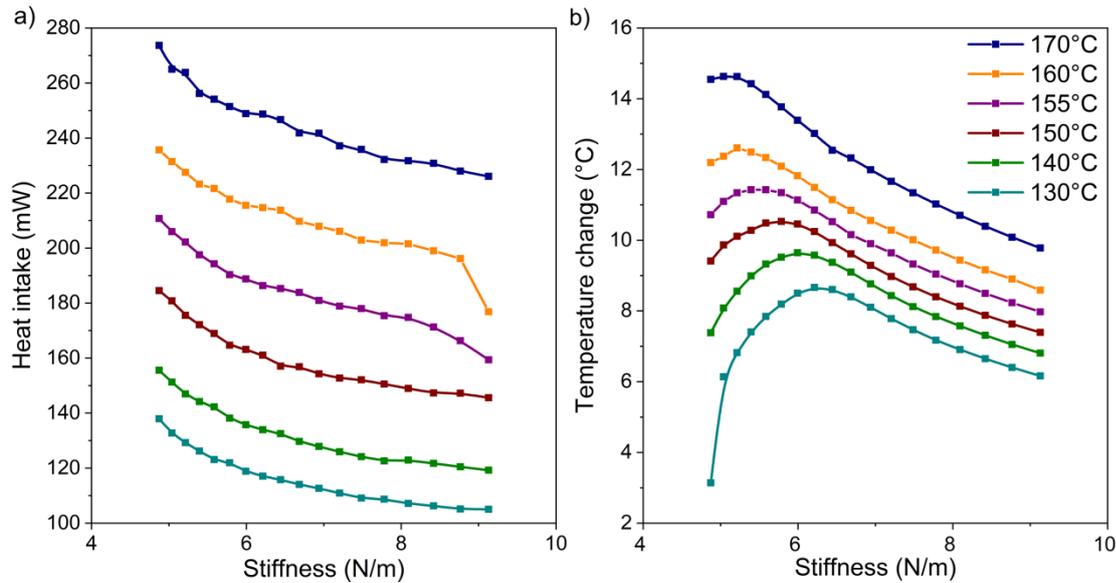


**Figure 66** LEM simulation of the effect of cantilever stiffness on (a) heat intake and (b) $\Delta T$ within the TM film of the TMG with 10 µm Ni-Mn-Ga film. Legend shown is $T_{source}$.

previous cases, the increased heat intake is not the reason for increased performance in the case of changing stiffness. The increase in stiffness results in a decrease in heat intake as lesser $\Delta T$ is required for the device to leave the surface of the magnet due to the higher reset force. The $\Delta T$ is only increasing when the stiffness is increased beyond the critical limit after which the resonant self-actuation is lost. **Figure 67** illustrates the effect of stiffness on the losses from the TM film in the TMG. The conduction losses follow an identical trend as the heat intake with slightly reduced values due to convection losses. The convection losses are also decreasing even though the device is operating at a higher frequency when the stiffness is increased. The increased frequency causes an increase in the convective heat transfer coefficient, however, the overall heat intake and thermal losses required for sustaining resonant self-actuation are reduced due to the increase in stiffness causing a decrease in convection.
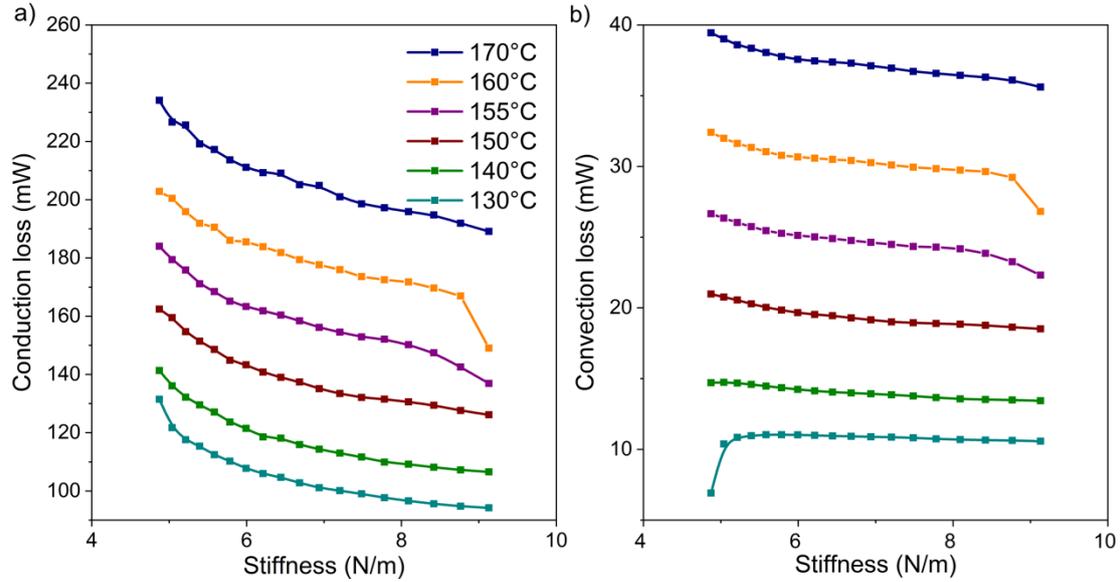
**Figure 67** LEM simulation of the effect of stiffness, (a) conduction losses, (b) convection losses. Legend shown is $T_{source}$.

## 5.2.4. Effect of pick-up coil
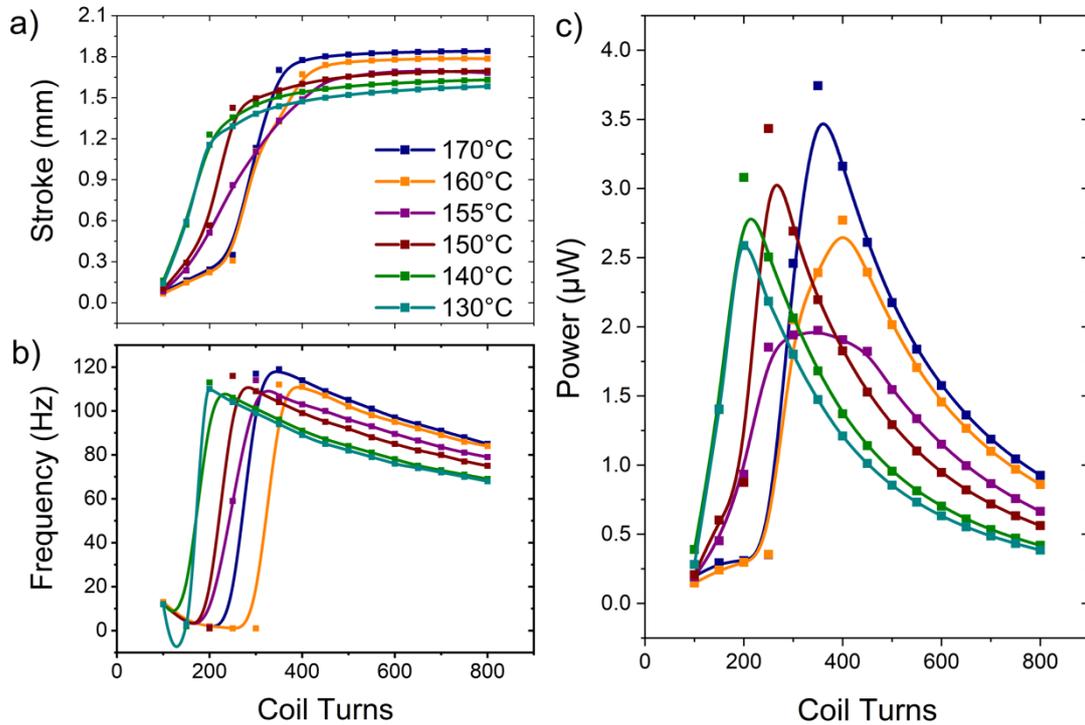


**Figure 68** LEM simulation of effect of pick-up coil on performance of the TMG with 10 µm Ni-Mn-Ga film, (a) stroke, (b) frequency, and (c) power output. Legend shown is $T_{source}$.

The lateral size of the pick-up coil is fixed by the width of the beam and the cross-sectional area of the magnet. Having the pick-up coil larger than the cantilever beam is not ideal as it would cause additional undesirable air-damping. Having a larger pick-up coil size than the cross-sectional area of the magnet would result in having a pick-up coil at low concentration of magnetic field lines and low magnetic field gradient. This would still generate energy, but the increase in mass of the pick-up coil would cause a larger decrease in power output than the increase due to the additional size.

For all devices in this thesis work, the size of the pick-up coil is kept at 2 mm x 2 mm x 0.3 mm. Using LEM simulations, it is possible to analyze the effect of increasing pick-up coil turns (also the added mass) in the TMG. **Figure 68** shows the effect of a number of turns in pick-up coil on the performance of the TMG. Increasing the number of pick-up coil turns results in an increase in performance until 400 turns and then the performance of the device decreases. This effect is due to the additional electromagnetic damping and added mass of the pick-up coil. Changing the stiffness, $R_b$, etc. can result in a different optimum number of pick-up coil turns. The $T_{source}$ range also affects the optimum pick-up coil turns in the TMG. Thus, the number of pick-up coil turns in a TMG should be optimized based on the operating $T_{source}$ range, $\Delta T$, TM film properties, operating load and $T_{amb}$ conditions.
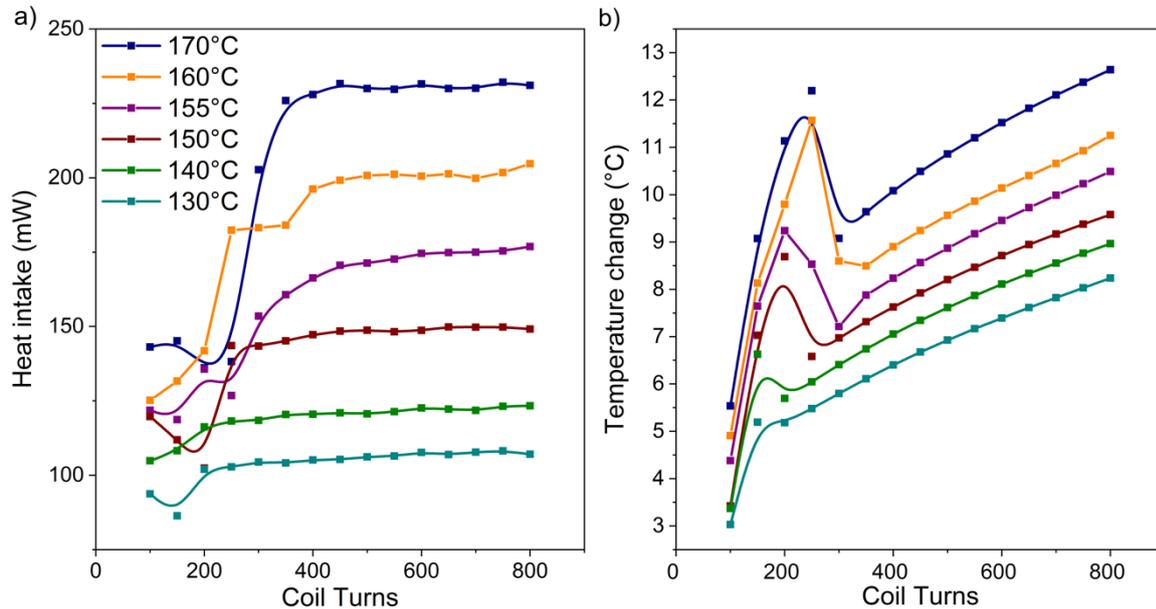


**Figure 69** LEM simulation of the effect of pick-up coil on (a) heat intake and (b) temperature change within the material of the TMG with 10 μm Ni-Mn-Ga film. Legend shown is $T_{source}$.

The frequency of the TMG is also dependent on the pick-up coil turns, but the effect is also affected largely by the $T_{source}$. **Figure 69** shows the effect of the number of pick-up coil turns on the heat intake and $\Delta T$ within the TM film. Although, the temperature of the pick-up coil does increase during operation of the TMG, due to its large thermal mass, the temperature does not change much after saturation within a few cycles of operation. Thus, thermally the addition of the pick-up coil turns does not affect the TMG, but the heat transfer is affected indirectly through the change in natural frequency of the TMG due to added mass and the added electromagnetic damping. The $\Delta T$ is increasing with $T_{source}$, but also with the increase in the number of pick-up coil turns. The large peak of $\Delta T$ at 300 turns for higher $T_{source}$ is a result of the TMG operating in non-resonant self-actuation mode for $T_{source}$ at 150 °C and above. At these points, the device is having a low frequency, stroke, and heat intake and losses.
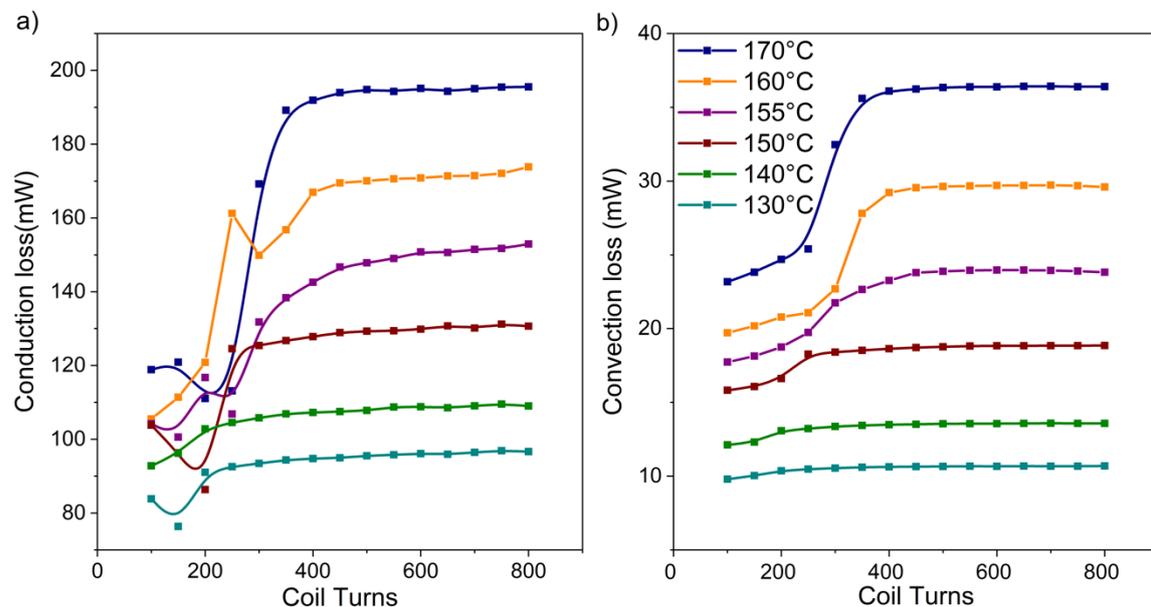


**Figure 70** LEM simulation of the effect of pick-up coil turns on heat dissipation of the TMG with 10 μm Ni-Mn-Ga film, (a) conduction losses, (b) convection losses. Legend shown is $T_{source}$.

The stroke of the device and heat intake of the device slightly increase with the increase in pick-up coil turns, but the frequency of the device reduces due to the mass which has a higher effect on the performance. **Figure 70** demonstrates the dissipation losses in the TMG with respect to the changing number of pick-up coil turns. The convection heat losses seem to increase with the increased pick-up coil turns even when the frequency of the device is low because of the increase in heat intake. Both losses and heat intake increase when the $T_{source}$ is increased, which is unaffected by the change in pick-up coil turns.

## 5.2.5. Effect of Curie temperature

If the magnetization curve of the material is kept the same and only the transformation temperature is changed, the minimum operation $T_{source}$ changes accordingly. But consequently, the performance of the device at the minimum $T_{source}$ is also affected. By keeping the ambient conditions the same, LEM simulations are conducted to understand the effect of $T_c$ on the minimum $T_{source}$. **Figure 71**b illustrates how the minimum $T_{source}$ is reducing with the reduction in $T_c$.
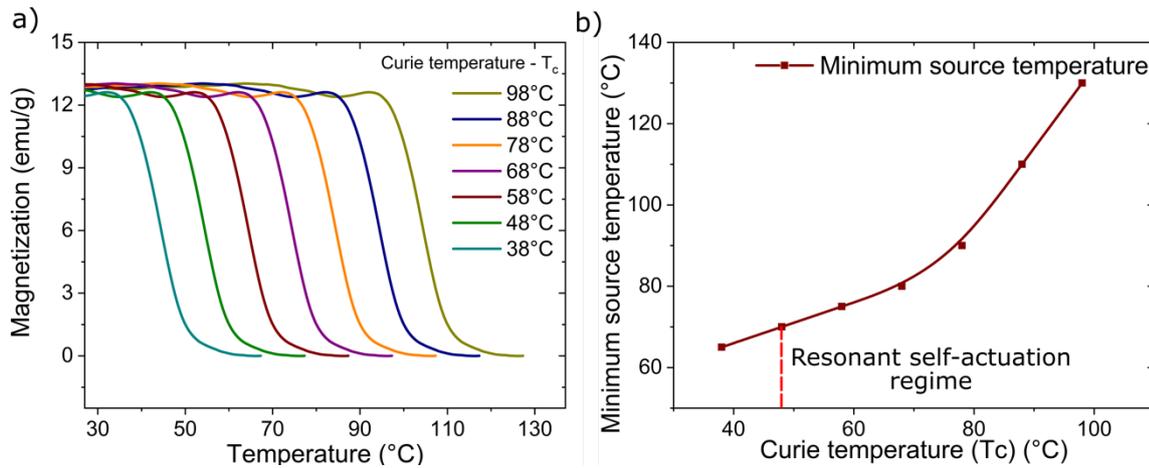


**Figure 71** (a) LEM simulated values of magnetization vs temperature characteristics shifted for decreasing Curie temperature ($T_c$), (b) LEM simulation of minimum $T_{source}$ for different values of $T_c$. Part of data pre-published in Joseph et al.[128]

To keep consistency the design of the device is kept constant. The critical $T_{source}$ is seen at 38 °C as the device goes out of resonant self-actuation. The simulation is done from 38 °C to 98 °C of $T_c$ with a 10 °C step. **Figure 71**a shows the shifted magnetization curves used, and only the values of magnetization values for a magnetic field of 0.05 T are shown. Only the $T_c$ is shifted by 10 °C, keeping all the other trends the same. The minimum $T_{source}$ is also shifting along with the shift in $T_c$. The change in minimum $T_{source}$ reduces linearly until $T_c$ = 68 °C and then the slope of drop changes slightly. One of the advantages of Heusler alloy is the ability to tune the $T_c$ of the alloy by changing the composition of the alloy and its heat treatment properties. The minimum $T_{source}$ can be further adjusted by changing the magnetization values and design of the TMG. Having a high magnetization value is key to achieving high performance at lower temperature differences as it allows for the use of high stiffness of the cantilever which would result in higher frequency operation and thus more power output. The curve of the minimum $T_{source}$ appears to be satura-

gFigure 71b has been published in similar form by the author in Joseph et al.[128]
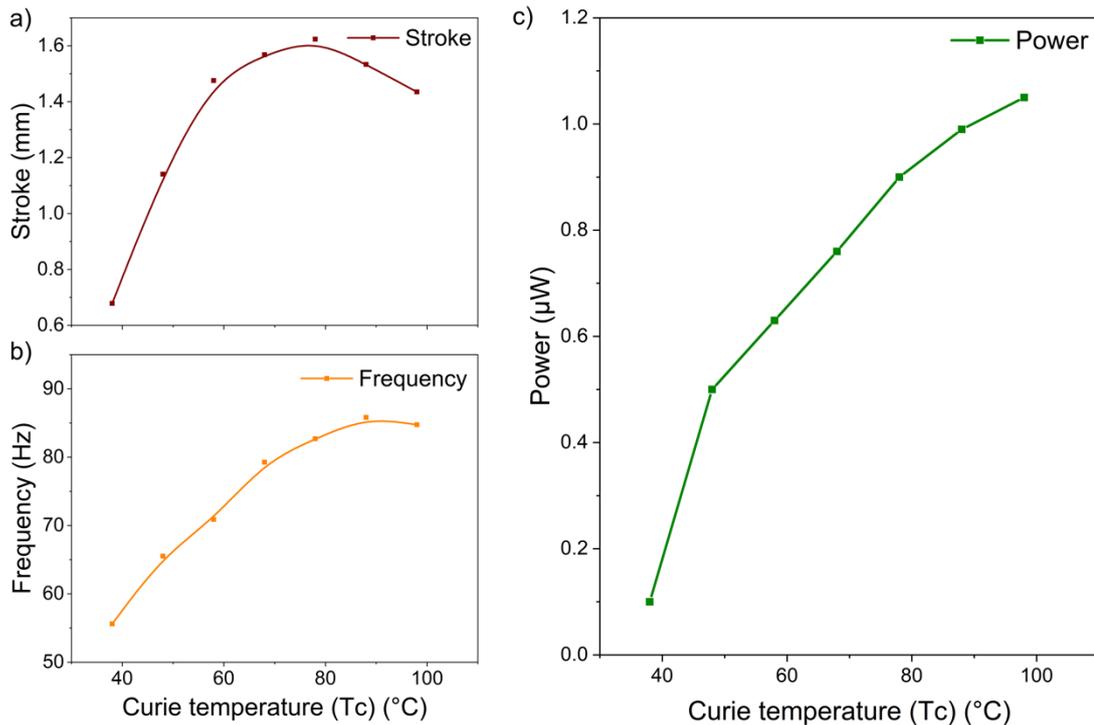
**Figure 72** LEM simulation of the effect of Tc on the performance of the TMG with 10 µm Ni-Mn-Ga film at minimum source temperature, (a) stroke, (b) frequency, (c) power output.

ting as the $T_{amb}$ is kept constant at 22 °C.The device goes out of resonant self-actuation for the same reason, as the Tc is getting closer to the $T_{amb}$. The device would only be able to work at lower Curie temperatures if the design is modified to accommodate these changes. To finally get the device working at $T_{source}$ values of 38 °C and below and to increase performance at lower operating temperatures close to $T_{amb}$, several solutions could be possible, like;

- Change the design of the device to optimize it for higher thermal performance at lower values of $T_{source}$.
- To change the magnetization properties of the material
- To lower the $T_{amb}$.

Such change would result in higher performance requiring very low ∆T within TM film. **Figure 72** shows the LEM simulations for the performance of the TMG at the minimum $T_{source}$ for a given $T_c$ ($T_{source}$ is not same for all points but rather the $T_{source}$ in each case is the minimum temperature possible). The device power output falls close to zero when the TMG goes out of resonant operation. The power output of the device also reduces as the $T_c$ is reduced without modifying the design of the device. This also illustrates the importance of the TMG design and configuration and its dependence on the $T_c$ with respect
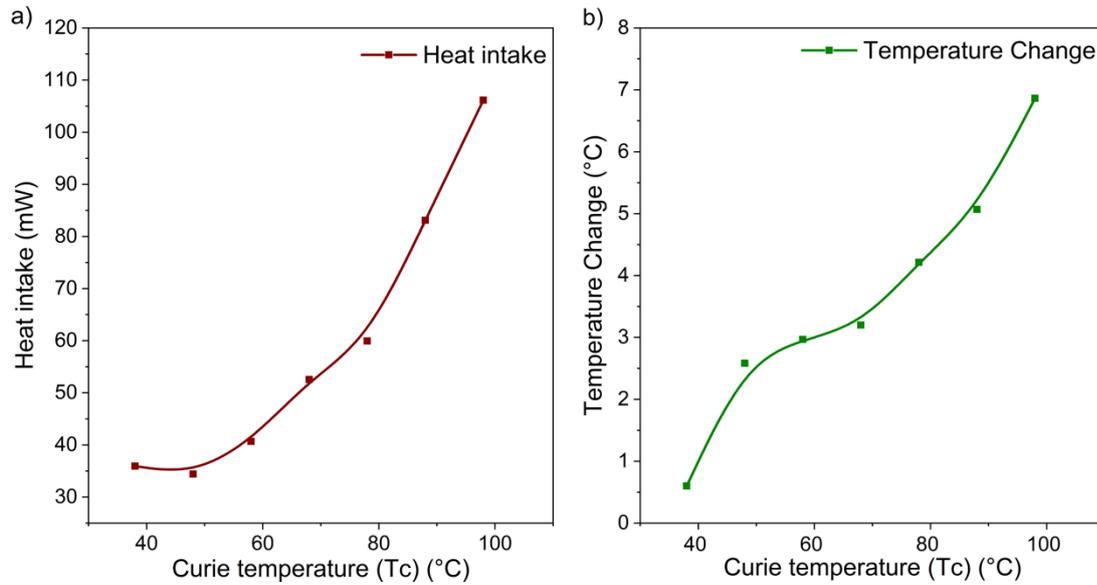
**Figure 73** LEM simulation of the effect of curie temperature ($T_c$) on the TMG with 10 μm Ni-Mn-Ga film (a) heat intake and (b) temperature change in the TM film.

to its operation range and ambient conditions. The heat intake and $\Delta T$ seem to follow the trend of power output with continuous reduction until the device loses resonant self-actuation. The heat intake and $\Delta T$ at $T_c$ of 48 °C are only 35 mW and 2.5 °C respectively as shown in **Figure 73**. The thermal losses from the TM film also decrease with the decrease in $T_c$ and $T_{source}$ values.
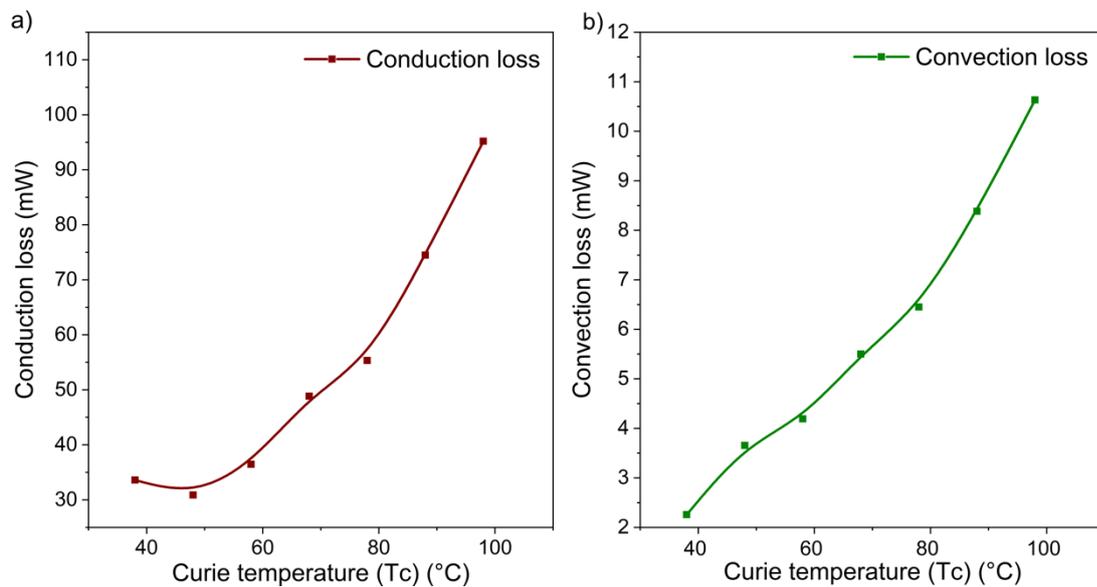


**Figure 74** LEM simulation of effect on loss mechanisms of the TMG with 10 μm Ni-Mn-Ga film, (a) conduction losses, (b) convection losses.

It can be seen in **Figure 74**a that the conduction losses saturate as $T_c$ reaches 48 °C and slightly increase as the $T_c$ is reduced further due to failure to achieve resonant self-actuation. The minimum $T_{source}$ at which the TMG is able to sustain resonant self-actuation for $T_c$ of 48 °C is 70 °C as shown in **Figure 71**b as the $\Delta T$ is at its critical limit of 2.5 °C. However, the convection losses do not saturate even at a $T_{source}$ of 65 °C and reach a minimum value of 2.3 mW suggesting the low heat dissipation capability, due to the lower frequency of operation and the lower heat intake.

## 5.3. Discussion

The requirements for resonant self-actuation, which enables effective conversion of thermal energy into electrical energy, are investigated using LEM simulations. The effect of distance and dimensions on the magnetic field and field gradient of a permanent magnet is discussed. The material composition and remanent magnetic field are kept constant. It is shown that the magnetic field is the maximum at the surface of the magnet, and it reduces exponentially as the distance from the surface of the magnet is increased. The effect of dimensions on the magnetic field and field was presented earlier in the section. The magnetic field strength determines the magnetization of the TM film in the TMG, while the magnetic field gradient causes the magnetic force when a magnetized material is placed in it. Thus, to achieve maximum magnetic force, the field and field gradient needs to be maximum. At 2 mm both the magnetic field and field gradient are already very low and reach their minimum. Thus, the TMG is always designed to operate with a stroke close to 2 mm so that the device still achieves a large stroke but at the same time is not moving out of the magnet's peak magnetic field and magnetic field gradient.

The dynamics of heat absorption upon mechanical contact with the heat source and heat dissipation via heat conduction and convection via the oscillating cantilever are discussed. The heat transfer coefficient ($h_f$) turns out to be an important design factor when it comes to heat intake. It is crucial to build TM films with a large enough surface-to-volume ratio to support high heat flows and quick $\Delta T$ in the TM film. For the best thermal contact, a heat source with a smooth surface finish is also necessary. The temperature difference between the heat source (permanent magnet) and the TM film affects how much heat is transferred. Generally speaking, the power output will increase as $h_f$ increases. According to the results, the critical value of $h_f$ is around 8 kW/($m^2$K) in the case of the TMG with 10 µm Ni-Mn-Ga film. Above this point, consistent operation in resonant self-actuation with large stroke and frequency is observed yielding high power output. At large $T_{source}$ values

of 160 °C and above, when $h_f$ was reduced below the critical limit, the device performance degrades as the $\Delta T$ decreases. This is resulting from imbalance between heat intake and dissipation. The system can no longer maintain resonant self-actuation below a threshold $\Delta T$ of several degrees, depending on the thickness of the TM film. The essential $\Delta T$ in the considered case is around 6 °C.

The thermal resistance ($R_b$) of the bonding layer is another important design factor. It controls how heat is transferred from the TM film to the cantilever, which is the heat sink of the TMG. The thickness of the non-conductive bonding layer can be modified to vary this parameter, which produces a thermal boundary between the TM film and the cantilever. This results in a high enough $\Delta T$ at low heat intake. LEM simulation results show that for all $T_{source}$ values, there is a critical value of $R_b$ of around 10 K/W above which stable performance occurs and is associated with high values of oscillation stroke, frequency, and power. A strong reduction in $\Delta T$ below the critical threshold results from an imbalance between heat intake and dissipation, which deteriorates the TMG performance. The device performance will be greatly reduced if the $R_b$ is lower, and it will finally stop operating in the resonant self-actuation mode if $\Delta T$ falls below the critical threshold of 6 °C. At $T_{source}$ values of 160 °C and above, where resonant self-actuation ceases operation below the critical limit, the bonding layer's impact on the device's performance is more obvious.

The stiffness of the cantilever also affects the performance of the cantilever and choosing the appropriate stiffness is key in optimizing the performance of the TMG and also to achieve resonant self-actuation. If the stiffness is too low or too large, the device loses resonant self-actuation mode and results in a large reduction in power. If the stiffness is too small, the device stays in contact for a longer time with the magnet resulting in excess heat flow into the TM film, which in turn heats the cantilever causing a very large $\Delta T$, but at the expense of frequency. The stiffness is adjusted in terms of thickness and then fine-tuned by adjusting the length of the cantilever so that the device is capable of achieving resonant self-actuation mode with a stroke of around 2 mm. The number of turns in the pick-up coil affects the performance in two ways, one with the change in electromagnetic damping and the other due to the change in mass of the pick-up coil. In either case, the number of turns in the pick-up coil needs to be optimized to achieve maximum output power. If all the other parameters are constant it can be seen that the power output is maximized at different pick-up coil turns at different $T_{source}$ values. This is due to the proper balance between the TMG's electromagnetic damping, pick-up coil mass, and the thermal

cycling of the device at various $T_{source}$ values. This shows the importance of optimizing the design for operating conditions like the $T_{source}$ and $T_{amb}$ to achieve maximum power output.

The $T_c$ of the device has major effects on the TMG's minimum $T_{source}$ requirement above which it would be capable of achieving resonant self-actuation. If the material properties like magnetization and $\Delta M/\Delta T$ at the transition are kept the same, it can be seen that the power output reduces as the $T_c$ is reduced. This is due to the inability of the device to maintain the same conditions of heat intake and heat dissipation for lower $T_{source}$ values while the $T_{amb}$ is remaining constant. Increasing the magnetization allowing the TMG to have higher stiffness for the cantilever is one of the solutions to overcome this loss in power. Increasing the value of $\Delta M/\Delta T$ is also another method by which higher power outputs could be achieved, but this also results in a lower range of operation temperature as the device would be highly sensitive to $T_{source}$ and would only exhibit resonant self-actuation within a narrower temperature range. The findings show that device performance can be further enhanced in terms of heat intake and dissipation, leading to an increase in electrical power output while operating in resonant self-actuation mode.

**Table 3** Modeling parameters used in simulation by LEM of the TMG. Part of data pre-published in Joseph et al.[91,128]

| Mechanical parameter | Unit | Value | References |
|---|---|---|---|
| Pick-up coil mass | Kg | $6 \times 10^{-6}$ | This work |
| Cantilever density | Kg/m$^3$ | 8500 | [143] |
| TM film density | Kg/m$^3$ | 8020 | [144] |
| Bonding layer density | Kg/m$^3$ | 920 | [145] |
| Structural and air damping | Ns/m | $2.8 \times 10^{-5}$ | This work |
| Impact damping | Ns/m | 0.1 | This work |
| Contact stiffness | N/m | 10000 | This work |
| Young's modulus | Pa | $1 \times 10^{11}$ | [146] |
| | | | |
| **Electrical & Magnetic Parameters** | **Unit** | **Value** | **References** |
| Remanent magnetic field | T | 1.07 | This work |
| Area of pick-up coil | m$^2$ | $2.81 \times 10^{-6}$ | This work |

| Load resistance ($R_L$) | Ω | 400 | This work |
|---|---|---|---|
| | | | |
| **Thermal Parameters** | **Unit** | **Value** | **References** |
| Cantilever thermal conductivity | W/mK | 109 | [147] |
| TM film thermal conductivity | W/mK | 23.2 | [148] |
| Bonding layer thermal conductivity | W/mK | 0.225 | [145] |
| Cantilever heat capacity | J/kgK | 400 | [143] |
| TM film heat capacity | J/kgK | 490 | [148] |
| Bonding layer heat capacity | J/kgK | 2100 | [145] |
| Convective heat transfer coefficient | W/m$^2$K | 40-140 | This work |

# 6. Upscaling of TMG

Parts of this section has been published in Joseph et al.[28,150] This section provides the results of the investigation of upscaling and the resulting effects on performance metrics, and coupling effects in parallel operating TMGs. The investigation utilized TMGs with Ni-Mn-Ga as active TM material. The first device with resonant self-actuation is presented in Gueltig et al.[92] with a high power density of 118 $mW/cm^3$. This is normalized to the active material volume, which is consistent with theoretical predictions of up to 300 $mW/cm^3$ for thin plates.[108] No external actuation or influence is required for operation, as this is a self-actuating and self-adjusting device, with the only requirement of operation being the thermal energy source. But the absolute power output from the device is only 2.4 µW, corresponding to a power per footprint of 14.2 µW/cm² and in order to make the TMG attractive for most applications it is required to increase the amount of raw power output. There are two different ways to increase the power output or to upscale the TMG, one is to increase the power output from a single device (power output per area), second is to add more devices operating in parallel to combine the overall output. Section **6.1** shows the effects of upscaling the material thickness to achieve higher power output from consumed area. Section **6.2** describes the effects of devices operating in parallel close to each other.

## 6.1. Upscaling TMG by volume of active material

In order to upscale the power per footprint of the TMG, the amount of active material in the device needs to increased. The scaling of the TM film is done by increasing the thickness, so the lateral area of the TMG is kept constant for comparison. The main goal is to scale the TMG without losing benefits of high efficiency and rapid heat transfer found in film-based devices while meeting power levels for applications at different scales. Cantilever dimensions are adjusted accordingly to maintain resonant self-actuation which is required for maintaining the large power output while operating at high frequencies. The TMG performance is then analyzed using LEM to describe the thermal processes in the TMG. The modeling parameters are summarized in **Table 4** (p. 125)

---

[h]Section 6.1 has been published in similar form by the author in Joseph et al.[28]

## 6.1.1. Design of the device

The Ni-Mn-Ga film thickness of three demonstrators is chosen to be 10, 20, and 40 µm, respectively. Due to limitations in sputtering duration and associated film homogeneity, film thicknesses are yet restricted to a maximum of around 10 µm. Therefore, as shown in **Figure 75**, the thickness is sequentially raised by stacking identical Ni-Mn-Ga films of 10 µm thickness above one another. These films have the same lateral dimensions and magnetic properties. The film stack is fixed utilizing conductive bonding layers between the films and a non-conductive bonding layer in between the film stack and cantilever. The performance of the TM generator is significantly impacted by the increase in heat and inertia mass during upscaling. To sustain the conditions of rapid heat transfer and resonant self-actuation, a variety of challenges must be resolved. In particular, heat intake during contact between the film stack and the heat source (permanent magnet) as well as heat dissipation, both of which depend on the dynamics of the cantilever motion, are important. This also includes fabrication technology, optimization of cantilever geometry affecting footprint, electrical load resistance ($R_L$), and other factors.
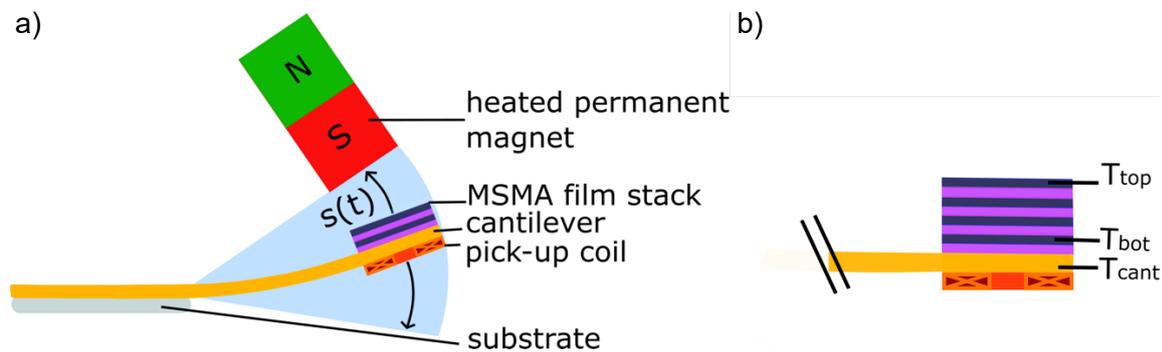


**Figure 75** Design of film stack to increase the thickness (a) schematic of the TMG with oscillating cantilever and Ni-Mn-Ga film stack, (b) section of the cantilever front showing the film stack with multiple layers of Ni-Mn-Ga films. Adapted from Joseph et al.[28]

## 6.1.2. Fabrication of TMG

Having thermally conductive bonding layers within the TM film layer increases the average thermal mass and the thermal resistance of the layer. Thickness of the TM layers is taken as 10 µm, 20 µm, and 40 µm. However, the actual thickness of the whole layer is 10 µm, 33 µm, and 82 µm respectively due to the added size of the bonding layer between. The bonding layer thickness is hard to control due to the size of the conductive particles (silver

in this case) within the bonding layer. To achieve the minimum thickness of the bonding layer between the films and keep the thermal resistance of the bonding layer to a minimum, specific steps are taken. The fabrication of the TMG is then completed in the same manner as for the TMG with 10 μm Ni-Mn-Ga film.

### 6.1.3. Effects of upscaling Ni-Mn-Ga thickness

The performance of the TMG increases when the thickness of the TM film is increased from 10 μm to 40 μm. This is due to the additional volume which results in the excess magnetization of the TM film which corresponds to higher magnetic forces. This allows for modifying the design of the TMG with higher stiffness of the cantilever to compensate for the additional magnetic force. The stroke and frequency also increase with the increase in thickness of the TM film.
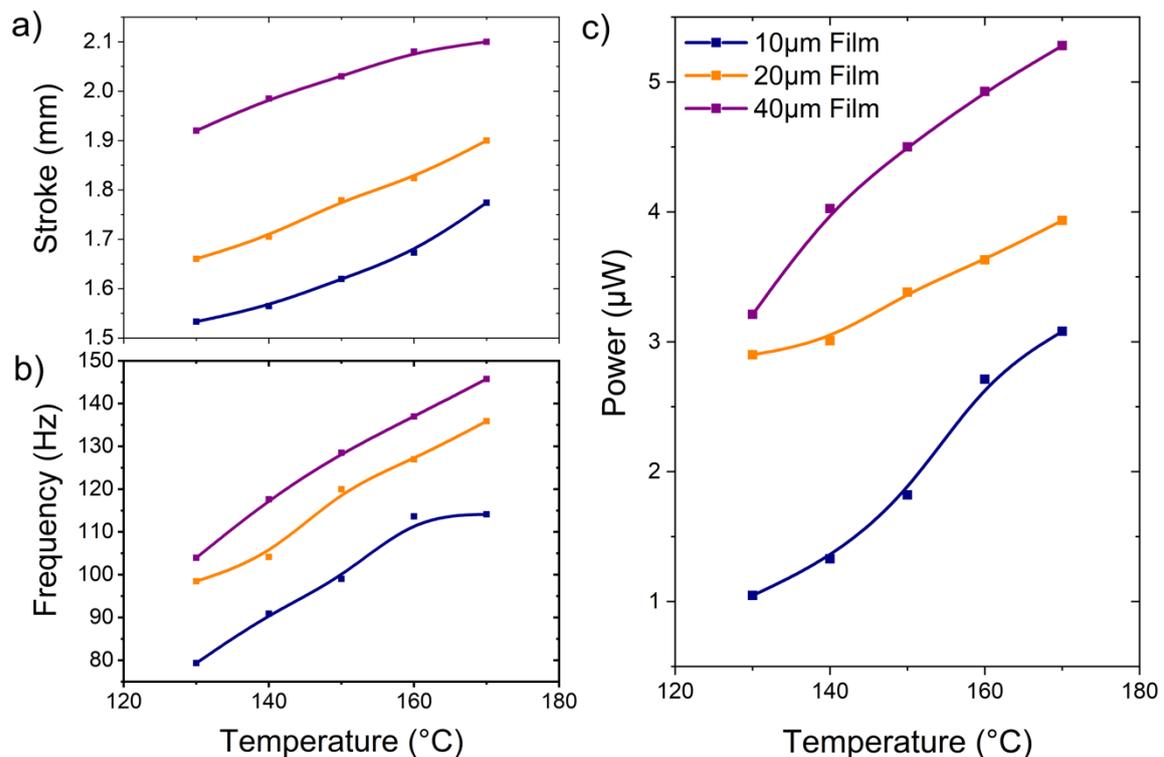


**Figure 76** Effect of film thickness on the performance of the device, (a) stroke, (b) frequency, (c) power output. Data pre-published in Joseph et al.[28]

**Figure 76** shows the general trend of performance with increasing $T_{source}$ when the Ni-Mn-Ga film thickness is scaled. It can be observed that the power output increases as the thickness of the TM film is increased. For the TMG with 10 μm TM film, the maximum generated power output is around 3.1 μW. This value increases to 4 μW for the TMG with

20 μm TM film and finally reaches a maximum value of 5.4 μW for the TMG with 40 μm TM film. This is the result of increased stroke and frequency. The thickness of the TM film cannot be increased any further as the overall thickness of the stack has already reached 82 μm for a TM film thickness of 40 μm. LEM simulations showed that Increasing the TM stack thickness by adding any additional film would result in too much thermal resistance within the stack and effectively result in reduced performance. But having a homogenous material without any thermal resistance of the bonding layer would enable going further than 40 μm. The effect of load resistance and source temperature on the TMG performance for varying Ni-Mn-Ga film thickness is given in **Figure A *2*** to **Figure A *4***. Performance results are summarized in **Table 5** (p.128).
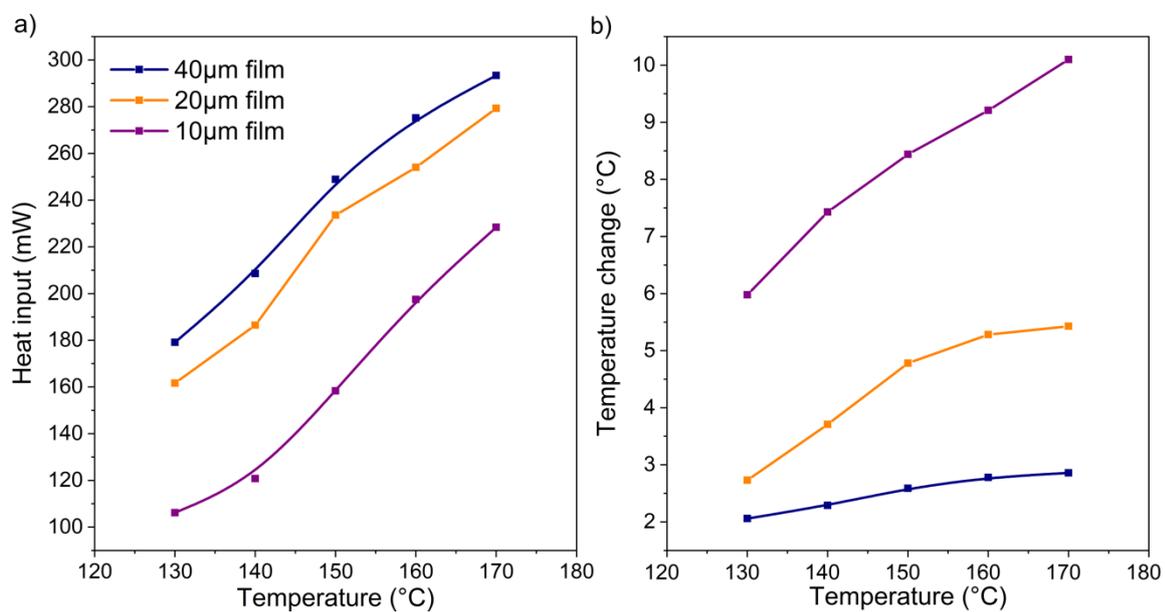


**Figure 77** LEM simulation of the effect of film thickness on (a) heat intake and (b) the average temperature change within the TM film. Data pre-published in Joseph et al.[28]

From **Table 5** it is clear that having a homogenous material layer instead of TM stack without thermal resistive layer results in a minor performance increase due to added benefit of higher thermal performance. The heat intake into the TM film stack on contact is shown in **Figure 77**a. The increase in heat intake when the thickness is increased is due to the increase in heat transfer coefficient ($h_f$) as a result of the higher contact force from additional magnetization (more material) and impact force owing to inertia. This results in a higher frequency of operation as the ΔT required in the material to achieve the magnetization change is now much less as the volume of the material is increased. Thus, the ΔT
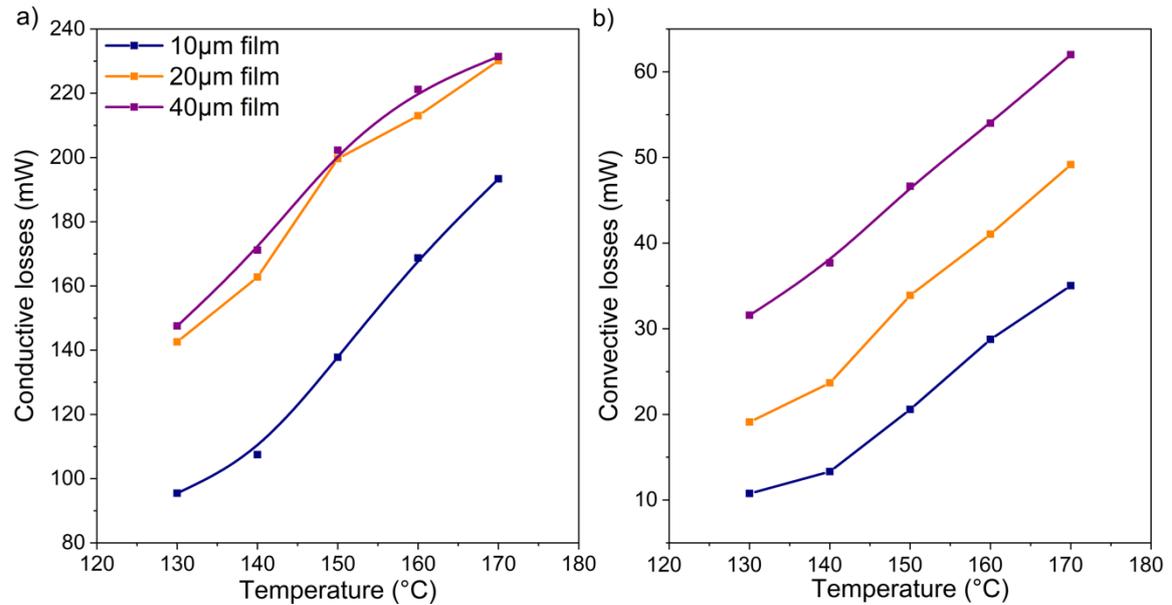
**Figure 78** LEM simulation of the effect of thickness on losses, (a) conduction losses, (b) convection losses. Data pre-published in Joseph et al.[28]

within the TM film stack reduces during operation when the thickness of the film is increased. The losses by conduction and convection are also increasing in response to the increase in the thickness of the TM film stack.

But the increase in conduction losses can be seen stagnating as the thickness is increased to 40 μm. This is due to the thermal resistance of bonding layers within the TM film stack. Since TMGs with 20 μm and 40 μm, TM film stacks have multiple layers of TM film, the temperature of the individual layers is different as they are separated by the conductive bonding layer which still has much higher thermal resistance compared to the TM film. The temperature of the top layer is always higher and the bottom layer is the lowest. But this gradient of temperature within the stack is slightly increasing with the increase in $T_{source}$. The ΔT within the individual TM film layers can be observed in **Figure 79**a. **Table A 1** provides the maximum temperature ($T_{max}$) and minimum temperature ($T_{min}$) that provides the value of ΔT in the TM film. For the TMG with a 40 μm TM film stack, the ΔT distribution is given in **Figure 79**b. The maximum ΔT occurs in the top film at a $T_{source}$ of 170 °C and the ΔT within the layers as we move from second to fourth shows only slight reduction. Maximum ΔT at $T_{source}$ of 170 °C is 2.9 °C in the top layer, while the bottom layer shows only a ΔT of 2 °C. **Figure 79** shows that the top layer experiences the maximum change in magnetization during operation and contributes more to the change in magnetic force change compared to the layers below. The bottom film at 130 °C only experiences 1.6 °C of change and still sustains the resonant self-actuation.
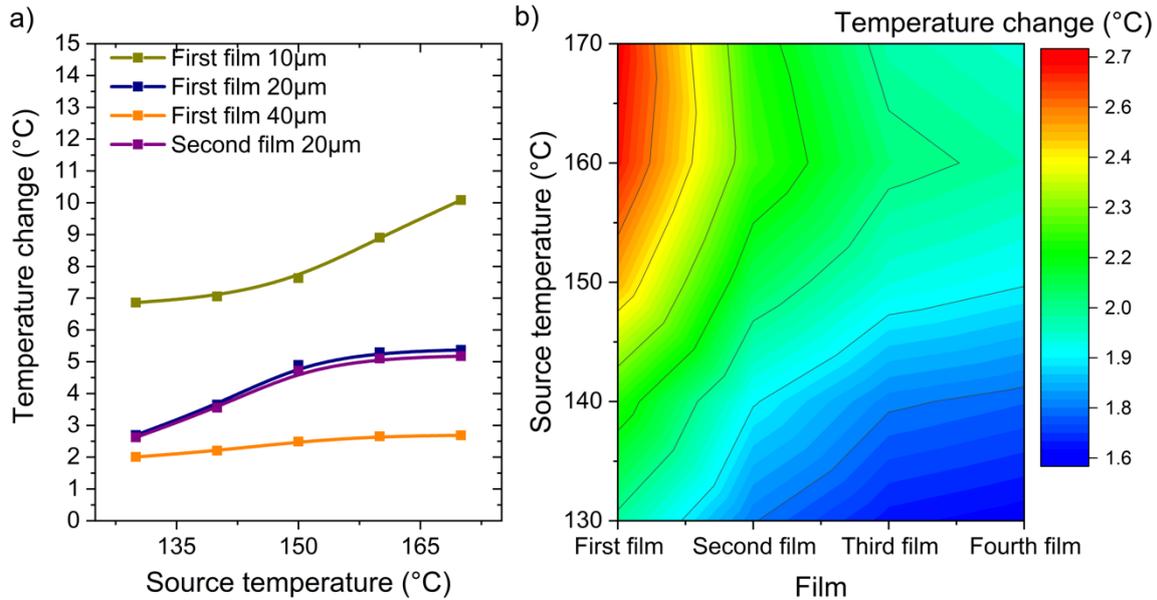
**Figure 79** LEM simulation of (a) temperature change within different film layers in a TM film stack (b) temperature profile within the TM film stack in a TMG with 4 films (40 μm effective thickness). Part of data pre-published in Joseph et al.[28]

Even in the case of homogenous TM film, there would be a temperature gradient from top to bottom, but this would still be much lower than when the TMG is made with multiple layers bonded together. One of the advantages of upscaling the TM film layer is that the footprint occupied by the TMG reduces to as result of device design.
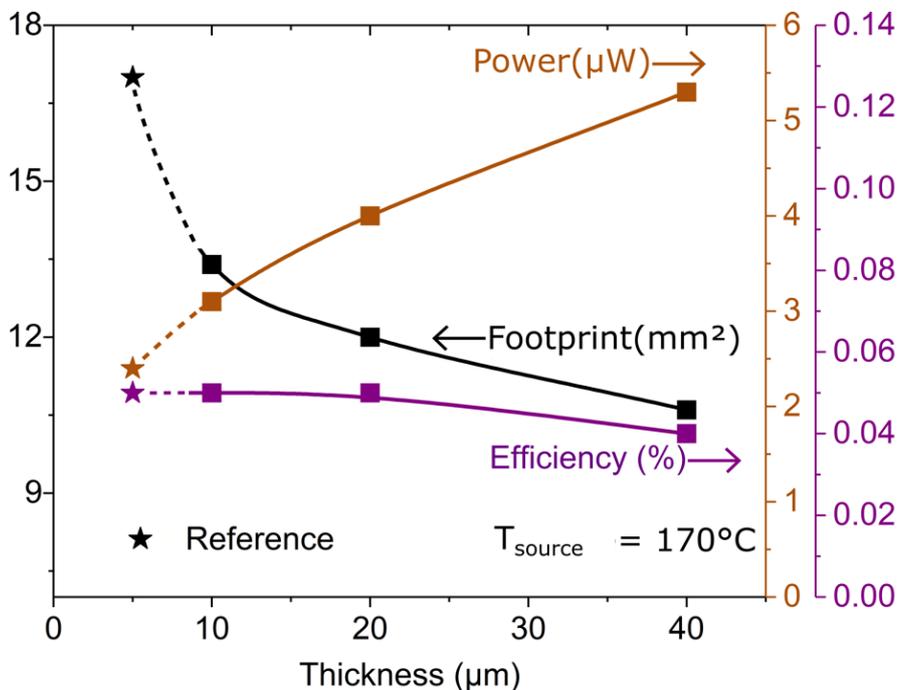


**Figure 80** Effect of scaling on power, footprint, and efficiency. Adapted from Joseph et al.[28]

This is due to the reduction in the total length of the cantilever to increase the stiffness of the TMG to match the increased magnetic force and modified thermal cycle. The lateral area occupied by the TMG is reducing with an increase in thickness of the TM layer. The efficiency of the TMG in terms of magnetic energy converted from the thermal energy is staying almost constant even when the TMG is scaled. **Figure 80** shows that the footprint is reduced to 10.6 mm$^2$ while the power increased to 5.3 µW. Here the important result is upscaling the power output per footprint by about 3.4 times to a high value of 50 µW/cm$^2$, when compared to the reference device of the TMG with 5 µm Ni-Mn-Ga film for the same $T_{source}$ of 170 °C.

## 6.2. Upscaling TMG by array of parallel devices

Upscaling the power output of the TMG by adding more devices operating in parallel is yet another method by which higher power outputs could be achieved from the TMG. The operation of the TMG could either be in synchronization or without synchronization with each other. However, being oscillating devices, it can be assumed that TMGs would have some form of cross-coupling between them while operating in close proximity to one another, as they have pick-up coils and TM films that change their magnetization. Both of these might cause an electromagnetic coupling. Moving air between the devices might result in mechanical or thermal coupling of the device. Understanding such coupling effects between the TMG devices operating at close distances is crucial to realize upscaling of the TMG as an array of multiple parallel devices. The power output from a single TMG device would be limited and in order to increase the power output further while still keeping the benefits of resonant self-actuation, rapid heat transfer, and thin TM film architecture, it is inevitable to have multiple TMGs operating under the same heat source.

### 6.2.1. Layout of two device array

Two devices are operated under the same magnet with enlarged dimensions 3 mm x 30 mm x 8 mm. The distance between the devices (D) is varied from 6 mm to 0.3 mm. The lower limit of separation between the devices is due to the physical limitation to accommodate the devices without mechanical contact between the two devices (due to the wires coming out of the pickup-coil. The design of the device is the same as in section **4.4**. TMG's with a brass cantilever of 7.2 mm x 2 mm lateral dimensions and thickness of 20 µm is chosen. TMGs are prepared by keeping close tolerances as the devices need to be as identical as possible.

---

[i]Section 6.2.1 has been published in similar form by the author in Joseph et al.[150]
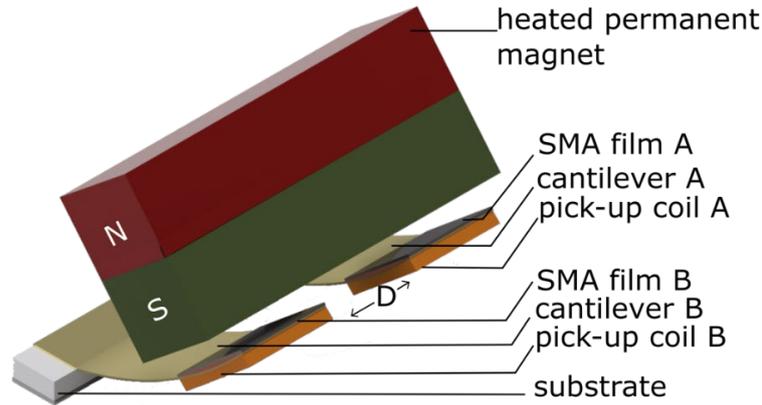
**Figure 81** Schematic of two TMG's operating in parallel under a long magnet. Adapted from Joseph et al.[150]

One of the TMGs is placed under the magnet and moved across the surface while measuring power output, frequency, and stroke to make sure the effects of magnetic misalignment and precision position stage misalignments are alleviated. Once the magnet and position stages are all aligned, the second TMG is placed at a distance of 5 mm. The separation between the TMGs is varied in steps. **Figure 81** shows the schematic of the TMG. At each position, ten measurements of a duration of ten seconds are taken after giving a few minutes for the device to stabilize after moving the device closer. As explained
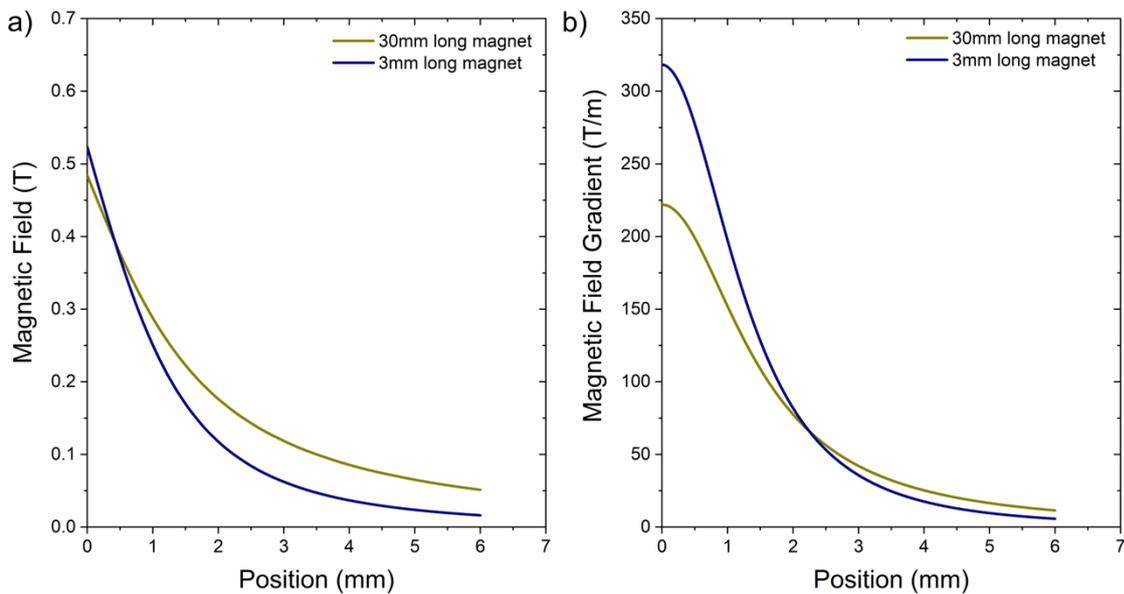


**Figure 82** Comparison of (a) magnetic field and (b) magnetic field gradient of 3 mm long and 30 mm long magnet based on LEM simulations.

in detail in section **5.1**, the change in the dimension of the permanent magnet affects the magnetic field and magnetic field gradient of the magnet. Therefore, absolute numbers can hardly be compared between the results in previous sections **4.4**, **5** and **6.1. Figure 82** illustrates the variation of magnetic field and magnetic field gradient with respect to distance from magnet surface. Both magnets are made of SmCo to be operational at higher temperatures. The 3 mm long magnet has a remanent magnetic field of 1.07 T and the 30 mm long magnet has a remanent magnetic field of 1.08 T due to a different composition of the magnetic material. The difference in magnetic field due to the slightly higher remanent magnetic field is really low as the change is only 0.1 % of the value. The 30 mm long magnet has higher magnetic field and slightly higher magnetic field gradient at a longer distance from the surface of the magnet compared to the magnet with 3mm length used in section **4.4.** At the surface of the 3 mm long magnet, the magnetic field intensity is around 525 mT, while the 30 mm long magnet can only generate a magnetic field intensity of 480 mT at the surface of the magnet.

Closer to the magnet, the magnetic field and field gradients are low on the longer magnet. This results in lower magnetization of TM film and consequently lower magnetic forces at the tip of the cantilever beam. Thus, the operation frequency will be lower, and the generated power will be lower as well due to the lower magnetic field gradient experienced by the pick-up coil. The increase in the remanent magnetic field by changing the composition is not enough to counter the reduction in the magnetic field and magnetic field gradient of the 30 mm long magnet compared to the 3 mm long magnet. The TMG with 10 µm thick Ni-Mn-Ga film is generating around 1.3 µW under the large magnet while it is placed as a single operating device under the magnet. At 5 mm away from each other, the devices are assumed to be at the same performance level as the distance between them is too large to cause any significant coupling effects.

## 6.2.2. Performance results of two device array

When two identical devices with very tight tolerances are operating near each other, the performance of the device is affected by the device nearby. **Figure *83*** shows the effect of separation between the TMG devices for a $T_{source}$ temperature of 170 °C and 140 °C. For high source temperature of 170 °C, the device shows reduction in performance as the separation is reduced below 1 mm. The device shows breaks in operation when the separation is further reduced to 300 µm.

---

[j]Section 6.2.2 has been published in similar form by the author in Joseph et al.[150]
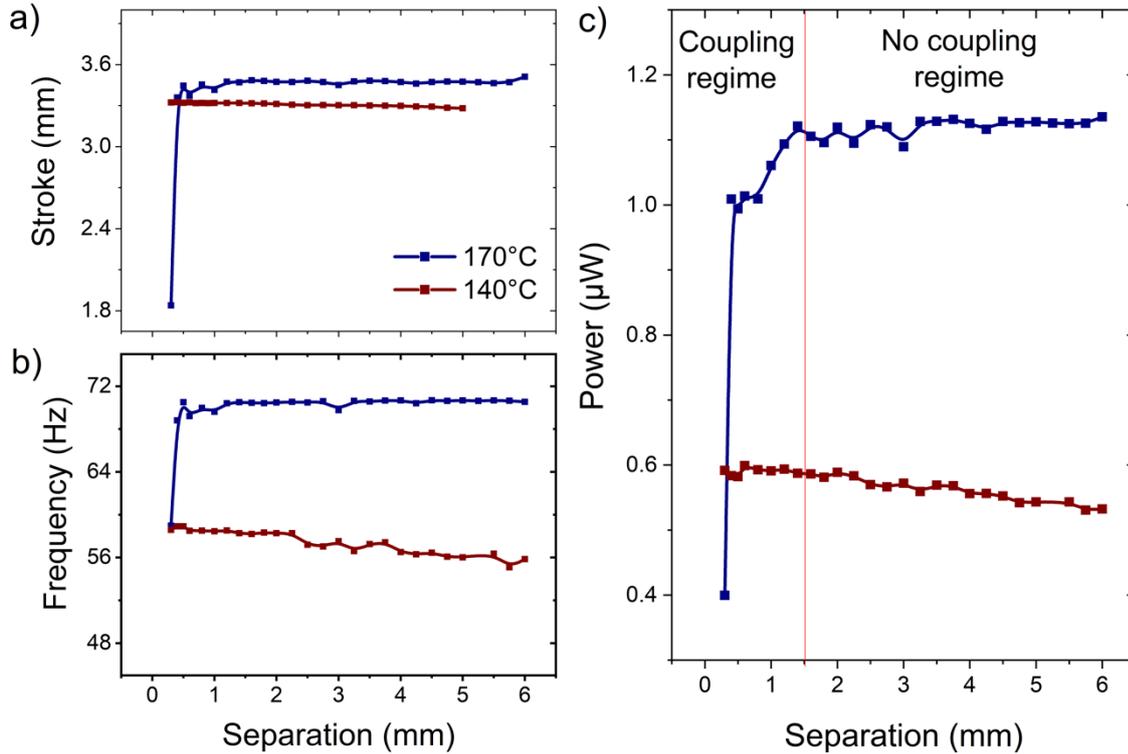
**Figure 83** Effect of separation on the TMG at $T_{source}$ of 170 °C and 140 °C. (a) Stroke of the deflection of the TMG, (b) Frequency of operation of the TMG, (c) power output of the TMG. Part of data pre-published in Joseph et al.[150]

On the other hand, at lower source temperature of 140 °C, the TMG devices seems not to show any coupling effects even at close separation of 300 µm. It is also visible that the power output even increases slightly as the devices are brought closer to each other. **Figure 84** illustrates the behavior of the TMGs when the separation between them is varied at different $T_{source}$ values from 170 °C to 110 °C. At lower $T_{source}$ when the frequency stroke and power output are already low, the separation does not seem to have any effect. When the temperature of the heat source is increased, the device starts to show some coupling effects when the separation is small. When the $T_{source}$ is 150 °C and above, the power seems to drop continuously as the separation is reduced below 1 mm. However, the devices show coupling effects when separation below 1.5mm. At 140 °C, TMG was operating with low power output even at 6 mm separation suggesting the device was operating closer to the magnet than its optimal operating distance where it would generate maximum output. Thus, this shows that if the device is operated at suboptimal conditions where the power output is reduced, the TMG could be operated at very close distances. This also
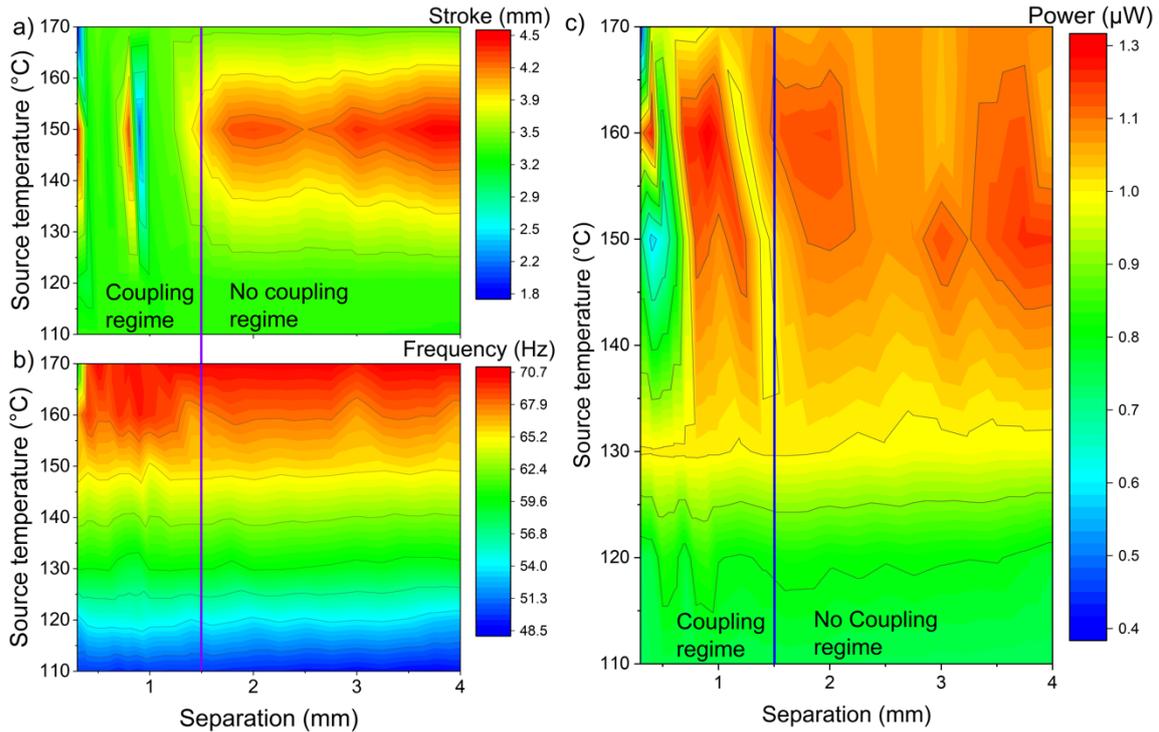
**Figure 84** Effect of separation on performance of TMGs. (a) Stroke of deflection, (b) frequency of operation, (c) power output.

explains the slight increase in power output that was observed as the separation was reduced suggesting there is still potential to optimize the power output. It is clear that at higher source temperatures, the devices become highly unstable and continuously stop-operation resulting in large fluctuation in power output. Further examination of **Figure 84** reveals that the average stroke is showing reduced values below 1.5 mm, while the frequency shows an increase at high source temperatures above 150 °C. This slight peak in frequency of operation results in an increase in output of the device before it stops operation suggests a thermal build-up in the Ni-Mn-Ga films when the devices have a small separation between them.

Further analysis is only possible by checking individual performance as the average values are only showing the device trend. To understand the coupling effects that cause break in operation, it is necessary to examine the time correlated performance of the TMG devices. **Figure 85** shows the output generated by the TMG, measured by an Oscilloscope (Keysight DSOX1204A). The oscilloscope is connected parallel to the load resistor so as to measure the voltage across the resistor. The measurement is taken for a long duration of 180 seconds. The device stops operation due to the increased temperature of the Ni-Mn-Ga film and restarts itself as soon as the film is cooled enough to resume operation.
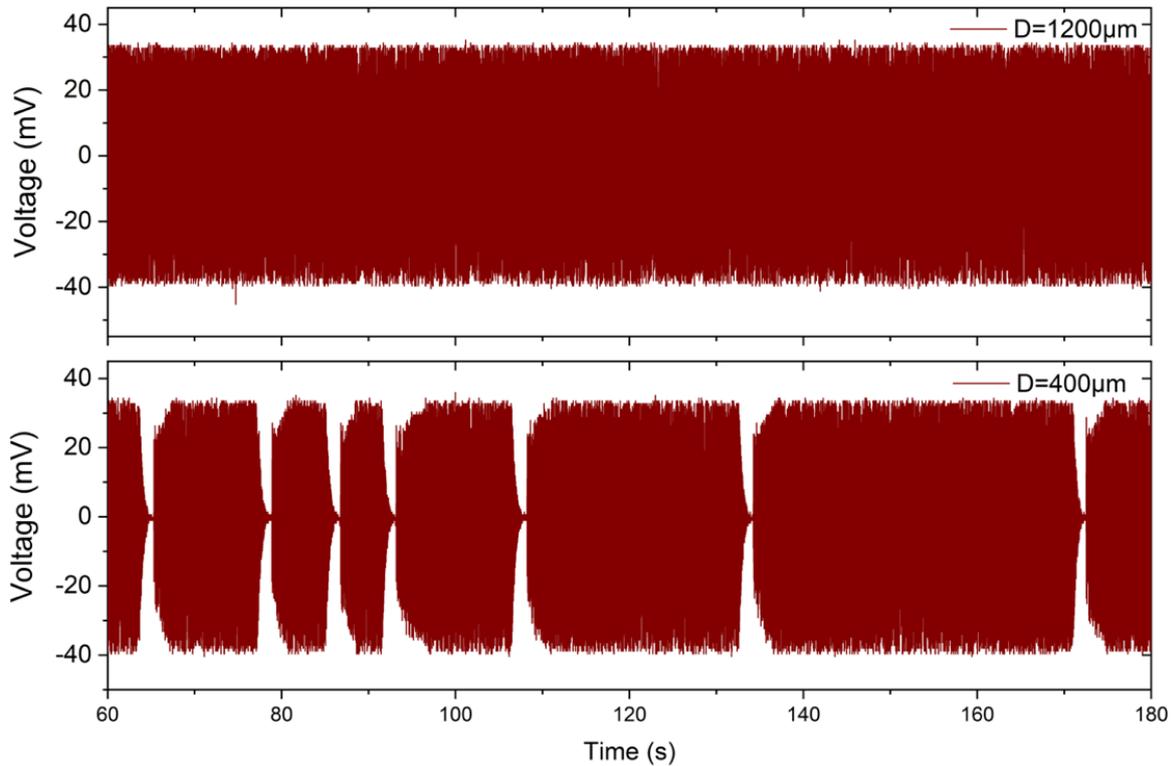
**Figure 85** Output performance of the TMG (a) at a separation of 1200 μm between devices and (b) 400 μm between devices. Data pre-published in Joseph et al.[150]

This is clear from the increase in voltage before damped oscillations appear. But the interval of this intermittent break is not regular showing that the mutual coupling effects of the TMGs are random.

The mutual effects could be visualized by plotting the output of the TMGs together as shown in **Figure 86.** The output of the two devices TMG A and TMG B denoting two of the TMGs operating in parallel is mutually coupled at small separations. The output of the device TMG B increases when TMG A stops operation and shows adaptation to a lower power output operation point as soon as device A is back in resonant operation. However, this mutual correlation is not present in all the data, which suggests that such a correlation can occur but is not required when the devices are operating in parallel. The mutual correlation is occurring due to the ability of TMG A to cool itself better as the device nearby stops operation. This shows the ability of the TMG to adapt its performance according to ambient conditions. In cases where the correlation is absent, it can be assumed that the devices are not coupled to each other and thus a momentary halt in the operation of the nearby device is not enough to cause an increase in the thermal performance of the other

device. From **Figure 85**, it can be assumed that there is no mechanical effect due to the air movement between the devices other than the indirect effect on the TMG thermal dissipation. This is because in case of mechanical coupling between devices due to air movement or electromagnetic coupling between coils, the TMG would have shown reduced frequency and voltage output before going out of resonance. But in the present case the TMG shows an increase in frequency and voltage before going out of resonance. This increase in frequency and voltage is the result of heat buildup as the device is not cooling enough, hence the TMG requires less time to heat up, but eventually this causes a momentary halt in the operation. The TMG continues operation once the TM film is cooled enough to be attracted to the magnet so that the cycle could be restarted. Thus, it is concluded that only thermal coupling effects are present without any mechanical or electromagnetic coupling effects between the TMG devices operating in parallel under a common magnet.
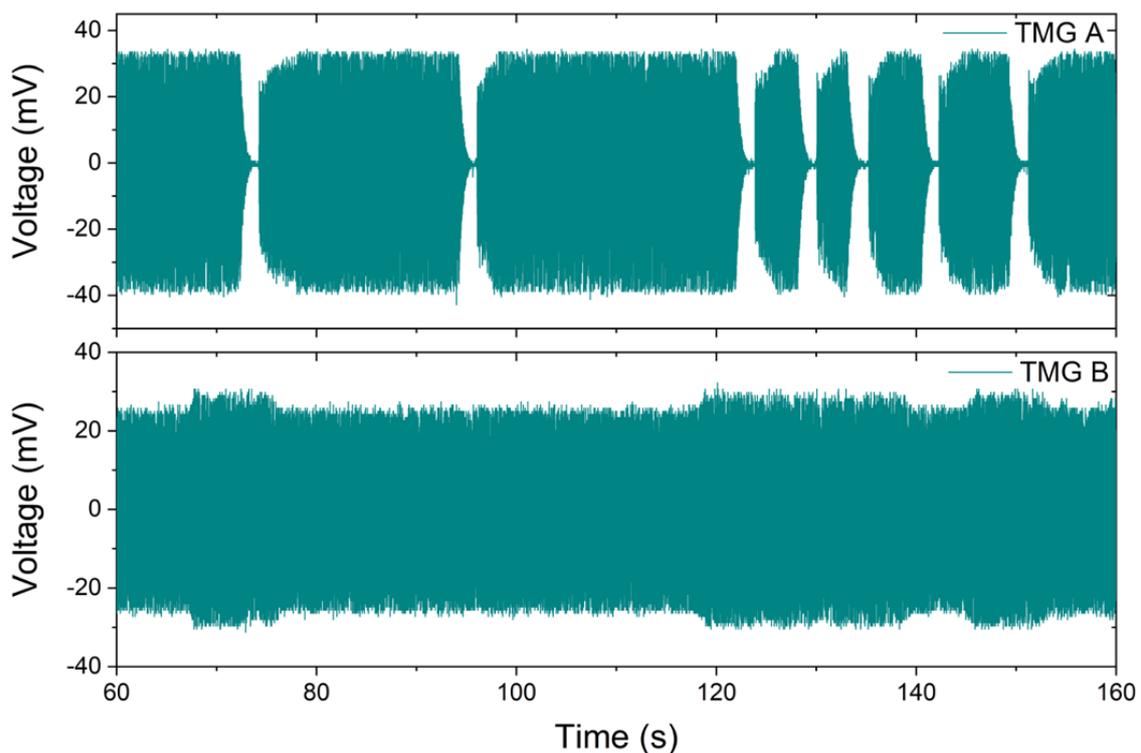


**Figure 86** Simultaneous performance comparison of the TMG devices. The $T_{source}$ is maintained at 170 °C and separation is 1000 µm, (a) voltage output across load resistance for TMG sample A, (b) voltage across load resistance for TMG sample B. Data pre-published in Joseph et al.[150]

121

## 6.2.3. Layout of three device array

Having two devices operating in parallel is symmetric with both devices experiencing the same ambient conditions. Adding more devices in parallel would result in TMG's experiencing different ambient conditions. The TMGs at the ends would have one neighboring device and all in between TMGs would have TMGs operating on either side of them. To see the effect of having two devices operating on either side of the device, a total of three identical devices are prepared. Thereby keeping very tight tolerances are placed under the 30 mm long magnet used in the case of two device array explained in section **6.2.1.** **Figure 87** shows the schematic of three TMG device array. The substrate for the center device is rotated by 90° to allow very low separation between devices. The overall power output of the center device is reduced to around 0.7 µW.
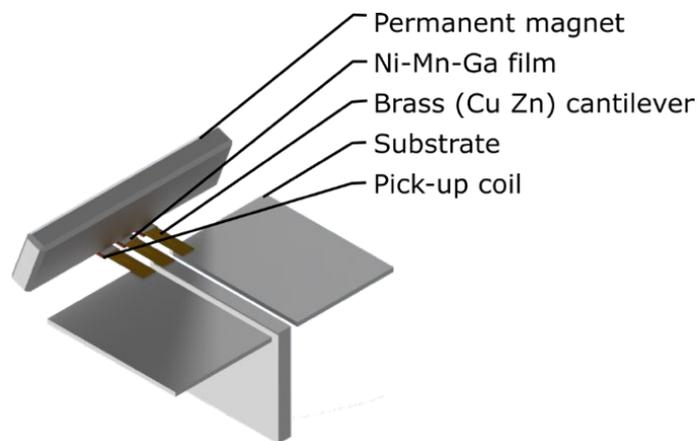


**Figure 87** Parallelization with three devices, with the substrate for the center device rotated by 90° to allow low separation between devices.

compared to 1.3 µW in the case of devices at the end. Like in the case of two device array operating in parallel, the coupling effects are present from a $T_{source}$ of 150 °C and gets worse as the separation between the device is below 1 mm. **Figure 88** shows the effect of separation on the performance of the center TMG for various $T_{source}$ values ranging between 140 °C to 160 °C. As mentioned earlier the device is operating by generating lower power compared to the devices at the side, suggesting even at 5 mm the device is having an effect. Reducing the separation from 5 mm to 1 mm does not affect the performance of the device with power output and frequency staying constant. Reducing separation below 1 mm accelerates the decrease of power output and causes an increase in the frequency of the device due to thermal build-up in the Ni-Mn-Ga film. The average frequency increase is different from the case of two device array as in that case the average frequency is

constant and only an increase in frequency is observed locally near the intermittent stop in the TMG operation. The present case with three device array also exhibits a sudden increase in frequency before breaking resonant self-actuation. But on top of it, there is an increase in the average frequency of the operation. The power first increases and then decreases as the separation is reduced below 1 mm at higher temperatures. At 140 °C, the power is increasing slightly as the devices are closer with separation below 1 mm.
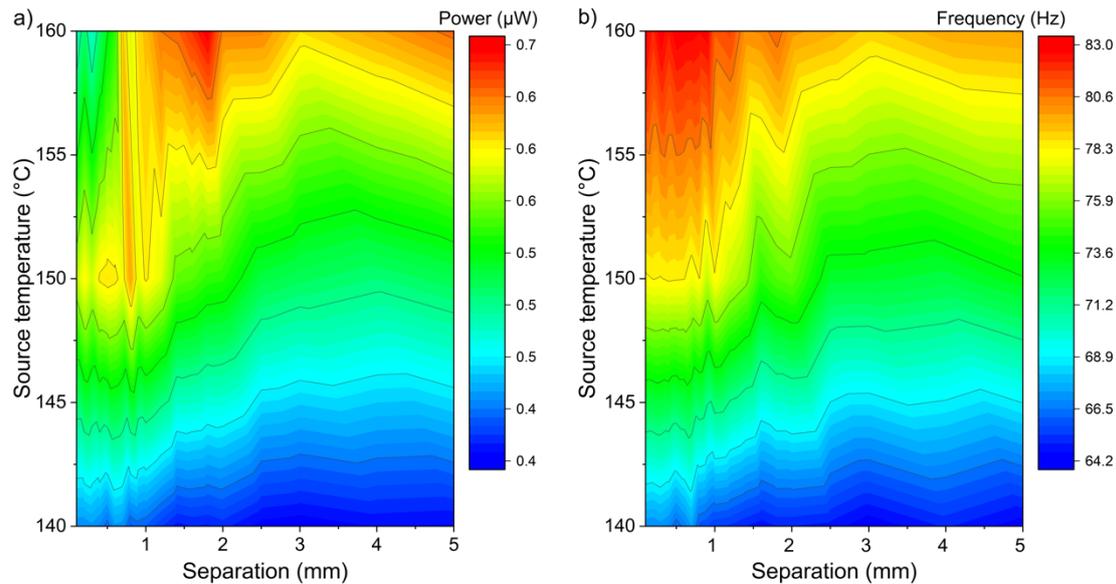


**Figure 88** Performance of the center device (the TMG with 10 µm Ni-Mn-Ga film) in an array of three devices as the separation is gradually reduced. The two neighboring devices are moved and kept at the same separation. (a) power output of the TMG (b) frequency of the TMG.

## 6.2.4. Effect of upscaling on coupling effects

Upscaling the device from having a Ni-Mn-Ga film of 10 µm thickness to a device with 20 µm thick Ni-Mn-Ga provides insight into effects of scaling on coupling effects while in parallel operation. It is shown earlier in section **6.1** that upscaling of the TMG results in increased power and decreased footprint. A single TMG device with 20 µm Ni-Mn-Ga film under the 30 mm long magnet generates 1.8 µW of power compared to the 1.3 µW. But when placed in the array, the center device only generates 0.8 µW. When compared to the power output of 0.7 µW for the TMG with 10 µm Ni-Mn-Ga film, it is only an increase of 14.3 %.

At higher $T_{source}$ values the power output of the TMG is decreasing as the separation is below 1 mm. But the frequency increases as the device gets closer as can be seen from **Figure 89**. At lower $T_{source}$ values the power increases as the separation between the devices is reduced below 1 mm. This also suggests thermal imbalance with the TMG requiring additional optimization to operate at full capacity when placed in an array. The highest power output is observed at the closest distance of 100 μm separation. This is also observed in **Figure 89** where at 140 °C, the power output increases as the separation is reduced. This shows that the design of a TMG with multiple devices in parallel would require additional design optimization depending on whether the device would be operating in between or at the end of the TMG array.
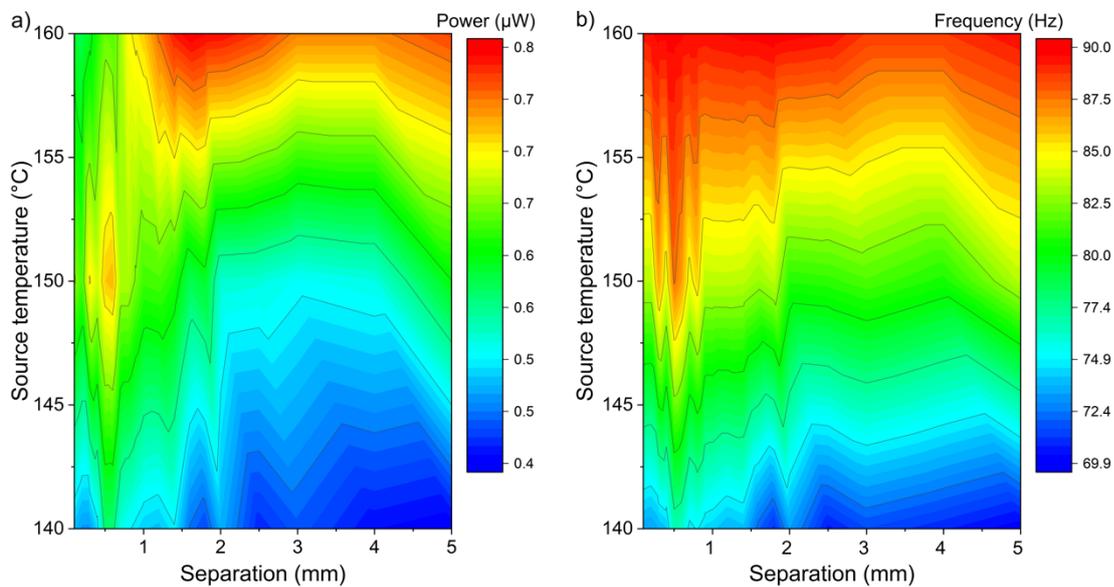


**Figure 89** Performance of center device in the TMG array of three devices with 20 μm Ni-Mn-Ga film, (a) power output, (b) frequency of operation.

## 6.3. Discussion

The large increase in electrical power for increasing film thickness up to 40 μm while simultaneously decreasing the footprint is a notable result of this work. As a result, when increasing film thickness from 10 to 20 μm, the magnetic power per footprint calculated from the magnetic cycle increases from 0.8 mW/cm$^2$ to a maximum of 1.1 mW/cm$^2$. A further increase in layer thickness to 40 μm causes a marginal drop in power density to 1.05 mW/cm$^2$. The magnetic power is taken as the enclosed area in the magnetization vs magnetic field curve. This curve shows also shows the thermomagnetic cycle followed by

the TMG, an example of thermomagnetic cycle depicted in **Figure A 1** for the case of the TMG with 40 µm film. This is due to the added thermal resistance of the conductive bonding layer between the TM film stack (Ni-Mn-Ga) As the heat intake rises further with increasing film thickness, this decrease is correlated with a little decline in efficiency. The electrical power produced by electromagnetic induction in the pick-up coil, however, increases continuously with film thickness and peaks at 5.3 µW at a thickness of 40 µm for the Ni-Mn-Ga film. 50 µW/cm$^2$ is the proportional electrical power per footprint. In this instance, only a 3 °C periodic temperature change in the film stack is needed. This represents an increase of more than 3.4 times when compared to the reference device with a 5 µm film thickness from the previous work.[92] When it comes to length scales in the cm range and small temperature differences, this performance rivals that of cutting-edge thermoelectric generators. [151]

**Table 4** Model parameters for thermal, electromagnetic, and mechanical components being used in LEM simulation of the TMG upscaling. Part of the data pre-published in Joseph et al.[28,91,128]

| Mechanical Parameters | Value | Units | Reference |
|---|---|---|---|
| Pick-up coil mass | $6 \times 10^{-6}$ | kg | This work |
| Cu-Zn density | 8500 | kg/m$^3$ | [143] |
| Ni-Mn-Ga density | 8020 | kg/m$^3$ | [144] |
| Young's modulus (Cu-Zn) | $1 \times 10^{11}$ | N/m$^2$ | [146] |
| Contact stiffness beam-magnet | $10^4$ | N/m | This Work |
| Structural and air damping | $1.12 \times 10^{-5}$ | Ns/m | This Work |
| Impact damping | 0.1 | Ns/m | This work |
| Length of the Ni-Mn-Ga stack | 2 | mm | This work |
| Width of the Ni-Mn-Ga stack | 2 | mm | This work |
| Thickness of the Ni-Mn-Ga stack | 10-40 | µm | This work |
| Length of the Cu-Zn cantilever | 4.3-5.7 | mm | This work |
| Width of the Cu-Zn cantilever | 2 | mm | This work |

| | | | |
|---|---|---|---|
| Thickness of the Cu-Zn cantilever | 20 | $\mu$m | This work |
| | | | |
| **Electromagnetic Parameters** | | | |
| Remanent magnetic field strength | 1.07 | T | This work |
| Number of turns of pick-up coil | 400 | - | This work |
| Area of pick-up coil | $1.96 \times 10^{-6}$ | $m^2$ | This work |
| Electrical resistance (pick-up coil) | 250 | $\Omega$ | This work |
| Electrical resistance (load) | 400 | $\Omega$ | This work |
| | | | |
| **Thermal Parameters** | | | |
| Range of contact heat transfer coefficient | 8400-13300 | $W/m^2K$ | This work |
| Range of convective heat transfer coefficient | 150-220 | $W/m^2K$ | This work |
| Thermal conductivity Cu-Zn | 109 | $W/mK$ | [147] |
| Thermal conductivity Ni-Mn-Ga | 23.2 | $W/mK$ | [148] |
| Thermal conductivity of conductive bonding layer (BL) | 2.5 | $W/mK$ | [145] |
| Thermal conductivity of non-conductive BL | 0.33 | $W/mK$ | [145] |
| Heat capacity Cu-Zn | 400 | $J/KgK$ | [143] |
| Heat capacity of Ni-Mn-Ga | 490 | $J/KgK$ | [148] |
| Heat capacity of conductive BL | 904 | $J/KgK$ | [145] |
| Heat capacity of non-conductive BL | 2100 | $J/KgK$ | [145] |
| Area of thermal contact | 4 | $mm^2$ | This work |

In order to maintain the resonant self-actuation mode, the strategy to boost power depends on tuning the magnetic attraction force, mechanical reset force, and heat transfer dynam-

ics. The realized increase in power results from the rise in the oscillatory motion's mechanical energy, which rises with increasing mass and frequency as long as resonance conditions are upheld and, in turn, sustains magnetic cycles with rising variations in magnetic energy. The presented results show that the upscaling strategy is ultimately constrained by the heat transfer kinetics for a given ferromagnetic material and magnetic field gradient. The scaling dependency of heat input, heat dissipation, and the ensuing temperature fluctuations in the Ni-Mn-Ga layers are analyzed using LEM for describing the thermal processes in the TMG. The dynamic actuation of the cantilever is limited by the thermal processes that are result of parameters like TM film thicknesses, load resistance, coil parameters, ambient temperature and $T_{source}$ values The LEM is also used to determine the heat transfer coefficient ($h_f$) values by matching simulation results with the experimental results. **Table 4** provides the modeling parameters of the LEM simulation model.

According to LEM simulation results, heat input rises as film thickness increases, with conductive heat losses serving as the main mode of heat dissipation. As a result, with increasing film thickness from 10 μm to 40 μm, respectively, the corresponding fraction of average retained input heating power increases from roughly 80 % to 94 %. These fractions only differ slightly and exhibit the same thickness dependency at lower $T_{source}$ values. This finding demonstrates that a significant portion of heat is retained in the SMA film stack and contributes to the ΔT, a necessary condition for achieving large power output. But as the film thickness increases, the ΔT of the film stack during oscillation decreases, which has two significant effects. First, the effectiveness of increasing film thickness is reduced as ΔT decreases. Second, the diminishing ΔT places a severe restriction on the further scaling up of film thickness.

The results of the current study clearly show that a minimum ΔT is necessary for resonant self-actuation, which is dependent on the specifics of material properties, operating temperatures, and device design. This limit is between two and three degrees Celsius for the TMG with 40 μm Ni-Mn-Ga film. **Table 5** summarizes the key findings of the demonstrator's performance. The attainable ΔT is no longer sufficient to induce enough change in magnetization ΔM to support resonant self-actuation when the film thickness is too high. The TM film's bonding layers minimize heat transmission, resulting in a low temperature gradient (<1 °C) from top to bottom that minimizes the contribution of the bottom layers to resonant self-actuation. LEM simulation allows to evaluate important temperatures of the TMG demonstrator, which are provided in **Table A 1**. LEM simulation is carried out to examine this impact, replacing the stack of four Ni-Mn-Ga films and thermally conductive

connecting layers with a single homogenous Ni-Mn-Ga layer that is 40 µm thick, leaving only one non-conductive bonding layer that is 15 µm -20 µm thick. This resulted in a 10 % increase in power output which could be increased further as the thickness of the actual device was 82 µm for the TMG with 40 µm NI-Mn-Ga film designed for experiments. If the whole thickness could be active material that would result in large power output as the magnetization of the active material is now larger and, hence, a higher stiffness of the cantilever and a higher frequency of operation could be attained as the thermal mass would be comparable.

Each TMG generates a significant amount of power density up to 30 mW/cm$^3$ with respect to its TM film when operated in a parallel configuration. A parallel architecture of numerous TMGs is necessary to raise the power level for particular purposes, because the absolute power of a single TMG is not enough for direct application. However, placing numerous TMGs close to one another with a little gap between them raises the problem of cross-coupling, which could impair resonant self-actuation. When two devices with close toler-ances are operated in parallel under the same magnet, the separation does not appear to have any impact at lower source temperatures when the frequency, stroke, and power output are already low. The TMGs don't appear to have any coupling effects even at an extremely close spacing of 300 µm. When the $T_{sourse}$ increases, the TMG begins to exhibit coupling effects at close distances. The power appears to continuously decrease as the spacing (D) is decreased below 1 mm when the $T_{source}$ is 150 °C or above. The frequency of operation slightly peaks and causes an increase in the device's output voltage before it ceases operation at small separation. Which suggests a heat buildup in the TM film.

**Table 5** performance results when the TMG is upscaled from having 10 µm thick Ni-Mn-Ga film to 40 µm thick Ni-Mn-Ga. Data pre-published in Joseph et al.[28]

| Film Thickness | Footprint | Frequency | Stroke | ΔT | Magnetic power per footprint | η | Electrical Power |
|---|---|---|---|---|---|---|---|
| (µm) | (mm$^2$) | (Hz) | (mm) | (K) | (mW/cm$^2$) | (%) | (µW) |
| 10 | 13.4 | 114 | 1.8 | 10.1 | 0.8 | 0.047 | 3.1 |
| 20 | 12 | 136 | 1.9 | 5.4 | 1.1 | 0.046 | 4 |

| | | | | | | | |
|---|---|---|---|---|---|---|---|
| 40 | 10.6 | 145 | 2.1 | 2.9 | 1.05 | 0.041 | 5.3 |
| 40[b] | 10.6 | 146 | 2.1 | 3.2 | 1.23 | 0.045 | 5.7 |

Even though not all of the data exhibits a mutual correlation, it can be observed that it is possible for mutual correlation to exist when the devices operate in parallel where the performance of one TMG is dependent on the neighbor. The ability of the TMG to cool itself more effectively as the neighboring device ceases functioning is the cause of the mutual correlation. On the other hand, this also demonstrates the TMG's capacity to modify its performance in accordance with the surrounding ambient condition. When the correlation is missing, it can be inferred that a pause in the operation of the nearby device is not enough to produce an increase in the device's thermal performance in some cases. According to the observations, the airflow between the devices has no further mechanical effects besides an indirect impact on the TMG thermal dissipation. This could potentially be evident as additional oscillations before the device ceases operation. However, since only the frequency spike and amplitude increase are discernible in the raw data, it can be said that only thermal coupling effects exist between the TMGs operating in parallel under a single magnet, without any mechanical or electromagnetic coupling effects.

**Table 6** lists the key parameters of the TMG demonstrator considered for this study. When three devices are working in parallel, the coupling effects are present for the center device starting at a $T_{source}$ of 150 °C and deteriorate when the distance between the devices is reduced to less than 1 mm. In the case of two parallel devices, the average frequency is constant, and the only rise in frequency that is noticed locally is close to the intermittent pause in the TMG operation. This is where the average frequency increase differs from the case of two parallel devices. When three devices are operating in parallel, the same traits are observed, but there is also a rise in the frequency of operation. At higher temperatures, as the spacing decreases below 1 mm, the power output decreases.

As the devices become closer with a spacing of under 1 mm at 140 °C, the power output increases slightly. This shows that somehow the TMG in the center has found a different stable oscillation frequency and stroke when compared to the TMG devices in the end. The thermal equilibrium that is reached when resonant self-actuation is achieved results in the high frequency operation and large stroke. In this case the thermal equilibrium that is reached by the TMG at center to achieve resonant self-actuation is different from the TMG at either ends of the array. This is also visible when the TMG are spaced at 5 mm

from each other. Two device arrays showed no effect at 5 mm distance, while the center device in three device array showed low output power and frequency even with 5 mm spacing. Hence, it shows that the TMG is operating at suboptimal conditions which is made worse by bringing the TMG devices closer. This causes an increase in output as the heat dissipation is affected causing the device to slowly buildup heat. This results in the increased frequency as the separation is reduced.

**Figure A 5** and **Figure A 6** show the effect of resistance on the performance of the TMG when separation is varied. When operating the devices individually, the highest power is still recorded at 400 Ohm. When the resistance is lower than 300 Ohm or lower, the power appears to grow as the separation decreases, with the highest power being recorded for 200 Ohm. Similar behavior is exhibited by the frequency, which has peaked at 200 Ohm and 600 Ohm and a relatively low frequency at 400 Ohm. Frequency reduces as the separation is increased. This performance difference under different load resistances implies that the new thermal equilibrium at which the resonance is achieved is no longer optimum and has the potential to be improved further by device design.

**Table 6** TMG parameters for the devices considered for experiments. Part of data is pre-published in Joseph et al.[28]

| Parallel operation with two devices | | |
|---|---|---|
| **Parameter** | **Unit** | **Value** |
| Ni-Mn-Ga width | mm | 2 |
| Ni-Mn-Ga length | mm | 2 |
| Ni-Mn-Ga thickness | µm | 10 |
| Cu-Zn cantilever width | mm | 2 |
| Cu-Zn cantilever length | mm | 7-7.2 |
| Cu-Zn cantilever thickness | µm | 20 |
| Number of turns in pick-up coil | - | 400 |
| Parallel operation with three devices | | |
| **Parameter** | **Unit** | **Value** |
| Ni-Mn-Ga width | mm | 2 |
| Ni-Mn-Ga length | mm | 2 |

| Ni-Mn-Ga thickness | μm | 10-20 |
|---|---|---|
| Cu-Zn cantilever width | mm | 2 |
| Cu-Zn cantilever length | mm | 5.4-6.4 |
| Cu-Zn cantilever thickness | μm | 20 |

# 7. TMG near ambient temperature

Parts of this section has been published in Joseph et al.[152] Thermal energy below 200 °C is considered low-grade waste heat as this energy is usually taken as lost to the ambient. By adjusting the TMG design parameters mentioned in section **5** and choosing materials with lower $T_c$, it is possible to achieve TMGs operating in resonant self-actuation mode that are able to convert thermal energy from heat sources from below 100 °C. This enable an enormous variety of applications as the heat source temperature would be below the boiling temperature of water. As the temperature of the heat source is reduced further, TMGs operating with a heat source proximal to ambient temperature could be achieved. But when the heat source gets closer to the ambient conditions, the thermal performance of the TMG would be heavily affected. In this section, TMGs with TM film material of Gadolinium (Gd) and hydrogenated Lanthanum Iron Silicon alloy (La-Fe-Si-H) are investigated.

## 7.1. TMG with Gadolinium

The TMG with Ni-Mn-Ga as the active material have shown that the concept of resonant self-actuation enables miniature TMG devices to be competitive with thermoelectric devices.[28,92] However, the range of suitable heat source temperatures was restricted to 100-170 °C due to the ferromagnetic transition temperature $T_c$ of the Ni-Mn-Ga films being 98 °C. To utilize the notion of resonant self-actuation for the recovery of low-grade thermal energy, further suitable thermomagnetic film materials with $T_c$ around room temperature must be developed.[128] Gd films with a $T_c$ around room temperature, a large magnetization ($M$) under a moderate magnetic field, and a large temperature-dependent change in magnetization ($\Delta M / \Delta T$) are promising prospects. The ease with which they may be removed from the substrate on which they are placed helps their incorporation into devices.[153] In this study, a miniature-scale Gd-film TMG device is presented that operates in resonant self-actuation mode and associated physical performance qualities are analyzed near ambient temperature for lowering heat source temperatures from 75 °C to 40 °C.

---

[k]Section 7.1 has been published in similar form by the author in Joseph et al.[152]

## 7.1.1. Material properties

The active material in this study is a Gd film with a thickness of 40 μm. **Figure 90**a depicts typical temperature-dependent magnetization properties for applied magnetic field levels ranging from 0.1 to 0.5 T. At the Curie temperature Tc, a substantial rapid change in magnetization $\Delta M$ occurs within a small temperature change $\Delta T$ induced by a ferromagnetic to paramagnetic phase transition. The transition is hysteresis-free due to its second order character. An Arrott plot analysis of isothermal $M(T)$ readings yields a Tc value of 20 °C, which is consistent with the stated value for bulk Gd.
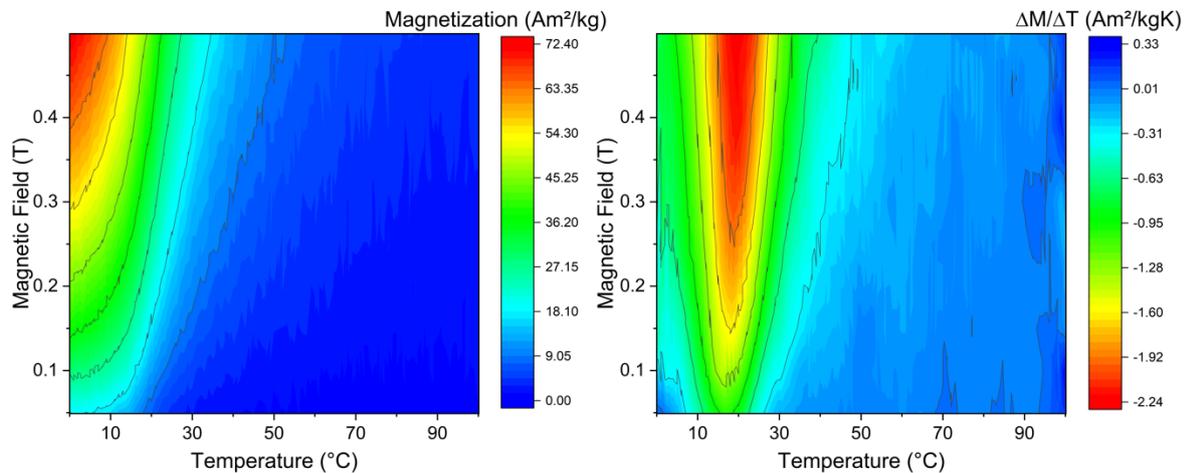


**Figure 90** (a)Magnetization measurement taken by varying temperature at different magnetic fields (b) Magnetization gradient, derived from the magnetization measurement. Data is pre-published in Joseph et al.[152]

**Figure 90**b depicts the temperature-dependent change in magnetization M/T. An extraction magnetometer was used to characterize the magnetic properties of the Gd film. The maximal $\Delta M/\Delta T$ point shifts somewhat field-dependently from 17 °C at 0.1 T to 19 °C at 0.5 T. The substantial variation in $\Delta M/\Delta T$ near ambient temperature of up to 2.3 Am$^2$kg$^{-1}$K$^{-1}$ is the primary impetus for developing a Gd film-based generator in this study. The maximum value of ΔM/ΔT is spread into wider temperatures at higher magnetic fields.

## 7.1.2. Design

Upscaling of TMGs by array showed that operating TMGs close to each other is possible by proper design and parameter adjustment. One of the major hurdles to operating devices

so close is the free-hanging copper wire from the pick-up coil bonded to the connection pin. Since this is through the side, it takes up space and sometimes gets stuck to nearby



a)        b)
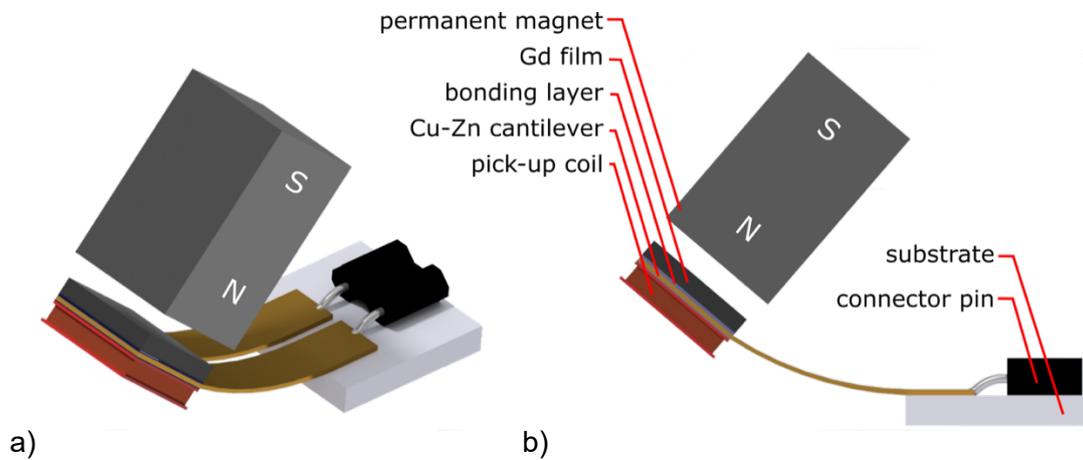
**Figure 91** (a) 3D schematic of the double beam TMG with Gadolinium film at the tip, (b) side view of the TMG showing the component names. Adapted image from Joseph et al.[152]

devices. To avoid this, fixed electrodes are desirable. One solution to circumvent this issue is to split the cantilever beam into two independent beams electrically separated and connect the pick-up coil to the cantilever itself at the tip of the cantilever. Since the cantilever is made from brass with a lateral width of 0.9 mm and 25 µm thickness, this approach results in electrical resistance of only 0.0165 Ohm.
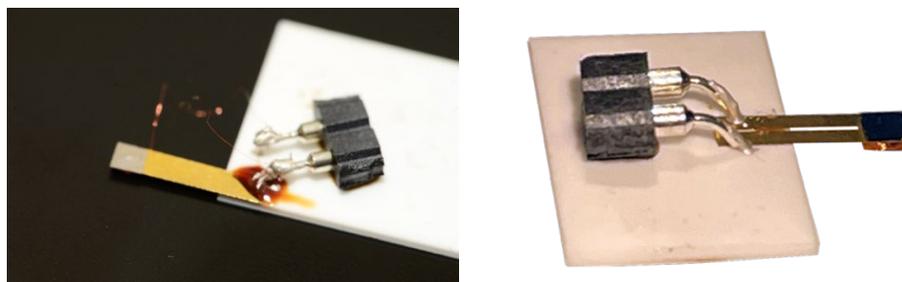


**Figure 92** (a) Device with overhanging copper wires from pick-up coil attached to the connector (b) TMG with double beam brass cantilever as electrodes with no overhang. Adapted image from Joseph et al.[152]

The resistance of the copper wire (15 µm diameter) for the same length is larger with a value of 0.68 Ohm. This is due to the cross-sectional area being much smaller even though copper has only one third value of electrical resistivity compared to brass. **Figure 91** shows the new design for the TMG with a double beam cantilever with Gadolinium as the TM active material and **Figure 92** shows the visual comparison between the previous design and the new design.

## 7.1.3. Fabrication

The Gd film was created by triode sputtering a 3N purity Gd target onto a spinning Si substrate with a diameter of 100 mm at a temperature of 400 °C.[154] Ta buffer and capping layers of 100 nm thickness were also deposited at 400 °C to preserve the Gd layer. The Ta/Gd/Ta trilayer laminate may be easily peeled off the Si substrate because of the higher deposition temperature.[152,154,155] The hcp crystallographic structure of the Gd layer was verified by X-ray diffraction. The film is then removed using a tweezer from the substrate by pulling. The cantilever is prepared by using an ultra-short, pulsed femtosecond laser with a double cantilever shape by keeping the connection at one end. **Figure 93** shows the steps involved in the fabrication of the TMG with Gd film with a double beam cantilever. Step 1 involves the preparation of an alumina substrate using a diamond saw. The cantilever is bonded to a ceramic substrate (Alumina) using a two-part non-conductive bonding adhesive in step II. The pick-up coil is fabricated using the semi-automatic coil winder presented in the section **2.7.8.** The ends of the copper wires are attached to the bottom side of each of the cantilever beams using a conductive bond containing silver particles in step III. In step IV the pick-up coil is flipped and bonded to the bottom of the cantilever beam using a non-conductive bonding layer on top of the electrical bond made with the copper wires. This is done to ensure that the electrical bond is provided with additional strength to withstand the high impact forces during operation. Sandwiching the electrical connection between the pick-up coil and the cantilever ensures that the electrical connection is not affected and does not develop additional contact electrical resistance during operation.
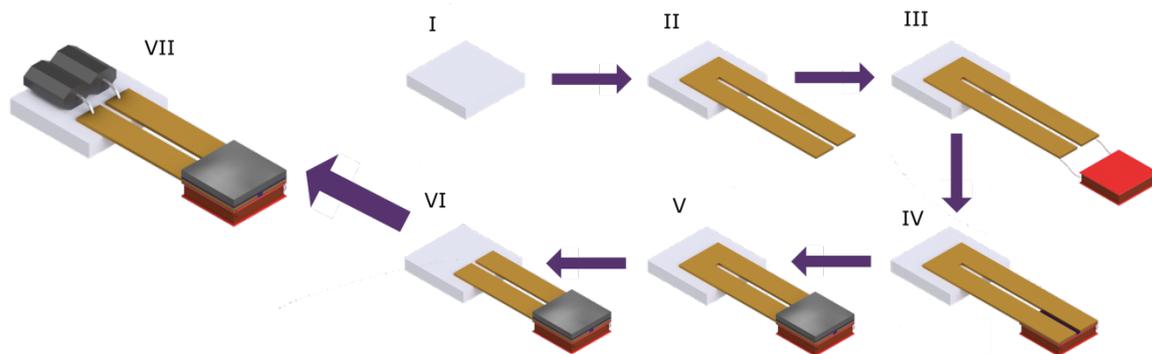


**Figure 93** Fabrication steps involved in the preparation of a TMG with Gadolinium as the TM active material. Adapted image from Joseph et al.[152]

The Gd film of 40 μm thickness is mechanically cut to 2 mm x 2 mm using a mechanical cutter and is fixed on the top side of the cantilever using a non-conductive bonding layer in step V. Step VI comprises severing the excess connected end of the beam after checking its dimensions. A connector bush pin is bonded to the substrate and then electrically bonded to the cantilever end using conductive adhesive in step VII completing the assembly. Electrical resistance is checked to ensure the internal resistance is in the range of 200 Ohm – 220 Ohm, to ensure no additional contact electrical resistance is developed during fabrication.

## 7.1.4. Performance

The cantilever tip shows time-resolved deflections with large strokes and high frequencies when resonant conditions are fulfilled, as seen in **Figure *94*a** and b. It is important to highlight that resonant self-actuation is bound within a narrow range of source temperatures, $T_{source}$. In the case shown in **Figure *94***, at an ambient temperature of 11 °C, resonant self-actuation begins around 40 °C and suddenly ends at 71 °C. The stroke maintains above 1.5 mm throughout this temperature range and reaches a maximum of 2 mm at 60 °C. The frequency, on the other hand, begins at 65 Hz and progressively climbs to 106 Hz at 65 °C before abruptly decreasing at the critical maximum source temperature. **Figure 93**c shows how the stroke and frequency performance connects with the power output. The power output is already 1.3 μW at the lower limit of the heat source temperature of 40 °C, equivalent to a power per footprint of 10.3 μW/cm$^2$ (8.1 mW/cm$^3$ power per Gd volume), which is among the highest values recorded for Gd-based TMGs when the temperature difference between heat source and ambient ($T_{source}$-$T_{amb}$) is only 29 °C. When the temperature of the source is raised, the power output increases gradually at first, then rapidly, peaking at 3 μW at 65 °C, equating to a power per footprint of 23.8 μW/cm$^2$ (18.8 mW/cm$^3$). The load resistance of the electrical circuit was adjusted to its ideal value throughout these experiments.

In these investigations the electrical circuit's load resistance was adjusted to its ideal value of roughly 500 Ohm, which is larger than the internal resistance of the pick-up coil, which is around 220 Ohm. The power output may be enhanced further by raising the load resistance above 220 Ohm, as shown in **Figure A 7** in Appendix, since the reduction in electromagnetic damping leads to an increase in stroke and frequency. The capability of the Gd-based thin film TMG to operate under resonant self-actuation conditions is critical for practical applications, particularly when operating near room temperature. As a result,
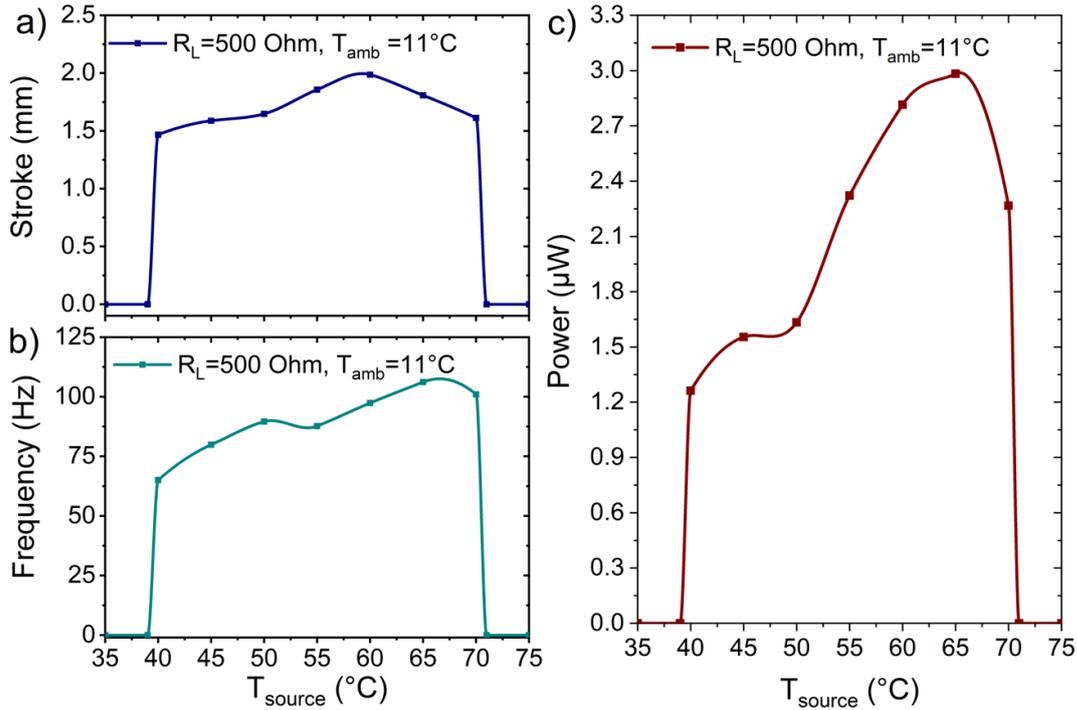
**Figure 94** Mechanical and electrical performance of the Gd-film TMG as a function of heat source temperature ($T_{source}$) at 11 °C ambient temperature: a) Cantilever-front stroke during resonant self-actuation, b) cantilever oscillation frequency, c) electrical power output at a load resistance of 500 Ohm. Data pre-published in Joseph et al.[152]

the ambient temperature range, $T_{amb}$, within which resonant self-actuation occurs for the specified Gd film must be investigated. **Figure 95** depicts the actuation strokes, oscillation frequencies, and electrical power output of the TMG for various $T_{amb}$ values ranging from 9 to 19 °C, while the source temperature, $T_{source}$, varies between 35 and 75 °C. The results show that resonant self-actuation occurs within a narrow range of ambient temperatures, and that the TMG can maintain it up to a $T_{amb}$ of 19 °C, beyond which it becomes unsustainable. At 19 °C, the TMG still generates roughly 1 µW at 50 °C and 1.4 µW at 65 °C $T_{source}$. Furthermore, when $T_{amb}$ increases to 19 °C, the allowed range of source temperatures moves towards higher values. For example, the lower and higher limits of allowed source temperatures shift from 40 °C <$T_{source}$ <70 °C at $T_{amb}$ of 9 to 50 °C <$T_{source}$ <75 °C when $T_{amb}$ is increased by 10 °C. In terms of stroke and frequency, a maximum stroke of roughly 2 mm occurs at $T_{amb}$ of 11 °C, while the stroke gradually decreases with rising $T_{amb}$, reaching a minimum value of 800 µm at $T_{amb}$ of 19 °C. Furthermore, changes in $T_{amb}$ inside the resonance area have no effect on frequency. However, at low source temperatures, the frequencies are low and tend to decline more as $T_{amb}$ increases until resonant self-actuation ceases to occur.
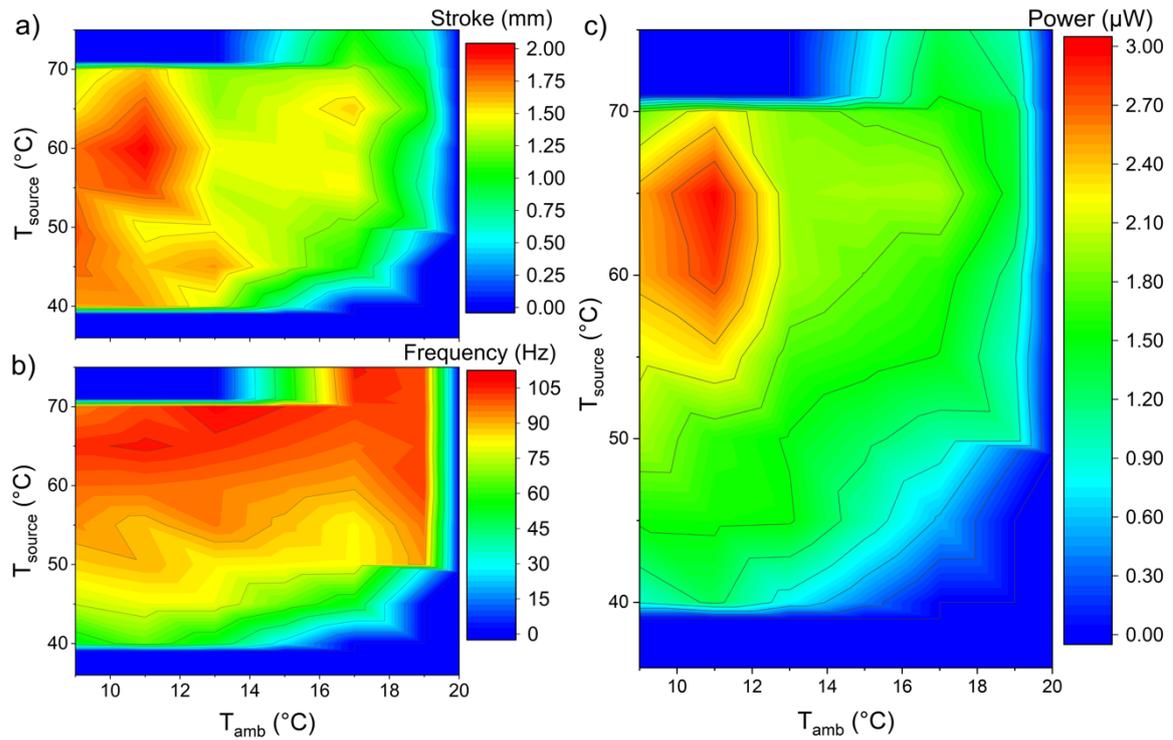
**Figure 95** Effect of ambient temperature on the performance of the device, (a) stroke of cantilever deflection, (b) frequency of cantilever oscillation, (c) power output. Reprinted from Joseph et al.[152]

Furthermore, the TMG's power output has a clear maximum at $T_{amb}$ of 11 °C, which corresponds to the maximum stroke and frequency at source temperatures ranging from 55 to 70 °C. **Figure A 8** to **Figure A *12*** provide further charts summarizing the mechanical and electrical performance of the TMG device as a function of load resistance and heat source temperature at various ambient temperatures. Heat intake and heat dissipation owing to conduction and convection, as well as temperature fluctuations in the Gd film, were simulated using LEM. **Figure 96** depicts an overview of the heat intake and temperature change in Gd film. This demonstrates that the heat intake is proportional to the heat source temperature $T_{source}$. The largest heat absorption occurs at low ambient temperatures, ranging from 70 mW at 40 °C to 97 mW at 70 °C. Heat intake reduces with rising ambient temperature, with minimum values of 40 mW recorded at an ambient temperature of 19 °C. The heat transfer coefficient ($h_f$) at contact between the Gd film and the heat source is the most important parameter determining heat intake. According to LEM simulations, $h_f$ should be as large as feasible. A heat transfer coefficient more than a critical value is necessary, at which steady resonant oscillation with a large stroke and frequency occurs. The needed minimal heat transfer coefficient in the present the case of the TMG with Gd as active

material is determined to be 4000 $Wm^2K^{-1}$, which was consistent with observations in section **5.2.1** and published data.[78,91,149]

The results shown in **Figure 97** show that the simulated heat dissipation from the Gd film to the cantilever by heat conduction through the bonding layer has the same $T_{amb}$ and $T_{source}$ dependency as the heat intake. The largest heat dissipation by heat conduction was recorded at lower ambient temperatures, ranging from 60 mW at Tsource of 40 °C to 79 mW at $T_{source}$ of 70 °C.
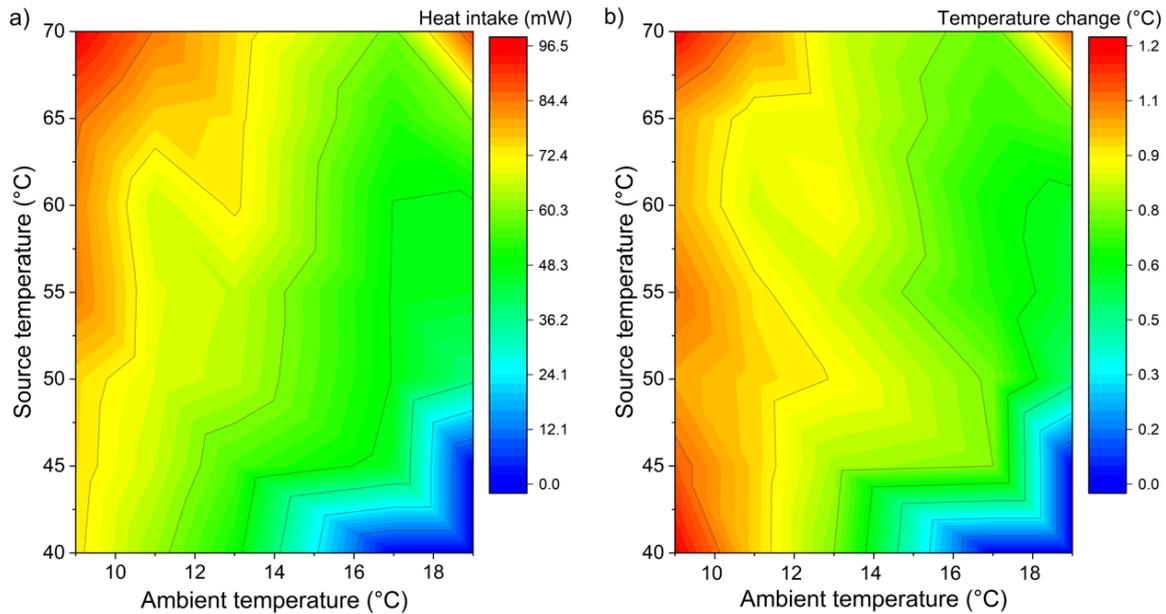


**Figure 96** LEM simulation of the effect of ambient temperature on thermal performance (a) average heat intake into the Gadolinium film on contact, (b) average temperature change of the Gadolinium film. Reprinted from Joseph et al.[152]

It is worth mentioning that heat conduction accounts for the major proportion of heat dissipation when compared to heat convection. As a result, the cantilever is functioning as a critical primary heat sink. Heat convection from the Gd film to the ambient air, on the other hand, correlates with the stroke and frequency of oscillation. The consistence between heat dissipation by conduction and convection and simulated heat intake validate the overall consistency of the data. The bonding layer's thermal resistance ($R_b$) between the Gd film and the cantilever is identified as the essential parameter influencing conductive heat dissipation. As a result, its value must be tailored during the TMG device's design to match the heat intake during contact with the heat source for effective heat transfer.
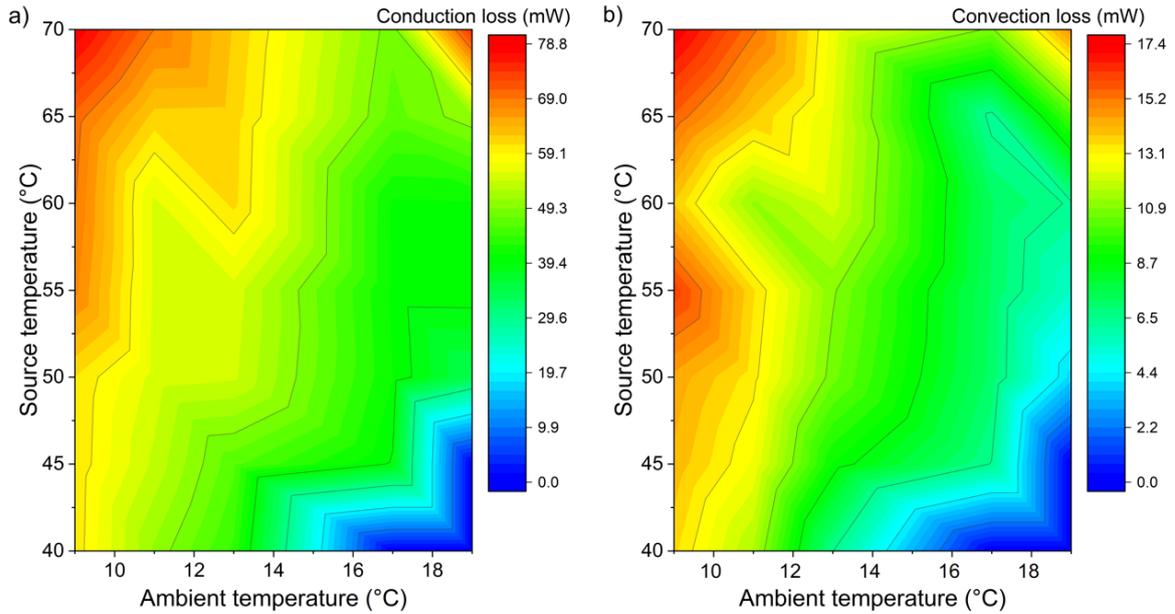
**Figure 97** LEM simulation of the effect of ambient temperature on the loss mechanism (a) conduction losses from the Gadolinium film into the cantilever, (b) convection losses into the ambient air from the Gadolinium film. Reprinted from Joseph et al.[152]

Temperature changes (ΔT) in **Figure 98**b are relatively small due to the high frequency of oscillation and short heat transfer durations, ranging from 1.2 °C at low ambient temperatures of 9 °C to around 0.45 °C at high ambient temperatures of 19 °C. Despite minor ΔT values, the resonant self-actuation conditions are still sustained and the TMG can operate in a steady manner. Aside from the ΔT seen in **Figure 98**b, the cantilever temperature $T_{cant}$ is another important thermal parameter to examine. **Figure 98**a shows the simulated cantilever temperature $T_{cant}$ at various ambient and source temperatures. $T_{cant}$ rises with rising $T_{amb}$ and source temperatures $T_{source}$, with minimum values of 25 °C and highest values of 34 °C. However, increasing $T_{cant}$ causes a decrease in heat dissipation from the Gd layer, limiting heat input. As illustrated in **Figure 96**, a decrease in heat dissipation and an increase in $T_{amb}$ are both connected. As a result, the rise in $T_{cant}$, heat dissipation, and heat intake for rising ambient temperature are all interconnected. These results are interesting because a small temperature change ($\Delta T$), as shown in **Figure 96**b, is sufficient for stable operation in resonant self-actuation mode.

$T_{cant}$ is observed to be 28.4 °C at the optimal power point, which occurs at an ambient temperature of 11 °C and a source temperature of 65 °C. The temperature of the Gd film ($T_{film}$) oscillates roughly between 28.5 and 29.4 °C throughout this time, resulting in a $\Delta T$ of 0.9 °C, as shown in **Figure 98**b. **Figure 98**c depicts the equivalent heat intake in small

pulses lasting roughly 0.5 ms, each of which coincides with the contact between the heated magnet and the Gd layer. Following cooling takes roughly 9 ms. In contrast, with an ambient temperature of 19 °C and a source temperature of 50 °C, the lowest limit of operation is found. The cantilever temperature $T_{cant}$ is roughly the same in this situation, at 28.6 °C, while the temperature of the Gd film Tfilm only shows a $\Delta T$ of only 0.45 °C. According to our observations, this value of $\Delta T$ acts as a lower limit for resonant self-actuation. Below this threshold, the magnetization change $\Delta M$ falls below the critical limit, and the magnetic attraction force can no longer compensate for damping losses.
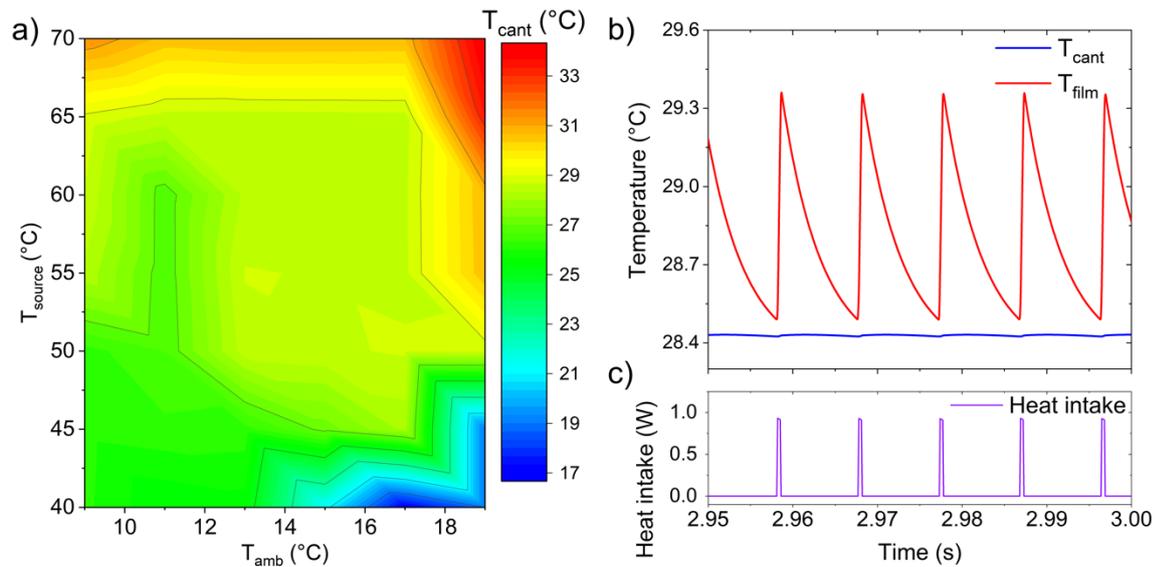


**Figure 98** (a) temperature of the cantilever (b) Temperature profile of the TMG layers. Reprinted from Joseph et al.[152]

## 7.2. TMG with La-Fe-Si-H

To achieve high power output and to develop TMGs that are operating at ambient temperatures above and near room temperature, TM films with $T_c$ near room temperature are required. La-Fe-Si (Lanthanum Iron Silicon) alloy is a very promising alternative with tunable $T_c$ by hydrogenation, and Manganese or Cobalt addition around the region of 27 °C to 50 °C. The advantage of La-Fe-Si alloy is the very large magnetization values and sharp drop at $T_c$. These properties are very important for the presented TMGs to operate near room temperatures with high power output and frequency.

## 7.2.1. Material properties

The magnetization of the La-Fe-Si-H film reaches a maximum value of 171 Am$^2$/kg when the material is ferromagnetic. After the transition at 48 °C, the material still retains a magnetization value of 15 Am$^2$/kg. The high value of 14.6 Am$^2$/kgK for ΔM/ΔT is unprecedented and results in a very sharp drop in magnetization within a few degrees. It can be seen in **Figure 99** that the whole transformation is confined to a few degrees around T$_c$. **Figure 99** shows that the Curie temperature (T$_c$) is slightly shifting to higher temperatures at higher magnetic fields. The average value of T$_c$ is 48.3 °C. The La-Fe-Si-H film is prepared by melt spinning. By arc melting in an environment of Argon (Ar) gas, La$_1$Fe$_{11.6}$Si$_{1.4}$ alloys are
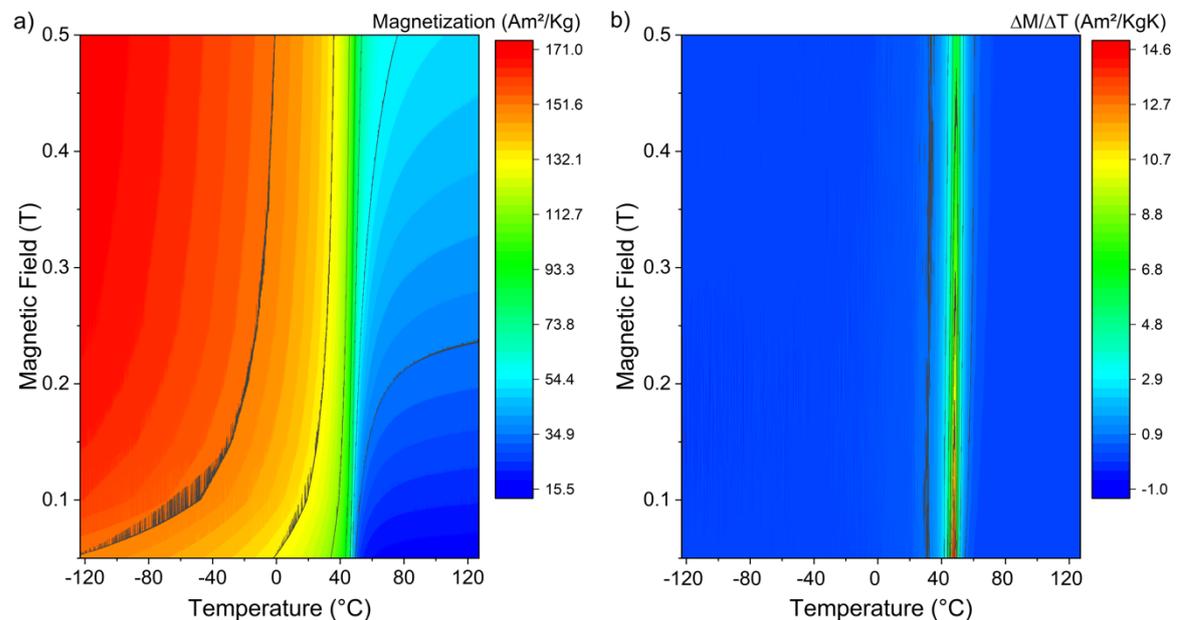


**Figure 99** (a)Magnetization measurement for the La-Fe-Si-H sample, (b) ΔM/ΔT for La-Fe-Si-H sample with respect to changing temperature.

prepared. Then ingot fragments are placed through a nozzle into a quartz tube. High-purity Ar is then injected into the chamber after the air had been evacuated to create a vacuum. By employing a pressure difference, the samples are induction melted and expelled through the nozzle. Cu wheel is spun, and the molten alloy solidifies into a ribbon as it gets in contact with the Cu wheel as mentioned in section **2.7.2**. The as-spun ribbons are subsequently annealed. Further information regarding the preparation of La-Fe-Si samples using melt spinning can be obtained from Gutfleisch et al.[156] Unlike DC RF magnetron

sputtering, the melt spinning technique does not yield a very smooth surface. The surface is rough and further polishing is limited due to the material being very brittle and would break with the slightest pressure on the films. But the advantage is that it is possible to achieve a large thickness in the range of 50 µm which is large compared to DC RF magnetron sputtering of Ni-Mn-Ga films which is limited to 10 µm due to film homogeneity. The samples are then hydrogenated to bring the $T_c$ above room temperature to finish the fabrication of La-Fe- Si-H ribbons.

## 7.2.2. Fabrication

The device fabrication and design of the TMG are similar to the TMG with Ni-Mn-Ga films. The fabrication process involved is described in section **4.4.2**. 50 µm La-Fe-Si samples are cut using an ultra short pulse femtosecond laser to a lateral size of 2 mm x 2 mm. A single cantilever beam is made from a brass sheet with a thickness of 30 µm, which is also structured using the laser. The pick-up coil is fabricated out of 15 µm enamel-coated copper wire with a total of 400 turns around a core of 1 $mm^2$ area. The cantilever is attached to the substrate using a thermally conductive but electrically isolating bonding layer. Both the pick-up coil and La-Fe-Si are attached to the tip of the cantilever, with the former on the bottom side and later on the top side of the cantilever using a non-conductive bonding layer. The ends of the copper wires from the pick-up coil are attached to the connector bush pin which is connected to the substrate. The electrical connection is made using an electrically conductive bonding layer. The surface of the La-Fe-Si-H sample is polished by hand to improve the surface roughness. This step is done last as the material is very brittle, causing it to break if attempted to polish in a free-standing state.

## 7.2.3. Performance

Since the $\Delta M/\Delta T$ value for La-Fe-Si-H film is very large and confined to a few degrees, the resulting device would exhibit very high performance in a small temperature window and would experience performance loss as the conditions are changed. This reduction in tolerance is a consequence of the very small temperature range in which the material transforms, unlike Ni-Mn-Ga films or Gd films both of which exhibit a more gradual change in magnetization over a wide range of temperatures. **Figure 100** shows the performance measurement of the TMG with La-Fe-Si-H as TM film. The large power output is confined to a single $R_L$ of 400 Ohm. At 90 °C source temperature ($T_{source}$) the device is capable of generating 4.2 µW. The TMG can sustain the resonant self-actuation from a minimum

144

$T_{source}$ of 70 °C which is limited by the $T_c$ of the material. At a $T_{source}$ of 70 °C, the maximum power output of the TMG is around 2.2 µW, which increases as the $T_{source}$ is increased. But after increasing the $T_{source}$ beyond 90 °C, the performance of the device reduces. The device loses resonant self-actuation when the TMG is operated with a $T_{source}$ of more than
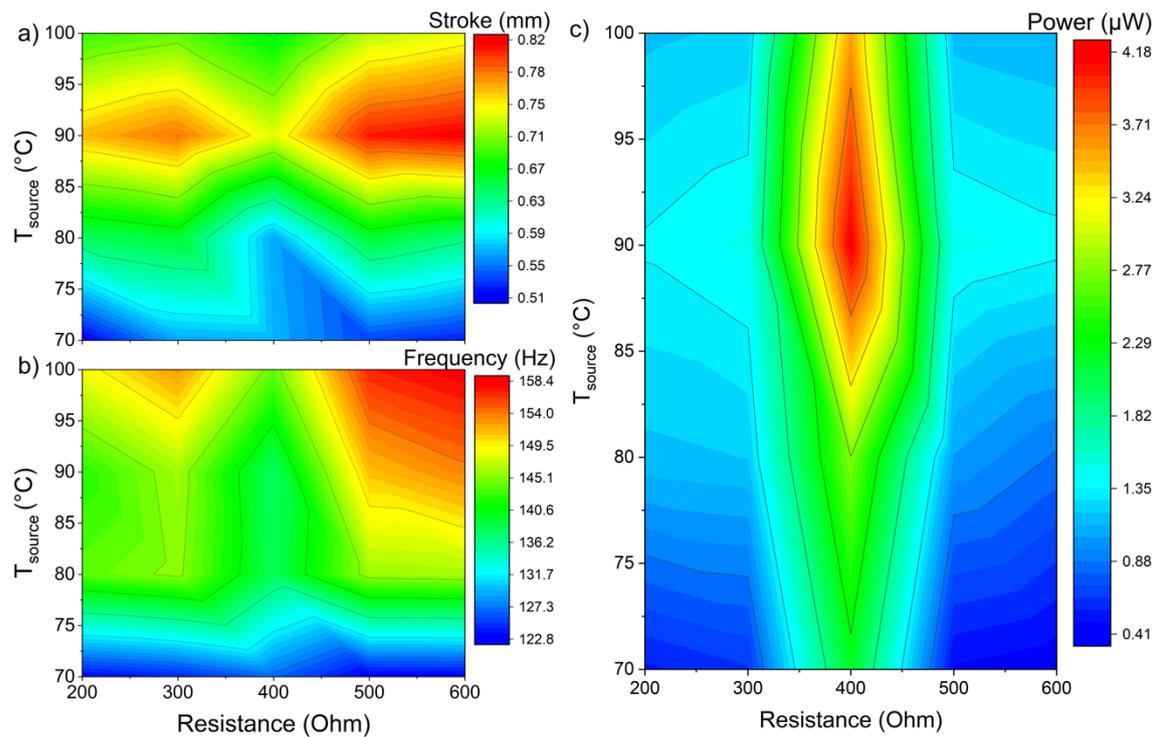


**Figure 100** performance of the TMG with La-Fe-Si-H as TM film, (a) stroke of the deflection of the cantilever tip during resonant self-actuation, (b) frequency of oscillation of the cantilever, (c) power output from the pick-up coil

100 °C. LEM simulations are used to determine the heat intake in the La-Fe-Si-H film on contact. **Figure 101**a shows the heat intake values corresponding to the value of the $T_{source}$. It can be seen that the average value of heat intake is much lower than that of the TMG with Gd as TM film and much lower than that of the TMG with Ni-Mn-Ga as Tm film. **Figure 101**b illustrates that the TMG is capable of sustaining resonant self-actuation even though the ΔT within the material is below 1 °C. The ΔT is 0.22 °C at a $T_{source}$ of 70 °C and increases to 0.5 °C at a $T_{source}$ of 100 °C. The TMG is able to operate in resonant self-actuation with such low ΔT in the material due to the very large ΔM/ΔT. **Figure 102** shows the LEM simulation values of heat dissipation from the La-Fe-Si-H film. This shows that conduction is the main form of dissipation and the trend of the change in conduction losses is similar to the change in heat intake. The change in convection loss on the other hand is
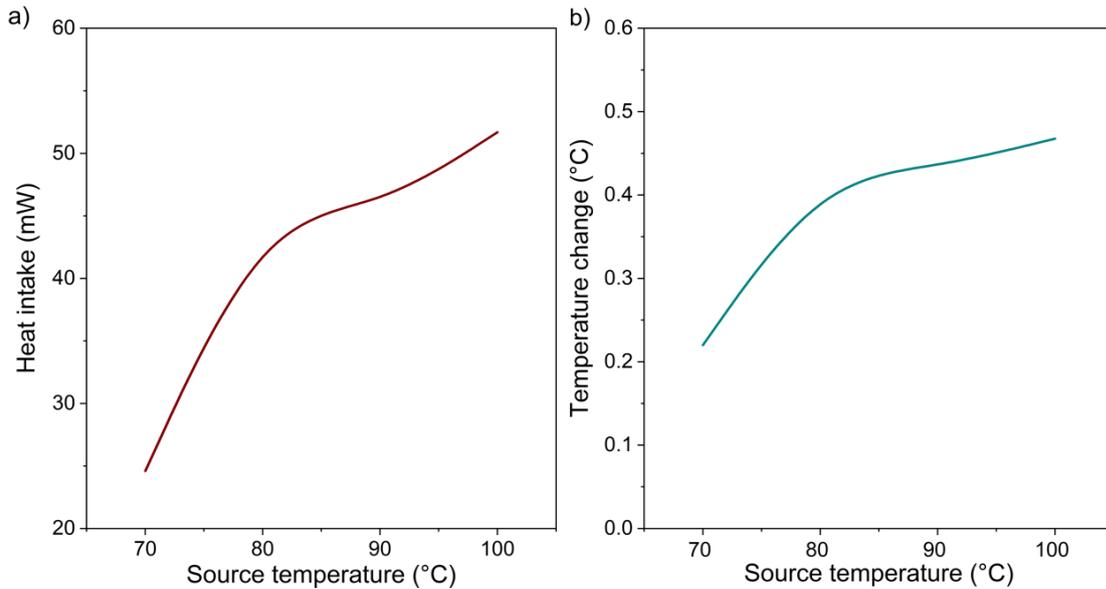
**Figure 101** LEM simulation of the thermal processes, (a) heat intake into the La-Fe-Si film, (b) temperature change within the La-Fe-Si film

slightly different from the conduction as this value is also dependent on the $T_{amb}$, frequency of operation, and the convective heat transfer coefficient. The TMG is operating at a maximum frequency of 137 Hz even with the low contact heat transfer coefficient ($h_f$), suggesting that the performance of the TMG could be increased many folds and the minimum $T_{source}$ could also be reduced further by increasing the $h_f$ between the magnet and the TM film, which could be done by minimizing the surface roughness of the TM film.
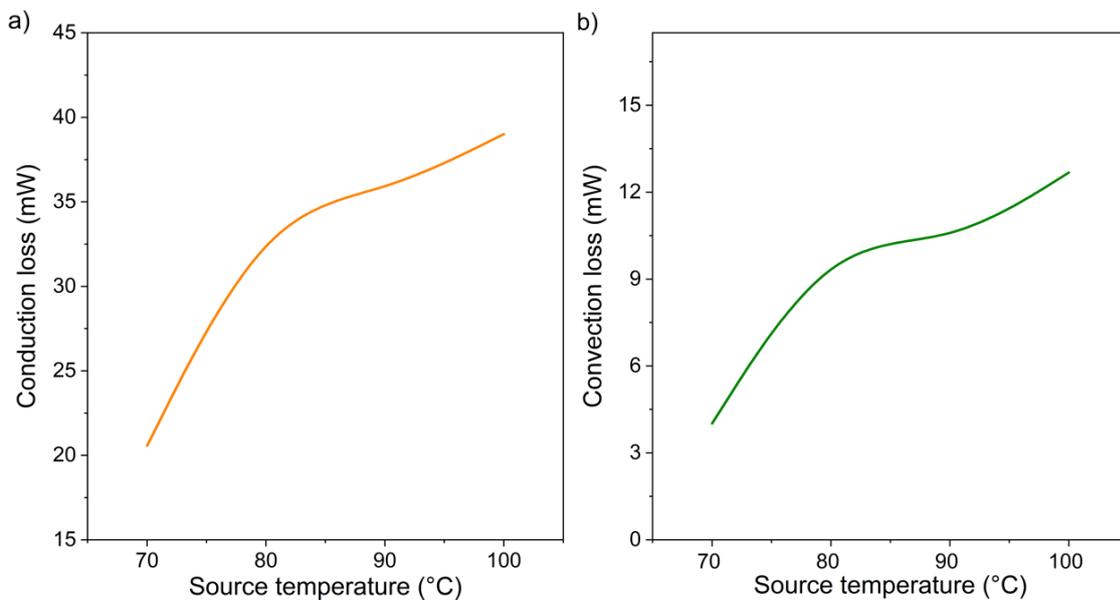


**Figure 102** LEM simulation of thermal losses, (a) conduction losses from the La-Fe-Si film to the cantilever through the $R_b$, (b) convection losses from the film directly to the ambient.

146

## 7.3. Discussion

Because of its capacity to function in the resonant self-actuation mode, which allows for high frequency and stroke, film-based thermomagnetic generators (TMGs) are capable of efficient conversion of thermal energy into electrical energy. However, the useful range of heat source temperatures for these devices is restricted by the thermomagnetic material's ferromagnetic to paramagnetic transition temperature (Tc). For example, a Ni-Mn-Ga film with a $T_c$ of 98 °C at 0.5 T can only function between 100 and 170 °C. To recover low-grade waste heat, appropriate thermomagnetic films with $T_c$ close to room temperature must be designed and applied. Gd, which has a $T_c$ of 20 °C, is one interesting candidate material for this purpose.

The thermo-magneto-mechanical performance of a Gd-film TMG at room temperature is investigated in this work as the heat source temperature is gradually reduced from 75 °C to 35 °C to assess its potential for low-grade waste heat recovery. The LEM simulation model of the TMG is reported in section **4.2** and presented also by Joseph et al.[128] to describe the TMG performance. This entails regulating the resonance frequency, improving the heat input, matching heat dissipation, and determining the best performance parameters for optimum power and efficiency during resonant self-actuation at the highest feasible ambient temperature. While film-based TMG devices exhibit self-adapting performance, research on a Gd-film TMG discloses a severely limited range of ambient and source temperatures necessary for resonant self-actuation.

**Table 7** Modeling parameters for the LEM simulation of the TMG with Gadolinium. Data pre-published in Joseph et al.[152]

| Mechanical parameter | Unit | Value | References |
|---|---|---|---|
| Pick-up coil mass | Kg | $6 \times 10^{-6}$ | This work |
| Cantilever density | $Kg/m^3$ | 8500 | [143] |
| Gadolinium density | $Kg/m^3$ | 7900 | [154] |
| Bonding layer density | $Kg/m^3$ | 920 | [145] |
| Structural and air damping | Ns/m | $2.8 \times 10^{-5}$ | This work |
| Impact damping | Ns/m | 0.1 | This work |

| | | | |
|---|---|---|---|
| Contact stiffness | N/m | 10000 | This work |
| Young's modulus | Pa | $1 \times 10^{11}$ | [146] |
| Cantilever length | m | 0.0045 | This work |
| Cantilever width | m | 0.0009 (each) | This work |
| Cantilever slit (gap between beams) | m | 0.0002 | This work |
| Cantilever thickness | m | 0.000025 | This work |
| | | | |
| **Electrical & Magnetic Parameters** | **Unit** | **Value** | **References** |
| Remanent magnetic field | T | 1.07 | This work |
| Number of turns | - | 400 | This work |
| Area of pick-up coil | $m^2$ | $2.81 \times 10^{-6}$ | This work |
| Pick-up coil internal resistance | Ω | 250 | This work |
| Load resistance ($R_L$) | Ω | 500 | This work |
| | | | |
| **Thermal Parameters** | **Unit** | **Value** | **References** |
| Cantilever thermal conductivity | W/mK | 109 | [147] |
| Gadolinium thermal conductivity | W/mK | 11 | [157] |
| Bonding layer thermal conductivity | W/mK | 0.225 | [145] |
| Cantilever heat capacity | J/kgK | 400 | [143] |
| Gadolinium heat capacity | J/kgK | 300 | [158] |
| Bonding layer heat capacity | J/kgK | 2100 | [145] |
| Contact heat transfer coefficient | $W/m^2K$ | 4600-6600 | This work |
| Convective heat transfer coefficient | $W/m^2K$ | 40-140 | This work |

The highest limit of ambient temperature ($T_{amb}$) corresponds to the temperature at which $\Delta M/\Delta T$ is maximum (19 °C at 0.5 T), beyond which resonant self-actuation is no longer sustainable, regardless of heat source temperature ($T_{source}$). TMG devices, at Tamb = 19 °C, can still generate 1 µW at minimum and maximum heat source temperatures of 50 and 75 °C, respectively. At lower ambient temperatures, such as $T_{amb}$ = 11 °C, resonant self-actuation quickly kicks in, yielding a power output of 1.3 µW at lower heat source temperatures, with $T_{source}$ = 40 °C. At just 29 °C temperature difference between heat source and ambient, the associated relative power per footprint of 10.3 µW/cm$^2$ (8.1 mW/cm$^3$ power per Gd volume) is among the highest values found for Gd-based TMGs. The resonant self-actuation of the TMG is lost abruptly above 71 °C. The efficiency of the TMG, given by the ratio of electrical output power and thermal power intake, is 0.0021 % at $T_{source}$ = 40 °C, while the corresponding relative efficiency, given by the ratio of absolute and Carnot efficiency, is estimated to be 0.045 %. Thereby, the cantilever temperature is assumed to be the heat sink temperature, as it accounts for 80 % of heat dissipation. The efficiency of the related Gd film material is 0.02 %, as evaluated by the ratio of output magnetic energy to thermal input energy, where output magnetic energy is obtained from the thermomagnetic cycle of the Gd film illustrated in **Figure A *13*** (Appendix). The notion of resonant self-actuation does not rely on utilizing the whole temperature range of the magnetic transition for energy conversion, but rather on generating the highest electrical power output with the least amount of temperature change of the film ($T_{film}$), rather than optimum.

The La-Fe-Si-H boasts a much higher value for the magnetization in its ferromagnetic state and also shows a very sharp drop in magnetization with a very high value of 14.6 Am$^2$/kgK for the ΔM/ΔT. This sharp drop comes with advantages like high frequency of operation due to the very low ΔT required in the material for achieving the required magnetization to release the cantilever tip from the magnet surface. The fabrication process of melt spinning does present a set of challenges for achieving resonant self-actuation with the prepared La-Fe-Si-H samples. The surface roughness results in a very low thermal contact between the magnet and the La-Fe-Si film. The minimum $T_{source}$ is not only limited by the $T_c$ of the material, but also by the very low $h_f$ between the TM film and the magnet. Even though the magnet is polished to a mirror finish, the TM film had a very rough surface due to the fabrication process (melt spinning) The roughness is large enough to cause a major reduction in $h_f$. This is confirmed by LEM simulations by matching the performance of the TMG suggesting a $h_f$ value between 2800 and 3200 W/m$^2$K. Thus, even though the device does possess the potential to operate at higher frequencies (over 200 Hz, estimated from

the natural frequency of the assembly), the device operation is limited to a maximum frequency of 137 Hz due to the heat transfer times required to intake required amount of heat at contact. The material also has a very low thermal conductivity of 8 W/mK which further restricts the heat dissipation from the material.

**Table 8** Modeling parameters for the TMG with La-Fe-Si-H as the active TM film

| Mechanical parameter | Unit | Value | References |
|---|---|---|---|
| Pick-up coil mass | Kg | $6 \times 10^{-6}$ | This work |
| Cantilever density | $Kg/m^3$ | 8500 | [143] |
| La-Fe-Si-H density | $Kg/m^3$ | 7245 | [159] |
| Bonding layer density | $Kg/m^3$ | 920 | [145] |
| Structural and air damping | Ns/m | $2.8 \times 10^{-5}$ | This work |
| Impact damping | Ns/m | 0.1 | This work |
| Contact stiffness | N/m | 10000 | This work |
| Young's modulus | Pa | $1 \times 10^{11}$ | [146] |
| Cantilever length | m | 0.0053 | This work |
| Cantilever width | m | 0.0009 (each) | This work |
| Cantilever slit (gap between beams) | m | 0.0002 | This work |
| Cantilever thickness | m | 0.000025 | This work |
| | | | |
| **Electrical & Magnetic Parameters** | **Unit** | **Value** | **References** |
| Remanent magnetic field | T | 1.07 | This work |
| Number of turns | - | 400 | This work |
| Area of pick-up coil | $m^2$ | $2.81 \times 10^{-6}$ | This work |
| Pick-up coil internal resistance | Ω | 250 | This work |
| Load resistance ($R_L$) | Ω | 500 | This work |
| | | | |

| Thermal Parameters | Unit | Value | References |
|---|---|---|---|
| Cantilever thermal conductivity | W/mK | 109 | [147] |
| La-Fe-Si thermal conductivity | W/mK | 8 | [160] |
| Bonding layer thermal conductivity | W/mK | 0.225 | [145] |
| Cantilever heat capacity | J/kgK | 400 | [143] |
| La-Fe-Si heat capacity | J/kgK | 600 | [161] |
| Bonding layer heat capacity | J/kgK | 2100 | [145] |
| Contact heat transfer coefficient | W/m$^2$K | 2800-3200 | This work |
| Convective heat transfer coefficient | W/m$^2$K | 40-140 | This work |

After several design optimizations including the $R_b$, cantilever stiffness, and polishing of the surface of the La-Fe-Si-H film, resonant self-actuation is achieved. In resonant self-actuation, the TMG is able to generate a maximum power output of 4.2 µW at a $T_{source}$ of 90 °C. Since the temperature span in which the material transformation occurs is curbed to a few degrees, the performance of the device also shows similar trends. The device exhibits a lack of tolerance to the ambient conditions, unlike the TMG with Gd film. Even while changing the $R_L$, it has a major effect on the electromagnetic damping at the cantilever tip causing the performance to have a clear peak at 400 Ohm. When the resistance is changed from this value, the performance of the TMG reduces drastically. This is also compounded by the lower field gradient experienced by the pick-up coil.

In most TMGs the surface of the TMG active material is placed on the surface of the magnet surface in such a way that the pick-up coil experiences the higher field gradient at the edges of the magnets. But in this case, due to the lower contact $h_f$, the TMG has to be placed close to the center of the magnet causing a large reduction in the magnetic field gradient experienced by the pick-up coil during actuation even though the effect on the actuation itself is not much. This effect can be observed in **Figure 100**, where the frequency and stroke are reduced at 400 Ohm even though it is the point at which the power output is also the maximum. This is caused due to the additional current through the pick-up coil at this point. At other $R_L$s the conditions are different, and the device fails to achieve the same level of magnetic field gradient throughout the actuation cycle. In other TMGs, the tolerance of the device to adjust itself to the changing ambient conditions help the

device to avoid such a performance peak and to form a more gradual increase or decrease in performance.

It is also unprecedented that resonant self-actuation is achieved with just a ΔT of 0.22 °C. This is observed at a $T_{source}$ of 70 °C. Since currently, the surface roughness is still large to have a major impact on the $h_f$, it can be assumed that the $T_{source}$ values including maximum, minimum, and the $T_{source}$ at which maximum output occurs would shift towards lower temperatures as the $h_f$ is improved. This can be achieved either by polishing the surface further or to coat the surface with a material with high thermal conductivity to even out the surface imperfections. The heat intake into the La-Fe-Si-H film at the cantilever tip is low when compared to the TMG with Ni-Mn-Ga film.

Adding manganese to La-Fe-Si-H has shown great potential in reducing the $T_c$ of the material which is also another way in which the minimum operating temperature could be reduced further and brought closer to the room temperature.[162] **Figure 18** shows an example of a La-Fe-Si-Mn-H sample with its magnetization dropping abruptly at around 25 °C. This shows further potential to bring the TMG operation temperature closer to room temperature and crossing the point of 37 °C for the $T_{source}$. This would result in the development of miniature TMGs operating with body heat, which is of special interest for miniature scale medical applications.

**Table 9** TMG parameters for devices considered for experiments. Part of data pre-published in Joseph et al.[152]

| TMG based on Gadolinium | | |
|---|---|---|
| **Parameter** | **Unit** | **Value** |
| Gadolinium width | mm | 2 |
| Gadolinium length | mm | 2 |
| Gadolinium thickness | µm | 40 |
| Cu-Zn cantilever width (each) | mm | 0.9 |
| Cu-Zn cantilever length | mm | 5.3 |
| Cu-Zn cantilever thickness | µm | 30 |
| Number of turns in pick-up coil | - | 400 |

| TMG based on La-Fe-Si | | |
|---|---|---|
| **Parameter** | **Unit** | **Value** |
| La-Fe-Si-H width | mm | 2 |
| La-Fe-Si-H length | mm | 2 |
| La-Fe-Si-H thickness | µm | 50 |
| Cu-Zn cantilever width (each) | mm | 0.9 |
| Cu-Zn cantilever length | mm | 4.5 |
| Cu-Zn cantilever thickness | µm | 30 |
| Number of turns in pick-up coil | - | 400 |

# 8.  Discussion

This section presents a detailed evaluation of the TMG performances presented in Sections **4-7** and the influences of all design parameters. The TMG designs will be compared with respect to the target objectives, i.e. maximum power output, optimum efficiency and adjustment of the range of source temperature.

## 8.1.  Discussion of results

### 8.1.1.  Lumped element model

The presented multi-physical lumped element model (LEM) of the cantilever-based TMGs has been validated with experimental results. Thus, it is used as a powerful tool to design and optimize the TMG performances. Identifying the different physical domains of the TMG is the first step in preparing a LEM. The presented TMG is identified to have four physical domains involved, namely (1) magnetic, (2) mechanical, (3) thermal and electrical domains. Each domain is modeled by taking into consideration its effect on other domains. Most importantly the LEM simulation is the key in ensuring that the design of the TMG is compatible with resonant self-actuation before the device is fabricated.

(1) Magnetic domain: Modeling of magnetic properties of the permanent magnet used in the TMG is presented. The analytical model is capable of calculating generated magnetic field and magnetic field gradient of the permanent magnet, based on the dimensions of the magnet and the remanent magnetic field (dependent on the material composition of the permanent magnet). The magnetization of the material is temperature dependent, and the values are directly taken as a lookup table prepared from the experimental measurement of the magnetization.

(2) Mechanical domain: The mechanical oscillations of the cantilever beam with tip mass are modeled by solving the partial differential equations (PDEs) for oscillations in z direction corresponding to the 1-Dimensional assumption of the spring

155

damper system. The magnetization of the active TM film, inertia, stiffness of the cantilever, and magnetic field gradient determines the effective force at the cantilever tip, which would either cause the tip to bend towards the magnet or away from it depending on its direction. This effective force is modeled by the LEM by solving the thermal, magnetic, electrical, and mechanical sections simultaneously. Since each section of the model is dependent on the outputs of other sections of the model, the initial point is taken as the position of the cantilever at zero actuation with no reset force present.

(3) Thermal domain: The thermal section of the model shows the most sensitivity toward performance optimization and it is observed that a minute change in parameters in the thermal section would result in a large deviation in performance. The values like heat transfer coefficient ($h_f$) and convective heat transfer coefficients are assumed initially to design the basic TMG. Once the design is completed, the prototype is fabricated and experimentally tested. The assumed values are readjusted to match the experimental values to represent the TMG properly.

(4) Electrical domain: The electrical section of the model uses Faraday law of induction to determine the electrical power conversion in the pick-up coil. The mechanical oscillations of the cantilever tip correspondingly results in a varying magnetic field gradient in the pick-up coil generating a voltage. The generated voltage is converted to current accordingly based on the internal resistance of the TMG and the load resistance connected. The electromagnetic damping force resulting from the conversion of oscillations to voltage is also modelled in this section.

LEM simulation allows to interpret the results of the experiments in a meaningful way and to understand the thermal and magnetic processes within the TMG, both of which are difficult to measure. The $\Delta T$ of the active TM film and the temperature of the cantilever are crucial in achieving resonant self-actuation and LEM simulation gives a detailed conception of these processes. In the presented example of the capability of LEM, a TMG based on 10 μm Ni-Mn-Ga film as active TM film is analyzed in detail. The experimental analysis of the device is also completed and presented to validate the model.

## 8.1.2. Impact of parameters on the performance

Many parameters influence the design and performance of the TMG. These parameters could be broadly classified into (1) TM film parameters, (2) cantilever material parameters, and (3) geometrical and operation parameters. The TM film parameters depend on the composition of the material and heat treatment conditions.

### (1) TM film parameters

Following are the material parameters that affect the design and performance of the TMG:

- Magnetization ($M$)
- Change in magnetization with temperature change ($\Delta M / \Delta T$)
- Curie temperature ($T_c$)
- Surface roughness
- Thermal conductivity
- Thermal capacity

Magnetization: The value of magnetization determines the maximum possible stiffness of the cantilever as in the cold start case when the cantilever is at its initial position, the magnetic force must be strong enough to bend the cantilever tip to the magnet surface. A high value of the magnetization would enable the design of the TMG with high frequency provided the thermal cycle is also capable of high frequency operation.

$\Delta M / \Delta T$: The value of $\Delta M / \Delta T$ affects the range of $T_{source}$ values in which the device is able to sustain resonant self-actuation and also the $\Delta T$ required for achieving self-actuation. A high value of $\Delta M / \Delta T$ would result in very high frequency operation as the heat intake and temperature required for resonant self-actuation is low. A second-order transformation without hysteresis, high value of magnetization, and high value of $\Delta M / \Delta T$ would be the ideal characteristics of the material for the TMG as this combination would result in a very high operation frequency and high power output.

Curie temperature: $T_c$ in this work is taken as the temperature at which the material exhibits the maximum $\Delta M / \Delta T$. This value determines the operation temperature of the TMG in which the device would be able to sustain resonant self-actuation. TM film material with higher $T_c$ would require higher $T_{source}$ to achieve self-actuation and consequently even higher temperature to achieve resonant self-actuation. Material with closer to room temperature (slightly above) values of $T_c$ would enable the development of the TMG with near room temperature operation.

157

Surface roughness: Section **2.5.4** shows how the surface roughness of the contact surfaces affects value of $h_f$. Surfaces with higher surface roughness would result in a lower value of $h_f$. This would mean a longer heat transfer time to achieve the same amount of heat flow. For the presented design of the TMGs, it is beneficial to have a smooth surface with a very low surface roughness to achieve high values of $h_f$.

Thermal conductivity and thermal capacity: Thermal conductivity and thermal capacity of the TM film would affect the heat intake and the heat dissipation capability of the material. Material with higher thermal conductivity tends to have a lower value of thermal capacity and vice versa. The higher thermal conductivity and lower thermal capacity would result in a large $\Delta T$ for a small amount of heat flow. The heat flow required to achieve the same temperature would increase with an increase in the thermal capacity of the material.

### (2) Cantilever material parameters

The following material parameters are the ones affecting the design and performance of the TMG:

- Young's modulus
- Thermal conductivity
- Thermal capacity
- Corrosion resistance

Young's modulus: The young's modulus affects the stiffness of the material. The higher the Young's modulus, the higher would be the stiffness for the same dimensions of the cantilever beam.

Thermal conductivity & thermal capacity: The thermal conductivity of the cantilever material affects the thermal dissipation of the film. The convective heat transfer from the cantilever to the ambient air and the thermal conduction from the film to the cantilever is both affected by the thermal conductivity of the cantilever material. The higher thermal capacity of the material is also desirable, and this would result in a stable temperature in the cantilever during operation without much thermal cycling.

Corrosion resistance: The material chosen for the cantilever should have high corrosion resistance. This is important for the durability of the TMGs and also to maintain the performance over time.

### (3) Geometrical and operation parameters

Following are the important design parameters that have major effects on the performance of the TMG and its ability to achieve resonant self-actuation:

- Magnetic field
- Magnetic field gradient
- Ambient temperature
- Heat source temperature
- Stiffness of the cantilever
- Contact heat transfer coefficient
- Bonding layer thermal resistance
- Pick-up coil turns
- Load resistance

Magnetic field: The magnetic field is affected by the dimension of the magnet and the material of the permanent magnet. The magnetic field at the surface increase as the aspect ratio (ratio between the height along the magnet along easy axis and lateral cross-sectional area) increases. But this would also result in a lower magnetic field at a distance from the magnet surface. A higher magnetic field is desirable both at the surface (during operation) and at a distance (for the cold start of the device) for a TMG with cantilever based design.

Magnetic field gradient: Magnetic field gradient at the surface increases with the increased aspect ratio of the magnet dimensions. The magnetic field gradient is slightly lower at a distance for a higher aspect ratio. A higher magnetic field gradient is desirable to have a higher magnetic force and higher power output from the pick-up coil.

Ambient temperature ($T_{amb}$): Ambient air is the final sink into which all the heat is dissipated. For a TMG, the heat sink of the device is the cantilever. Which finally dissipates it to the ambient air. Thus, the temperature of the ambient air is an important factor that determines if the device is capable of sustaining resonant self-actuation. Which requires high rates of heat intake and heat dissipation to achieve the minimum $\Delta T$ in the material.

Heat source temperature ($T_{source}$): This forms a major part of the TMG design, as the TMG design could be adjusted to operate at different $T_{source}$ values. But the minimum value of $T_{source}$ is limited by the $T_c$ of the TM film. The TMG does tolerate a range of heat source temperatures at which it will exhibit resonant self-actuation. The heat source temperature

159

affects the performance of the TMG and usually has an optimum $T_{source}$ at which the power output is maximum which is unique for the TMG depending on its other parameters.

Stiffness of the cantilever: Maximum stiffness of the cantilever is limited by the magnetic force at the initial state of the cantilever position. The stiffness is given by both the material property Young's modulus and the geometric properties like length, width and thickness of the cantilever. But the designed stiffness would be tailored to match the natural frequency of the beam with the thermal cycling frequency of operation. Thus, the final frequency is also affected by the thermal processes within the TMG.

Contact heat transfer coefficient ($h_f$): The heat flow at contact is the driving force of the TMG operation. This heat flow is governed by the $h_f$ at contact, which needs to be maximized to achieve optimum performance. Achieving a smooth surface at the contact is crucial to have large values for the $h_f$. A critical minimal value of $h_f$ of 8 kW/m$^2$K is observed for a TMG with 10 μm Ni-Mn-Ga film below which resonant actuation fails.

Bonding layer thermal resistance ($R_b$): The value $R_b$ between the TM film and the cantilever beam is important for all TMGs. A critical minimal value of Rb of 5 K/W is observed for a TMG with 10 μm Ni-Mn-Ga film. Below this value, the cantilever and the TM film becomes thermally coupled resulting in failure to achieve resonant self-actuation. Increasing the thermal resistance results in a very sharp increase in the power output. But power output saturates when $R_b$ is increased over 10 K/W. Showing only marginal increase when the $R_b$ is increased further.

Pick-up coil turns: The number of turns in the pick-up coil has a direct impact on the amount of energy converted from mechanical oscillation to electrical energy. The electromagnetic damping is caused by energy conversion from mechanical energy into electrical energy. Thus, it is desirable to have maximum electromagnetic damping to maximize energy conversion. But too much electromagnetic damping would result in the device falling out of resonant self-actuation. Hence the number of turns of the pick-up coil needs to be optimized depending on the configuration of the TMG. A TMG with a material having a large magnetization value would possess large stiffness for the cantilever which could tolerate a higher number of pick-up coil turns as the device possesses higher magnetic force and reset force.

Load resistance ($R_L$): The $R_L$ connected to the TMG would limit the current through the pick-up coil. Thus, higher $R_L$ at the ends of the pick-up coil would result in lower electromagnetic damping due to the lower current flowing through the pick-up coil. Increasing the

frequency and thus resulting in higher power output. The transfer efficiency is maximum when the $R_L$ is matched to the internal resistance of the pick-up coil. Thus, the transfer efficiency is reduced as the $R_L$ value is moving further away from the value of the internal resistance. But as the $R_L$ is increased further, the transfer efficiency keeps on decreasing and after a point, it would result in a reduction in power output even when the frequency and stroke are increasing. This causes the system to have an optimum $R_L$ at which the TMG would generate the maximum output. This value also depends on the design and configuration of the TMG.

The validated LEM model is utilized to perform the parameter study to understand the effect of different design parameters on the performance of the TMG including the thermal processes within the TMG. It is observed that the critical minimal value of $\Delta T$ of the active TM layer determines the limit below which the TMG would lose its resonant self-actuation. This value is affected by both heat intake and heat. The heat intake is controlled by the temperature difference between the magnet and the TM film and the value of $h_f$. But the $h_f$ is dependent on the contact area which is governed by the surface roughness of the contact surfaces. The magnet in each case of the TMG is polished to a mirror finish to achieve maximum possible contact. The sputtered films have low surface roughness. Thus, the combination of these films and the polished magnet surface would result in a large portion of the film being in contact and hence a large value of $h_f$. The melt spun film on the other hand would have a rough surface, these films need to be polished to reduce the surface roughness so that at least reasonable values of $h_f$ can be achieved between the magnet surface and the TM film on contact.

## 8.1.3. Upscaling of TMG

The method to increase power focuses on the tuning of the magnetic attraction force, mechanical reset force, and heat transfer dynamics in order to sustain resonant self-actuation. As long as resonance conditions are maintained, the mechanical energy of oscillatory motion increases with increasing mass and frequency, sustaining magnetic cycles with rising variations in magnetic energy. This increase in mechanical energy is what leads to the realized increase in power. The results demonstrate that the heat transfer kinetics for a specific ferromagnetic material and magnetic field gradient eventually limit the upscaling technique.

According to LEM simulations, conductive heat losses serve as the primary source of heat dissipation, and heat input grows as film thickness increases. As a result, the corresponding fraction of average retained input heating power increases from about 80 % to 94 % with increasing film thickness from 10 μm to 40 μm, respectively. These fractions display the same thickness dependence at lower $T_{source}$ values and only slightly deviate from one another. This study shows that a sizeable fraction of heat is maintained in the SMA film stack and contributes to the $\Delta T$. The $\Delta T$ of the film stack during oscillation, however, diminishes as the film thickness rises, which has two significant effects. First, as $\Delta T$ reduces, the effectiveness of increasing film thickness decreases. Second, the continued scaling up of film thickness is severely limited by the declining $\Delta T$ due to the increased thermal mass of the stack.

The absolute power of a single TMG is insufficient for most applications. Therefore, a parallel architecture of many TMGs is required to boost the power level for specific uses. Cross-coupling, which could hinder resonant self-actuation, is a concern when many TMGs are placed next to one another with a small separation between them. At lower temperatures, when the frequency, stroke, and power output are already low, the separation does not appear to have any effect when two devices with near tolerances are run in parallel under the same magnet. Even at an extremely close spacing of 300 μm, the TMGs don't seem to have any coupling effects. At higher $T_{source}$ values, thermal cross-coupling effects are observed between devices when the separation between the devices is reduced below 1 mm. Correlation in performance between devices is observed for some of the instances suggesting it is possible for devices to develop a synchronization in their operation where its performance is dependent on the neighboring device due to thermal coupling.

### 8.1.4. Expanding the range of operation temperature

TMGs with Ni-Mn-Ga has shown the potential of the concept of resonant self-actuation but this is limited to temperatures well above 100 °C due to the $T_c$ of the material. Thus, in order to expand the range of heat source temperature under which resonant self-actuation could be achieved, Gadolinium film and La-Fe-Si based alloys are used. Dzekan et al.[163,164] gives an overview of novel thermomagnetic materials for power generation. Section **5.2.5** has presented the effect of $T_c$ on the minimum heat source temperature.

Using the Gd film under optimum conditions, a large power output of 3 μW resulting in a power per footprint of 23.8 μW/cm$^2$ was achieved at a $T_{source}$ of 65 °C and $T_{amb}$ of 11 °C.

This opens up a wide variety of applications as the temperature required for achieving resonant self-actuation is well below the boiling point of water. But this investigation revealed strict boundaries of temperatures for both the ambient ($T_{amb}$) and heat source ($T_{source}$) where the TMG could maintain resonant self-actuation. Since the $T_c$ of Gd film was 20 °C, maximum $T_{amb}$ was limited to 19 °C above which the TMG stops operation. Even though, the TMG is able to sustain resonant self-actuation at a $T_{source}$ of 40 °C, the minimum value of $T_{source}$ increases to 50 °C as the $T_{amb}$ is increased to 19 °C.But even at the maximum $T_{amb}$ of 19 °C and minimum $T_{source}$ of 50 °C, the TMG is capable of generating 1 µW resulting in a power per footprint of 8.7 µW/cm$^2$. While under optimum ambient conditions the value reaches 10 µW/cm$^2$ even at the minimum $T_{source}$ of 40 °C.

Due to the large magnetization and low $T_c$ of La-Fe-Si based alloys, these materials are suitable for developing TMGs with high performance near room temperature. For the investigation presented in this work, La-Fe-Si ribbon fabricated by melt spinning and later hydrogenated are used. This TMG generated a very large power output of 4.2 µW while operating at a $T_{source}$ of 90 °C despite having very low value of $h_f$. This low value of $h_f$ is the result of the fabrication process which makes the surface very rough and thus minimizing the contact area between TM film and magnet during operation. But in order to reduce the $T_{source}$ under which resonant self-actuation could be achieved for TMGs with La-Fe-Si and to be able to generate maximum output, further optimizations are required. By using Gd, La-Fe-Si-H and Ni-Mn-Ga, a whole range of TMGs are presented. These devices make use of $T_{source}$ starting from 40 °C all the way up to 170 °C. The TMG based on Gd operated from 40 °C to 70 °C, while the TMG based on La-Fe-Si-H operated between 70 °C and 100 °C. The Ni-Mn-Ga operates between 110 °C and 170 °C.

## 8.2. Benchmarking

All demonstrators in this work are fabricated with similar dimensions with an overall lateral footprint of the final device in the range from 10 mm$^2$ to 14 mm$^2$. All TMGs presented are compared with each other and then a few of them have been compared to other demonstrators from literature.

## 8.2.1. TMGs within this work

The peak performance of the device at higher $T_{source}$ values and the performance at the minimum operating temperatures are shown in **Figure 103**. The maximum power per footprint of 50 µW/cm² is observed for a TMG with 40 µm thick Ni-Mn-Ga film at $T_{source}$ of 170 °C and then drops to a value of 28 µW/cm² when the $T_{source}$ is reduced to 130 °C. At lower $T_{source}$ values of 90 °C, the TMG with La-Fe-Si-H as the active TM film generates a power per footprint of 38 µW/cm². This marks a milestone in TM energy generation as the waste heat from water boilers is now accessible to this technology as the $T_{source}$ is below 100 °C. The power per footprint value reduces to 20 µW/cm² when the $T_{source}$ is reduced to 70 °C. Gadolinium based TMG is able to generate a power per footprint of 24 µW/cm² from an even lower $T_{source}$ of 65 °C. At a heat source of 40 °C which is the minimum for all the TMGs discussed in this work, the TMG with Gd film as TM film is still capable of gen-
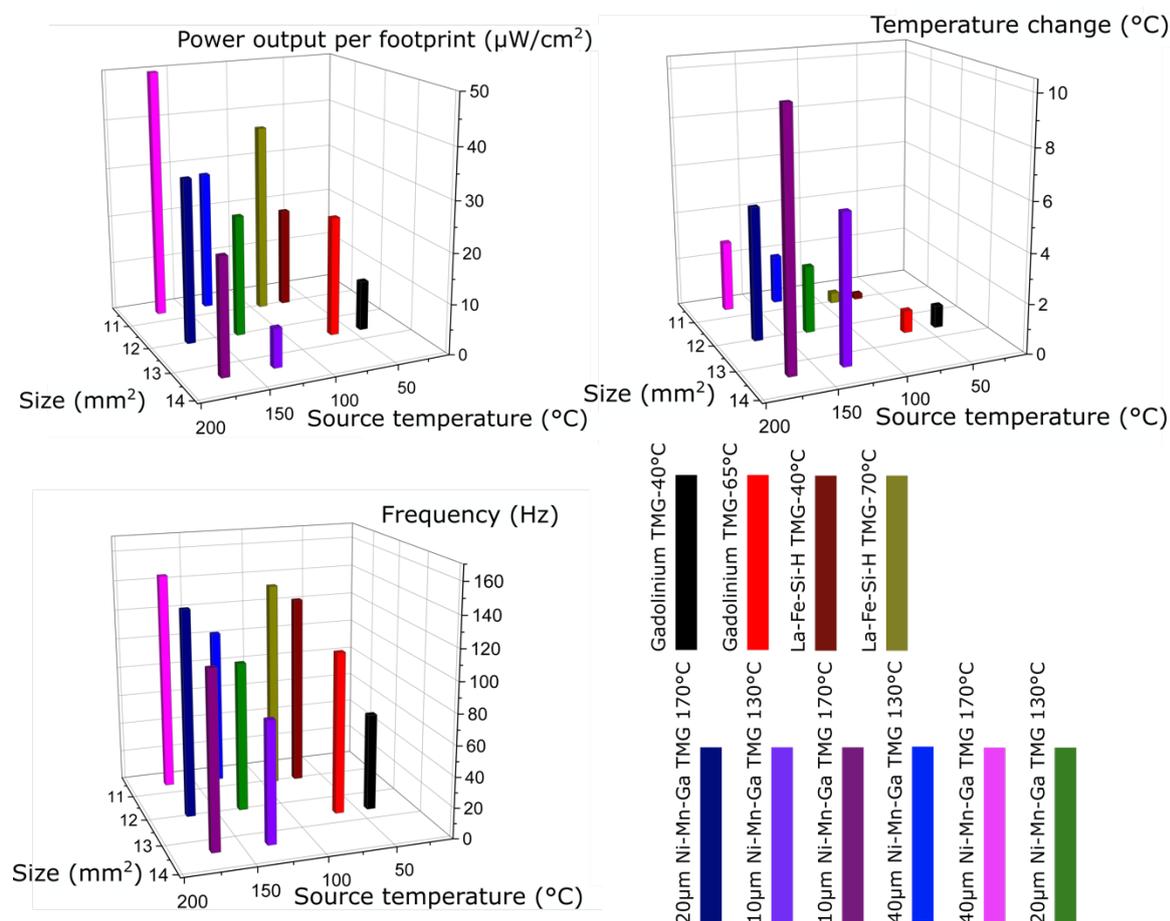


**Figure 103** Comparison of thermomagnetic generators presented as part of this work (a) power per footprint of devices, (b) temperature change within active material of the device, (c) frequency of operation of the devices.

164

erating 10 µW/cm$^2$. This is also another milestone in the development of TMGs near room temperature as we are getting closer to human body temperature. All the demonstrators presented in this work are operating with high frequencies. The highest frequency of 146 Hz is observed for the TMG with 40 µm Ni-Mn-Ga film. La-Fe-Si-H based TMG is operating with a frequency of 137 Hz, but this is restricted due to the low value of $h_f$. Once this is improved, it does have the potential to operate at close to 200 Hz (assumption based on the natural frequency of cantilever assembly) at a low $T_{source}$ of 90 °C. The TMG with Gd film shows that it is possible to sustain resonant self-actuation with a frequency of 107 Hz and 54 Hz at 70 °C and 40 °C $T_{source}$ values respectively.

**Figure 103** also shows the $\Delta T$ in the TM films for the respective TMG demonstrators. It can be observed that $\Delta T$ is higher in thinner TM films and is lower as the thickness of the sample is increasing resulting in the large thermal mass of the thick films. The Ni-Mn-Ga films show much larger ΔT even at higher thicknesses compared to Gd and La-Fe-Si-H films. Ni-Mn-Ga film shows a ΔT between 3 °C to 10 °C for the TMG with TM film thicknesses between 40 µm to 10 µm. Gd film shows a ΔT of 0.45°C at a $T_{source}$ value of 40 °C and the La-Fe-Si-H shows the least ΔT value of 0.22 °C at a $T_{source}$ of 70 °C. Even at the higher $T_{source}$ of 90 °C, the ΔT is only 0.43 °C. Unlike, frequency and power output, the ΔT required for operation should be as low as possible. This is also dependent on the thermal mass (volume of the material). But if the material volume is assumed to be the same, then a lower ΔT requirement for resonant self-actuation is desirable as it would also result in a lower heat intake requirement.

**Table 10** Performance of different TMGs are presented.

| Material | Thickness of film (µm) | T$_{source}$ (°C) | ΔT (°C) | Size (mm$^2$) | Power (µW) | Power per footprint (µW/cm$^2$) | Frequency (Hz) |
|---|---|---|---|---|---|---|---|
| Ni-Mn-Ga | 40 | 130 | 2 | 10.6 | 3 | 28.3 | 104 |
| | 40 | 170 | 2.9 | | 5.3 | 50 | 146 |
| | 20 | 130 | 2.7 | | 2.9 | 24.2 | 98 |

| | | | | | | | |
|---|---|---|---|---|---|---|---|
| | 20 | 170 | 5.4 | 12 | 4 | 32.8 | 136 |
| | 10 | 130 | 5.9 | 13.4 | 1 | 7.8 | 79 |
| | 10 | 170 | 10 | | 3 | 23 | 114 |
| Gadolinium | 40 | 40 | 1 | 12.6 | 1.26 | 10 | 64 |
| | | 65 | 0.9 | | 3 | 23.8 | 107 |
| La-Fe-Si-H | 50 | 70 | 0.2 | 11 | 2.2 | 20 | 127 |
| | | 90 | 0.4 | | 4.2 | 38 | 138 |

## 8.2.2. Benchmarking

TMGs with 40 µm Ni-Mn-Ga film, Gd film, and La-Fe-Si-H film are selected for comparison with other similar TMG demonstrators presented in the literature. Several published examples are considered that use the TM energy conversion principle and TM films to convert thermal energy into electrical energy. Many more potential energy-generating systems have been proposed, but they primarily establish the actuation state, which transforms thermal energy into mechanical energy.[111,165] It can be seen that in terms of power per footprint the 40 µm Ni-Mn-Ga is the peak performing TMG. The closest competition is provided by the TMG presented by Waske et al.[110] But even though the power output is considered without taking into account the energy required for powering the pump used to circulate the heat transfer fluid, the power per footprint is 32 µW/cm$^2$ while operating at a frequency of 1 Hz. The TMG with 40 µm Ni-Mn-Ga film generates 56 % more power per footprint while operating at 146 Hz.

It can also be seen that all demonstrators presented in this work are among the smallest devices. The frequency of the operation is also among the highest with no other device being in even the same order of magnitude. The ΔT in the material under operation is among the lowest. Both TMGs with La-Fe-Si-H film and Gd film show a ΔT that is more than an order of magnitude lower than the other devices.
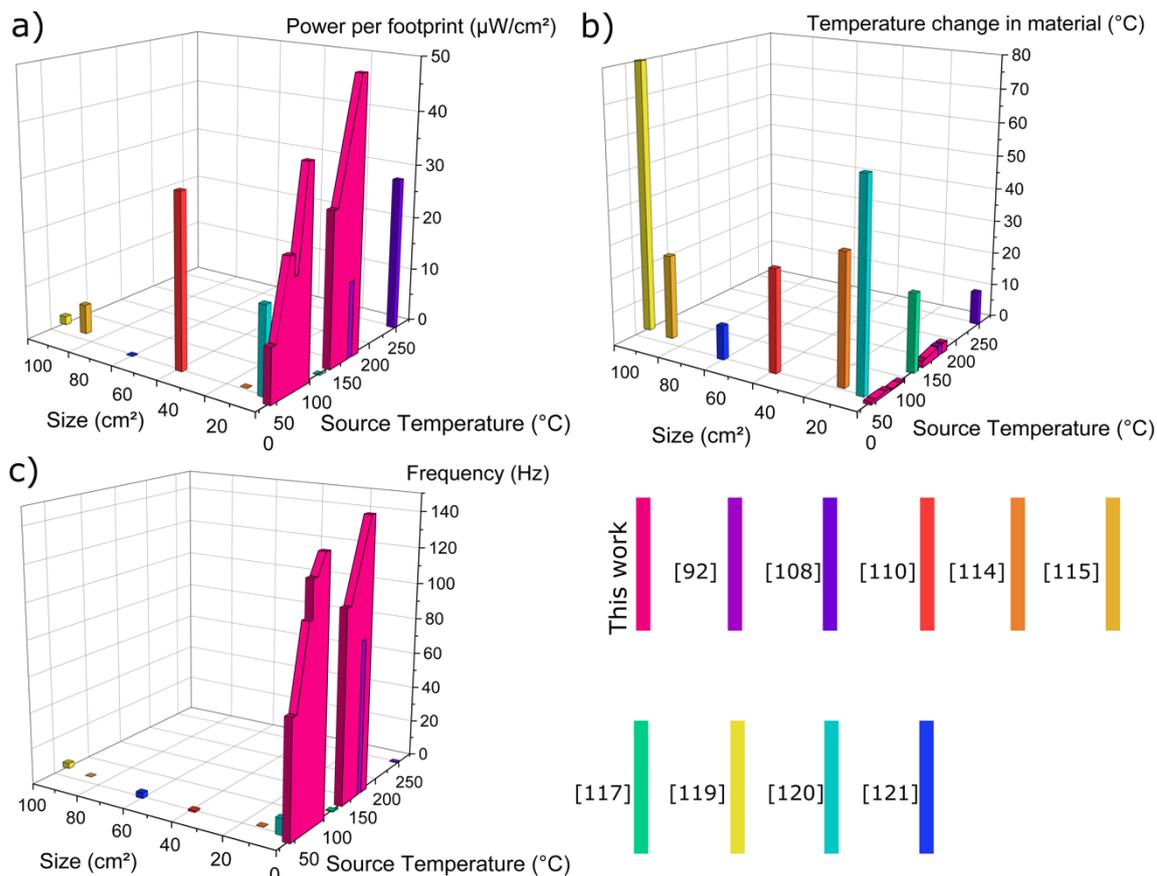
**Figure 104** Comparison with similar devices from literature, only best performing thermo-magnetic generators from this work are included, (a) power per footprint of devices, (b) temperature change within the active material of the device, (c) frequency of operation of the devices. Waske et. al.,[110] Ahmim et. al.,[114] Rodrigues et. al.,[115] Chun et. al.,[120] Lallart et. al.,[117] Srivastava et. al.,[108] Chun et. al.,[119] Gueltig et. al.,[92] Carlioz et. al.[121] Adapted image from Joseph et al.[152]

**Table 11** Performance of TMG from literature sources.

| Source | $T_{source}$ (°C) | ΔT (°C) | Size (mm²) | Power (µW) | Power per foot-print (µW/cm²) | Frequency (Hz) |
|---|---|---|---|---|---|---|
| Waske et al.[110] | 50 | 30 | 3900 | 1240 | 31.8 | 1 |

| Ahmim et al.[114] | 56 | 35 | 3316.6 | 4.2 | 0.13 | 0.12 |
|---|---|---|---|---|---|---|
| Rodrigues et al.[115] | 65 | 25 | 8800 | 481.4 | 5.47 | 0.011 |
| Chun et al.[120] | 70 | 80 | 10000 | 158 | 1.58 | 3 |
| Lallart et al.[117] | 115 | 23 | 28 | 0.0058 | 0.021 | 0.35 |
| Srivastava et al.[108] | 250 | 10 | 176.7 | 50 | 28.3 | 0.05 |
| Chun et al.[120] | 50 | 60 | 500 | 80 | 16 | 9 |
| Gueltig et al.[92] | 160 | 15 | 17 | 2.4 | 14.12 | 84 |
| Carlioz et al.[121] | 50 | 10 | 6079 | 3.2 | 0.053 | 3.1 |

# 9. Conclusions and outlook

This section concludes the work on power generation by resonant self-actuation with a summary of the presented work and an outlook to further develop resonant self-actuated thermomagnetic generators.

## 9.1. Conclusions

With the increasing demand for connected IoT (internet of things) devices which are forming a grid to sense its environment conditions, remote power generation is ever more in demand. The ability to generate useful amounts of power on site would enable widespread adaption. Since this would reduce the maintenance efforts, this development is also beneficial to the economy in long term. Since much of the waste energy is in the form of low-grade thermal energy in the environment which would otherwise be lost, a technology to harvest this energy has a widespread interest. Thermal energy harvesting using thermoelectric devices utilizing the Seebeck effect is popular at higher temperatures, but when it comes to low heat source temperature regime below 200 °C and miniature size of a few millimeters, this method of thermal energy harvesting lacks the power density required to stay competitive.

Using thin films and the recently established concept of resonant self-actuation, this thesis presents several TMGs operating with high power output per footprint. In addition an extensive study on device performances and the factors affecting the performance is presented based on LEM simulations.

The Key results can be summarized as follows;

1. LEM model and parameter study: Different domains of the model are dedicated to the different physical principles that drive the TMG. The magnetic part of the model is utilized to derive the magnetic field and magnetic field gradient of the permanent magnet at various positions. The mechanical domain of the TMG is used to model and understand the oscillation behavior due to the stiffness, mass, damping, and magnetic

force. The magnetic force is dependent on the magnetic field, which causes the magnetization of the TM film and the magnetic field gradient which causes the magnetic force. The thermal domain of the LEM simulation models the heat flow through the different layers using thermal resistances and capacitances. The validated LEM gives a valuable conception of the thermal processes within the TMG and supports the development of novel thermomagnetic generators that operate in resonant self-actuation mode. This allows the model to derive the temperatures of different components of the TMG during its transient operation. Since the TMG never reaches thermal equilibrium and always operates in transient mode, understanding the thermal processes in the TMG is crucial to achieving resonant self-actuation mode. The electrical domain of the LEM simulation is used to model the energy generation from the mechanical oscillation that is converted to electrical energy with the pick-up coil that moves in the changing magnetic field gradient. All domains of the LEM simulation are solved simultaneously so that mutual interactions between the different cycles can be modeled appropriately. The simulation model is validated by comparing, stroke, frequency and power output of the TMG from experiments. To design a TMG with a TM film, initially, the $h_f$ is postulated as this value is very hard to measure accurately. After fabricating the designed TMG, the device is tested and then the simulation is readjusted to match the performance of the TMG by matching the $h_f$.

Different parameters affect the performance of the TMG. The material of the magnet and its dimension affect the magnetic field and magnetic field gradient generated by the permanent magnet. It is also shown how having a higher aspect ratio (between the height of the magnet along the easy axis and cross-sectional area) would result in a higher magnetic field gradient which would increase the magnetic force, but would also result in a lower magnetic field at a distance, as a result, causing a reduction in magnetization of the TM film. Hence choosing the proper dimensions of the permanent magnet is essential in achieving optimum performance of the TMG as the maximum stroke, stiffness (hence frequency), and power output would be dependent on this. The effect of different thermal processes on the performance of the TMG is also discussed. It is shown there is a critical value for both $h_f$ (8 kW/m$^2$K) and $R_b$ (5 K/W) between the TM film and cantilever that affect the heat intake into the material and heat dissipation from the material respectively. Above the critical value increasing the $h_f$ increased the output power and frequency of the TMG. Similar observations are made for increasing $R_b$. But after reaching the peak value for the $\Delta T$, the $\Delta T$ is slightly showing a reduction suggesting that further increase might cause a reduction in power

172

output and there would be a maximum critical value for the bonding layer $R_b$ above which resonant actuation would fail. But the investigated $R_b$ of 45 K/W corresponds to a bonding layer thickness of 40 μm for material with thermal conductivity of 0.225. This is already four times the size of the 10 μm Ni-Mn-Ga film used for investigation suggesting the higher limit is beyond reach in practical applications.

The effect of cantilever stiffness is also studied in detail, and it is found that increased stiffness would result in higher power output and frequency due to the increased natural frequency of cantilever assembly. But beyond a critical stiffness, the device stops operating as the device's mechanical oscillation cycle does not match with the TMG's thermal cycling. The heating and cooling cycles of the TMG needs to be in balance with the oscillation cycle in order to sustain resonant self-actuation. The pick-up coil turns in the device are also affecting the performance. It is possible to optimize the number of turns in the pick-up coil according to the $T_{source}$, magnetic force, and stiffness of the cantilever to achieve the maximum power output. This is the result of optimizing the electromagnetic damping to generate maximum power output. The $T_c$ of the TM film used as the active material in the TMG also affects the performance defines the operating temperature range of the TMG. The TMG with high $T_c$ of the TM film would require higher $T_{source}$ while the TMG with lower $T_c$ of the TM film would require lower $T_{source}$ values. As the $T_c$ is approaching the $T_{amb}$, additional effects due to lack in dissipation capability are observed that cause a reduction in power output. Further an increase in magnetization is required to overcome this limitation. The load resistance ($R_L$) connected to the TMG also affects the performance as this regulates the current through the pick-up coil. The current in the pick-up coil causes electromagnetic damping at the cantilever tip. Thus, the $R_L$ also needs to be matched to the TMG to achieve maximum output. It is also observed that increasing $R_L$ would cause an increase in power generated due to the reduced electromagnetic damping, resulting in higher frequency and stroke. But the transfer efficiency decreases as the value of the $R_L$ is increased further (more than the internal resistance of the pick-up coil) resulting in an optimum value of $R_L$.

2. Upscaling: The upscaling of the TMG is investigated to achieve higher power output.

   a). Increase in active material volume: The TMG is successfully upscaled from generating 2.4 μW to 5.3 μW resulting in a gain of 3.4 times power output per footprint with values reaching 50 μW/cm$^2$ by increasing the active material volume. The effects of upscaling are studied in detail using experiments and LEM simulation to

173

understand the thermal and mechanical effects of scaling. The upscaling is limited by the lack of homogeneous thin films of Ni-Mn-Ga films beyond 10 μm thickness, demanding the fabrication of thin film stacks prepared by stacking Ni-Mn-Ga using a conductive bonding layer. The thermal mass of the stack is causing the ΔT in the material to drop and 40 μm is the limit beyond which it is not possible to increase the power output due to the additional passive thermal load of the conductive bonding layer.

b). Increasing the lateral size: The lateral size of the effective area of power generation of the TMG could be upscaled by adding multiple TMGs in parallel. Adding multiple TMGs in parallel under a single magnet surface may result in coupling effects between the devices. It is observed that only thermal coupling effects affect the performance. For the TMG using 10 μm Ni-Mn-Ga films, the coupling effects are observed only at higher $T_{source}$ values above 150 °C. This shows the tolerance of the TMGs to changes in the ambient condition and the potential to upscale in terms of the number of devices operating in parallel close to each other. The thermal coupling effects are caused due to the inability of the TMGs to dissipate the heat that is taken in during contact effectively because of the neighboring devices. It is possible for the TMGs to operate in correlation to each other, with the TMG increasing its output as soon as the neighboring TMG stops operation and as soon the neighboring TMG resumes operation, the primary device reduces its power output to accommodate the thermal coupling.

3. Expanding the range of operation temperature: Operation near room temperature is achieved using Gd and La-Fe-Si-H as the active TM films. The TMG using La-Fe-Si-H film with $T_c$ of 48 °C is able to operate in resonant self-actuation mode even at a $T_{source}$ of 70 °C. The TMG using a Gd film, on the other hand, with a $T_c$ of 20 °C enable operation in resonant self-actuation at a minimum $T_{source}$ of 40 °C. Since the change in magnetization of these two materials is different, it is possible to understand how both, the gradual change of magnetization and the abrupt change of magnetization, could be utilized to develop devices, which can either sustain resonant self-actuation in a wide range of ambient conditions or devices that can perform with large power output and very high frequency at a small range of temperature, respectively. The TMGs using Gd film is generating 3.1 μW at its peak performance state with a $T_{source}$

of 65 °C while also generating 1 µW at 40 °C. The TMG using a La-Fe-Si-H film generates around 4.2 µW at a $T_{source}$ of 90 °C and is also capable of generating 2.2 µW of power at a $T_{source}$ of 70 °C. The performance of the TMG with La-Fe-Si-H film is limited by the surface roughness of the material as a result of the fabrication process.

With this thesis work, TMGs operating within a range of 40 °C to 170 °C for $T_{source}$ values are developed. A LEM simulation tool is developed for design and optimization of film based TMGs for various other materials and layouts. These preliminary results point out a route for future investigations, which are discussed in more detail in section **9.2.**

## 9.2. Outlook

Developing thermomagnetic generators operating near room temperature comes with a lot of challenges. Although many of these challenges have been tackled during the course of this thesis, further work needs to be undertaken to achieve more TMGs, e.g., that may utilize body heat as the heat source. For optimization, the procedures below, in particular, need to be taken into account:

- Extending the LEM simulation model for impact of coupling effects in TMGs operating in parallel
- Optimizing bi-stable TMGs by integrating a pyroelectric element
- Improving the surface roughness of La-Fe-Si-H samples to increase power output
- In vacuum operation could be achieved if support of convection could be completely avoided.
- Developing novel materials with high magnetization ($M$), large magnetization changes with respect to temperature ($\Delta M / \Delta T$) and $T_c$ near room temperature

Continuous innovation in the field of TM energy generation is required to achieve near-room temperature resonant self-actuation in TMGs which are capable of generating a large amount of power from a small area. Since the absolute power output of the TMG would be small considering its miniature dimensions, it is inevitable that multiple devices need to be operated side by side to achieve sufficient energy output required to continuously power a sensor node. To optimize the power output and thermal performance of the TMGs, the thermal coupling between the devices need to be investigated experimentally and by using a LEM simulation model.

TMG with La-Fe-Si-H film shows a lot of potential, and the device design suggests high frequency operation that is attainable with good surface contact with the magnet. Improving the surface roughness of the La-Fe-Si-H sample would increase the $h_f$ between the film and the magnet. This would increase the power output many folds and also improve the minimum $T_{source}$ at which the device is capable of sustaining resonant self-actuation. The surface roughness could be improved either by an additional layer of conductive material and then polishing the material or by choosing an alternative fabrication process for the material. Adding manganese would allow further tuning of the material properties of the material to achieve operation at even lower $T_{source}$ values. In particular, accessing $T_{source}$ less than 37 °C by TMGs based on La-Fe-Si-Mn-H films would open up a large field of new applications particularly in the medical field.

Currently, the thermal dissipation in the TMG is actively controlled by utilizing thermal convection to ambient air. This is achieved as the convection is increased many folds as soon as the device is rapidly oscillating and is negligible when the device is in contact as the cantilever is not moving. If this active component of the TMG is integrated into the cantilever design to avoid support of convection, then it is possible to develop TMGs capable of operating in a vacuum by relying solely on conductive dissipation of heat energy. This would allow encapsulation of the TMG and increase the thermal performance many folds by taking the effects of thermal convection away. Multiple devices can also be operated at a very close distance as the thermal coupling effects could be completely avoided by avoiding convective dissipation.

Further, new novel ferromagnetic materials with high value of magnetization in ferromagnetic state and low $T_c$ near room temperature need to be developed. It would also be possible to integrate materials showing low or zero hysteresis first-order transformation into the present design to achieve resonant self-actuation which could potentially generate large amounts of power owing to its abrupt first-order transformation.

# References

1.  Cho, S., Yun, C.-B., Lynch, J.P., Zimmerman, A.T., Spencer, B.F.Jr., and Naga-yama, T. (2008). Smart wireless sensor technology for structural health monitoring of civil structures. Steel Structures *8*, 267–275.

2.  Loncar-Turukalo, T., Zdravevski, E., Machado da Silva, J., Chouvarda, I., and Trajkovik, V. (2019). Literature on Wearable Technology for Connected Health: Scoping Review of Research Trends, Advances, and Barriers. J Med Internet Res *21*, e14017. doi:10.2196/14017.

3.  Kohl, M., Joseph, J., and Seigner, L. (2022). Energy Harvesting Using Magnetic Shape Memory Alloys. In: Encyclopedia of Smart Materials (Elsevier), pp. 96-103. doi:10.1016/B978-0-12-815732-9.00040-1.

4.  Teresa Penella, M., Albesa, J., and Gasulla, M. (2009). Powering wireless sensor nodes: Primary batteries versus energy harvesting. In: 2009 IEEE Intrumentation and Measurement Technology Conference (IEEE), pp. 1625–1630. doi:10.1109/IMTC.2009.5168715.

5.  Zeeshan, Panigrahi, B.K., Ahmed, R., Mehmood, M.U., Park, J.C., Kim, Y., and Chun, W. (2021). Operation of a low-temperature differential heat engine for power generation via hybrid nanogenerators. Appl Energy *285*, 116385. doi:10.1016/j.apenergy.2020.116385.

6.  Prauzek, M., Konecny, J., Borova, M., Janosova, K., Hlavica, J., and Musilek, P. (2018). Energy harvesting sources, storage devices and system topologies for en-vironmental wireless sensor networks: A review. Sensors (Switzerland) *18*. doi:10.3390/s18082446.

7.  Kiziroglou, M.E., and Yeatman, E.M. (2012). Materials and techniques for energy harvesting. In: Functional Materials for Sustainable Energy Applications (Elsevier), pp. 541–572. doi:10.1533/9780857096371.4.539.

8.  Beeby, S.P., Tudor, M.J., and White, N.M. (2006). Energy harvesting vibration sources for microsystems applications. Meas Sci Technol *17*, R175–R195. doi:10.1088/0957-0233/17/12/R01.

9.  Bader, S., Ma, X., and Oelmann, B. (2014). On the Modeling of Solar-Powered Wireless Sensor Nodes. Journal of Sensor and Actuator Networks *3*, 207–223. doi:10.3390/jsan3030207.

10. Buratti, C., Conti, A., Dardari, D., and Verdone, R. (2009). An Overview on Wireless Sensor Networks Technology and Evolution. Sensors *9*, 6869–6896. doi:10.3390/s90906869.

11. Wei, C., and Jing, X. (2017). A comprehensive review on vibration energy harvesting: Modelling and realization. Renewable and Sustainable Energy Reviews *74*, 1–18. doi:10.1016/j.rser.2017.01.073.

12. Spreemann, D., and Manoli, Y. (2012). Electromagnetic Vibration Energy Harvesting Devices (Netherlands, Springer). doi:10.1007/978-94-007-2944-5.

13. Anton, S.R., and Sodano, H.A. (2007). A review of power harvesting using piezoelectric materials (2003–2006). Smart Mater Struct *16*, R1–R21. doi:10.1088/0964-1726/16/3/R01.

14. Wang, H., and Jasim, A. (2020). Piezoelectric energy harvesting from pavement. In: Eco-Efficient Pavement Construction Materials (Elsevier), pp. 367–382. doi:10.1016/B978-0-12-818981-8.00014-X.

15. Sezer, N., and Koç, M. (2021). A comprehensive review on the state-of-the-art of piezoelectric energy harvesting. Nano Energy *80*, 105567. doi:10.1016/j.nanoen.2020.105567.

16. Quattrocchi, A., Freni, F., and Montanini, R. (2021). Power Conversion Efficiency of Cantilever-Type Vibration Energy Harvesters Based on Piezoceramic Films. IEEE Trans Instrum Meas *70*, 1–9. doi:10.1109/TIM.2020.3026462.

17. Liedtke, L., Gueltig, M., and Kohl, M. (2019). Miniature-scale energy harvesting based on the inverse magnetic shape memory effect. International Journal of Applied Electromagnetics and Mechanics *59*, 377–383. doi:10.3233/JAE-171038.

18. Olzhabay, Y., Ng, A., and Ukaegbu, I.A. (2021). Perovskite PV Energy Harvesting System for Uninterrupted IoT Device Applications. Energies (Basel) *14*, 7946. doi:10.3390/en14237946.

19. Vorobiev, Yu., González-Hernández, J., Vorobiev, P., and Bulat, L. (2006). Thermal-photovoltaic solar hybrid system for efficient solar energy conversion. Solar Energy *80*, 170–176. doi:10.1016/j.solener.2005.04.022.

20. Saracoglu, B.O., Ohunakin, O.S., Adelekan, D.S., Gill, J., Atiba, O.E., Okokpujie, I.P., and Atayero, A.A. (2018). A framework for selecting the location of very large photovoltaic solar power plants on a global/supergrid. Energy Reports *4*, 586–602. doi:10.1016/j.egyr.2018.09.002.

21. Divakaran, S.K., Krishna, D. Das, and Nasimuddin (2019). RF energy harvesting systems: An overview and design issues. International Journal of RF and Microwave Computer-Aided Engineering *29*, e21633. doi:10.1002/mmce.21633.

22. Serdijn, W.A., Mansano, A.L.R., and Stoopman, M. (2014). Introduction to RF Energy Harvesting. In: Wearable Sensors (Elsevier), pp. 299–322. doi:10.1016/B978-0-12-418662-0.00019-2.

23. Kishore, R.A., and Priya, S. (2018). A review on design and performance of thermomagnetic devices. Renewable and Sustainable Energy Reviews *81*, 33–44. doi:10.1016/j.rser.2017.07.035.

24. Kitanovski, A. (2020). Energy Applications of Magnetocaloric Materials. Adv Energy Mater *10*, 1903741. doi:10.1002/aenm.201903741.

25. Bucsek, A.N., Nunn, W., Jalan, B., and James, R.D. (2020). Energy Conversion by Phase Transformation in the Small-Temperature-Difference Regime. Annu Rev Mater Res *50*, 1–36. doi:10.1146/annurev-matsci-082019-021824.

26. Arnott, W.P., Raspet, R., and Bass, H.E. Thermoacoustic engines. In IEEE 1991 Ultrasonics Symposium (IEEE), pp. 995–1003. doi:10.1109/ULTSYM.1991.234265.

27. Lee, S.W., Yang, Y., Lee, H.-W., Ghasemi, H., Kraemer, D., Chen, G., and Cui, Y. (2014). An electrochemical system for efficiently harvesting low-grade heat energy. Nat Commun *5*, 3942. doi:10.1038/ncomms4942.

28. Joseph, J., Ohtsuka, M., Miki, H., and Kohl, M. (2020). Upscaling of Thermomagnetic Generators Based on Heusler Alloy Films. Joule *4*, 2718–2732. doi:10.1016/j.joule.2020.10.019.

29. Snyder, G.J., and Toberer, E.S. (2008). Complex thermoelectric materials. Nat Mater *7*, 105–114. doi:10.1038/nmat2090.

30. Snyder, G.J. Thermoelectric Energy Harvesting. In Energy Harvesting Technologies (New York, Springer US), pp. 325–336. doi:10.1007/978-0-387-76464-1_11.

31. Amatya, R., and Ram, R.J. (2010). Solar Thermoelectric Generator for Micropower Applications. J Electron Mater *39*, 1735–1740. doi:10.1007/s11664-010-1190-8.

32. Min, G. (2010). Thermoelectric Energy Harvesting. In Energy Harvesting for Autonomous Systems, S. P. Beeby and N. White, eds. (Norwood, MA : Artech House), pp. 135–155.

33. Bierschenk, J.L. (2009). Optimized Thermoelectrics For Energy Harvesting Applications. In: Energy Harvesting Technologies, S. Priya and D. J. Inman, eds. (Springer US), pp. 337–350. doi:10.1007/978-0-387-76464-1.

34. Batra, Ashok K, and Aggarwal, M.D. Pyroelectric Energy Harvesting. In: Pyroelectric Materials: Infrared Detectors, Particle Accelerators, and Energy Harvesters (Society of Photo-Optical Instrumentation Engineers), pp. 135–174. doi:10.1117/3.1000982.ch7.

35. Ravindran, S.K.T., Kroener, M., and Woias, P. (2012). A bimetallic micro heat engine for pyroelectric energy conversion. Procedia Eng *47*, 33–36. doi:10.1016/j.proeng.2012.09.077.

36. Ravindran, S.K.T., Huesgen, T., Kroener, M., and Woias, P. (2011). A self-sustaining micro thermomechanic-pyroelectric generator. Appl Phys Lett *99*, 1–4. doi:10.1063/1.3633350.

37. Phillips, J.D. (2021). Energy Harvesting in Nanosystems: Powering the Next Generation of the Internet of Things. Frontiers in Nanotechnology *3*. doi:10.3389/fnano.2021.633931.

38. Madou, M.J. (2018). Fundamentals of Microfabrication: The Science of Miniaturization, Second Edition. (Boca Raton, CRC Press). doi:10.1201/9781482274004

39. Lyshevski, S.E. (2018). MEMS and NEMS: Systems, Devices, and Structures. (Boca Raton, CRC Press). doi:10.1201/9781315220246

40. Kohl, M., Dittmann, D., Quandt, E., Winzek, B., Miyazaki, S., and Allen, D.M. (1999). Shape memory microvalves based on thin films or rolled sheets. Materials Science and Engineering: A *273–275*, 784–788. doi:10.1016/S0921-5093(99)00416-5.

41. Kohl, M., Just, E., Pfleging, W., and Miyazaki, S. (2000). SMA microgripper with integrated antagonism. Sens Actuators A Phys *83*, 208–213. doi:10.1016/S0924-4247(99)00385-4.

42. Brugger, D., Kohl, M., and Krevet, B. (2006). Ferromagnetic shape memory microscanner with large deflection angles. International Journal of Applied Electromagnetics and Mechanics *23*, 99–105. doi:10.3233/JAE-2006-722.

43. Kohl, M., Gueltig, M., Pinneker, V., Yin, R., Wendler, F., and Krevet, B. (2014). Magnetic Shape Memory Microactuators. Micromachines *5*, 1135–1160. doi:10.3390/mi5041135.

44. Grund, T., Guerre, R., Despont, M., and Kohl, M. (2008). Transfer bonding technology for batch fabrication of SMA microactuators. Eur Phys J Spec Top *158*, 237–242. doi:10.1140/epjst/e2008-00681-3.

45. Megnin, C., and Kohl, M. (2013). Shape memory alloy microvalves for a fluidic control system. Journal of Micromechanics and Microengineering *24*, 25001. doi:10.1088/0960-1317/24/2/025001.

46. Bhattacharya, K., and James, R.D. (2005). The Material Is the Machine. Science (1979) *307*, 53–54. doi:10.1126/science.1100892.

47. Graf, T., Winterlik, J., Müchler, L., Fecher, G.H., Felser, C., and Parkin, S.S.P. (2013). Magnetic Heusler Compounds. In Handbook of Magnetic Materials, pp. 1–75. doi:10.1016/B978-0-444-59593-5.00001-5.

48. Ullakko, K., Huang, J.K., Kantner, C., O'Handley, R.C., and Kokorin, V. V. (1996). Large magnetic-field-induced strains in Ni 2 MnGa single crystals. Appl Phys Lett *69*, 1966–1968. doi:10.1063/1.117637.

49. Chernenko, V.A., Ohtsuka, M., Kohl, M., Khovailo, V. V., and Takagi, T. (2005). Transformation behavior of Ni-Mn-Ga thin films. Smart Mater Struct *14*, S245–S252. doi:10.1088/0964-1726/14/5/012.

50. Krenke, T., Duman, E., Acet, M., Wassermann, E.F., Moya, X., Manosa, L., and Planes, A. (2005). Inverse magnetocaloric effect in ferromagnetic Ni-Mn-Sn alloys. Nat Mater *4*, 450–454. doi:10.1038/nmat1395.

51. Kainuma, R., Imano, Y., Ito, W., Sutou, Y., Morito, H., Okamoto, S., Kitakami, O., Oikawa, K., Fujita, A., Kanomata, T., et al. (2006). Magnetic-field-induced shape

recovery by reverse phase transformation. Nature *439*, 957–960. doi:10.1038/nature04493.

52. Nye, J.F. (1985). Physical Properties of Crystals: Their Representation by Tensors and Matrices. (Oxford, Clarendon Press).

53. Purcell, E.M., and Morin, D.J. (2013). Electricity and Magnetism. Third edition. (Cambridge, Cambridge University Press).

54. Chikazumi, S. (2009). Physics of Ferromagnetism Second edition. (Oxford, Oxford University Press).

55. Spaldin, N.A. (2010). Magnetic Materials: Fundamentals and Applications. 2nd ed. (Cambridge, Cambridge University Press). doi:10.1017/CBO9780511781599.

56. Griffiths, D.J. (2017). Introduction to Electrodynamics Fourth edition. (Cambridge, Cambridge University Press). doi:10.1017/9781108333511.

57. Du, H., Akakuru, O.U., Yao, C., Yang, F., and Wu, A. (2022). Transition metal ion-doped ferrites nanoparticles for bioimaging and cancer therapy. Transl Oncol *15*, 101264. doi:10.1016/j.tranon.2021.101264.

58. Harcourt, R.D., and Harcourt, A. (1973). A simple demonstration of the origin of hund's rule for the helium 2S and 2P states. Chem Phys *1*, 238–243. doi:10.1016/0301-0104(73)85018-9.

59. Kittel, C. (2005). Introduction to Solid State Physics Eighth edition. (New York, Wiley).

60. Ruiz, E. (2013). Exchange Coupling in Di- and Polynuclear Complexes. In: Comprehensive Inorganic Chemistry II (Elsevier), pp. 501–549. doi:10.1016/B978-0-08-097774-4.00922-0.

61. Cullity, B.D., and Graham, C.D. (2008). Introduction to Magnetic Materials (New York, Wiley). doi:10.1002/9780470386323.

62. Porter, D.A., Easterling, K.E., and Easterling, K.E. (2009). Phase Transformations in Metals and Alloys (Revised Reprint) (Boca Raton, CRC Press). doi:10.1201/9781439883570.

63. Lagoudas, D.C. (2008). Shape Memory Alloys: Modeling and Engineering Applications (Texas, Springer US). doi:10.1007/978-0-387-47685-8.

64. Popov, P., and Lagoudas, D.C. (2007). A 3-D constitutive model for shape memory alloys incorporating pseudoelasticity and detwinning of self-accommodated martensite. Int J Plast *23*, 1679–1720. doi:10.1016/j.ijplas.2007.03.011.

65. Webster, P.J., and Ziebeck, K.R.A. (1988). 1.5.5.1 Crystallographic structure. In: Alloys and Compounds of d-Elements with Main Group Elements. Part 2 (Springer-Verlag), pp. 75–79. doi:10.1007/10353201_12.

66. Krenke, T., Acet, M., Wassermann, E.F., Moya, X., Mañosa, L., and Planes, A. (2005). Martensitic transitions and the nature of ferromagnetism in the austenitic and martensitic states of Ni-Mn-Sn alloys. Phys Rev B Condens Matter Mater Phys *72*, 1–9. doi:10.1103/PhysRevB.72.014412.

67. Srivastava, V., Chen, X., and James, R.D. (2010). Hysteresis and unusual magnetic properties in the singular Heusler alloy Ni45Co5Mn40Sn10. Appl Phys Lett *97*, 014101. doi:10.1063/1.3456562.

68. Sutou, Y., Imano, Y., Koeda, N., Omori, T., Kainuma, R., Ishida, K., and Oikawa, K. (2004). Magnetic and martensitic transformations of NiMnX(X=In, Sn, Sb) ferromagnetic shape memory alloys. Appl Phys Lett *85*, 4358–4360. doi:10.1063/1.1808879.

69. Greiner, W. (1998). Faraday ' s Law of Induction. In: Classical Electrodynamics, pp. 237–249. (New York, Springer). doi:10.1007/978-1-4612-0587-6_12

70. Tran, V.-K., Han, P.-W., and Chun, Y.-D. (2022). Design of a 120 W Electromagnetic Shock Absorber for Motorcycle Applications. Applied Sciences *12*, 8688. doi:10.3390/app12178688.

71. Said, S.M., Sabri, M.F.M., and Salleh, F. (2017). Ferroelectrics and Their Applications. In: Reference Module in Materials Science and Materials Engineering (Elsevier). doi:10.1016/B978-0-12-803581-8.04143-6.

72. Bain, A.K., and Chand, P. (2022). Pyroelectric Materials. (Weinheim, Wiley).

73. Whatmore, R.W. (1986). Pyroelectric devices and materials. Reports on Progress in Physics *49*, 1335–1386. doi:10.1088/0034-4885/49/12/002.

74. GILCHRIST, J.D. (1977). Heat Transfer. In: Fuels, Furnaces and Refractories (Elsevier), pp. 150–171. doi:10.1016/B978-0-08-020430-7.50018-9.

75. Bergman, T.L., Lavine, A.S., Incropera, F.P., and DeWitt, D.P. (2020). Fundamentals of Heat and Mass Transfer Eighth edition.  (New York, Wiley).

185

76.     Çengel, Y.A., and Boles, M.A. (2010). Thermodynamics: An Engineering Approach Seventh edition. (New York, McGraw-Hill).

77.     Holman, J.P. (1981). Heat transfer Fifth edition. (New York, McGraw-Hill Inc).

78.     Wang, A., and Zhao, J. (2010). Review of prediction for thermal contact resistance. Sci China Technol Sci *53*, 1798–1808. doi:10.1007/s11431-009-3190-6.

79.     Schütze, T. (2008). AN2008-03: Thermal equivalent circuit models. Application Note. V1.0. Germany: Infineon Technologies AG.

80.     Handbook of Physical Vapor Deposition (PVD) Processing (2010). (Amsterdam, William Andrew-Elsevier). doi:10.1016/C2009-0-18800-1.

81.     Hassan, M.M. (2018). Antimicrobial Coatings for Textiles. In: Handbook of Antimicrobial Coatings (Elsevier), pp. 321–355. doi:10.1016/B978-0-12-811982-2.00016-0.

82.     Tudose, I.V., Comanescu, F., Pascariu, P., Bucur, S., Rusen, L., Iacomi, F., Koudoumas, E., and Suchea, M.P. (2019). Chemical and physical methods for multifunctional nanostructured interface fabrication. In: Functional Nanostructured Interfaces for Environmental and Biomedical Applications (Elsevier), pp. 15–26. doi:10.1016/B978-0-12-814401-5.00002-5.

83.     Mostafaei, A., Rodriguez De Vecchis, P., Stevens, E.L., and Chmielus, M. (2018). Sintering regimes and resulting microstructure and properties of binder jet 3D printed Ni-Mn-Ga magnetic shape memory alloys. Acta Mater *154*, 355–364. doi:10.1016/j.actamat.2018.05.047.

84.     Ohtsuka, M., and Itagaki, K. (2001). Effect of heat treatment on properties of Ni-Mn-Ga films prepared by a sputtering method. International Journal of Applied Electromagnetics and Mechanics *12*, 49–59. doi:10.3233/JAE-2000-194.

85.     Czaja, P., Przewoźnik, J., and Fitta, M. (2021). Heat treatment effect on the evolution of magnetic properties of martensite in magnetic shape memory Ni48Mn39.5Sn9.5Al3 Heusler alloy ribbons. Mater Res Bull *135*, 111120. doi:10.1016/j.materresbull.2020.111120.

86.     Morgan, C., Shan Chen, G., Boothroyd, C., Bailey, S., and Humphreys, C. (1992). Ultimate limits of lithography. Physics World *5*, 28–34. doi:10.1088/2058-7058/5/11/27.

87.   Deubel, M., von Freymann, G., Wegener, M., Pereira, S., Busch, K., and Soukoulis, C.M. (2004). Direct laser writing of three-dimensional photonic-crystal templates for telecommunications. Nat Mater *3*, 444–447. doi:10.1038/nmat1155.

88.   Mann, R.P., Nayak, A.P., Islam, M.S., Logeeswaran, V.J., Bormashenko, E., Wilson, K.A., and Vollmer, F. (2012). Wet Etching. In: Encyclopedia of Nanotechnology (Springer Netherlands), pp. 2829–2830. doi:10.1007/978-90-481-9751-4_431.

89.   Priya, S., and Inman, D.J. (2009). Energy Harvesting Technologies S. Priya and D. J. Inman, eds. (New York, Springer). doi:10.1007/978-0-387-76464-1.

90.   Gültig, M. (2016). Thermal Energy Harvesting based on Magnetic Shape Memory Alloys (Doctoral thesis, Karlsruhe Institute of Technology). doi:10.5445/IR/1000062034.

91.   Joseph, J., Ohtsuka, M., Miki, H., and Kohl, M. (2022). Thermal processes of miniature thermomagnetic generators in resonant self-actuation mode. iScience *25*, doi:104569. 10.1016/j.isci.2022.104569.

92.   Gueltig, M., Wendler, F., Ossmer, H., Ohtsuka, M., Miki, H., Takagi, T., and Kohl, M. (2017). High-Performance Thermomagnetic Generators Based on Heusler Alloy Films. Adv Energy Mater *7*, 1601879. doi:10.1002/aenm.201601879.

93.   Kishore, R.A., and Priya, S. (2018). A Review on low-grade thermal energy harvesting: Materials, methods and devices. Materials *11*. doi:10.3390/ma11081433.

94.   Kishore, R.A., Singh, D., Sriramdas, R., Garcia, A.J., Sanghadasa, M., and Priya, S. (2020). Linear thermomagnetic energy harvester for low-grade thermal energy harvesting. J Appl Phys *127*, 044501. doi:10.1063/1.5124312.

95.   Hsu, C.J., Sandoval, S.M., Wetzlar, K.P., and Carman, G.P. (2011). Thermomagnetic conversion efficiencies for ferromagnetic materials. J Appl Phys *110*, 123923. doi:10.1063/1.3672844.

96.   Edison T. Pyromagnetic Motor. Patent No. 380,100. 1888 Mar 27.

97.    Tesla N. Thermo Magnetic Motor. Patent No. 396,121. 1889 Jan 15.

98.   Tesla N. Pyromagneto Electric Generator. Patent No. 428,057. 1890 May 13.

99.   Edison TA. Pyromagnetic Generator. Patent No. 476,983. 1892 June 14.

100.  Brillouin, L., and Iskenderian, H.P. (1948). Thermomagnetic Generator. Electronic Communications *25*, 300–311.

101.  Rosensweig, R.E. (1967). Theory of an improved thermomagnetic generator. Proceedings of the Institution of Electrical Engineers *114*, 405. doi:10.1049/piee.1967.0088.

102.  Elliott, J.F. (1959). Thermomagnetic Generator. J Appl Phys *30*, 1774–1777. doi:10.1063/1.1735054.

103.  Stauss, H.E. (1959). Efficiency of Thermomagnetic Generator. J Appl Phys *30*, 1622–1623. doi:10.1063/1.1735020.

104.  Dan'kov, S.Yu., Tishin, A.M., Pecharsky, V.K., and Gschneidner, K.A. (1998). Magnetic phase transitions and the magnetothermal properties of gadolinium. Phys Rev B *57*, 3478–3490. doi:10.1103/PhysRevB.57.3478.

105.  Kirol, L.D., and Mills, J.I. (1984). Numerical analysis of thermomagnetic generators. J Appl Phys *56*, 824–828. doi:10.1063/1.334015.

106.  Solomon, D. (1988). Improving the performance of a thermomagnetic generator by cycling the magnetic field. J Appl Phys *63*, 915–921. doi:10.1063/1.340033.

107.  Song, Y., Bhatti, K.P., Srivastava, V., Leighton, C., and James, R.D. (2013). Thermodynamics of energy conversion via first order phase transformation in low hysteresis magnetic materials. Energy Environ Sci *6*, 1315. doi:10.1039/c3ee24021e.

108.  Srivastava, V., Song, Y., Bhatti, K., and James, R.D. (2011). The Direct Conversion of Heat to Electricity Using Multiferroic Alloys. Adv Energy Mater *1*, 97–104. doi:10.1002/aenm.201000048.

109.  Christiaanse, T., and Brück, E. (2014). Proof-of-Concept Static Thermomagnetic Generator Experimental Device. Metallurgical and Materials Transactions E *1*, 36–40. doi:10.1007/s40553-014-0006-9.

110.  Waske, A., Dzekan, D., Sellschopp, K., Berger, D., Stork, A., Nielsch, K., and Fähler, S. (2019). Energy harvesting near room temperature using a thermomagnetic generator with a pretzel-like magnetic flux topology. Nat Energy *4*, 68–74. doi:10.1038/s41560-018-0306-x.

111.  Ujihara, M., Carman, G.P., and Lee, D.G. (2007). Thermal energy harvesting device using ferromagnetic materials. Appl Phys Lett *91*, 093508. doi:10.1063/1.2775096.

112.  Bulgrin, K.E., Ju, Y.S., Carman, G.P., and Lavine, A.S. (2009). A Coupled Thermal and Mechanical Model of a Thermal Energy Harvesting Device. In: Volume 6: Emerging Technologies: Alternative Energy Systems; Energy Systems: Analysis,

Thermodynamics and Sustainability (ASMEDC), pp. 327–335. doi:10.1115/IMECE2009-13040.

113. Ahmim, S., Almanza, M., Pasko, A., Mazaleyrat, F., and LoBue, M. (2019). Thermal energy harvesting system based on magnetocaloric materials. The European Physical Journal Applied Physics *85*, 10902. doi:10.1051/epjap/2019180284.

114. Ahmim, S., Almanza, M., Loyau, V., Mazaleyrat, F., Pasko, A., Parrain, F., and LoBue, M. (2021). Self-oscillation and heat management in a LaFeSi based thermomagnetic generator. J Magn Magn Mater *540*, 168428. doi:10.1016/j.jmmm.2021.168428.

115. Rodrigues, C., Pires, A., Gonçalves, I., Silva, D., Oliveira, J., Pereira, A., and Ventura, J. (2022). Hybridizing Triboelectric and Thermomagnetic Effects: A Novel Low-Grade Thermal Energy Harvesting Technology. Adv Funct Mater *32*, 2110288. doi:10.1002/adfm.202110288.

116. Wang, Z.L. (2013). Triboelectric Nanogenerators as New Energy Technology for Self-Powered Systems and as Active Mechanical and Chemical Sensors. ACS Nano *7*, 9533–9557. doi:10.1021/nn404614z.

117. Lallart, M., Yan, L., Miki, H., Sebald, G., Diguet, G., Ohtsuka, M., and Kohl, M. (2021). Heusler alloy-based heat engine using pyroelectric conversion for small-scale thermal energy harvesting. Appl Energy *288*, 116617. doi:10.1016/j.apenergy.2021.116617.

118. Chen, C.C., Chung, T.K., Tseng, C.Y., Hung, C.F., Yeh, P.C., and Cheng, C.C. (2015). A Miniature Magnetic-Piezoelectric Thermal Energy Harvester. IEEE Trans Magn *51*. doi:10.1109/TMAG.2015.2395385.

119. Chun, J., Song, H.-C., Kang, M.-G., Kang, H.B., Kishore, R.A., and Priya, S. (2017). Thermo-Magneto-Electric Generator Arrays for Active Heat Recovery System. Sci Rep *7*, 41383. doi:10.1038/srep41383.

120. Chun, J., Kishore, R.A., Kumar, P., Kang, M.-G., Kang, H.B., Sanghadasa, M., and Priya, S. (2018). Self-Powered Temperature-Mapping Sensors Based on Thermo-Magneto-Electric Generator. ACS Appl Mater Interfaces *10*, 10796–10803. doi:10.1021/acsami.7b17686.

121. Carlioz, L., Delamare, J., and Basrour, S. (2009). Temperature threshold tuning of a thermal harvesting switch. In TRANSDUCERS 2009 - 2009 International Solid-

State Sensors, Actuators and Microsystems Conference (IEEE), pp. 1385–1388. doi:10.1109/SENSOR.2009.5285830.

122. Brungsberg HJ. Device for converting thermal energy into electrical or mechanical energy by means of a magnetic system. Patent No. DE3106520A1. 1982 Dec 23.

123. Ohkoshi, M., Kobayashi, H., Katayama, T., Hirano, M., and Tsushima, T. (1976). A Proposal of Application of Spin Reorientation Phenomenon to the Thermomagnetic Power Generation. Jpn J Appl Phys *15*, 2019–2020. doi:10.1143/jjap.15.2019.

124. Gueltig, M., Ossmer, H., Ohtsuka, M., Miki, H., Tsuchiya, K., Takagi, T., and Kohl, M. (2014). High frequency thermal energy harvesting using magnetic shape memory films. Adv Energy Mater *4*, 1400751. doi:10.1002/aenm.201400751.

125. Kohl, M., Gueltig, M., and Wendler, F. (2018). Coupled Simulation of Thermomagnetic Energy Generation Based on NiMnGa Heusler Alloy Films. Shape Memory and Superelasticity *4*, 242–255. doi:10.1007/s40830-018-0148-1.

126. Kohl, M., Krevet, B., Ohtsuka, M., Brugger, D., and Liu, Y. (2006). Ferromagnetic shape memory microactuators. Mater Trans *47*, 639–644. doi:10.2320/matertrans.47.639.

127. Kohl, M., Brugger, D., Ohtsuka, M., and Takagi, T. (2004). A novel actuation mechanism on the basis of ferromagnetic SMA thin films. Sens Actuators A Phys *114*, 445–450. doi:10.1016/j.sna.2003.11.006.

128. Joseph, J., Ohtsuka, M., Miki, H., and Kohl, M. (2021). Lumped Element Model for Thermomagnetic Generators Based on Magnetic SMA Films. Materials *14*, 1234. doi:10.3390/ma14051234.

129. Sumali, H., and Carne, T.G. (2008). Air-drag Damping on Micro-Cantilever Beams. Conference Proceedings of the Society for Experimental Mechanics Series, 1–7. Available at https://www.osti.gov/servlets/purl/1146165. (Accessed online: 15.10.2022)

130. Onorato, P., and De Ambrosis, A. (2012). Magnetic damping: Integrating experimental and theoretical analysis. Am J Phys *80*, 27–35. doi:10.1119/1.3647997.

131. Rubin, S. (1962). Concepts in Shock and Data Analyses. In Harris' Shock and Vibration Handbook, C. M. Harris and A. G. Piersol, eds. (New York, McGRAW-HILL), pp. 65–66.

132. Engel, A., and Friedrichs, R. (2002). On the electromagnetic force on a polarizable body. American Journal of Physics 70, *70*, 428–432. doi:10.1119/1.1432971.

133. Xiao-fan, G., Yong, Y., and Xiao-jing, Z. (2004). Analytic expression of magnetic field distribution of rectangular permanent magnets. Appl Math Mech *25*, 297–306. doi:10.1007/BF02437333.

134. Sidebotham, G. (2015). Thermal Circuits. In Heat Transfer Modeling: An Inductive Approach (Berlin, Springer International Publishing), pp. 3–29. doi:10.1007/978-3-319-14514-3_1.

135. Sozinov, A., Likhachev, A.A., Lanska, N., and Ullakko, K. (2002). Giant magnetic-field-induced strain in NiMnGa seven-layered martensitic phase. Appl Phys Lett *80*, 1746–1748. doi:10.1063/1.1458075.

136. Heczko, O., Seiner, H., and Fähler, S. (2022). Coupling between ferromagnetic and ferroelastic transitions and ordering in Heusler alloys produces new multifunctionality. MRS Bull *47*, 618–627. doi:10.1557/s43577-022-00354-x.

137. Musiienko, D., Straka, L., Klimša, L., Saren, A., Sozinov, A., Heczko, O., and Ullakko, K. (2018). Giant magnetic-field-induced strain in Ni-Mn-Ga micropillars. Scr Mater *150*, 173–176. doi:10.1016/j.scriptamat.2018.03.020.

138. Suzuki, M., Ohtsuka, M., Suzuki, T., Matsumoto, M., and Miki, H. (1999). Fabrication and Characterization of Sputtered Ni2MnGa Thin Films. Materials Transactions, JIM *40*, 1174–1177. doi:10.2320/matertrans1989.40.1174.

139. Chernenko, V.A., Besseghini, S., Hagler, M., Müllner, P., Ohtsuka, M., and Stortiero, F. (2008). Properties of sputter-deposited Ni–Mn–Ga thin films. Materials Science and Engineering: A *481–482*, 271–274. doi:10.1016/j.msea.2006.12.206.

140. Kohl, M., Chernenko, V.A., Ohtsuka, M., Reuter, H., and Takagi, T. (2004). Magnetic properties of submicron Ni-Mn-Ga martensitic thin films1. MRS Proceedings *855*, W2.8. doi:10.1557/PROC-855-W2.8.

141. Chernenko, V. (1999). Compositional instability of β-phase in Ni-Mn-Ga alloys. Scr Mater *40*, 523–527. doi:10.1016/S1359-6462(98)00494-1.

142. Ohtsuka, M., Sanada, M., Matsumoto, M., Takagi, T., and Itagaki, K. (2003). Shape memory behavior of Ni-Mn-Ga sputtered films under a magnetic field. Mater Trans *44*, 2513–2519. doi:10.2320/matertrans.44.2513.

143. Beiss, P. (2002). Non-ferrous materials. In Powder Metallurgy Data Landolt-Börnstein - Group VIII Advanced Materials and Technologies., P. Beiss, R. Ruthardt, and H. Warlimont, eds. (Berlin, Springer-Verlag), pp. 194–204. doi:10.1007/b83029.

144. Tickle, R., and James, R.D. (1999). Magnetic and magnetomechanical properties of Ni2MnGa. J Magn Magn Mater *195*, 627–638. doi:10.1016/S0304-8853(99)00292-9.

145. Assmus, W., Brühne, S., Charra, F., Chiarotti, G., Fischer, C., Fuchs, G., Goodwin, F., Gota-Goldman, S., Guruswamy, S., Gurzadyan, G., et al. (2005). Springer Handbook of Condensed Matter and Materials Data W. Martienssen and H. Warlimont, eds. (Berlin, Springer). doi:10.1007/3-540-30437-1.

146. Gere, J.M., and Timoshenko, S. (1997). Mechanics of Materials 4th ed. (PWS, Boston). Available at https://trove.nla.gov.au/version/172816358. (Accessed online: 15.10.2022).

147. Young, H., and Freedman, R.A. (2016). Sears and Zemansky's University physics with modern physics Fourteenth edition (Harlow, England : Pearson Education Limited).

148. Söderberg, O., Aaltio, I., Ge, Y., Heczko, O., and Hannula, S.P. (2008). Ni-Mn-Ga multifunctional compounds. Materials Science and Engineering A *481–482*, 80–85. doi:10.1016/j.msea.2006.12.191.

149. Karwa, R. (2017). Thermal contact resistance. In: Heat and Mass Transfer (Singapore, Springer Nature), pp. 101–104. doi:10.1007/978-981-15-3988-6.

150. Joseph, J., Wehr, M., Miki, H., Ohtsuka, M., and Kohl, M. (2021). Coupling Effects in Parallel Thermomagnetic Generators Based on Resonant Self-Actuation. In: 2021 21st International Conference on Solid-State Sensors, Actuators and Microsystems (Transducers) (IEEE), pp. 463–466. doi:10.1109/Transducers50396.2021.9495569.

151. Nozariasbmarz, A., Collins, H., Dsouza, K., Polash, M.H., Hosseini, M., Hyland, M., Liu, J., Malhotra, A., Ortiz, F.M., Mohaddes, F., et al. (2020). Review of wearable thermoelectric energy harvesting: From body temperature to electronic systems. Appl Energy *258*, 114069. doi:10.1016/j.apenergy.2019.114069.

152. Joseph, J., Fontana, E., Devillers, T., Dempsey, N.M., and Kohl, M. (2023). A Gd-Film Thermomagnetic Generator in Resonant Self-Actuation Mode. Adv Funct Mater, 2301250. doi:10.1002/adfm.202301250.

153. Nguyen Ba, D., Zheng, Y., Becerra, L., Marangolo, M., Almanza, M., and LoBue, M. (2021). Magnetocaloric Effect in Flexible, Free-Standing Gadolinium Thick Films for Energy Conversion Applications. Phys Rev Appl *15*, 064045. doi:10.1103/PhysRevApplied.15.064045.

154. Ba, D.N., Becerra, L., Casaretto, N., Duvauchelle, J.-E., Marangolo, M., Ahmim, S., Almanza, M., and LoBue, M. (2020). Magnetocaloric Gadolinium thick films for energy harvesting applications. AIP Adv *10*, 035110. doi:10.1063/1.5130014.

155. Fontana, E. (2022). Development of functional magnetic materials for energy harvesting at the micro-scale (Doctoral dissertation, Université Grenoble Alpes). Retrieved from https://theses.hal.science/tel-03828636. (Accessed online: 15.04.2023)

156. Gutfleisch, O., Yan, A., and Müller, K.-H. (2005). Large magnetocaloric effect in melt-spun LaFe13−xSix. J Appl Phys *97*, 10M305. doi:10.1063/1.1847871.

157. Arajs, S., and Colvin, R. V. (1964). Thermal Conductivity and Lorenz Function of Gadolinium between 5° and 310°K. J Appl Phys *35*, 1043–1044. doi:10.1063/1.1713370.

158. Griffel, M., Skochdopole, R.E., and Spedding, F.H. (1954). The Heat Capacity of Gadolinium from 15 to 355°K. Physical Review *93*, 657–661. doi:10.1103/PhysRev.93.657.

159. Li, Y.Q., Wu, Q.C., Shen, F.R., Zhou, H.B., Hu, F.X., Wang, J., Sun, J.R., and Shen, B.G. (2019). Mechanical and magnetocaloric properties of La(Fe,Mn,Si)13Hδ/Cu plates prepared by Cu-binding prior to hydrogenation. Intermetallics (Barking) *106*, 124–129. doi:10.1016/j.intermet.2019.01.003.

160. Fukamichi, K., Fujita, A., and Fujieda, S. (2006). Large magnetocaloric effects and thermal transport properties of La(FeSi)13 and their hydrides. J Alloys Compd *408–412*, 307–312. doi:10.1016/j.jallcom.2005.04.022.

161. Bahl, C.R.H., Navickaitė, K., Neves Bez, H., Lei, T., Engelbrecht, K., Bjørk, R., Li, K., Li, Z., Shen, J., Dai, W., et al. (2017). Operational test of bonded magnetocaloric

plates. International Journal of Refrigeration *76*, 245–251. doi:10.1016/j.ijre-frig.2017.02.016.

162.   Wang, F., Chen, Y.-F., Wang, G.-J., and Shen, B.-G. (2003). The effect of Mn substitution in LaFe $_{11.7}$ Si $_{1.3}$ compound on the magnetic properties and magnetic entropy changes. J Phys D Appl Phys *36*, 1–3. doi:10.1088/0022-3727/36/1/301.

163.   Dzekan, D., Waske, A., Nielsch, K., and Fähler, S. (2021). Efficient and affordable thermomagnetic materials for harvesting low grade waste heat. APL Mater *9*, 011105. doi:10.1063/5.0033970.

164.   Dzekan, D., Diestel, A., Berger, D., Nielsch, K., and Fähler, S. (2021). Can gadolinium compete with La-Fe-Co-Si in a thermomagnetic generator? Sci Technol Adv Mater *22*, 643–657. doi:10.1080/14686996.2021.1957657.

165.   Post, A., Knight, C., and Kisi, E. (2013). Thermomagnetic energy harvesting with first order phase change materials. J Appl Phys *114*, 033915. doi:10.1063/1.4815933.

# Table of Figures

199

204

# Table of Tables

# Appendix

**Table A 1** Important values of temperatures for the TMG upscaling

| Device film thickness: 40 µm | | | | | |
|---|---|---|---|---|---|
| Source temperature | 130 | 140 | 150 | 160 | 170 |
| Sink temperature ($T_{cant}$) | 87 | 87 | 87 | 87 | 87 |
| $T_{top}$ (max) | 91 | 91.1 | 91.2 | 91.3 | 91.3 |
| $T_{top}$ (min) | 88.9 | 88.8 | 88.6 | 88.4 | 88.4 |
| $T_{bot}$ (max) | 90.3 | 90.4 | 90.4 | 90.4 | 90.4 |
| $T_{bot}$ (min) | 88.8 | 88.7 | 88.6 | 88.4 | 88.4 |
| Temperature change ($T_{top}$) | 2.1 | 2.3 | 2.6 | 2.8 | 2.9 |
| Temperature change ($T_{bot}$) | 1.5 | 1.7 | 1.8 | 2 | 2 |
| **Device film thickness: 20 µm** | | | | | |
| Source temperature | 130 | 140 | 150 | 160 | 170 |
| Sink temperature | 91 | 91 | 91 | 91 | 91 |
| $T_{top}$ (max) | 96.5 | 96.6 | 96.7 | 96.8 | 96.9 |
| $T_{top}$ (min) | 93.8 | 92.9 | 91.5 | 91.5 | 91.5 |
| $T_{bot}$ (max) | 96.4 | 96.5 | 96.6 | 96.7 | 96.7 |
| $T_{bot}$ (min) | 93.8 | 92.9 | 91.5 | 91.5 | 91.5 |
| Temperature change ($T_{top}$) | 2.7 | 3.7 | 4.8 | 5.3 | 5.4 |

| Temperature change (T$_{bot}$) | 2.6 | 3.6 | 5.1 | 5.2 | 5.2 |
| **Device film thickness: 10 μm** | | | | | |
| Source temperature | 130 | 140 | 150 | 160 | 170 |
| Sink temperature | 93 | 93 | 93 | 93 | 93 |
| T$_{top}$ (max) | 100.9 | 101 | 101 | 101.1 | 101.1 |
| T$_{top}$ (min) | 94,9 | 93,6 | 92,6 | 91,9 | 91 |
| Temperature change (T$_{top}$) | 6 | 7.4 | 8.4 | 9.2 | 10.1 |
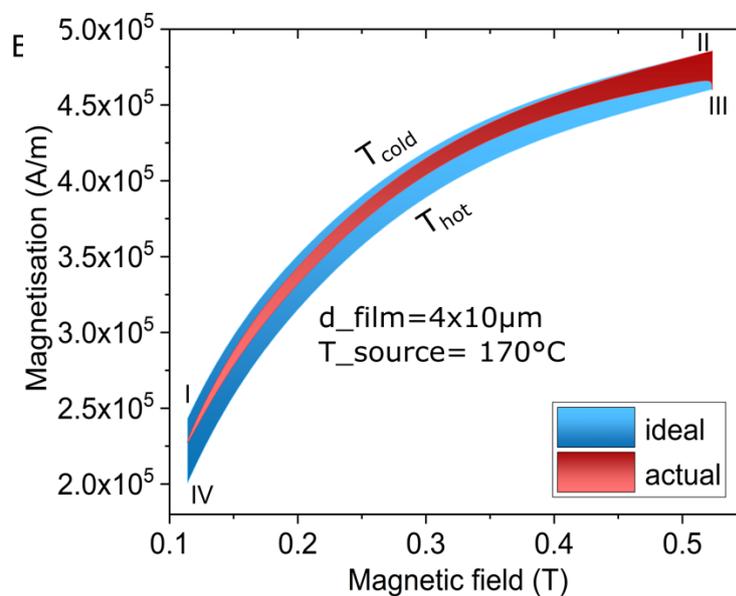


**Figure A 1** The magnetization cycle in TMG, with values corresponding to operation in resonant self-actuation mode of TMG with 40μm Ni-Mn-Ga film. Adapted from Joseph et al.[28]

$R_L$ has a significant impact on TMG performance. When $R_L$ is matched to the internal resistance of the pick-up coil, which is roughly 220 Ohm, the transfer efficiency is greatest. However, as $R_L$ is raised, the power increases owing to reduced electromagnetic damping, leading in a greater frequency and stroke of operation. Simultaneously, the transfer efficiency decreases, and a distinct maximum occurs at 500 Ohm. Even if the frequency and stroke are still growing at higher $R_L$, the decrease in electromagnetic damping is insufficient to compensate for the loss in transfer efficiency.
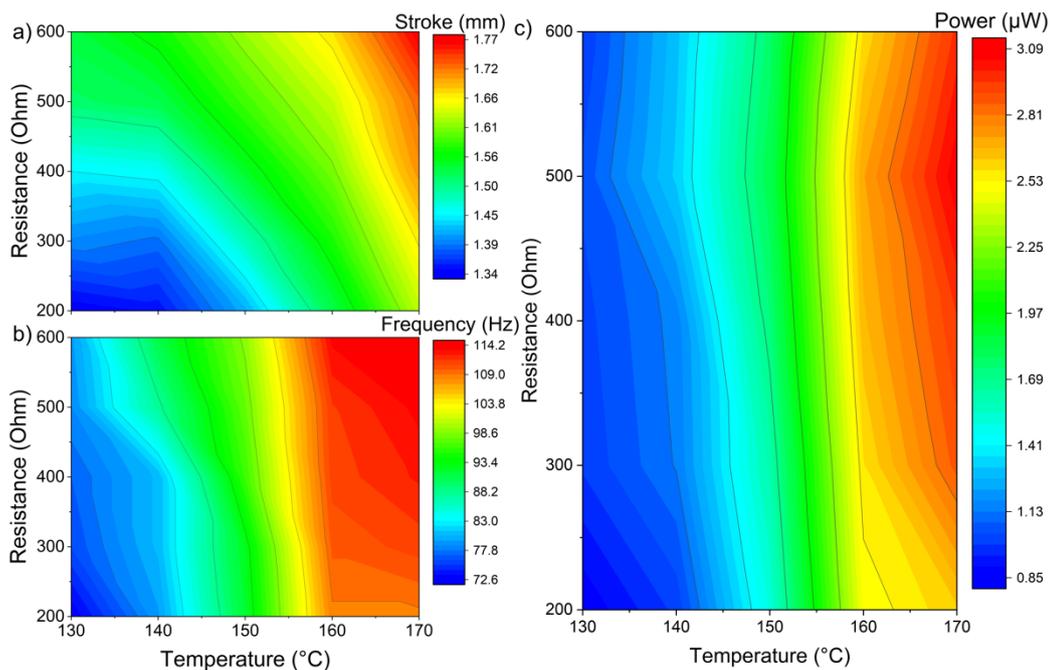
**Figure A 2** The mechanical and electrical performance of the TMG device with Ni-Mn-Ga 10µm as a function of load resistance ($R_L$) and heat source temperature ($T_{source}$). The supplied color code can be used to calculate numerical values. (a) Stroke during resonant self-actuation, (b) oscillation frequency, (c) electrical power output.
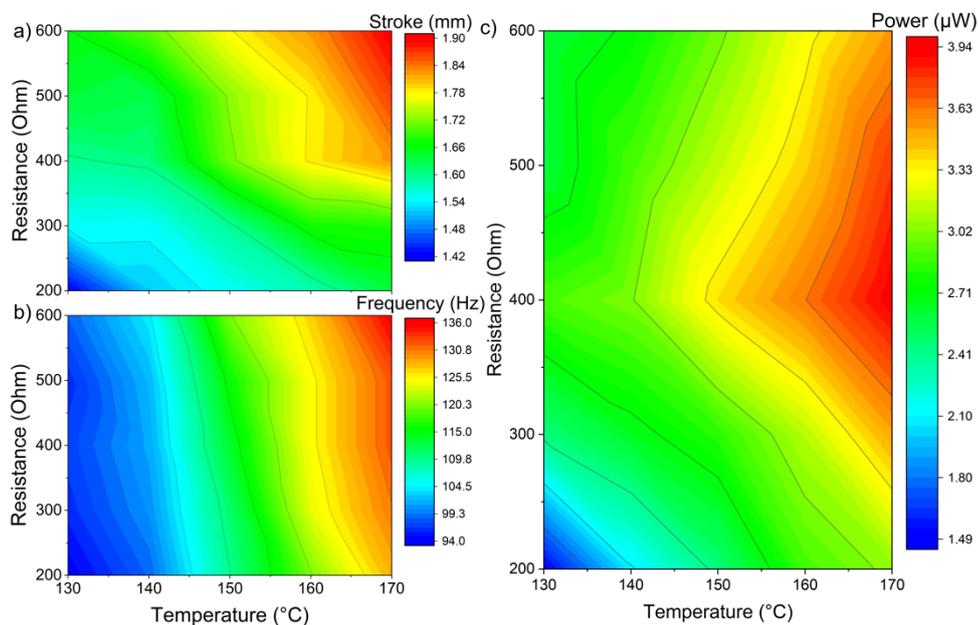


**Figure A 3** The mechanical and electrical performance of the TMG device with Ni-Mn-Ga 20µm as a function of load resistance ($R_L$) and heat source temperature ($T_{source}$). The supplied color code can be used to calculate numerical values. (a) Stroke during resonant self-actuation, (b) oscillation frequency, (c) electrical power output.
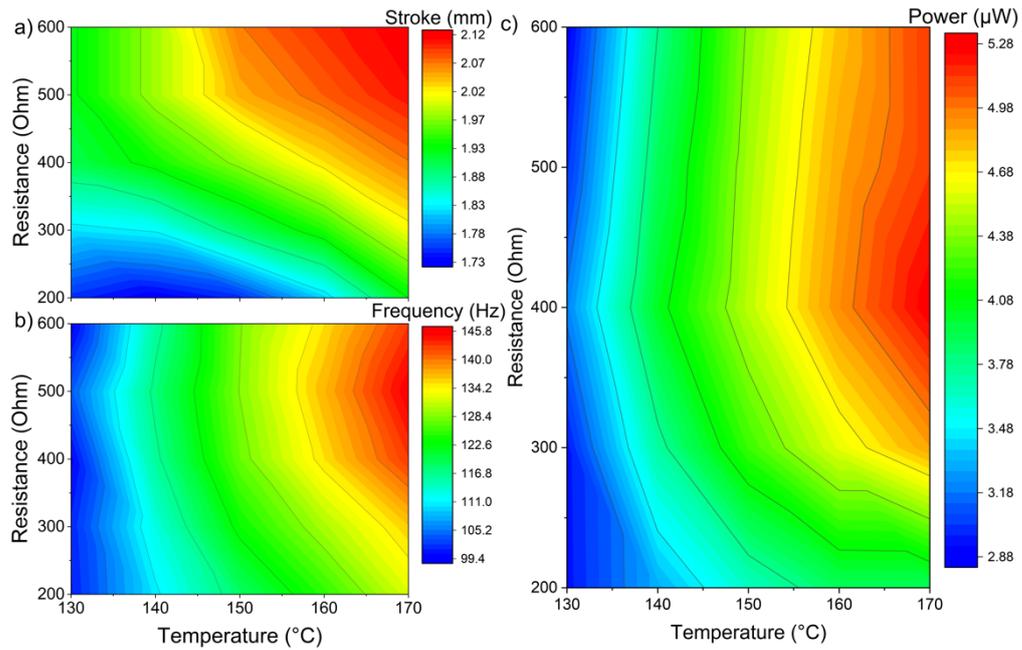
**Figure A 4** The mechanical and electrical performance of the TMG device with Ni-Mn-Ga 40µm as a function of load resistance ($R_L$) and heat source temperature ($T_{source}$). The supplied color code can be used to calculate numerical values. (a) Stroke during resonant self-actuation, (b) oscillation frequency, (c) electrical power output.
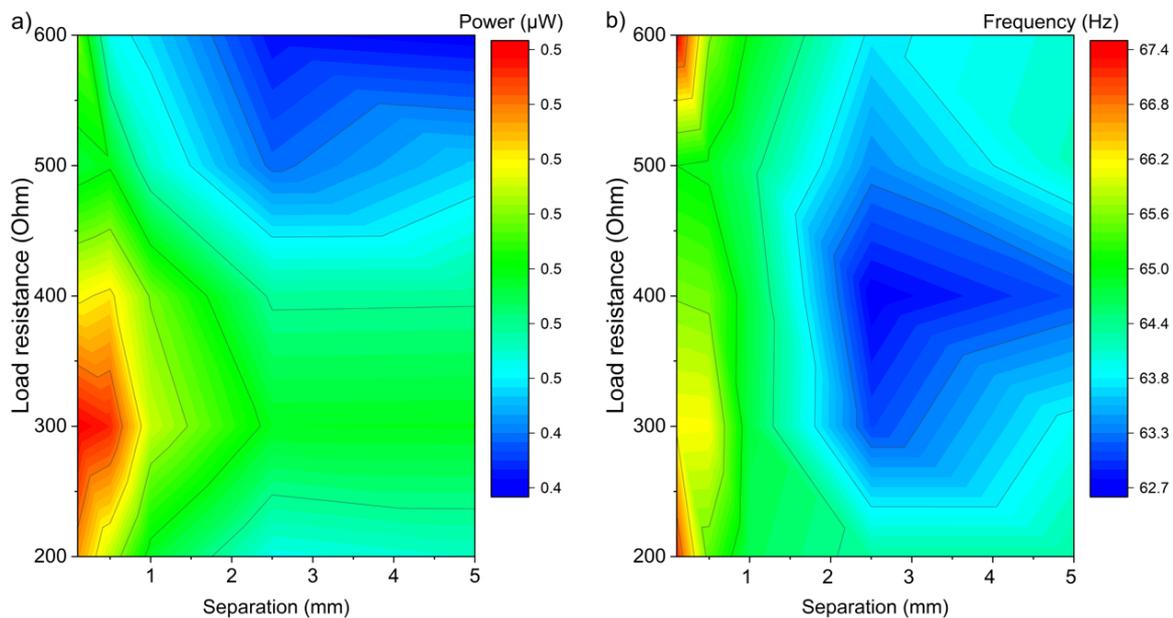


**Figure A 5** Effect of resistance and separation on performance of TMG at center in three device array with 10µm Ni-Mn-Ga. (a) Power output of TMG, (b) frequency of operation of TMG.
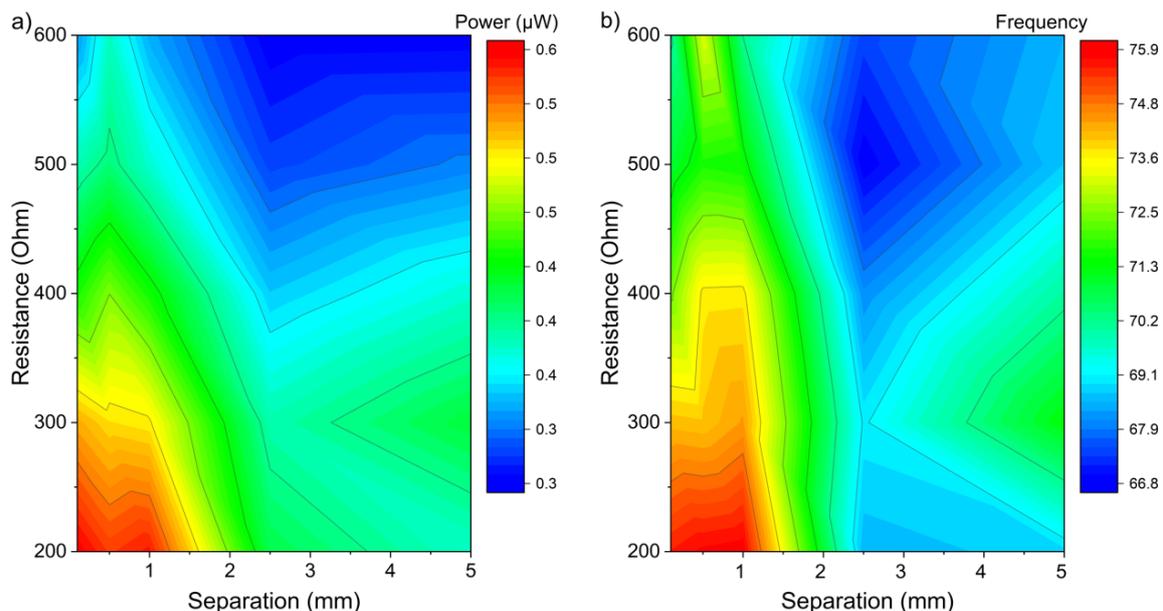
**Figure A 6** Effect of resistance and separation on performance of TMG in three device array with 20μm Ni-Mn-Ga film. (a) Power output of TMG, (b) frequency of TMG operation.
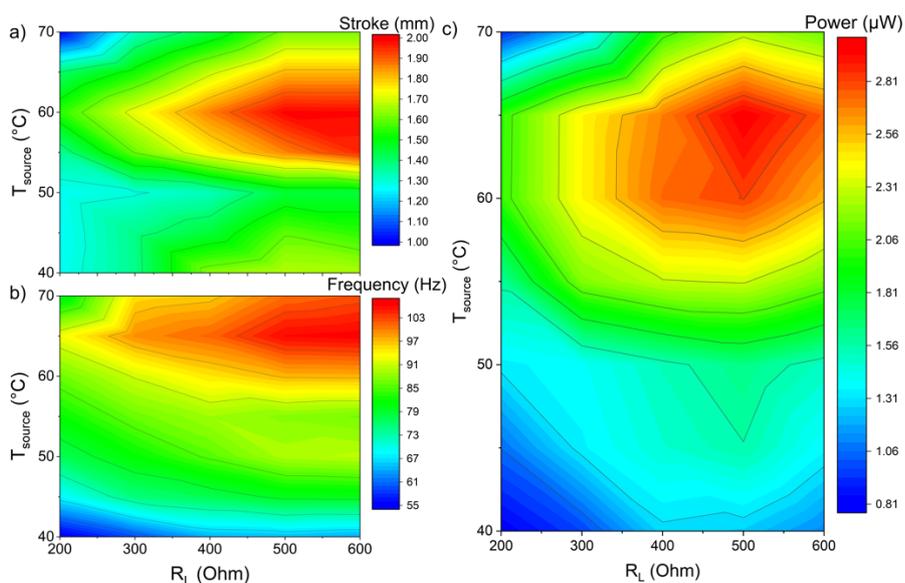


**Figure A 7** The mechanical and electrical performance of the Gd TMG device as a function of load resistance ($R_L$) and heat source temperature ($T_{source}$) at 11 °C ambient temperature were investigated. The supplied color code can be used to calculate numerical values. (a) Cantilever front stroke during resonant self-actuation, (b) cantilever front oscillation frequency, (c) electrical power output.
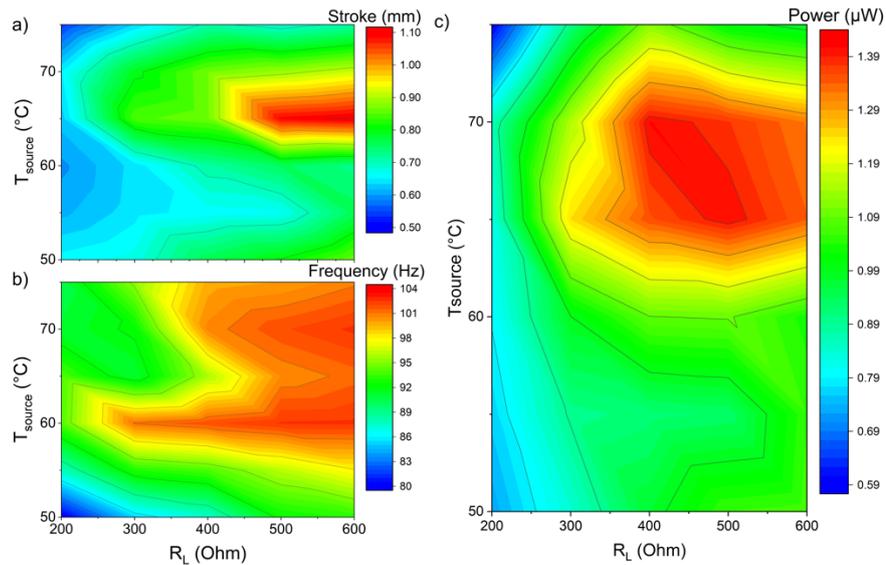
**Figure A 8** The mechanical and electrical performance of the Gd TMG device as a function of load resistance (R$_L$) and heat source temperature (T$_{source}$) at 19 °C ambient temperature were investigated. The supplied color code can be used to calculate numerical values. (a) Cantilever front stroke during resonant self-actuation, (b) cantilever front oscillation frequency, (c) electrical power output determined from the induced current of the pick-up coil.
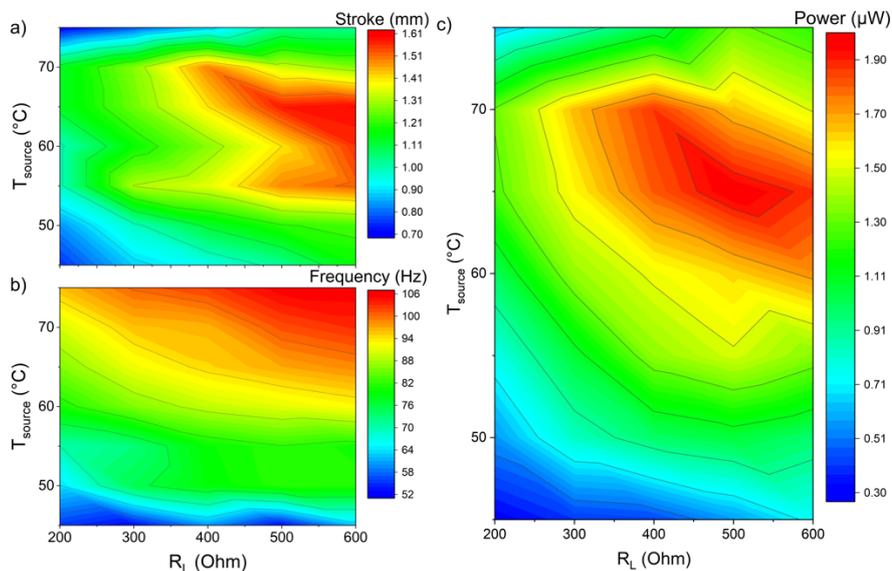


**Figure A 9** The mechanical and electrical performance of the Gd TMG device as a function of load resistance (R$_L$) and heat source temperature (T$_{source}$) at 17°C ambient temperature were investigated. The supplied color code can be used to calculate numerical values. (a) Cantilever front stroke during resonant self-actuation, (b) cantilever front oscillation frequency, (c) electrical power output determined from the induced current of the pick-up coil.
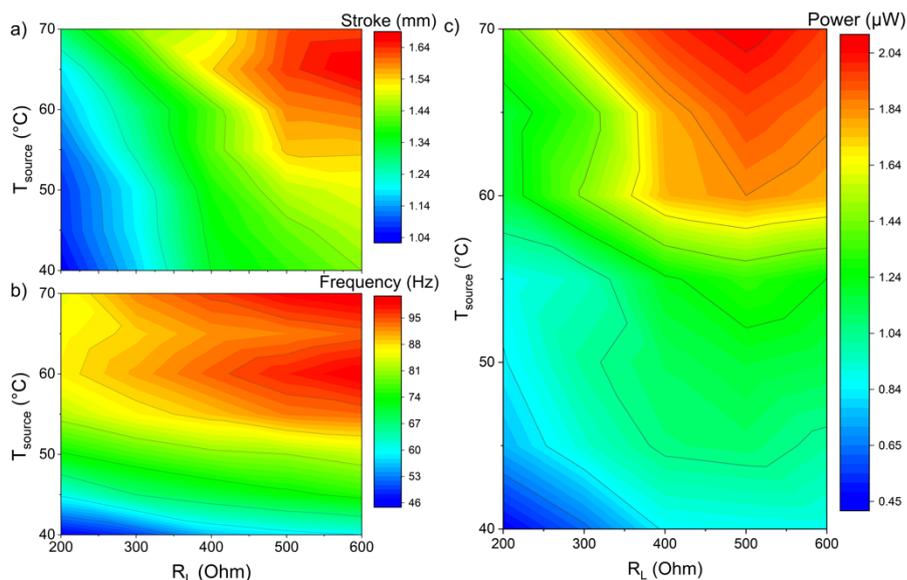
**Figure A 10** The mechanical and electrical performance of the Gd TMG device as a function of load resistance ($R_L$) and heat source temperature ($T_{source}$) at 15 °C ambient temperature were investigated. The supplied color code can be used to calculate numerical values. (a) Cantilever front stroke during resonant self-actuation, (b) cantilever front oscillation frequency, (c) electrical power output determined from the induced current of the pick-up coil.
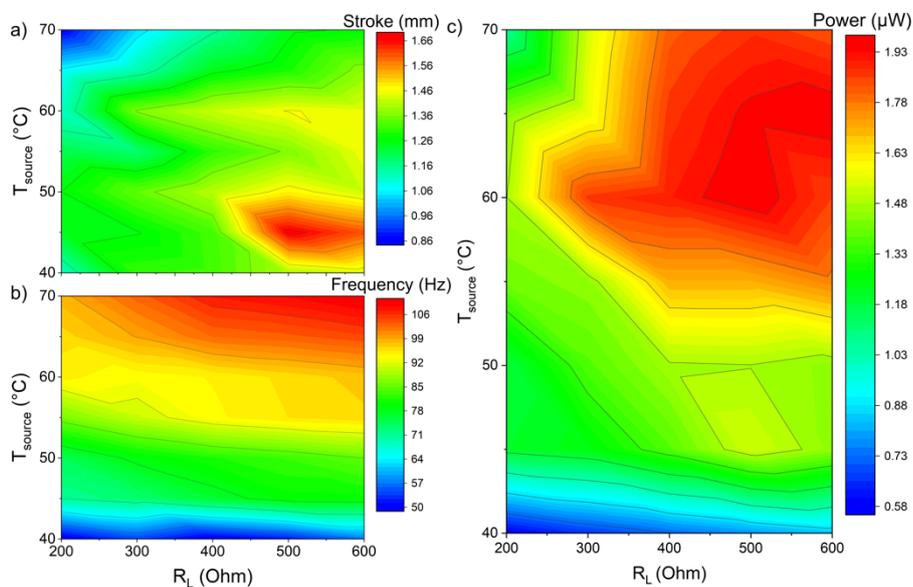


**Figure A 11** The mechanical and electrical performance of the Gd TMG device as a function of load resistance ($R_L$) and heat source temperature ($T_{source}$) at 13 °C ambient temperature were investigated. The supplied color code can be used to calculate numerical values. (a) Cantilever front stroke during resonant self-actuation, (b) cantilever front oscillation frequency, (c) electrical power output determined from the induced current of the pick-up coil.
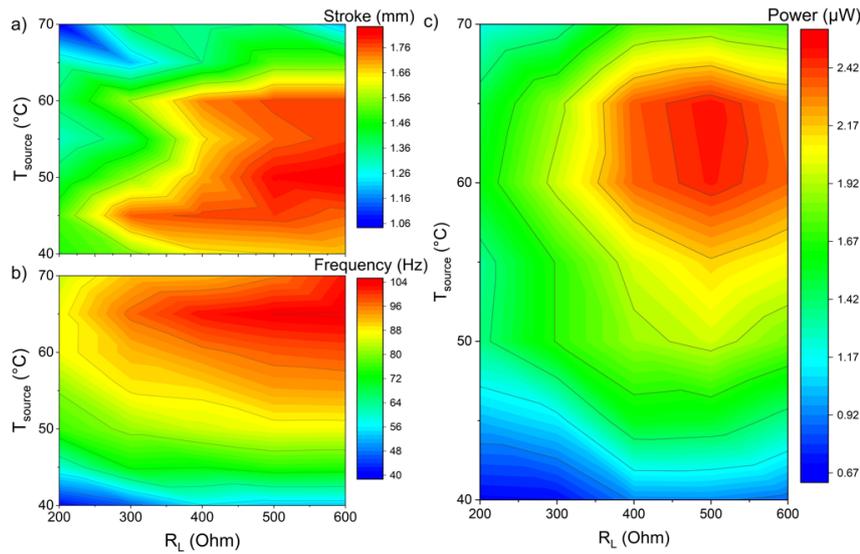
**Figure A 12** The mechanical and electrical performance of the Gd TMG device as a function of load resistance ($R_L$) and heat source temperature ($T_{source}$) at 9 °C ambient temperature were investigated. The supplied color code can be used to calculate numerical values. (a) Cantilever front stroke during resonant self-actuation, (b) cantilever front oscillation frequency, (c) electrical power output determined from the induced current of the pick-up coil.
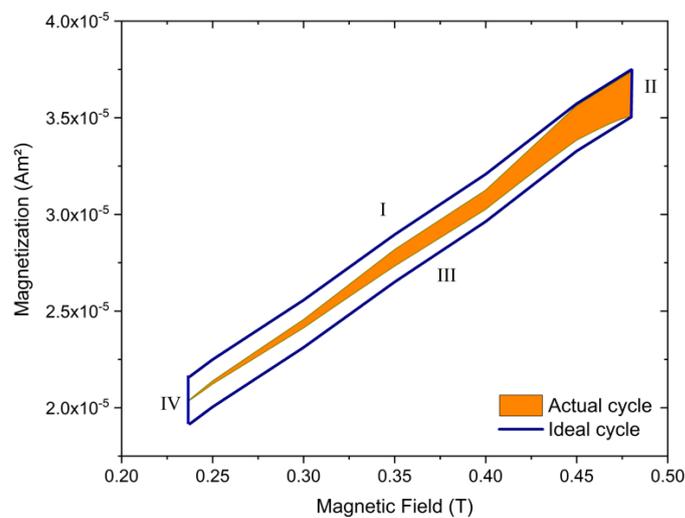


**Figure A 13** The thermomagnetic cycle of the Gd-film TMG was simulated using LEM for $T_{source}$ of 40 °C and $T_{amb}$ of 11 °C. In an ideal world, the cycle would consist of four phases shown by stages I-IV. But in the actual cycle, stages III, IV and I are combined into an continuous path as the device is not maintaining adiabatic conditions in stage III and I, nor does it have a heat sink at stage IV. We evaluate the material's efficiency using the simulated thermomagnetic cycle, which is represented by the ratio of output magnetic energy $EMag$ to input heat energy $Qinput$ ($\eta = {}^{EMag}/_{Qinput}$).

**Table A 2** LEM simulation values of major thermal properties of TMG

| **TMG based on Gadolinium film** | | | | | | | |
|---|---|---|---|---|---|---|---|
| **Ambient temperature: 9°C** | | | | | | | |
| Source temperature ($T_{source}$) | 40°C | 45°C | 50°c | 55°C | 60°C | 65°C | 70°C |
| Sink temperature ($T_{cant}$) | 25.75 | 25.75 | 29.05 | 28.05 | 28.45 | 28.75 | 31.15 |
| $T_{film}$(max) | 27.15 | 27.15 | 27.14 | 29.15 | 29.55 | 29.85 | 32.45 |
| $T_{film}$ (min) | 25.85 | 25.85 | 29.05 | 28.15 | 28.55 | 28.85 | 31.25 |
| Temperature change (ΔT) | 1.3 | 1.3 | 1 | 1 | 1 | 1 | 1.2 |
| **Ambient temperature:11°C** | | | | | | | |
| Source temperature ($T_{source}$) | 40°C | 45°C | 50°c | 55°C | 60°C | 65°C | 70°C |
| Sink temperature ($T_{cant}$) | 25.15 | 26.06 | 26.45 | 26.55 | 26.55 | 28.35 | 30.35 |
| $T_{film}$ (max) | 26.15 | 27.05 | 27.55 | 27.55 | 27.55 | 29.35 | 31.55 |
| $T_{film}$(min) | 25.25 | 26.06 | 26.55 | 26.65 | 26.65 | 28.45 | 30.45 |
| Temperature change (ΔT) | 1 | 1 | 1 | 0.9 | 0.9 | 0.9 | 1.1 |
| **Ambient Temperature: 13°C** | | | | | | | |
| Source temperature ($T_{source}$) | 40°C | 45°C | 50°c | 55°C | 60°C | 65°C | 70°C |
| Sink temperature ($T_{cant}$) | 25.25 | 26.05 | 28.25 | 28.45 | 30.25 | 30.35 | 30.55 |
| $T_{film}$ (max) | 26.15 | 26.85 | 29.25 | 29.45 | 31.25 | 31.35 | 31.45 |
| $T_{film}$ (min) | 25.35 | 26.05 | 28.35 | 28.55 | 30.35 | 30.45 | 30.65 |
| Temperature change (ΔT) | 0.8 | 0.8 | 0.9 | 0.9 | 0.9 | 0.9 | 0.8 |
| **Ambient Temperature: 17°C** | | | | | | | |
| Source temperature ($T_{source}$) | 40°C | 45°C | 50°c | 55°C | 60°C | 65°C | 70°C |
| Sink temperature ($T_{cant}$) | - | 27.85 | 28.45 | 28.35 | 28.35 | 29.35 | 30.45 |
| $T_{film}$ (max) | - | 28.75 | 29.35 | 29.15 | 29.15 | 20.35 | 31.25 |
| $T_{film}$(min) | - | 27.95 | 28.55 | 28.45 | 28.45 | 29.85 | 30.55 |
| Temperature change (ΔT) | - | 0.8 | 0.8 | 0.7 | 0.7 | 0.5 | 0.7 |

| Ambient Temperature: 19°C | | | | | | | |
|---|---|---|---|---|---|---|---|
| Source temperature ($T_{source}$) | 40°C | 45°C | 50°c | 55°C | 60°C | 65°C | 70°C |
| Sink temperature ($T_{cant}$) | - | - | 28.55 | 28.45 | 30.45 | 33.15 | 34.05 |
| $T_{film}$ (max) | - | - | 29.05 | 31.05 | 31.15 | 33.95 | 35.25 |
| $T_{film}$(min) | - | - | 28.65 | 28.55 | 30.55 | 33.25 | 34.15 |
| Temperature change (ΔT) | - | - | 0.5 | 0.5 | 0.6 | 0.7 | 1.1 |

| TMG based on La-Fe-Si-H film | | | | |
|---|---|---|---|---|
| Source temperature ($T_{source}$) | 70°C | 80°C | 90°C | 100°C |
| Sink temperature ($T_{cant}$) | 49.05 | 47.83 | 48.48 | 49.17 |
| $T_{film}$ (max) | 49.85 | 49.25 | 49.95 | 50.75 |
| $T_{film}$(min) | 49.65 | 48.85 | 49.55 | 50.35 |
| Temperature change (ΔT) | 0.2 | 0.4 | 0.4 | 0.4 |